

**DEVELOPMENT OF VIBRATION-BASED
MULTI-RESONANCE ENERGY HARVESTERS USING
PIEZOELECTRIC MATERIALS**

A thesis submitted to the University of Manchester for the degree of Doctor of Philosophy
in Faculty of Engineering and Physical Sciences

2014

Xingyu Xiong

School of Mechanical, Aerospace and Civil Engineering

TABLE OF CONTENTS

TABLE OF CONTENTS	2
LIST OF FIGURES	6
LIST OF TABLES	7
NOMENCLATURE.....	8
LIST OF ABBREVIATIONS	11
ABSTRACT.....	12
DECLARATION	13
COPYRIGHT STATEMENT	14
ACKNOWLEDGMENTS	15
CHAPTER 1 INTRODUCTION	16
1.1 Background on energy harvesting	16
1.1.1 Energy harvesting for health monitoring.....	16
1.1.2 Energy harvesting techniques	17
1.1.3 Piezoelectric effect.....	21
1.2 Motivations.....	22
1.3 Aims and objectives of thesis	24
1.4 Contributions to knowledge	25
1.5 Outline of thesis.....	26
CHAPTER 2 LITERATURE REVIEW	29
2.1 Overview	29
2.2 Power conversion efficiency	29
2.3 Piezoelectric materials.....	31
2.3.1 Common piezoelectric materials	31
2.3.2 Piezoelectric composites.....	32
2.3.3 High performance single crystal	36
2.4 Cantilevered beam harvesters.....	38

2.5 Broadband harvesters	41
2.5.1 Multi-resonance harvesters	41
2.5.2 Nonlinear techniques	44
2.5.3 Tuning techniques.....	46
2.6 Rectifier circuits	48
2.7 Conclusions	49
CHAPTER 3 MODELLING METHODOLOGY AND THEORETICAL BACKGROUND	50
3.1 Introduction	50
3.2 Distributed parameter electromechanical modelling.....	51
3.2.1 Analytical modelling of cantilevered beam harvester	51
3.2.2 FEA derivation of the modal parameters	56
3.3 A modal approach	59
3.3.1 Corrected SDOF model	59
3.3.2 Mass ratio.....	61
3.3.3 A modal approach using mass ratio and EMCC.....	62
3.3.4 Implementation of the modal approach using FEA	64
3.3.5 A configurational optimization strategy for multi-resonance harvesters.....	64
3.4 Summary	67
CHAPTER 4 RESEARCH OVERVIEW AND CONTRIBUTIONS	68
4.1 Introduction	68
4.2 Research overview	68
4.3 Outline of published/submitted papers	72
4.3.1 Modal electromechanical optimization of cantilevered piezoelectric vibration energy harvesters by geometric variation	72
4.3.2 Optimal design of two-layer stacked vibration energy harvesters using a modal approach.....	73
4.3.3 Tapered two-layer broadband vibration energy harvesters.....	73

4.3.4 A general modal approach for the development of optimal multi-layer stacked vibration energy harvesters	74
4.3.5 Modal optimization of doubly-clamped base-excited multilayer broadband vibration energy harvesters	74
4.3.6 An equivalent circuit model using corrected lumped modal parameters for multi-resonance piezoelectric vibration energy harvesting	75
4.3.7 Design, analysis and experimental validation of the performance of multi-layer stacked vibration energy harvesters	75
4.3.8 Experimental study of the broadband performance of multi-layer vibration energy harvesters using PZT and PIMNT	76
4.4 Summary	76
CHAPTER 5 MODAL ELECTROMECHANICAL OPTIMIZATION OF CANTILEVERED PIEZOELECTRIC VIBRATION ENERGY HARVESTERS BY GEOMETRIC VARIATION	77
CHAPTER 6 OPTIMAL DESIGN OF TWO-LAYER STACKED VIBRATION ENERGY HARVESTERS USING A MODAL APPROACH.....	78
CHAPTER 7 TAPERED TWO-LAYER BROADBAND VIBRATION ENERGY HARVESTERS.....	79
CHAPTER 8 A GENERAL MODAL APPROACH FOR THE DEVELOPMENT OF OPTIMAL MULTI-LAYER STACKED VIBRATION ENERGY HARVESTERS	80
CHAPTER 9 MODAL OPTIMIZATION OF DOUBLY-CLAMPED BASE-EXCITED MULTILAYER BROADBAND VIBRATION ENERGY HARVESTERS	81
CHAPTER 10 AN EQUIVALENT CIRCUIT MODEL USING CORRECTED LUMPED MODAL PARAMETERS FOR MULTI-RESONANCE PIEZOELECTRIC VIBRATION ENERGY HARVESTING	81
CHAPTER 11 DESIGN, ANALYSIS AND EXPERIMENTAL VALIDATION OF THE PERFORMANCE OF MULTI-LAYER STACKED VIBRATION ENERGY HARVESTERS	83

CHAPTER 12 EXPERIMENTAL STUDY OF THE BROADBAND PERFORMANCE
OF MULTI-LAYER VIBRATION ENERGY HARVESTERS USING PZT AND PIMNT
.....84

CHAPTER 13 CONCLUSIONS AND FUTURE WORKS.....85

 13.1 Conclusions and summary of findings85

 13.2 Proposals for future work89

REFERENCE.....91

APPENDIX A PIEZOELECTRIC CONSTITUTIVE EQUATIONS AND COUPLING
COEFFICIENT96

LIST OF FIGURES

Figure 1.1: Power consumption of electronic devices and wireless sensor networks (WSN), and power supply from energy harvesting (EH) and batteries.....	17
Figure 1.2: Vibration energy harvesting schematics.....	19
Figure 1.3: Comparison of 5 years lifetime power density between energy harvesting and batteries	21
Figure 1.4: Piezoelectric Effect on a cylindrical piezo-ceramic	21
Figure 1.5: Orientations of electric dipoles of piezoelectric materials before, during and after the poling process	22
Figure 2.1: Two common coupling modes used in piezoelectric harvesters	30
Figure 2.2: Connectivity patterns of two-phase piezoelectric composites.....	32
Figure 2.3: Typical piezoelectric composite structures.....	33
Figure 2.4: Cutting and filling process to fabricate 2-2 and 1-3 piezoelectric composites..	33
Figure 2.5: A piezoelectric fibre composite.....	36
Figure 2.6: Tapered thick-film harvester.	40
Figure 2.7: Array of bimorph cantilevered beams harvester.....	41
Figure 2.8: Experimental setup of a dual-mass harvester	42
Figure 2.9: A modified dual-mass harvester	43
Figure 2.10: The zigzag energy harvester	44
Figure 2.11: 3dB-bandwidth comparisons between linear and nonlinear systems	45
Figure 2.12: Two typical bistable non-linear harvesters using magnets.....	46
Figure 2.13: A harvester using mechanical tuning method	47
Figure 2.14: A sketch of the harvester using magnetic tuning method.....	47
Figure 2.15: A sketch of the harvester using piezoelectric tuning method.....	48
Figure 2.16: Typical rectifier circuits schematics	49
Figure 3.1: A cantilevered bimorph harvester.....	52
Figure 3.2: Cross-section in y-z plane pf a cantilevered bimorph harvester.....	52
Figure 3.3: Maximum MSAPD as function of $k^2 Q_m$ with different mass ratio N.....	62
Figure 3.4: Flow charts for configurational designs of vibration energy harvesters.	63
Figure 3.5: Power FRFs of harvesters and broadband performance comparison	67
Figure 3.6: Flow chart of the configurational optimization strategy for multi-resonance..	67

LIST OF TABLES

Table 1.1: Energy and power sources comparisons	20
Table 1.2: Acceleration amplitudes and fundamental natural frequencies of some environmental vibration sources	20
Table 2.1: A comparison of piezoelectric properties between piezoelectric film, 0-3 composites and monolithic ceramic	34
Table 2.2: Structural properties of different PZT/P(VDF-HFP)-composites and bulky ceramic.	35
Table 2.3: Piezoelectric properties of the PMNT crystal and PZT-5H ceramics.....	36
Table 2.4: Comparison of experimental results using PMNT and PZT materials	37
Table 3.1: Equivalent coupling term θ and piezoelectric capacitance C_p in parallel and series connections of a RC harvester with bimorph structures	55

NOMENCLATURE

A	electrode area
b	width of beam
c_a	viscous damping coefficient from air
c_m	lumped modal damping coefficient
c_s	strain-rate damping coefficient
c_{11}^E	elastic matrix component of piezoelectric materials under constant electric field
C_p	equivalent piezoelectric capacitance
$[C]$	damping matrix
D_3	electric displacement in 3- or z-direction
e_{31}	piezoelectric constant in stress form for 3-1 mode
E_3	electric field in 3- or z-direction
$F_m; F_{mc}$	SDOF and corrected SDOF modal forcing function, respectively
F_r	mass-normalised modal mechanical forcing term in r-th mode
\tilde{F}_r	complex amplitude of mass-normalised modal mechanical forcing term in r-th mode
$\{\mathbf{F}\}$	mechanical force vector
h_p	thickness of each piezoelectric layer
h_{pc}	distance from centre of each piezoelectric layer to neutral axis of beam
h_s	thickness of substrate layer
$i; \tilde{i}$	real and complex electric current;
I	second moment of area
j	imaginary unit
$k; k_{31}; k_{33}$	piezoelectric electro-mechanical coupling coefficient; for 31-mode; for 33-mode
k_m	lumped modal stiffness
$[K]$	stiffness matrix
L	length of beam

m	mass per unit length of beam
m_e	effective mass
m_m	modal mass
m_T	total mass
\bar{M}	internal bending moment
$[M]$	mass matrix
N	mass ratio
P_{max}	maximum average power
Q_m	quality factor
$\{Q\}$	electrical charge vector
R_l	resistive load/resistor
S_1^s	axial strain of substrate layer
$T_1^p; T_1^s$	stress along 1- or x-direction of piezoelectric and substrate layer, respectively
T_{rel}	relative motion transmissibility
$T_{SDOF}; T_{SDOFc}$	SDOF and corrected SDOF relative motion transmissibility, respectively
$u; \tilde{u}$	real and complex vibration displacement of beam
u_0	amplitude of base excitation
u_b	absolute vibration base displacement
$u_{rel}; \tilde{u}_{rel}$	real and complex relative displacement relative to moving base u_b
$\{u\}$	vector of nodal displacements
$v; \tilde{v}$	real and complex voltage on piezoelectric layer
$\{v\}$	vector of nodal electric potential
x	1- or x-coordinate
Y_s	Young's modulus of substrate layer
z	3- or z-coordinate
α	lumped modal coupling factor
$\gamma; \Gamma$	modal participation factor
ϵ_{33}^s	permittivity under constant strain in 3- or z-direction
ζ	damping ratio
$\eta; \tilde{\eta}$	real and complex modal coordinates
θ	coupling term

$\lambda; \sigma$	dimensionless frequency numbers
ρ	mass density
χ	equivalent modal electromechanical coupling term
$\omega_r; \omega_n$	undamped angular resonance frequency
$\phi; \{\phi\}$	mass-normalised eigenfunction, eigenvector

LIST OF ABBREVIATIONS

CTC	convergent tapered cantilevered
DPM	distributed parameter electromechanical model
DTC	divergent tapered cantilevered
ECM	equivalent circuit method
EMCC	electromechanical coupling coefficient
FEA	finite element analysis
FRF	frequency response function
MDOF	multiple degrees of freedom
MEMS	micro-electromechanical systems
MSAPD	mean squared acceleration weighted power density
PIMNT	lead indium magnesium niobate titanate (relaxor ferroelectric single-crystal)
PMNT	lead magnesium niobate titanate (relaxor ferroelectric single-crystal)
PVDF	polyvinylidene difluoride
PZT	lead zirconium titanate
RC	rectangular cantilevered
SDOF	single degree of freedom
SSHI	synchronized Switch Harvesting on Inductor
VEH	vibration energy harvester

ABSTRACT

Xingyu Xiong – Doctor of Philosophy
The University of Manchester

Development of vibration-based multi-resonance energy harvesters using piezoelectric materials

The development of self-powered wireless sensor networks for structural and machinery health monitoring has attracted considerable attention in the research field during the last decade. Since the low-duty-cycle wireless sensor networks have significantly reduced the power requirements to the range of tens to hundreds of microwatts, it is possible to harvest environmental energy as the power supply instead of using batteries. Vibration energy harvesting using piezoelectric materials has become the most popular technique, which has a good potential to generate adequate power. However, there is a limitation for the conventional beam-shaped harvester designs in real applications due to their limited bandwidth. In order to overcome this limitation, the essential objective of this thesis is to develop harvesters with multi-resonance structures. The multi-resonance harvester with good broadband performance can achieve close resonance frequencies and relatively large power output in each vibration mode. The main tasks and contributions of this thesis are summarised as follows:

- A parametric analysis is presented to determine how the modal structural and electromechanical performances of cantilevered beam harvesters are affected by two modal factors designated as mass ratio and electromechanical coupling coefficient (EMCC). The modal performance of using rectangular, convergent and divergent tapered configurations with and without extra masses are systematically analysed by geometric variation using the finite element analysis (FEA) software ABAQUS.
- A modal approach using the two modal factors to evaluate the modal performance of harvesters is introduced and a configurational optimization strategy based on the modal approach is developed to pre-select the configurations of multi-resonance harvesters with better modal structural performance and close resonance frequencies in multiple modes. Using this optimization strategy obviates the need to run the full analysis at the first stage.
- A novel two-layer stacked harvester, which consists of a base cantilevered beam that is connected to an upper beam by a rigid mass, is developed. By altering the dimensions and the locations of the masses, the two-layer harvester can generate two close resonance frequencies with relatively large power output. The effects of using rectangular, convergent and divergent tapered beam configurations are systematically analysed.
- Multi-layer stacked harvesters with up to five layers are developed. The three-layer harvesters with different mass positions, which can generate three close resonance frequencies, are optimized using the configurational optimization strategy.
- A novel doubly-clamped multi-layer harvester, which is able to generate five close resonance frequencies with relatively large power output, is developed and thoroughly analysed.
- An experimental study of the multi-layer stacked harvester is presented to validate the simulated results and the configurational optimization strategy.
- An experimental study of the two-layer stacked harvester using high performance single crystal piezoelectric material PIMNT is presented. The harvester using PIMNT can generate nearly 10 times larger power output and 3.5 times wider bandwidth than using PZT. Besides, by modifying the location of the piezoelectric layer, anti-resonances between two adjacent modes can be eliminated.

DECLARATION

I declare that no portion of the work referred to in the thesis has been submitted in support of an application for another degree or qualification of this or any other university or other institute of learning

COPYRIGHT STATEMENT

The following four notes on copyright and the ownership of intellectual property rights must be included as written below:

- i. The author of this thesis (including any appendices and/or schedules to this thesis) owns certain copyright or related rights in it (the “Copyright”) and s/he has given The University of Manchester certain rights to use such Copyright, including for administrative purposes.
- ii. Copies of this thesis, either in full or in extracts and whether in hard or electronic copy, may be made **only** in accordance with the Copyright, Designs and Patents Act 1988 (as amended) and regulations issued under it or, where appropriate, in accordance with licensing agreements which the University has from time to time. This page must form part of any such copies made.
- iii. The ownership of certain Copyright, patents, designs, trade marks and other intellectual property (the “Intellectual Property”) and any reproductions of copyright works in the thesis, for example graphs and tables (“Reproductions”), which may be described in this thesis, may not be owned by the author and may be owned by third parties. Such Intellectual Property and Reproductions cannot and must not be made available for use without the prior written permission of the owner(s) of the relevant Intellectual Property and/or Reproductions.
- iv. Further information on the conditions under which disclosure, publication and commercialisation of this thesis, the Copyright and any Intellectual Property and/or Reproductions described in it may take place is available in the University IP Policy (see <http://documents.manchester.ac.uk/DocuInfo.aspx?DocID=487>), in any relevant Thesis restriction declarations deposited in the University Library, The University Library’s regulations (see <http://www.manchester.ac.uk/library/aboutus/regulations>) and in The University’s policy on Presentation of Theses

ACKNOWLEDGMENTS

I would like to thank my girlfriend who has always encouraged me about my study.

I would also like to thank my supervisor, Dr. Sunday Olutunde Oyadiji, who has always been extremely responsible to his students.

I would also like to thank my friends and colleagues who have helped me a lot during my study.

Special thanks to my mom and my dad. They really love me and support me in no conditions at any time.

CHAPTER 1 INTRODUCTION

1.1 Background on energy harvesting

1.1.1 Energy harvesting for health monitoring

Many sources of environmental energy are harvestable, such as waste heat, vibration, human motion, electromagnetic waves, wind, flowing water, and solar energy. The technique to harness such environmental energy and convert it into electrical energy is designated as energy harvesting. In fact, some energy harvesting techniques can provide huge amounts of clean electrical power. For example, solar and wind energy harvesting techniques are well-developed and already play important roles in our lives. However, some small-scale ambient energy sources, such as vibration and human motion, are normally ignored and have not been sufficiently used. This thesis focuses on the utilisation of such small-scale ambient energy. In particular, the vibration energy harvesting technique using piezoelectric materials are investigated.

Before introducing existing energy harvesting techniques in further details, smart materials, structures and systems need to be discussed. Smart materials have the capability to respond to stress, temperature, moisture, pH, electric or magnetic fields to exhibit adaptive characteristics, and eventually achieve multifunction and reduce life-cycle cost when integrated with other conventional materials and structures. The ideal smart system, which consists of the smart materials and structures, can adapt the required structural characteristics, monitor the structural health condition, achieve self-diagnosis and self-repair, morph the shape, and undergo controlled motion over different operating conditions [1]. To achieve such ambitious goal eventually, great efforts have been made progressively in multidisciplinary frontiers in the past few decades.

Structural and machinery health monitoring play an imperative role in smart structures and systems. Wireless sensor networks are widely used to collect and transmit the monitoring

data. However, the conventional wireless sensor nodes are powered by batteries. In order to replace the batteries periodically, continuous maintenance is required. Then, the applications of such wireless sensor nodes are limited. Because of the developments of very-large-scale integration system, the low-duty-cycle wireless sensor networks have significantly reduced the power requirements to the range of tens to hundreds of microwatts [2]. For such low power needs, instead of using batteries, it is possible to develop self-powered and maintenance-free wireless sensor nodes by harvesting environmental energy.

Apart from the self-powered wireless sensor networks, environmental energy can also be harvested for small electronic devices and portable micro-electromechanical systems (MEMS), such as implanted medical sensors, mobile phones, wearable electronic devices (see Figure 1.1). According to this, the small-scale ambient energy harvesting techniques have become attention-grabbing topics in the last decade [3-6].

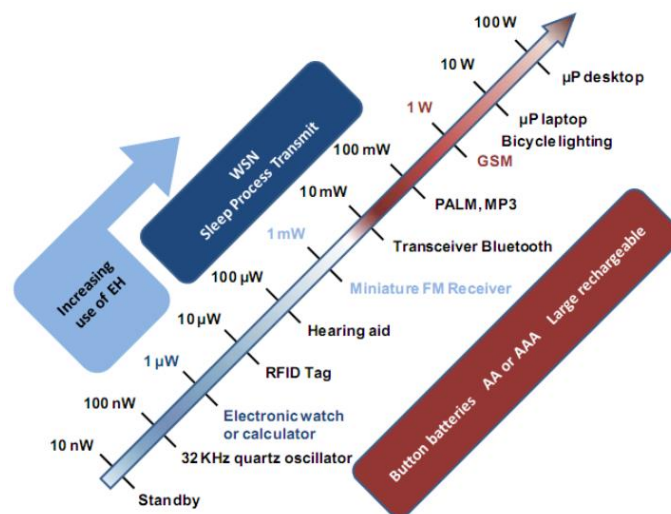


Figure 1.1: Power consumption of electronic devices and wireless sensor networks (WSN), and power supply from energy harvesting (EH) and batteries [7]

1.1.2 Energy harvesting techniques

In this section, some typical energy harvesting techniques are briefly introduced. One of the most common energy harvesting technique is to convert light into electricity using solar cells based on the photovoltaic effect. A large-scale system normally consists of array

of solar cells, charging circuit and signal processing circuit. Solar energy harvesting systems have many advantages, such as high power density under direct sunlight, ease of integration, lack of noise, and rich energy resources. The disadvantages include low power density for cloudy days, continuous power supply required for the signal processing circuit, and relatively large surface area required for arrays of solar cells. For small-scale uses in wireless sensor networks and portable MEMS, there are other drawbacks such as limited applicability of installation under direct sunlight, very low power density for indoor situations, and low conversion efficiencies [4].

Another exiting technique is thermoelectric energy harvesting. The environmental temperature gradient generates heat flow, which can be used for energy conversion. However, the power density of a thermoelectric system is normally very low due to poor material efficiencies unless the temperature gradient is large [4, 5]. This has affected the applicability of thermoelectric energy harvesting. The thermoelectric wristwatch that converts body heat into electrical power is a successful application since it only requires extraordinarily low power ($1\mu\text{W}$) [5,6].

There is a large amount of electromagnetic wave sources in the environment, such as radio and television broadcasting networks, mobile telecommunications and Wi-Fi networks. Hence, harvesting electromagnetic waves is feasible. The main drawback for electromagnetic wave energy harvesting is that the power density is also very low. Currently, some prototypes have been designed for specific uses and the maximum power density is around tens of microwatts [5].

The implementation of an energy harvesting system using mechanical vibrations has become an area of considerable interest in the last decade [3-6, 8-10]. Vibration energy harvesting is mainly implemented by two mechanisms: applying strain energy to the piezoelectric material (piezoelectric effect) or oscillating magnets/electromagnetic coil (electromagnetic induction). Figure 1.2 (a) shows schematics of the typical vibration energy harvesting system using piezoelectric material. Two piezoelectric layers are bonded on a cantilevered brass substrate to create a bimorph configuration and an extra mass is attached near the tip. When the cantilevered harvester is oscillating around the natural frequency, the strain generated on the substrate is transferred to the piezoelectric layers. Then, the strain energy is converted to electricity based on the piezoelectric effect. Figure

1.2 (b) shows a prototype of an electromagnetic harvester. The magnets and proof mass are bonded on a cantilevered beam, and the electromagnetic coil is fixed on the base. When the magnets are displacing around the coil due to the oscillation of the beam, the kinetic energy is converted to electrical power. Between the two mechanisms, piezoelectric vibration harvesting, which has high electromechanical coupling and easy integration with MEMS, has received much attention [3, 4, 8, 10].

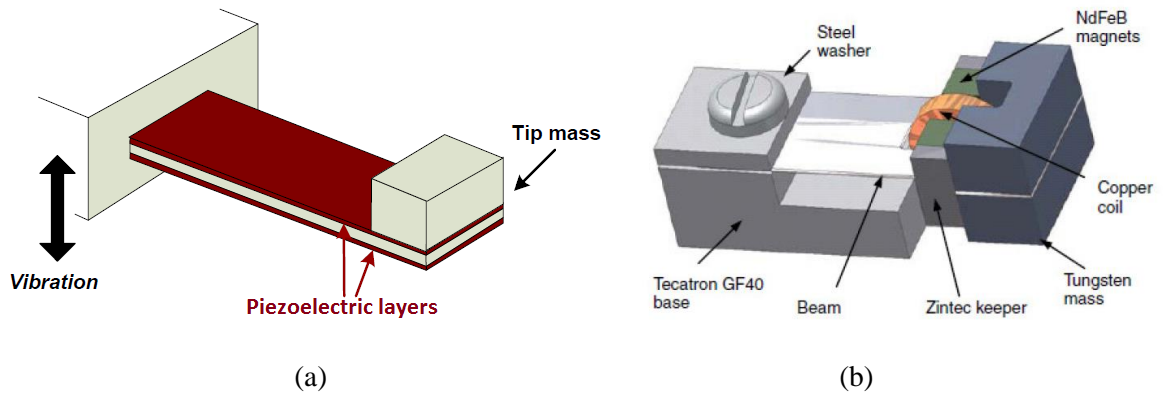


Figure 1.2: Vibration energy harvesting schematics: (a) a cantilevered bimorph piezoelectric harvester with a tip mass; (b) an electromagnetic harvester [11]

Table 1.1 shows some harvestable environmental energy sources and the corresponding converted electrical power density [12]. The data are taken from several existing research articles. The comparison shows that, except for the solar energy harvesting under direct sunlight and heat engine, vibration energy harvesting can generate the maximum power density. In fact, the power density of the vibration energy harvesting is largely affected by the amplitudes of the mechanical input. With lower natural frequency and larger acceleration excitation, a piezoelectric harvester can generate larger power density. Table 1.2 shows the maximum acceleration amplitudes and fundamental natural frequencies of some environmental vibration sources [13]. The maximum performances of the piezoelectric harvesting systems vary with different vibration sources.

Besides, an energy harvesting system may not always operate at its maximum performance in real applications. Therefore, to evaluate the performance of an energy harvesting system, considering an average power density over a long lifetime should be more reasonable. Figure 1.3 shows a comparison of 5 years lifetime power density between vibration and solar energy harvesting systems and batteries. In this case, the power of batteries will be depleted, which eventually reduces the power density while the power densities of energy harvesting systems are considered as infinity. The vibration energy harvesting system

can generate up to hundreds of microwatts average power density, and it has the potential to generate more power than the solar energy harvesting for indoor/dim light applications. Therefore, using piezoelectric materials to harvest ambient vibration sources has become an attention-grabbing topic for energy harvesting research.

Table 1.1: Energy and power sources comparisons [12]

Power source	Power (μW)/ cm^3	Energy (Joules)/ cm^3	Power (μW)/ cm^3/yr
Primary battery	N/A	2,880	90
Secondary battery	N/A	1,080	34
Micro fuel cell	N/A	3,500	110
Ultracapacitor	N/A	50–100	1.6–3.2
Heat engine	1×10^6	3,346	106
Radioactive (^{63}Ni)	0.52	1,640	0.52
Solar (outside)	15,000*	N/A	N/A
Solar (inside)	10*	N/A	N/A
Temperature	40*†	N/A	N/A
Human power	330	N/A	N/A
Vibrations	375	N/A	N/A
Pressure variation	17§	N/A	N/A

* Measured in power per square centimeter, rather than power per cubic centimeter.

† Demonstrated from a 5°C temperature differential.

§ Based on 1 cm^3 closed volume of helium undergoing a 10°C change once a day.

Table 1.2: Acceleration amplitudes and fundamental natural frequencies of some environmental vibration sources [13]

Vibration sources	Acceleration (m/s^2)	Frequency (Hz)
Car engine compartment	12	200
Base of 3-axis machine tool	10	70
Blender casing	6.4	121
Clothes dryer	3.5	121
Person nervously tapping their heel	3	1
Car instrument panel	3	13
Door frame just after door closes	3	125
Small microwave oven	2.5	121
HVAC vents in office building	0.2–1.5	60
Windows next to a busy road	0.7	100
CD on notebook computer	0.6	75
Second story floor of busy office	0.2	100

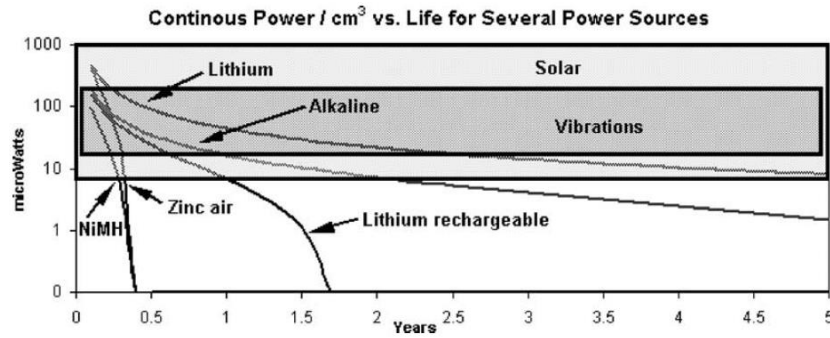


Figure 1.3: Comparison of 5 years lifetime power density between energy harvesting and batteries [13]

1.1.3 Piezoelectric effect

When a piezoelectric device undergoes strain, it yields electrical displacement and electrical potential due to the piezoelectric effect. By bonding electrodes on the piezoelectric material and connecting the electrodes with electrical components, the generated voltage and current from the piezoelectric layer are applied on the electrical components. Vibration energy harvesters are designed to collect this electrical energy by either consuming it directly or storing it for further usage.

The piezoelectric effect occurs in two domains, which are designated as the direct piezoelectric effect and the converse piezoelectric effect [14]. The direct effect describes the ability of piezoelectric materials to transform mechanical strain into electrical charge, and the converse effect represents the trait of piezoelectric materials to convert an applied electrical potential into mechanical strain (see Figure 1.4).

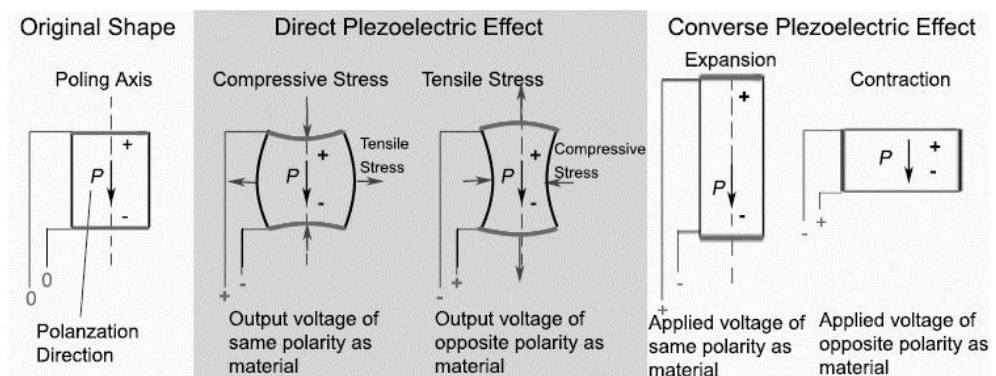


Figure 1.4: Piezoelectric Effect on a cylindrical piezo-ceramic [15]

A piezoelectric material has the feature that its molecular structure is oriented with a local charge separation, which is known as an electric dipole. The electric dipoles are oriented

randomly throughout the original material composition when the material is not poled. When the piezoelectric material is heated above its Curie temperature, and a very strong electric field is applied, the electric dipoles become reoriented along the direction of the electric field. This is called the poling process. After the poling process, the applied electric field is removed and the material is cooled down to room temperature. The orientations of the electric dipoles are maintained (see Figure 1.5), and the piezoelectric material starts to exhibit the piezoelectric effect [16].

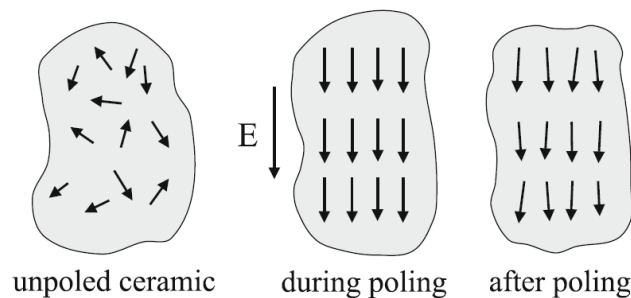


Figure 1.5: Orientations of electric dipoles of piezoelectric materials before, during and after the poling process [17]

1.2 Motivations

As mentioned above, mechanical vibration is an effective source of low-level ambient energy, while resonance is an effective way to generate large strain energy in piezoelectric materials. In real applications, the most common vibration sources are environmental vibrations, which are normally classified as low level, random vibrations within lower frequency ranges [18, 19]. Therefore, to design a general vibration energy harvester, the fundamental vibration mode is normally used especially for beam-shaped harvester designs [8, 13]. However, since the mechanical energy of random vibrations is distributed to broadband frequency ranges, any harvester operating at a specific resonance frequency only generates limited power output. Furthermore, for specific use, vibrations could be more energetic, especially on large industrial equipment. A large portion of the vibration energy on those devices could also concentrate on few resonance frequencies. However, the pre-designed harvester could easily operate off the desired resonance frequency due to manufacturing and assembling errors. The offset of resonance frequency will lead to a significant decrease in the power output. Therefore, the primary motivation of this thesis is

to enhance the broadband performance of harvesters based on multi-resonance technique. In order to cover a broadband frequency range with a wider effective bandwidth for a certain level of power output, the multi-resonance harvesters with good performance can generate close resonance frequencies with relatively large power output in each vibration mode.

Existing works normally use a distributed parameter electromechanical model (DPM), which was introduced by E Turk and Inman [20, 21], to evaluate the voltage and power output performance of the harvester with resistive loads. However, how the modal characteristics affect the maximum performance of harvesters cannot be directly determined using DPM. In some previous investigations reported in the literature, the predicted power outputs were actually affected by either one-sided or simultaneous changes of mechanical behaviour and electromechanical coupling, but there was no attempt made to analyse the individual effects of these two factors on the output power. Without clearly clarifying the effects from these two factors, the harvester cannot be fully optimized and the variation or improvement of power output in the published results could be confused when comparing results across several publications. Therefore, the secondary motivation is to explore and optimise the modal structural and electromechanical performance on the final power output initially before operating full analysis using DPM.

The conventional optimization using mathematical methods can provide the final optimization results directly but can be rather complex and time consuming. Many existing works are based on the single degree of freedom (SDOF) system or the two degrees of freedom system or the beam model with closed-form solutions [22-25]. However, the optimization process is complicated while only one or few variables are optimized. It is a parametric study and the variables may not be related to the physical configuration directly. Such optimization method is hard to apply to the multi-resonance harvester designs due to the complexity of the configurations. Besides, since the multi-resonance harvester is not a uniform beam, to derive the eigenfunction and other modal parameters analytically can be a tough task. To overcome the limitations, numerical solutions are normally used. The finite element analysis (FEA) software packages like ANSYS, which supports linear circuit simulations, are widely used in existing works [26-28]. However, using FEA software to predict the performance of multi-resonance harvester directly is also not effective. In order to predict the performance for multiple vibration modes, the frequency response functions

(FRFs) of the power output over a wide frequency band need to be provided whereas operating the steady-state analysis over such frequency band in FEA software requires long computing time. An effective optimization method for multi-resonance harvester designs is not provided in existing works. Without proper design, some modes can be far away from others, and some modes are barely active due to poor modal structural or eletromechanical performance. For such multi-resonance harvesters, the capabilities for broadband power output are limited. Therefore, the final motivation is to explore an effective optimization strategy for multi-resonance harvester designs using FEA.

1.3 Aims and objectives of thesis

The overall objectives of this thesis are given below:

- a) Determine how the modal structural and electromechanical performances affect the power output performance of the vibration energy harvesters around each vibration mode.
- b) Determine how the geometric variations of single cantilevered beam-shaped piezoelectric harvesters affect the modal structural and electromechanical performance using FEA, including the effects of using the rectangular, convergent and divergent tapered beam configurations with and without tip masses.
- c) Develop harvesters with good broadband power output performance based on the multi-resonance broadband technique. The configurations of the multi-resonance harvesters consist of multiple beam-shaped substructures that can generate up to five close resonance frequencies over the frequency range from 10 Hz to 100 Hz.
- d) Analyse the modal performance and power output on resistive loads of the multi-resonance harvesters and optimize the configurational performance of these harvesters using FEA.
- e) Validate the performance of the multi-resonance harvesters in experimental study.

- f) Use the high performance piezoelectric material “relaxor ferroelectric single-crystal lead indium magnesium niobate titanate (PIMNT), $\text{Pb}[\text{In}_{1/2}\text{Nb}_{1/2}]\text{O}_3$ – $\text{Pb}[\text{Mg}_{1/3}\text{Nb}_{2/3}]\text{O}_3$ – PbTiO_3 ” for multi-resonance harvester designs and compare with the broadband performance of the harvesters using the common piezoelectric material “lead zirconium titanate (PZT), $\text{Pb}[\text{Zr}_x\text{Ti}_{1-x}]\text{O}_3$ ” in experimental study.
- g) Develop an equivalent circuit method (ECM) for multi-resonance harvesters to connect the structural modelling to electrical circuitry modelling.

1.4 Contributions to knowledge

The main contributions to knowledge of this thesis are given below:

- a) The power outputs of harvesters are affected by the simultaneous changes of structural behaviour and electromechanical coupling. However, no attempt has been made in previous investigations to analyse the individual effects of these two factors on the output power. In this thesis, a parametric analysis is presented to determine how the modal structural and electromechanical performances are affected by two modal factors designated as mass ratio and electromechanical coupling coefficient (EMCC).
- b) A novel modal approach is presented to optimize the modal performance of rectangular, convergent and divergent tapered cantilevered beam harvesters via the optimisation of the mass ratio and EMCC.
- c) A novel configurational optimization strategy, based on the modal approach, is developed to produce multi-resonance harvesters with close resonance frequencies and relatively large power output in each mode to give good broadband performance. This is the first work in which an effective optimization method has been developed for the configurations of multi-resonance harvesters. Using the configurational optimization strategy enables easy selection of the configurations with optimal or near-optimal structural broadband performance from hundreds of

configurations and it obviates the need to operate full steady-state analysis at the first stage.

- d) Novel multi-layer stacked harvesters, which consist of a base beam that is connected to upper/lower beams by rigid masses, are developed. By varying the locations of the masses, the multi-layer harvesters can generate up to five close resonance frequencies with relatively large power output. The configurations with preferred broadband performance are determined using the configurational optimization strategy.
- e) It is shown both theoretically and experimentally that the two-layer stacked harvesters can generate 1.5 times wider bandwidth and the three-layer stacked harvesters can generate 2 times wider bandwidth than the single layer harvester with a tip mass. Thus, the benefit of stacking of harvesters is demonstrated theoretically and validated experimentally.
- f) This is the first work in which the high performance relaxor ferroelectric single-crystal PIMNT has been used in multi-resonance harvester designs and experimental tests. It has been found that the PIMNT-based multi-layer harvester can generate nearly 3.5 times wider bandwidth than the PZT-based harvester for the same configuration.
- g) A simplified implementation of the equivalent circuit method (ECM), which uses corrected lumped modal parameters, is developed.

More details can be found in Chapter 4, which presents the research overview and contribution summaries for the published, accepted and submitted journal papers presented in Chapters 5 to 12.

1.5 Outline of thesis

This thesis is written in *Alternative Format*. It consists of two parts. The first part includes chapter one (introduction), chapter two (literature review), chapter three (theoretical

background and modelling methodology), chapter four (research overview and contributions) and chapter thirteen (conclusions and future work). The citations in these four chapters are listed in the Reference section at the end of the thesis. The second part includes eight chapters from chapter five to chapter twelve, which are the published, accepted and submitted journal articles. Each paper is self-contained and, therefore, has a list of references at the end. In addition, the figures, tables, nomenclatures and abbreviations presented in each paper have not been summarized in the front of this thesis.

Chapter 1 presents an introduction of the thesis, including the background of energy harvesting, brief discussion of existing energy harvesting techniques, and aims and objectives of the thesis.

Chapter 2 presents a literature review of existing investigations, including piezoelectric effect and materials, configurational study and existing broadband techniques, and brief discussion of the existing rectifier circuit techniques.

Chapter 3 presents the theoretical background and modelling methodology used in this thesis.

Chapter 4 presents the research overview of research articles, and states the author's contributions to the work.

Chapter 5 presents a research article: "Modal electromechanical optimization of cantilevered piezoelectric vibration energy harvesters by geometric variation".

Chapter 6 presents a research article: "Optimal design of two-layer stacked vibration energy harvesters using a modal approach".

Chapter 7 presents a research article: "Tapered two-layer broadband vibration energy harvesters".

Chapter 8 presents a research article: "A general modal approach for the development of optimal multi-layer stacked vibration energy harvesters".

Chapter 9 presents a research article: "Modal optimization of doubly-clamped base-excited multilayer broadband vibration energy harvesters".

Chapter 10 presents a research article: "An equivalent circuit model using corrected lumped modal parameters for multi-resonance piezoelectric vibration energy harvesting".

Chapter 11 presents a research article: “Design, analysis and experimental validation of the performance of multi-layer stacked vibration energy harvesters”.

Chapter 12 presents a research article: “Experimental study of the broadband performance of multi-layer vibration energy harvesters using PZT and PIMNT”.

Chapter 13 presents the conclusions of the thesis including a critical review of the work and the ideas and possibilities of the future study.

CHAPTER 2 LITERATURE REVIEW

2.1 Overview

The aim to enhance the performance of piezoelectric vibration energy harvester has led to developing different techniques for different aspects. In this chapter, the reviews of the existing literatures are mainly focused on investigating the performances of piezoelectric materials and harvester configurations.

Since piezoelectric materials are used to transfer strain energy to electrical energy, the power conversion efficiency due to the properties of the piezoelectric materials and the corresponding coupling modes can largely affect the power output of harvesters. Besides, the common piezoelectric ceramics are normally brittle, which causes limitations in the power harvesting applications. The performances of some more flexible piezoelectric materials used in vibration energy harvesting are widely investigated in the last decade.

Cantilevered beam harvesters are widely used due to the easy fabrication and installation. However, the cantilevered beam harvester has limited broadband performance. To overcome this limitation, the broadband harvesters are developed based on different techniques. For example, the multi-resonance harvesters, the nonlinear harvesters with magnets and the resonance tuning technique have attracted much attention recently.

2.2 Power conversion efficiency

The piezoelectric system interacts between the mechanical and the electrical domains, and a coupling coefficient gives the connection between them. The coupling coefficient k can be defined using energy considerations for an arbitrary quasi-static state of the materials, and it is given by [29]

$$k^2 = \frac{W_{coup}}{W_{mech} + W_{elec}} \quad (2.5)$$

where W_{coup} is the coupled energy density, W_{mech} is the strain energy density and W_{elec} is the dielectric energy density. This explanation of the coupling coefficient is meaningful for the quasi-static electromechanical loading starting from zero initial conditions.

The characteristic coupling coefficient k is based on the piezoelectric material properties. It is a constant parameter and is tested under certain situation, for example, k_{31} of a common piezoelectric ceramic PZT-5A is 0.344. The coupling coefficients of piezoelectric materials can largely affect the actual electromechanical coupling coefficient (EMCC) of harvesters, which eventually affect the power output [30]. EMCC of harvesters can be smaller than the material coupling coefficient because their configurations are not purely piezoelectric but they are constructed with more flexible and stiffer support materials, e.g. steel and aluminium, and also because of the variation of strain. According to the energy explanation of the coupling coefficient k , it is an important factor to determine the power conversion efficiency of a harvester.

Figure 2.1 shows two common coupling modes used in piezoelectric harvesters. The x, y and z axes are designated as numbers 1, 2 and 3, respectively. By assuming the poling direction is 3, when the strain is generated along direction 1 and the voltage is generated along direction 3, the material is said to operate in 31-mode. The 31-mode is the most common coupling mode, and it is widely used in the vibration bending mode especially for beam-shaped harvesters [8, 13]. If the strain and voltage both act in the direction 3, the material is said to operate in 33-mode, which is often used in extension mode, such as piezoelectric stacks.

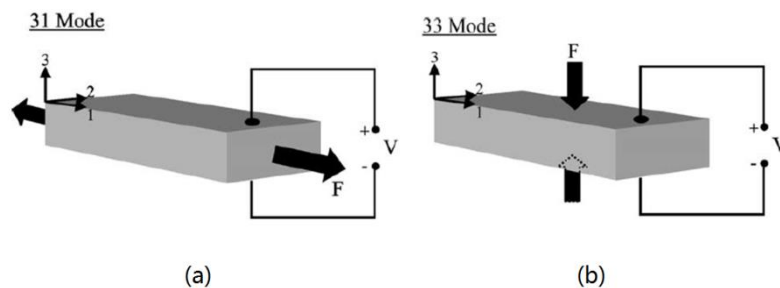


Figure 2.1: Two common coupling modes used in piezoelectric harvesters; (a) 31-mode; (b) 33-mode [13]

For common piezoelectric materials, their k_{33} are much larger than k_{31} , this means using 33-mode could generate higher coupling coefficient than using 31-mode, theoretically. However, existing works prove that a harvester operated in the 33-mode normally generated less power output than a harvester operated in the 31-mode [31]. In fact, large strain can be easily generated for a bending beam harvester using the 31-mode while a piezoelectric stack operated in the 33-mode is too stiff to straining. Besides, the beam-shaped harvesters operated in the 31-mode can generate much lower resonance frequencies, and eventually generate more power [13]. In order to operate a bending beam harvester in the 33-mode, cross-finger electrodes and piezoelectric fibre composites need to be used in a beam-shape harvester. However, research shows that such devices may still generated same level or less power output than devices using monolithic PZT materials [32, 33].

2.3 Piezoelectric materials

2.3.1 Common piezoelectric materials

Up to now, a number of different piezoelectric materials have been used in harvester designs and the results given by existing researches show that the properties of the piezoelectric materials can significantly affect the performance of harvesters.

Lead zirconate titanate is one of the most common piezoelectric materials. It is a piezoelectric ceramic, also known as PZT. PZT is widely used in harvesting applications in recent years [4, 8-10]. The main advantages for using PZT are: (1) PZT has good piezoelectric properties, (2) PZT can be easily used, and (3) the cost of PZT is relatively low in comparison with other piezoelectric materials. However, the piezoelectric ceramics are brittle, which causes limitations in the power harvesting applications. When subjected to large deflections and high frequency cyclic loading, the piezoelectric ceramics are susceptible to the initiation and growth of cracks and fatigue failure [34].

Another common piezoelectric material is piezoelectric polyvinylidene difluoride (PVDF). PVDF is a piezoelectric polymer that is widely used in sensor applications as it provides considerable flexibility in comparison with PZT. However, successful applications using PVDF in vibration energy harvesting are barely seen since the piezoelectricity of PVDF is too weak to generate sufficient power output unless very large vibration amplitude is applied [3, 10]. This has significantly limited its applicability. In fact, due to the

characteristics of the PVDF, it is more likely to be used suitably in flow energy harvesting, such as air flow and water flow [35, 36].

2.3.2 Piezoelectric composites

There are limitations for using single phase piezoelectric materials in vibration energy harvesting, such as the above-mentioned PZT and PVDF. The monolithic piezoelectric materials have good piezoelectricity but they are brittle. The harvesters with large vibration amplitude and large deflection may easily damage the piezoelectric ceramics since they are lacking required flexibility. The piezoelectric polymers are quiet flexible but they also have very weak piezoelectricity. Therefore, the piezoelectric composites, which have better flexibility than monolithic materials and better piezoelectricity than polymers, are widely studied and used for vibration energy harvesting [2, 3, 37-39].

Piezoelectric composites contain two different phases of materials [40], which are single phase piezoelectric ceramics and single phase polymers, such as PZT-epoxy composites. Each phase contains four different self-connectivities in a composite. A single phase may be self-connected in zero, one, two or three axis. The combination of the connectivities are designated as 0-0, 1-0 (0-1), 2-0 (0-2), 3-0 (0-3), 1-1, 2-1 (1-2), 3-1 (1-3), 2-2, 3-2 (2-3) and 3-3 [40]. Figure 2.2 illustrates the connectivities using cubic blocks; and Figure 2.3 presents some typical piezoelectric composite structures.

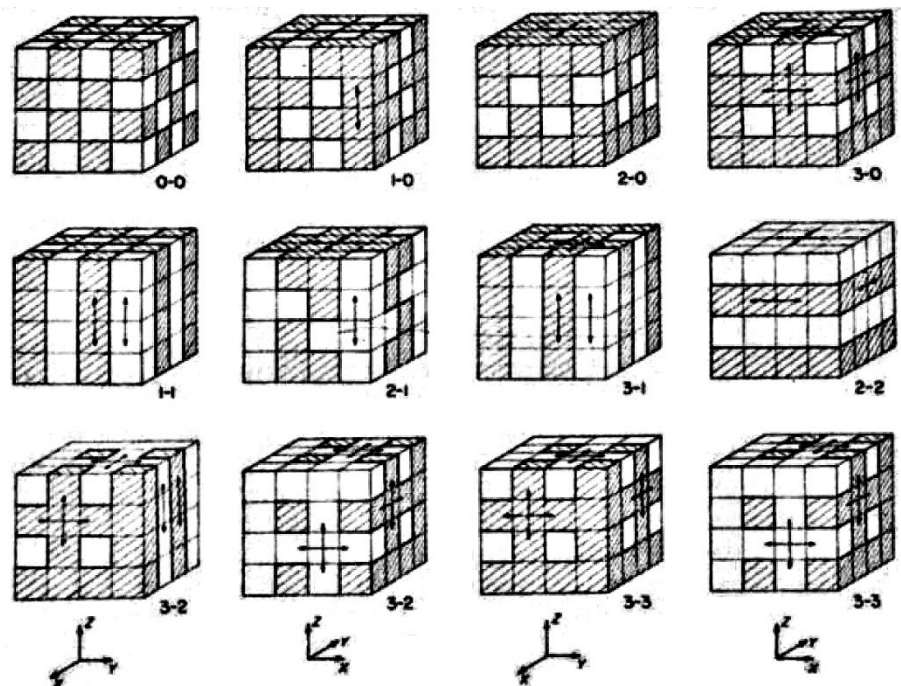


Figure 2.2: Connectivity patterns of two-phase piezoelectric composites [40]

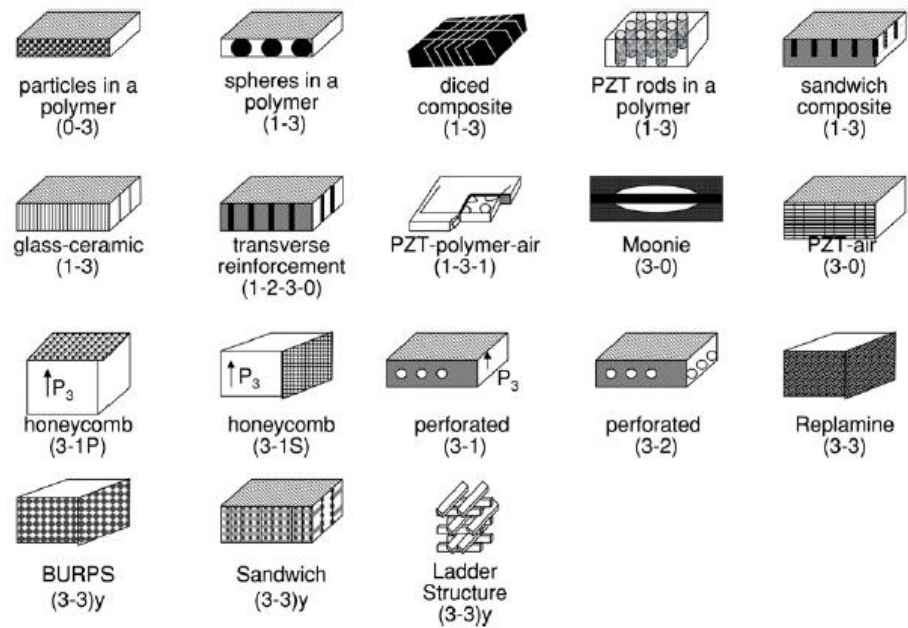


Figure 2.3: Typical piezoelectric composite structures [2]

Many existing works have demonstrated how to fabricate the piezoelectric composites [37, 38, 41], such as solution-mixing method, dicing and filling (as shown in Figure 2.4) and hot-pressed/cold-pressed technique. In fact, the different connectivities, composites structures, poling temperature/voltage/time affect properties of composites noticeably [42]. Thus, for a certain type of composite, a proper solution is always required in order to provide acceptable performance.

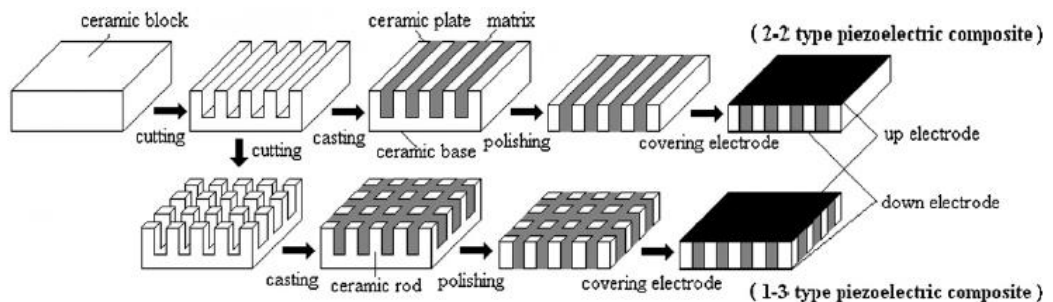


Figure 2.4: Cutting and filling process to fabricate 2-2 and 1-3 piezoelectric composites

[41]

One popular technique is to print a piezoelectric film using ceramic powders on harvesters directly. However, the use of piezoelectric film is restricted since the thickness of the film is normally less than $100\mu\text{m}$, which is too thin to generate enough EMCC on thicker substrates, e.g. 0.5mm . Therefore, the film printing technique is normally used in MEMS [37, 43]. Also, since the powders are not continuously connected in the film, the structure

is porous in comparison to the monolithic ceramics. Therefore, the piezoelectricity of the film is significantly reduced (see Table 2.1).

Since the fabrication of 0-3 piezoelectric composites is less complex, some researchers have investigated the 0-3 composites for energy harvesting applications in recent years. The method to fabricate the 0-3 piezoelectric composites is to mix ceramic powders with polymers, such as epoxy resin or PVDF. Ferrari, et al. developed a cantilevered harvester bonded with a 0.5mm thick PZT 66wt%-epoxy 33wt% composite [48]. Kim, et al. also developed cantilevered harvesters using PZT-epoxy composites, and the effects of different fractions of PZT on the piezoelectric properties were tested [49]. Lei Wang fabricated a dome-shaped harvester using PZT-epoxy composite [50]. However, those works did not generate satisfactory results due to the weak piezoelectricity of the 0-3 composites. In fact, for the 0-3 composite, the phase of the polymer is connected in three dimensions and the piezoelectric ceramic phase is isolated. Therefore, its flexibility is significantly enhanced while the piezoelectricity is substantially weakened.

Table 2.1 shows the comparison of piezoelectric properties between piezoelectric film, 0-3 composites and monolithic ceramic in some existing work. The transverse strain constant d_{31} was not determined in most works, but it is generally less than half of d_{33} . The results show that the piezoelectric film and 0-3 composite have much weaker piezoelectricity than the PZT-5A piezoceramic.

Table 2.1: A comparison of piezoelectric properties between piezoelectric film, 0-3 composites and monolithic ceramic

Researches	Year	Type of composites (volume fraction)	Piezoelectric strain constant		Relative dielectric constant
			d_{31} (pC/N)	d_{33} (pC/N)	ϵ_{33}^T
R.A. Dorey [44]	2004	PMN-PT film (85-15)		60	1800
Swee-Leong Kok [45]	2009	PZT-5H film	-28.6	82	617
S. Banerjee [46]	2011	PZT/Epoxy/Aluminium composites (60-20-20)		4.2	800
Duc Thang Le [47]	2011	KNLNT(lead-free)/epoxy composites (85-15)		44	146
		PZT-5A (monolithic ceramic)*	-171	374	1700

*Morgan Technical Ceramics standard

In fact, the piezoelectric performance of 0-3 composite is mainly contributed by the piezoelectric ceramics and its mechanical performance is based on the polymers. Thus, when the fraction of PZT is increased, the composites normally have better piezoelectricity. However, existing works also show that once the volume fraction of PZT is too large, the composites will become porous and even brittle [51]. This is like the situation in piezoelectric films in which the discontinuity of the piezoceramic particles causes porosity. In the case of the 0-3 composite, the insufficiency of the polymer makes the connectivity of the composite poor and the small gaps between ceramic particles are filled by air or kept vacuumed. This actually reduces the piezoelectricity and flexibility of the composite simultaneously. Table 2.2 shows the performance of PZT-PVDF 0-3 composites with different PZT volume fraction. When the fraction of the PZT material is more than 0.5, the composite becomes porous, which eventually decreases the piezoelectric properties.

Table 2.2: Structural properties of different PZT/P(VDF-HFP)-composites and bulky ceramic [51].

Ceramic-volume fraction ϕ	Density ρ (g cm^{-3})	Permittivity ε'	Piezoelectric coefficient d_{33} (pC N^{-1})	Comment
0	1.8	10.1	0	
0.19	2.9	20.2	4.1	
0.31	3.7	32.6	7.7	
0.41	4.1	49.4	8.9	
0.48	4.6	62.6	11.3	
0.53	4.5	59.9	10.0	Porous
0.58	4.0	64.2	9.4	Porous
0.61	—	—	—	Brittle
0.65	—	—	—	Brittle
1	7.8	1750	287	

In general, a lot of investigations have been concentrated on the 0-3 piezoelectric composites in the last decade [41-47]. Unfortunately, a well-designed 0-3 composite still generates much weaker piezoelectric performance than a single phase PZT ceramic. It is the most critical issue of using the 0-3 composites in vibration energy harvesting. Therefore, the 0-3 piezoelectric is only suggested for applications with large vibration amplitude and large deflections.

Current research has shown that 1-3 composites can improve the flexibility and piezoelectricity simultaneously in comparison with 0-3 connectivity, and harvesters using

the 1-3 composites are also reported in the literature [33, 36, 39, 52-54]. For example, Figure 2.5 shows a common 1-3 piezoelectric fibre composite, and it is fabricated using PZT fibre and epoxy. The existing products of PZT fibre normally have diameters from 10 to 250 μm . However, a well-designed 1-3 composite normally requires complex and precise fabrication techniques with expensive devices, but also have limitation of shapes and dimensions. This has substantially limited the applicability of the 1-3 composites in the vibration energy harvesting topic.

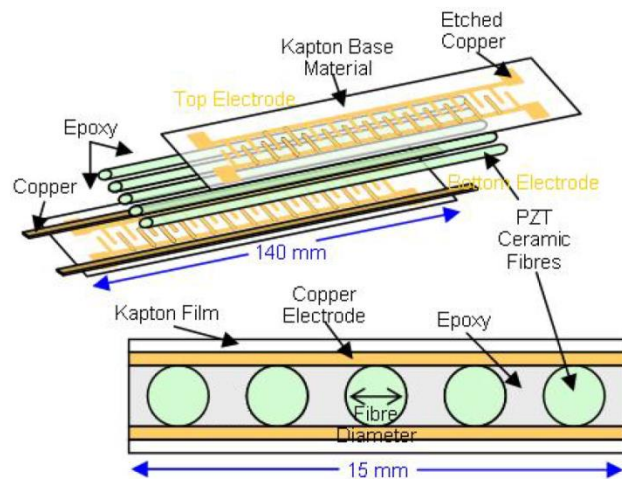


Figure 2.5: A piezoelectric fibre composite [54]

2.3.3 High performance single crystal

A high performance piezoelectric single crystal is considered as an alternative piezoelectric material in the vibration energy harvesting. It is much more sensitive than piezoelectric ceramics and has very strong piezoelectricity. Table 2.3 gives a comparison of piezoelectric properties between a relaxor ferroelectric single crystal lead magnesium niobate titanate (PMNT) and a typical commercial PZT-5H ceramic for transverse vibration applications.

Table 2.3: Piezoelectric properties of the PMNT crystal and PZT-5H ceramics

Material properties	PMNT*	PZT-5H**
Dielectric constant ϵ_{33}^T at 1kHz	6600	3400
Transverse piezoelectric constant d_{31} (pC/N)	-1800~-2500	-274
Transverse coupling factor k_{31}	92~95%	38.8%
Dissipation factor $\tan\delta$	<0.7%	0.8%

* Data given by Shanghai Institute of Ceramics, Chinese Academy of Sciences;

**Morgan Technical Ceramics standard.

Normally, the piezoelectric constant d_{31} (transverse mode) of the piezoelectric ceramics are less than half of the piezoelectric constant d_{33} (longitudinal mode). The PMNT single crystal has outstandingly large d_{31} , which is greater than its longitudinal constant and also 7 to 9 times greater in comparison with PZT-5H ceramics. With a high k_{31} and d_{31} , using the PMNT is expected to generate much better EMCC on the harvester. Some existing works show that the harvester using PMNT generates higher power density than the harvester using PZT ceramics. Table 2.4 gives a comparison of experimental results generated by using PMNT and PZT materials. The harvesters using PMNT [55, 56] generated greater normalized power density than the harvesters using PZT [57, 58].

Table 2.4: Comparison of experimental results using PMNT and PZT materials

	Frequency (Hz)	Base-excited acceleration (m/s ²)	Damping ratio	Power (mW)	Volume (cm ³)	MSAPD* (mW*s ⁴ /cm ³ *m ²)	Materials
H.J.Song [55]	60	0.98	≈0.01	4.6	29	0.165	PMNT
Seung E. M. [56]	630	4.91	0.03	0.08	0.1	0.033	PMNT
Roundy [57]	120	2.45	0.014	0.375	1	0.013	PZT
Ferrari [58]	181	6.97	≈0.01	0.029	0.075	0.008	PZT

* MSAPD: mean square acceleration power density (per cm³ per m/s²).

However, researches have proved that, for the system with enough strong electromechanical coupling, when the EMCC is increased, the maximum power output of the harvester will not be enhanced [25, 30]. Since PZT ceramics already have good piezoelectricity, using high performance single crystal will not significantly enhance the performance. For the applications with low vibration amplitude and limited piezoelectric coverage, using the high performance crystal is able to generate larger power output. Besides, for 1-3 piezoelectric composites, using high performance single crystal can significantly increase the coupling coefficient of the composite [59, 60].

Furthermore, for a multi-resonance harvester, its EMCC at higher modes is normally weaker than the EMCC at the fundamental mode. However, multi-resonance harvester designs using the high performance crystal are barely provided in existing literatures. This thesis has filled this gap in knowledge in Chapter 12 by using a high performance crystal PIMNT bonded on a multi-layer harvester to enhance the broadband performance.

2.4 Cantilevered beam harvesters

Since mechanical strain energy is converted to electrical energy based on the piezoelectric effect by a vibration energy harvester, in order to generate sufficient output power, the first step is to decide its mechanical configuration and the corresponding vibration characteristics.

The cantilevered beam, especially the rectangular cantilevered (RC) beam is the most popular structure in existing energy harvesting researches. It not only has the simplest structure to analyse, it is also easy to fabricate. With the overall goal to optimize the performance, by changing the beam's dimensions and adding different tip masses, existing configurational investigations of RC harvesters are normally focused on the power output of the fundamental mode with resistive loads.

Richter et al. [61] used a SDOF model to explore the effects of varying beam dimensions on the matching resistance and power output. However, the performance predicted by the SDOF model is oversimplified [30, 62]. Song et al. [55] also used the SDOF model to optimize their RC harvester design. However, their work is a special design and how their RC harvester design is improved in comparison with previous works has not been explored. The experimental results obtained by Song et al. are similar to the predicted results using SDOF model. This is because they added a very heavy tip mass, which actually makes the SDOF model generate smaller errors in comparison with more accurate prediction models and experimental results [63]. In fact, when very large tip mass is added, the power density of the fundamental mode is significantly increased, and the harvester behaves more like a spring-mass model since the modal participation factor of the fundamental mode is close to 1 [30, 62, 63]. Also, in Song et al.'s design, the high performance piezoelectric single crystal PMN-PT is used to ensure that the system electromechanical coupling is strong enough.

Zhu et al. [64] developed a coupled finite element model using ANSYS to establish a geometric study of RC harvesters. ANSYS allows piezoelectric elements to be coupled with linear circuit components in the steady-state analysis. However, since the power of a harvester is proportional to A^2/ω [30] (where ω is the frequency and A is the acceleration magnitude), Zhu incorrectly normalised the power output by dividing it by the base acceleration.

Erturk and Inman [20, 21] established an analytical model for RC harvesters based on the Bernoulli- Euler beam assumptions and predicted the power output with resistive loads using DPM. Patel et al. [65] developed a configurational study based on Erturk's model. In order to achieve a fixed resonance frequency, they slightly varied the dimensions of the RC beam and added bulk tip masses. However, like Song et al's work [55], the influences of attaching huge tip masses (nearly 15 times the beam mass) on the maximum power output were ignored in Patel's study.

Some works focused on enhancing EMCC of the cantilevered harvesters. Erturk et al. [66] investigated the effects of self-cancellation in higher vibration modes on the output current of RC harvesters. This is due to the strain distribution along the length of the beam being partly reversed at some critical strain nodes. Erturk suggested that, for a RC harvester with fully covered piezoelectric layer, the electrodes on the piezoelectric layer should be segmented at those strain nodes in order to avoid self-cancellations in higher modes. However, using the segmentation strategy causes significant self-cancellation in the first mode since there is no strain node. Because the fundamental mode of cantilevered harvesters can produce the highest power density, using segmentation to enhance the EMCC in higher modes is not effective [30].

Friswell and Adhikari [67] presented theoretical results that showed that the RC harvester with partial piezoelectric coverage can generate more power output than the fully covered devices in the fundamental mode. Bourisli and Al-Ajmi [22] also found that for different thickness ratio of the piezoelectric layer to the substrate layer, the EMCC of RC harvester in the fundamental mode can be optimized when the piezoelectric coverage is around 50% to 60%. However, these two works did not explore how the variations of the piezoelectric coverage affect the EMCC. Patel et al. [65] investigated the performance of RC harvesters with different piezoelectric coverage. However, Patel only analysed the modal backward coupling term, which is not the EMCC, and they incorrectly claimed that the changes of EMCC did not affect the maximum power. In fact, since their system is designed to have weak to medium electro-mechanical coupling, the variation of piezoelectric coverage on power output in their results is due to the changes of the EMCC directly [30].

Except for the RC beam, the tapered cantilevered structures (see Figure 2.6) have also been studied in existing works. Roundy et al. [12] claimed that, because the strain is distributed more evenly, using a convergent tapered cantilevered (CTC) structure is able to double the

power output of harvesters in comparison with using the RC structure. However, even though this idea has been used in several works, systematic study of the CTC structure about how it improves the power output have been barely provided [31, 68]. In fact, the study given by Xiong and Oyadiji [30] shows that, unless the EMCC of the harvester is very weak and the piezoelectric coverage is larger than 70%, CTC harvesters actually generate smaller power density than RC harvesters whereas using divergent tapered cantilevered (DTC) structures can generate larger power density than using RC structures.

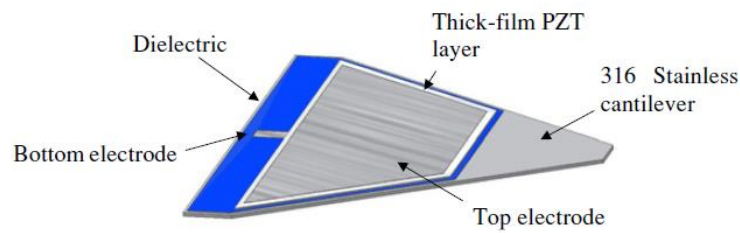


Figure 2.6: Tapered thick-film harvester [68].

Generally, for the configurational optimization of cantilevered harvesters, geometric analyses are based on specified parameters in existing studies. Several predicting models are used to calculate the power output with resistive loads directly. In fact, the modal mechanical behaviour and the modal electromechanical coupling can simultaneously affect the power outputs. However, how the geometric variations affect these two factors, which eventually affects the power output has not been stated clearly in existing works. Also, the individual effects of these two factors on the output power have been barely analysed. Therefore, the performance of harvesters reported in some existing works could be easily confused when compared to others' results. This is due to the fact that the effects of the modal mechanical behaviour and electromechanical coupling on the power output have not been clarified carefully.

In this thesis, Chapter 5 filled these gaps in knowledge and it has been published in Xiong and Oyadiji [30]. A parametric study is developed to identify the effects of the modal mechanical behaviour and electromechanical coupling on the power density systematically. The effects of geometric variations, including rectangular and tapered cantilevered configurations, extra masses and different piezoelectric coverage, on the modal mechanical behaviour and electromechanical coupling are comprehensively investigated.

2.5 Broadband harvesters

2.5.1 Multi-resonance harvesters

For the cantilevered harvester, normally the fundamental mode is used. The remaining higher modes are not only far away from the first mode, they also generate much lower power outputs. To overcome the limitations of cantilevered harvesters, multi-resonance harvesters, which generate multiple vibration modes with relatively large power output in a broader frequency band, are developed to improve the broadband performance.

The harvester with array of beams structure is a typical multi-resonance harvester. It normally consists of several individual beam structures. By tuning the resonance frequency of each beam, the harvester can generate close vibration modes. Existing researches have either theoretically or experimentally developed the harvesters with arrays of beams [58, 69, 70]. In these works reported in the literatures, the array of beams is designed to be physically decoupled whereas several cantilevered beams are electrically connected (see Figure 2.7). The advantage for this is that the fundamental modes of different beams can be tuned easily to generate close resonance frequencies and nearly same level of power outputs. However, for each vibration mode, only one cantilevered beam is working under its resonance frequency and the remaining beams are barely active. This could significantly affect the power density of the harvesters if too many beams are used. Besides, since a large part of the piezoelectric layer bonded on these passive beams only undergoes small strains while the piezoelectric capacitance is increased due to the increased surface of piezoelectric layer, the EMCC of the harvester is decreased significantly. Therefore, if too many beams are used, the performance of the harvester could be significantly reduced.

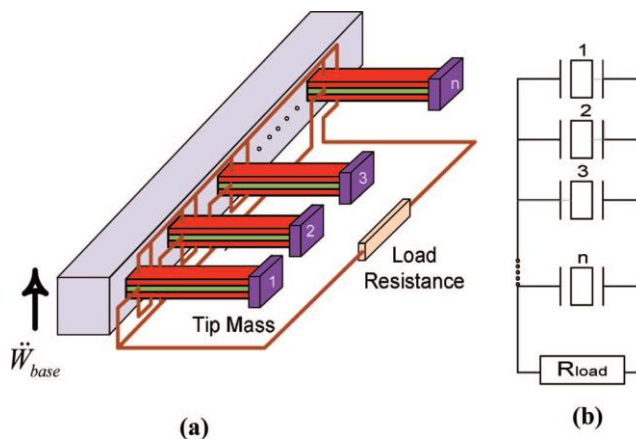


Figure 2.7: Array of bimorph cantilevered beams harvester [70]; (a) schematic drawing; (b) electrical connection

Qi et al. [53] developed a comb-shaped harvester. The cantilevered branches are physically connected on a common base, which is a clamped-clamped beam. The piezoelectric layer is only bonded on the common base. Therefore, the multiple vibration modes are generated due to the interaction between the common base and other cantilevered beams. However, in Qi et al.'s design, few of the vibration modes are dominant and generate too large power output, and the remaining modes only generate very small power output. This is clearly due to the lack of configurational optimization.

There is another typical multi-resonance design designated as dual-mass harvesters, which are also widely reported in existing literature [26, 71, 72]. It consists of two masses and one cantilevered beam. One mass is bonded at the free tip and another mass is bonded at the centre of the beam (see Figure 2.8). Since the cantilevered beam is separated into two parts by the two masses, two vibration modes can be generated due to the interaction of the two parts of the cantilevered beam. However, the dual-mass harvester cannot generate close enough resonance frequencies.

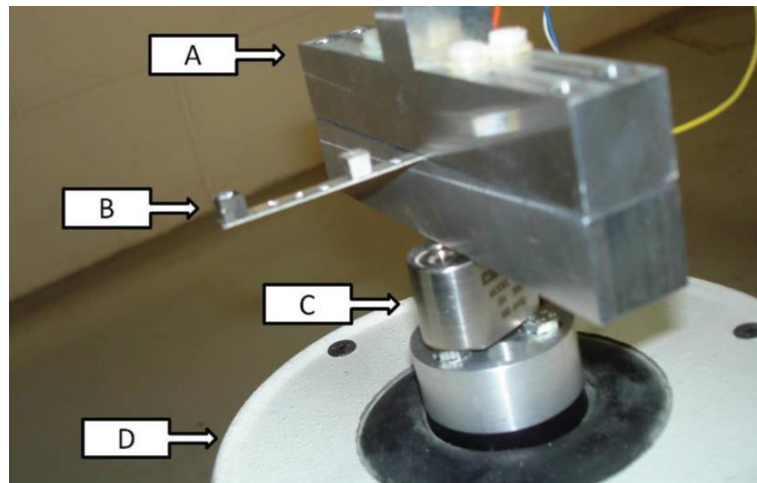


Figure 2.8: Experimental setup given by Ou et al. [71]: (a) clamp, (b) dual-mass harvester, (c) accelerometer, and (d) electromagnetic shaker

Wu et al. [27] developed a modified dual-mass harvester. They divided one part of the cantilevered beam into two parallel narrower parts with a gap between them. Another part of the cantilevered beam lies in the gap between the two parallel parts, and its free end pointed to the clamped end of the dual-mass harvester (see Figure 2.9). By changing the magnitudes of the two masses, Wu et al.'s model can generate closer resonances in comparison with conventional dual-mass models. However, Wu et al.'s work is only a special design without giving systematic analysis of how the mechanical configuration and

the electromechanical coupling affect the power output of the modified dual-mass harvester. Chen et al. [73] developed a multi-mass harvester using up to 9 masses bonded on one cantilevered beam. However, their design has limited applicability due to the cantilevered beam being too thin (0.2 mm) but too long (1 m) while heavier masses are bonded. In addition, due to lack of proper designs, Chen et al.'s multi-mass harvester generates uneven broadband power output since some modes are dominant and the other modes have poor performance.

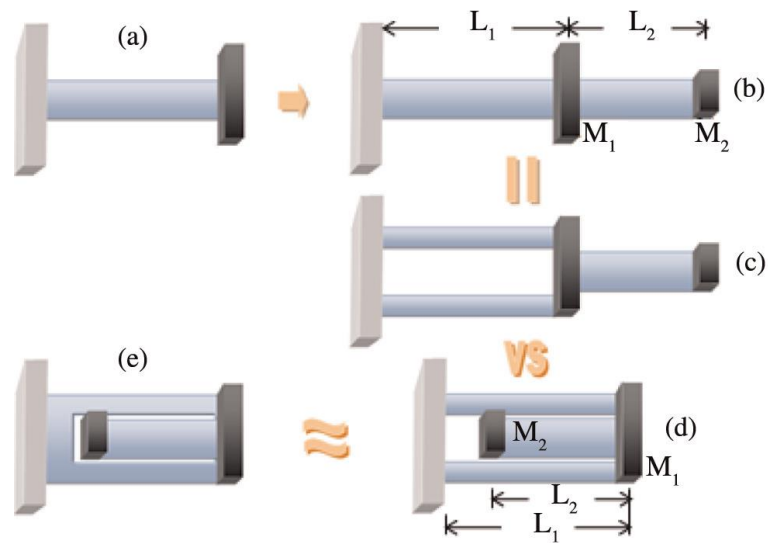


Figure 2.9: A modified dual-mass harvester given by Wu et al. [27]; (a) SDOF cantilever, (b) conventional dual-mass harvester, (c) equivalent dual-mass harvester, (d) and (e) modified dual-mass harvesters

Apart from the array of beam harvester and dual-mass harvester, there are some other multi-resonance designs that have been reported in existing literature. Erturk et al. [74] investigated an L-shaped harvester and found that the resonance frequency of the second mode can be two times higher than the resonance frequency of the first mode. Karami and Inman [75] developed a zigzag harvester with up to 11 sub-branches (see Figure 2.10). However, since the higher modes of the zigzag harvester are far away from the first mode, which is also dominant and generate the highest power output, Karami and Inman only focused on optimizing the performance of the first mode [76]. Therefore, the zigzag harvester only behaves as a single mode harvester and has limited broadband performance.

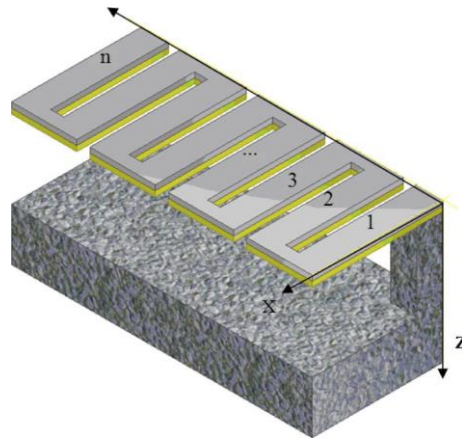


Figure 2.10: The zigzag energy harvester by Karami and Inman [75]

Generally, for a well-designed multi-resonance harvester, close resonance frequencies with relative large power output at each mode are required. However, except for the array of beams designs, which is physically decoupled, harvesting energy from several modes efficiently is not easy. In the existing multi-resonance harvester designs, optimization study for either mechanical structure or eletromechanical coupling are barely provided due to the complexity of the configurations. Even if the resonance frequencies are enough close, one or some modes of these harvesters can be very dominant, which eventually reduces the performance of the remaining modes. This actually significantly affects the broadband performance and it is clearly due to the lack of proper design. This thesis has substantially filled these gaps in knowledge. A novel optimization strategy using a modal approach is introduced and the optimal designs of some novel multi-resonance harvesters are provided from Chapter 6 to Chapter 9.

2.5.2 *Nonlinear techniques*

The main motivation to design harvesters using nonlinear techniques in some existing works is that the nonlinear behaviour of harvesters can generate wider bandwidth than linear harvesters around a single vibration mode [77, 78]. This strategy is normally realised by introducing a nonlinear stiffness into the harvester. There are two different kinds of nonlinear harvesters reported in the literatures: the monostable non-linear harvesters and the bistable non-linear harvesters.

It is well known that, with large vibration amplitude, the harvester can behave nonlinearly [21, 77]. The monostable non-linear harvesters have either hardening or softening

configurations, and their resonance curves are either bent to the right or to the left (see Figure 2.11 b). If the nonlinearity is large enough, the bandwidth of the power output can be widened significantly. However, to successfully achieve broadband performance, the harvester needs to always be operated in the upper branch region of the nonlinear behaviour. This has led to the requirement of linearly increasing or decreasing frequency sweep excitation, which limits the applicability in practice. Besides, Cammarano et al. [79] argue that, if assuming the harvester operates always in the lower branch solution of the nonlinear behaviour, the linear harvester will generate higher maximum power output. After the damping of the linear system is increased to maintain the same maximum power compared to the nonlinear system, the bandwidth of the linear harvester increases and it is wider than the bandwidth of the nonlinear system (see Figure 2.11 c and 2.11 d). In general, the operational conditions should be carefully investigated when using the monostable non-linear harvester to generate broadband power output, and it requires the following conditions to be met: large deflection, high nonlinearity and operating the harvester in the upper branch region of the nonlinear behaviour.

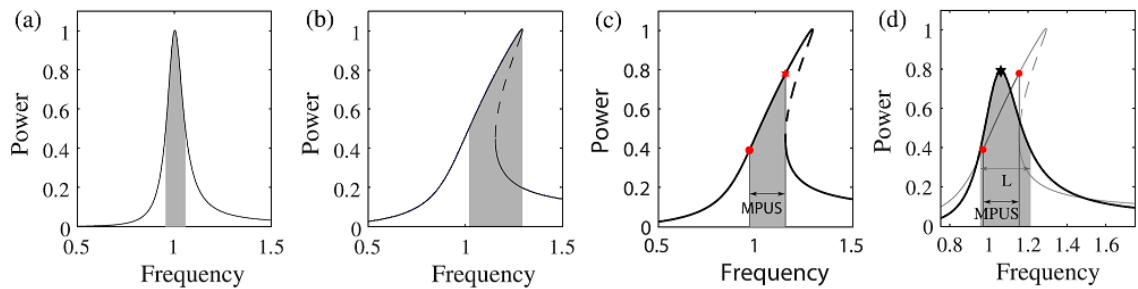


Figure 2.11: 3dB-bandwidth comparisons between (a) linear; (b) nonlinear (hardening) in the upper branch; (c) nonlinear in the lower branch, and (d) linear with larger damping [79]

The bistable non-linear mechanism is normally realised using magnets, which introduce the magnetic force to create the nonlinear stiffness into the harvester [78]. There are two typical setups using magnets: (a) a magnet is bonded on the tip of a beam-shaped harvester and an external magnet is fixed nearby the tip magnet (see Figure 2.12 a) [80], and (b) one or two external magnets are fixed nearby the tip of a ferromagnetic substrate (see Figure 2.12 b) [81]. When large vibration amplitude is achieved under either periodic force or stochastic force, the bistable non-linear harvester can be operated in the upper branch region of nonlinear behaviour. For the low-level periodic excitation, a perturbation

mechanism is required to drive the harvester to operate in its upper branch region. However, how to design and implement such mechanism is rarely provided in existing works. Therefore, for both the monostable and bistable nonlinear harvesters, in order to achieve fully nonlinear behaviour, the operational conditions should always be carefully chosen.

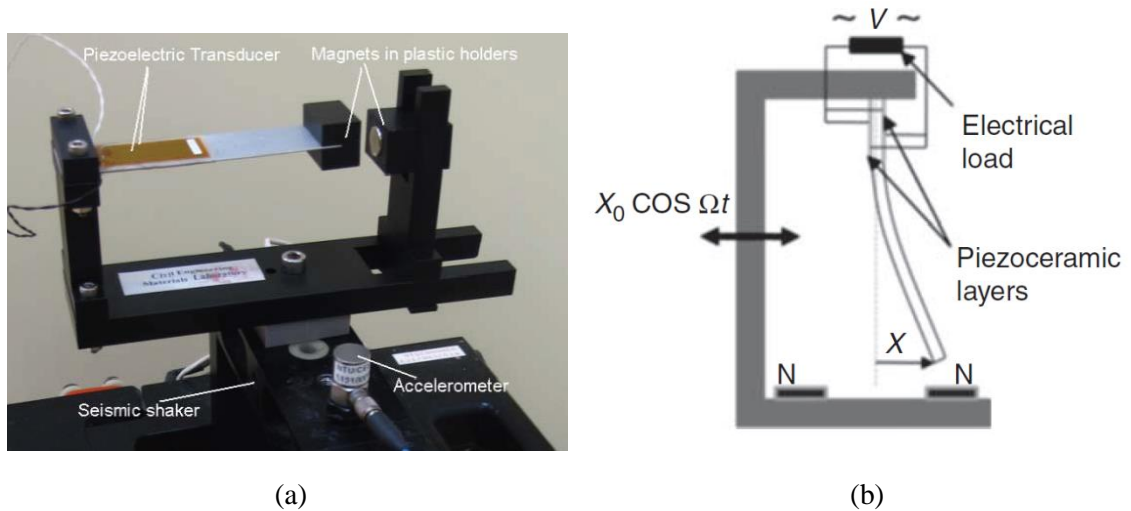


Figure 2.12: Two typical bistable non-linear harvesters using magnets; (a) harvester bonded with tip magnet [80]; (b) harvester using ferromagnetic substrate and external magnets [81]

2.5.3 Tuning techniques

Since linear harvesters have fixed resonance frequencies, in order to fit in possible variations of the excitation frequency, the tuning technique is developed to actively or passively tune the resonance frequency of harvesters. In particular, there are three ways to realise the tuning mechanism: the mechanical, magnetic and piezoelectric methods. The active tuning mechanism requires continuous power supply, and it is basically realised by the piezoelectric method. The passive mechanism tunes the frequency manually or only requires intermittent power, and no more power required after the tuning process. The passive tuning can be realised using both mechanical and magnetic methods. However, these tuning techniques normally have substantial drawbacks, which limit their applicability in practice [77].

The mechanical method can only tune the frequency manually, and it requires an external device to realise the tuning process. Figure 2.13 shows a mechanical tuning device given by Eichhorn et al. [82]. The resonance frequency of the generator shifts when the pre-stress

to the base given by the spring is changed. The mechanical method is not easy to implement and the added tuning device also significantly increases the volume of the harvester, which eventually decreases the power density.

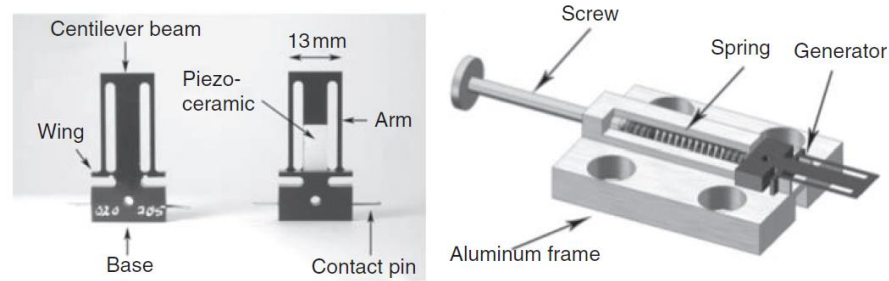


Figure 2.13: A harvester using mechanical tuning method [82]

The magnetic method also manually tunes the resonance frequency in most designs reported in the literature. It has the same mechanism as the nonlinear technique using magnets described in section 2.5.2. By changing the distance between the two magnets, the resonance frequency will shift (see Figure 2.14). One drawback of the magnetic tuning is that the system requires other mechanisms to ensure that the harvester is always operated in the upper branch region of the nonlinear behaviour in order to widen the bandwidth of power output. Besides, using the magnetic method also requires external devices, which increases the volume of the harvester.

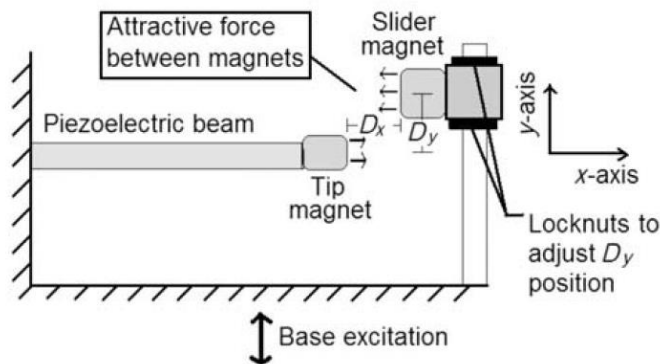


Figure 2.14: A sketch of the harvester using magnetic tuning method [83]

Active tuning is usually implemented by the piezoelectric tuning method. It is normally realised by introducing an intelligent structure, which consists of a piezoelectric actuator and a microcontroller, to automatically tune the resonance frequency of the harvester (see Figure 2.15). However, the most critical issue of the existing designs is that the actuator

and controller may require much more power than the power generated by the harvester itself. Thus, an external power supply is normally needed for the active tuning method.

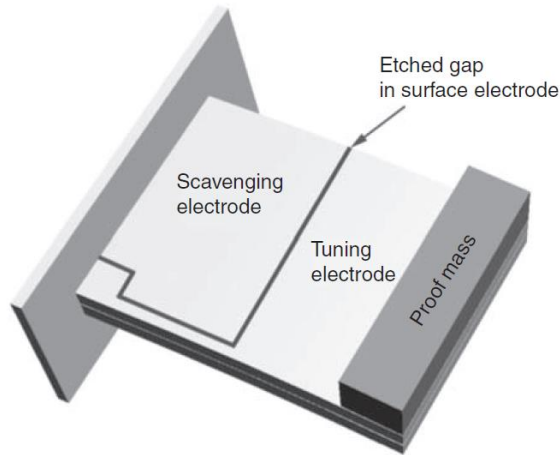


Figure 2.15: A sketch of the harvester using piezoelectric tuning method [84]

2.6 Rectifier circuits

Prior to this section, existing works on the materials and structural aspects of a harvester system have been reviewed. In this section, the investigations on the electrical circuitry required by a harvester are briefly discussed. In general, since the harvesters are developed as power supplies for wireless sensor networks, there are some critical issues for the use of the harvester: (a) the alternating current generated from the harvester needs to be converted into direct current, (b) the generated power from harvesters are normally insufficient, and (c) the environmental vibration sources are unlikely to be continuous. To overcome these drawbacks, great efforts have been made in recent years, such as: (a) the use of capacitors or rechargeable batteries [36, 85] to store the electrical energy, and (b) the development of synchronous circuits to synchronise the phase of the current with the voltage since there is a phase difference between the generated voltage and current [25, 86, 87].

A standard rectifier circuit is shown in Figure 2.16 (a). A diode-bridge is normally used as the rectifier. However, there is a voltage drop across the diode, and this causes electrical losses periodically once the harvester is excited [4, 25]. Besides, for a well-designed harvester especially the broadband harvester, the amplitude of the voltage should be sufficiently large in order to maintain its effective power output bandwidth.

Figure 2.16 (b) shows the parallel Synchronized Switch Harvesting on Inductor (SSHI) schematics. An inductor and a digital switch are connected in parallel with the harvester to synchronize the phase of the current. The predictions given by existing works have shown that the performance of harvester can be optimized with low EMCC using this mechanism, which significantly improves the power conversion efficiency. However, the added impedance from the SSHI components is equivalent to additional electrical losses. Besides, the digital switch needs to be activated periodically, which normally requires continuous power supply in practice. If the switch is self-powered, the effective output power may be significantly reduced or even eliminated when the required power is more than the generated power [88]. The investigations of similar synchronous circuits, including series SSHI and synchronous charge extraction circuit, are also widely reported in the literature [89, 90].

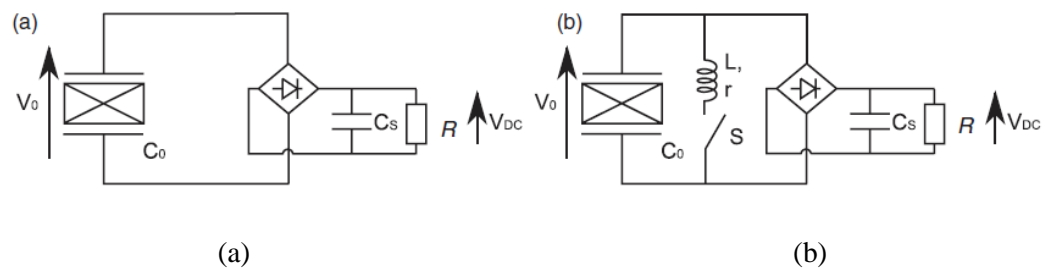


Figure 2.16: Typical rectifier circuits schematics; (a) a standard; (b) parallel SSHI [25]

2.7 Conclusions

In this chapter, a critical literature review on vibration energy harvesting using piezoelectric materials has been presented. It starts at reviewing the existing investigations on piezoelectric materials, which can significantly affect the power conversion efficiency and applicability of the harvester. Then, a comprehensive review of the configurational investigations is presented, including conventional beam-shaped harvesters and broadband harvesters. The configuration of a harvester determines its modal structural characteristics, and eventually determines the maximum performance. Since the major works of this thesis have been focused on the configurational optimization, the main contributions which fill the knowledge gaps are also highlighted in this section. At the last part of the literature review, the investigations on the rectifier circuits are briefly discussed.

CHAPTER 3 MODELLING METHODOLOGY AND THEORETICAL BACKGROUND

3.1 Introduction

In this chapter, the theoretical background and modelling techniques for vibration energy harvesting used in this thesis are presented. Erturk and Inman [20] introduced a fully coupled DPM to determine the power output of harvesters with resistive loads. The required modal parameters of rectangular cantilevered beam harvesters were derived based on the Bernouli-Euler beam assumption. The analytical model was successfully validated experimentally by themselves and other researchers thereafter. However, for harvesters in which the configurations are not uniform beams, such as tapered beam structures or multi-resonance harvesters with complex configurations, the derivations of closed-form analytical solutions for eigenfunctions and the other modal parameter becomes very complicated and in some cases not possible.

Alternatively, in this thesis, the FEA-based numerical solution is applied for such cases. Instead of using FEA software, such as ANSYS, to predict the power output on resistive loads directly like most existing works did, the required modal parameters are derived from FEA data and DPM is used to predict the performance of the harvesters. There are three main causes for doing this. Firstly, operating a full steady-state analysis in FEA software to predict voltage and power output FRFs for a wide frequency range requires long computing time, especially for complex configurations, which may require hours to a day to solve one model. On some occasions, multiple PCs or supercomputers have to be used. Secondly, the predicted data from one model is only for specific conditions, such as damping and resistance, which are unchangeable. For the case that multiple factors are varied, the repeated operations in FEA software requires even longer time. Thirdly, when directly predicting voltage and power output of harvesters using FEA, how the changes of configurations and factors have affected the modal performance cannot be clearly identified. These actually significantly affect the efficiency and currently there is no

effective optimization strategy that has been developed using FEA in existing literatures, especially for multi-resonance harvester designs due to the complexity of the configurations. In this thesis, simulations are operated only at resonance frequencies of harvesters and the modal parameters required for DPM are derived from the FEA data at each resonance frequency.

In existing works, DPM has been used to predict the voltage and power output FRFs of harvesters. However, it cannot directly determine the optimal performance of a harvester unless the model has been thoroughly analysed, and the optimal load has been determined. Guyomar et al. [25] used a modal electromechanical criterion $k^2 Q_m$ to predict the maximum average power output directly based on SDOF systems. However, in Guyomar et al.'s work, the modal mechanical behaviour cannot be accurately represented in multiple degrees of freedom (MDOF) systems. Erturk and Inman [62] introduced a correction factor to allow the SDOF model to be used in MDOF systems and compared the corrected displacement transmissibility FRFs to the same FRFs predicted using Bernouli-Euler beam assumption. However, Erturk and Inman only analysed the purely structural responses using the correction factor whereas the effects on the electrical behaviour and power output have been ignored.

In this thesis, a modal factor designated as mass ratio is introduced. It depends on the modal participation factor and represents the modal structural behaviour on power density directly. Mass ratio has been used in conjunction with EMCC to represent the effects of the modal structural and electromechanical properties on the maximum performance of harvesters and a modal approach is introduced based on these two factors. For multi-resonance harvester designs, a configurational optimisation strategy using FEA has been developed based on the modal approach.

3.2 Distributed parameter electromechanical modelling

3.2.1 Analytical modelling of cantilevered beam harvester

In this section, an analytical modelling of a bimorph harvester (see Figure 3.1) with a uniform rectangular cantilevered beam configuration is presented. The absolute transverse displacement of the beam at a distance x from the clamped end is given as (assuming small

rotation at the clamped end is neglected):

$$u(x, t) = u_{rel}(x, t) + u_b(x, t) \quad (3.1)$$

where $u_{rel}(x, t)$ is the absolute transverse displacement relative to the moving base of the beam at position x and $u_b(x, t)$ is the absolute transverse base displacement.

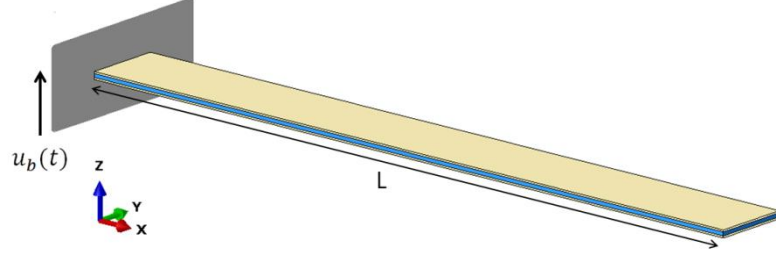


Figure 3.1: A cantilevered bimorph harvester

The bimorph structure has two piezoelectric layers bonded on the top and bottom of the substrate layer. Figure 3.2 shows the cross-section in the y - z plane of the bimorph harvester.

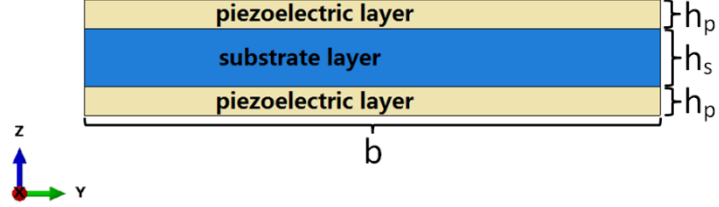


Figure 3.2: Cross-section in y - z plane of a cantilevered bimorph harvester

The governing equation of motion is given as [20]:

$$\begin{aligned} \frac{\partial^2 \bar{M}(x, t)}{\partial x^2} + c_s I \frac{\partial^5 u_{rel}(x, t)}{\partial x^4 \partial t} + c_a \frac{\partial u_{rel}(x, t)}{\partial t} + m \frac{\partial^2 u_{rel}(x, t)}{\partial t^2} \\ = -m \frac{\partial^2 u_b(x, t)}{\partial t^2} - c_a \frac{\partial u_b(x, t)}{\partial t} \end{aligned} \quad (3.2)$$

where $\bar{M}(x, t)$ is the internal bending moment, c_s is the strain-rate damping coefficient, I is the second moment of area for the composite cross section ($c_s I$ is the internal damping term from the composite beam), m is the mass per unit length of the beam and c_a is the viscous damping coefficient from the ambient air. It should be noted that the bimorph beam is assumed to satisfy the proportional damping model and the eigenfunction determined from the undamped free vibration system can be used for modal analysis. The internal

bending moment is the first moment of the axial stress field over the cross-section (see Figure 3.1) [21]:

$$\bar{M}(x, t) = b \left(\int_{-h_p - \frac{h_s}{2}}^{-\frac{h_s}{2}} T_1^p z dz + \int_{-\frac{h_s}{2}}^{\frac{h_s}{2}} T_1^s z dz + \int_{\frac{h_s}{2}}^{h_p + \frac{h_s}{2}} T_1^p z dz \right) \quad (3.3)$$

where b is the width of the beam, h_p is the thickness of each piezoelectric layer (p represents piezoelectric layer), h_s is the thickness of the substrate layer (s represents substrate layer), T_1^p is the stress along the length (1- or x-direction) of the piezoelectric layer, T_1^s is the stress along the length of the substrate layer, and

$$T_1^s = Y_s S_1^s \quad (3.4)$$

$$T_1^p = c_{11}^E S_1^p - e_{31} E_3 \quad (3.5)$$

where Y_s is the Young's modulus of the substrate layer, S_1^s is the axial strain, c_{11}^E is the elastic matrix component of piezoelectric materials under constant electric field, e_{31} is the piezoelectric constant in stress form, and E_3 is the electric field in the z-direction (polarization direction). The axial strain at a certain distance (z) from the neutral axis of the beam is proportional to the curvature of the beam and it is given as:

$$S_1(x, z, t) = -z \frac{\partial^2 u_{rel}(x, t)}{\partial x^2} \quad (3.6)$$

Then, internal bending moment can be obtained as:

$$\bar{M}(x, t) = YI \frac{\partial^2 u_{rel}(x, t)}{\partial x^2} + \theta v(t) \quad (3.7)$$

where YI is the bending stiffness of the composite cross section for the constant electric field (short-circuit condition for the piezoelectric layer), θ is the coupling term and $v(t)$ is the voltage crossing the piezoelectric layer. It should be noted that if the piezoelectric layer does not fully cover the substrate layer, $\theta v(t)$ should be multiplied by $[H(x) - H(x-L)]$, where $H(x)$ is the Heaviside function and L is the length of the beam. The bending stiffness is given by [21],

$$YI = \frac{2b}{3} \left\{ \frac{Y_s h_s^3}{8} + c_{11}^E \left[\left(h_p + \frac{h_s}{2} \right)^3 + \frac{h_s^3}{8} \right] \right\} \quad (3.8)$$

The coupling term θ can be different for series and parallel connections of the two piezoelectric layers and they are related by,

$$\theta_{seri.} = \frac{\theta_{para.}}{2} = \frac{e_{31} b}{2h_p} \left[\left(h_p + \frac{h_s}{2} \right)^2 - \frac{h_s^2}{4} \right] = e_{31} b h_{pc} \quad (3.9)$$

where h_{pc} is the distance from the centre of each piezoelectric layer to the neutral axis of

the beam for bimorph structure and it is written as:

$$h_{pc} = \frac{h_p}{2} + \frac{h_s}{2} \quad (3.10)$$

It should be noted that the polling directions of the two piezo-layers are opposite for a series connection and the polling directions are in the same direction for a parallel connection. Then, Equation 3.2 can be rewritten as [20],

$$\begin{aligned} YI \frac{\partial^4 u_{rel}(x, t)}{\partial x^4} + c_s I \frac{\partial^5 u_{rel}(x, t)}{\partial x^4 \partial t} + c_a \frac{\partial u_{rel}(x, t)}{\partial t} + m \frac{\partial^2 u_{rel}(x, t)}{\partial t^2} + \theta v(t) \\ = -m \frac{\partial^2 u_b(x, t)}{\partial t^2} - c_a \frac{\partial u_b(x, t)}{\partial t} \end{aligned} \quad (3.11)$$

In fact, Equation 3.5 is one of the two piezoelectric constitutive equations for d_{31} mode (transverse or length-extension mode of piezoelectric material) written in e-form (for other forms see Appendix A) [14], and another constitutive equation is given as:

$$D_3 = e_{31} S_1^p + \epsilon_{33}^S E_3 \quad (3.12)$$

where D_3 is the electric displacement along the thickness of the piezoelectric layer and ϵ_{33}^S is permittivity under constant strain. If assuming a resistive load is connected to the harvester, the function of electric current over time is obtained following Gauss's law by integrating D_3 over the electrode area A to get the total charge and it is:

$$i(t) = \frac{v(t)}{R_l} = \frac{d}{dt} \left(\int_A D_3 dA \right) \quad (3.13)$$

where the equivalent electrode area $A_{para.} = 2bL$ or $A_{seri.} = bL$. By substituting $E_3(t)_{para.} = -\frac{v(t)}{h_p}$ or $E_3(t)_{seri.} = -\frac{v(t)}{2h_p}$ and $S_1^p = -h_{pc} \frac{\partial^2 u_{rel}(x, t)}{\partial x^2}$ into Equation 3.13, the governing equation of electrical behaviour can be written as:

$$\frac{2\epsilon_{33}^S bL}{h_p} \frac{dv(t)}{dt} + \frac{v(t)}{R_l} + 2e_{31} b h_{pc} \int_{x=0}^L \frac{\partial^3 u_{rel}(x, t)}{\partial x^2 \partial t} dx = 0 \quad (\text{parallel}) \quad (3.14)$$

$$\frac{\epsilon_{33}^S bL}{2h_p} \frac{dv(t)}{dt} + \frac{v(t)}{R_l} + e_{31} b h_{pc} \int_{x=0}^L \frac{\partial^3 u_{rel}(x, t)}{\partial x^2 \partial t} dx = 0 \quad (\text{series}) \quad (3.15)$$

In fact, two equivalent terms, which are designated as the coupling term θ and piezoelectric capacitance C_p (see Table 3.1), can be used in Equations 3.14 and 3.15. Then, the governing equation of electrical behaviour is rewritten as:

$$C_p \frac{dv(t)}{dt} + \frac{v(t)}{R_l} + \theta \int_{x=0}^L \frac{\partial^3 u_{rel}(x, t)}{\partial x^2 \partial t} dx = 0 \quad (3.16)$$

Table 3.1: Equivalent coupling term θ and piezoelectric capacitance C_p in parallel and series connections of a RC harvester with bimorph structures

	Parallel	Series
θ	$2e_{31}bh_{pc}$	$e_{31}bh_{pc}$
C_p	$2\varepsilon_{33}^S bL/h_p$	$\varepsilon_{33}^S bL/2h_p$

The vibration response can be represented using modal analysis technique. Thus, the absolute transverse displacement relative to the moving base of the beam $u_{rel}(x, t)$ can be written as,

$$u_{rel}(x, t) = \sum_{r=1}^{\infty} \phi_r(x) \eta_r(t) \quad (3.17)$$

where $\phi_r(x)$ and $\eta_r(t)$ are the mass-normalised eigenfunction and the corresponding modal coordinates of the r^{th} mode of the beam, respectively. The mass-normalised eigenfunction for a cantilevered beam is given by [91],

$$\phi_r(x) = \sqrt{\frac{1}{mL}} \left[\cosh \frac{\lambda_r}{L} x - \cos \frac{\lambda_r}{L} x - \sigma_r (\sinh \frac{\lambda_r}{L} x - \sin \frac{\lambda_r}{L} x) \right] \quad (3.18)$$

where λ_r 's are the dimensionless frequency numbers obtained from the characteristic equation of a cantilevered (clamped-free) beam and it is given by,

$$1 + \cos \lambda_r \cosh \lambda_r = 0 \quad (3.19)$$

and σ_r is given by,

$$\sigma_r = \frac{\sinh \lambda_r - \sin \lambda_r}{\cosh \lambda_r - \cos \lambda_r} \quad (3.20)$$

It should be noted that $\phi_r(x)$ is for short-circuit condition ($v(t) = 0$). By substituting Equation 3.17 into Equation 3.11 and applying the orthogonality conditions of the eigenfunctions, the governing equation of the modal response of the beam in the mechanical domain can be written as [21],

$$\frac{d^2 \eta_r(t)}{dt^2} + 2\zeta_r \omega_r \frac{d\eta_r(t)}{dt} + \omega_r^2 \eta_r(t) - \chi_r v(t) = F_r(t) \quad (3.21)$$

where ζ_r , ω_r , χ_r and F_r are the damping ratio, undamped angular resonance frequency, equivalent modal electromechanical coupling term and modal mechanical forcing term, respectively, and they are given by [20,21]:

$$\zeta_r = \frac{c_s I \omega_r}{YI} + \frac{c_a}{2m\omega_r} \quad (3.22)$$

$$\omega_r = \lambda_r^2 \sqrt{\frac{YI}{mL^4}} \quad (3.23)$$

$$F_r(t) = \frac{d^2 u_b(x, t)}{dt^2} \int_{x=0}^L \phi_r(x) dx = \frac{d^2 u_b(x, t)}{dt^2} \frac{2\sigma_r}{\lambda_r} \sqrt{\frac{L}{m}} \quad (3.24)$$

$$\chi_r = \theta \left. \frac{d\phi_r(x)}{dx} \right|_{x=L} \quad (3.25)$$

The governing equation of the modal response of the beam in the electrical domain can be rewritten as

$$C_p \frac{dv(t)}{dt} + \frac{v(t)}{R_l} + \sum_{r=1}^{\infty} \chi_r \frac{d\eta_r(t)}{dt} = 0 \quad (3.26)$$

When a harmonic base acceleration is applied, the steady state solution of Equation 3.21 is,

$$\eta_r(t) = \frac{F_r - \chi_r v}{\omega_r^2 - \omega^2 + j2\zeta_r \omega_r \omega} e^{j\omega t} \quad (3.27)$$

The voltage across R_l can be represented by,

$$v(t) = \frac{\sum_{r=1}^{\infty} \frac{j\omega F_r \chi_r}{\omega_r^2 - \omega^2 + j2\zeta_r \omega_r \omega}}{\sum_{r=1}^{\infty} \frac{j\omega \chi_r^2}{\omega_r^2 - \omega^2 + j2\zeta_r \omega_r \omega} + \frac{1}{R_l} + j\omega C_p} e^{j\omega t} \quad (3.28)$$

The vibration response of the beam relative to its base is,

$$u_{rel}(x, t) = \sum_{r=1}^{\infty} \phi_r(x) \frac{F_r - \chi_r v}{\omega_r^2 - \omega^2 + j2\zeta_r \omega_r \omega} e^{j\omega t} \quad (3.29)$$

Solving the equations in the frequency domain gives $u_{rel}(t) = \tilde{u}_{rel}(j\omega)e^{j\omega t}$ and $v(t) = \tilde{v}(j\omega)e^{j\omega t}$, where \tilde{u}_{rel} and \tilde{v} are complex amplitudes of the respective time-varying quantities, and the complex power is given by $\tilde{v}(j\omega) \left(\frac{\tilde{v}(j\omega)}{R_l}\right)^*$. Under the assumption that no electrical losses occur due to rectification, the average power output is $|\tilde{v}|^2/2R_l$.

3.2.2 FEA derivation of the modal parameters

For the eigenvalue extraction analysis, the equation solved by the FEA software is:

$$[M]\{\ddot{\mathbf{u}}\} + [K]\{\mathbf{u}\} = 0 \quad \text{or} \quad (-\omega^2[M] + [K])\{\boldsymbol{\phi}\} = 0 \quad (3.30)$$

where $[M]$ is the mass matrix, $[K]$ is the stiffness matrix, $\{\mathbf{u}\}$ is the vector of nodal displacements and $\{\boldsymbol{\phi}\}$ is the eigenvector, which is the vibration mode shape. The FEA software solves the eigenvalue problem to determine the undamped angular natural frequencies ω_r , the generalised modal mass m_m and the modal participation factor γ associated with each mode.

For the piezoelectric analysis, the system equations solved by the FEA software are:

$$[M]\{\ddot{\mathbf{u}}\} + [C]\{\dot{\mathbf{u}}\} + [K]\{\mathbf{u}\} + [X]\{\mathbf{v}\} = \{\mathbf{F}\} \quad (3.31)$$

$$\{\mathbf{Q}\} + [X]\{\mathbf{u}\} - [D]\{\mathbf{v}\} = 0 \quad (3.32)$$

where $[C]$ is the damping matrix, $[X]$ is the piezoelectric coupling matrix, $[D]$ is the dielectric stiffness matrix, $\{\mathbf{v}\}$ is the vector of nodal electric potential, $\{\mathbf{F}\}$ is the mechanical force vector and $\{\mathbf{Q}\}$ is the electrical charge vector. By operating the steady-state analysis, the FEA software can determine the nodal displacements, electrical potential gradients and electrical flux densities.

For short-circuit condition in FEA simulations ($v=0$), then,

$$\{\mathbf{u}\} = \sum_{r=1}^n \eta_r \{\boldsymbol{\phi}\}^{(r)} = \sum_{r=1}^n \frac{\{\boldsymbol{\phi}\}^{(r)T} \{\mathbf{F}\} \{\boldsymbol{\phi}\}^{(r)}}{m_{mr}(\omega_r^2 - \omega^2 + j2\zeta_r \omega_r \omega)} \quad (3.33)$$

The reduced form of the relative displacement of the r -th mode can be written as,

$$\tilde{u}_r(j\omega) = \frac{\sqrt{m_{mr}} \tilde{F}_r}{m_{mr}(\omega_r^2 - \omega^2 + j2\zeta_r \omega_r \omega)} \quad (3.34)$$

where \tilde{F}_r is the complex amplitude of the mass-normalised modal mechanical forcing term and m_{mr} is the lumped modal mass. Then, for the resonance condition of the r -th mode, \tilde{F}_r is given by

$$\tilde{F}_r = 2j\zeta_r \omega_r^2 \tilde{u}_r \sqrt{m_{mr}} \Big|_{\omega=\omega_r} \quad (3.35)$$

Thus, using Equation 3.35, the amplitude \tilde{F}_r of the r -th mode can be determined using the transverse displacement data at the natural frequency of the r -th mode derived from the FEA steady-state analysis. For cantilevered beams, \tilde{u}_r is the relative displacement at the free tip at the modal angular frequency ω_r . It should be noted that, the displacement data is derived under short-circuit condition ($v=0$). In FEA models, the base excitation is applied along the z -axis and the voltage is applied on the top and bottom surfaces of the piezoelectric layer. The short-circuit condition of harvesters is realised by letting the

applied voltage go to zero on the electrode surfaces of the piezoelectric layer. Then, by applying base excitation along z-axis at each resonance frequency, the transverse displacement relative to the moving base under short-circuit condition can be derived from the FEA results.

For the short-circuit condition ($v = 0$), the first part of the left hand side of Equation 3.26 is eliminated. Substituting $i(t)$ for the second part $v(t)/R_l$, substituting $\eta_r(t)$ from Equation (3.27) into Equation (3.26) and solving the equation in the frequency domain gives current generated by the r-th mode as:

$$\tilde{i}_r(j\omega) = j\omega\chi_r\tilde{\eta}_r(j\omega_r) = \sum_{r=1}^n \frac{j\omega\tilde{F}_r \chi_r}{\omega_r^2 - \omega^2 + j2\zeta_r\omega_r\omega} \Bigg|_{\omega=\omega_r} \quad (3.36)$$

where \tilde{i}_r is the complex amplitude of the electric current, which can be derived under the short-circuit condition in FEA simulations. It should be noted that all elements of the piezoelectric layer need to be defined as piezoelectric elements. In the ABAQUS FEA software, the C3D20RE piezoelectric element can be used (20-node quadratic brick, reduced integration). The piezoelectric properties need to be assigned into the piezoelectric layer. For example, the permittivity ϵ_{33}^S and the piezoelectric constant e_{31} need to be defined. The piezoelectric elements involve the electromechanical-coupled governing equations based on the piezoelectric constitutive equations.

In order to derive the amplitude of the electric current at each resonance frequency, firstly, the short-circuit condition needs to be applied as stated above. Next, base excitation loading needs to be applied in the steady-state analysis step of ABAQUS at each resonance frequency. The piezoelectric elements generate the electrical flux vectors in different directions. The amplitudes of the vectors along the z-axis are the charge densities of piezoelectric elements on their top and bottom surfaces. The next step is to derive the charge of each piezoelectric element at each resonance frequency by multiplying the amplitudes of the electrical flux by the surface area of the element. This is followed by the calculation of the total complex charge \tilde{Q} , which is the sum of the charge of all piezoelectric elements. The complex current can then be determined by $\tilde{i}(j\omega) = j\omega\tilde{Q}$.

Then, the modal coupling term χ_r can be determined from Equation 3.36 for multiple modes or any single mode.

3.3 A modal approach

3.3.1 Corrected SDOF model

If a harmonic base excitation is applied to the RC harvester for short-circuit condition and $u_b(t) = u_0 e^{j\omega t}$, the steady-state modal response based on the Bernoulli-Euler beam assumption is given by (neglect rotational base excitation and external damping from air) [62]:

$$\eta_r(t) = \frac{m\omega^2}{\omega_r^2 - \omega^2 + j2\zeta_r\omega_r\omega} \frac{2\sigma_r}{\lambda_r} \sqrt{\frac{L}{m}} u_0 e^{j\omega t} \quad (3.37)$$

Substituting Equation 3.18 in Equation 3.17, the relative displacement is,

$$u_{rel}(x, t) = 2u_0 e^{j\omega t} \sum_{r=1}^{\infty} \left[\cosh \frac{\lambda_r}{L} x - \cos \frac{\lambda_r}{L} x - \sigma_r \left(\sinh \frac{\lambda_r}{L} x - \sin \frac{\lambda_r}{L} x \right) \right] \frac{\sigma_r \omega^2}{\lambda_r (\omega_r^2 - \omega^2 + j2\zeta_r \omega_r \omega)} \quad (3.38)$$

When $x=L$, the relative tip displacement is given by,

$$u_{rel}(x, t) = 2u_0 e^{j\omega t} \sum_{r=1}^{\infty} \left[\cosh \lambda_r - \cos \lambda_r - \sigma_r (\sinh \lambda_r - \sin \lambda_r) \right] \frac{\sigma_r \omega^2}{\lambda_r (\omega_r^2 - \omega^2 + j2\zeta_r \omega_r \omega)} \quad (3.39)$$

The reduced relative motion transmissibility based on the r -th mode is,

$$T_{rel}(j\omega) = 2\omega^2 \frac{\sigma_r [\cosh \lambda_r - \cos \lambda_r - \sigma_r (\sinh \lambda_r - \sin \lambda_r)]}{\lambda_r (\omega_r^2 - \omega^2 + j2\zeta_r \omega_r \omega)} \quad (3.40)$$

In the lumped SDOF model, the governing equation of motion is given by:

$$m_m \ddot{z}_s + c_m \dot{z}_s + k_m z_s = F_m \quad (3.41)$$

where z_s , c_m , k_m and F_m are the relative displacement, lumped modal damping coefficient, stiffness and forcing function, respectively. Then, the relative motion in SDOF model is given by:

$$z(t) = \frac{\omega^2 m_m}{k_m - \omega^2 m_m + j\omega c_m} u_0 e^{j\omega t} \quad (3.42)$$

The relative motion transmissibility in SDOF model is

$$T_{SDOF}(j\omega) = \frac{\omega^2}{(\omega_n^2 - \omega^2 + j2\zeta\omega_n\omega)} \quad (3.43)$$

where

$$c_m = 2\zeta\sqrt{k_m m_m}; \quad \omega_n = \sqrt{k_m/m_m} \quad (3.44)$$

Comparing the transmissibility expressions given by Equations 3.40 and 3.43, in order to allow the SDOF model to be used for beams, the correction factor γ for SDOF model is given by:

$$\gamma_r = \frac{\sigma_r [\cosh\lambda_r - \cos\lambda_r - \sigma_r (\sinh\lambda_r - \sin\lambda_r)]}{\lambda_r} \quad (3.45)$$

Then, the corrected relative motion transmissibility in SDOF model is rewritten as:

$$T_{SDOFc}(j\omega) = \frac{\gamma\omega^2}{(\omega_n^2 - \omega^2 + j2\zeta\omega_n\omega)} \quad (3.46)$$

and the corrected modal forcing function is rewritten as:

$$F_{mc}(j\omega) = \gamma\omega^2 m_m u_0 \quad (3.47)$$

In fact, γ is also called the modal participation factor and indicates how strongly motion in the x -, y - or z -direction about one of these axes is represented in the eigenvector of that mode [92]. For the first transverse vibration mode of RC beams without any tip mass, the modal participation factor is nearly fixed and it usually equals 1.566. In the natural frequency extraction step of the FEA software, the modal participation factor is given by [92]:

$$\Gamma_{ri} = \frac{1}{m_{mr}} \{\boldsymbol{\phi}\}^{(r)} [\mathbf{M}] \mathbf{T}_i \quad (3.48)$$

where T_i defines the magnitude of the rigid body response of a degree of freedom in the model (N) to imposed rigid body motion in the i -direction. For a node with the usual three displacements (if assuming no rotational motion), T_i^M is

$$T_i^M = \begin{pmatrix} 1 & 0 & 0 \\ 0 & 1 & 0 \\ 0 & 0 & 1 \end{pmatrix} \begin{Bmatrix} \tilde{e}_1 \\ \tilde{e}_2 \\ \tilde{e}_3 \end{Bmatrix} \quad (3.49)$$

where \tilde{e}_i is unity. Using the modal participation factor, the effective masses m_e can be written as [92],

$$m_{er} = \gamma_r^2 m_{mr}; \quad \sum_{r=1}^{\infty} m_{er} = m_T \quad (3.50)$$

The sum of the effective masses for all modes is the total mass m_T of the whole model. It should be noted that the generalized modal mass m_m in this thesis was called effective mass by Erturk and Inman [62].

Guyomar et al used an electromechanical coupling criterion $k^2 Q_m$ to evaluate the maximum average power output of a harvester based on a SDOF system for the standard rectifier interface (no electrical losses and optimal load is matched) [25]:

$$P_{max} = \frac{F_m^2}{2c_m} \frac{\pi k^2 Q_m}{(\pi + k^2 Q_m)^2} \quad \text{when } k^2 Q_m \leq \pi \quad (3.51)$$

$$P_{max} = \frac{F_m^2}{8c_m} \quad \text{when } k^2 Q_m \geq \pi \quad (3.52)$$

where $Q_m = 1/2\zeta$ is the quality factor, k is the modal electromechanical coupling coefficient (EMCC) and

$$k^2 = \frac{\alpha_r^2}{k_{mr} C_p + \alpha_r^2}; \quad \alpha = \chi \sqrt{m_{mr}} \quad (3.53)$$

α is the lumped coupling factor. However, since Guyomar et al.'s work is based on a SDOF system and the back coupling effect has not been correctly introduced in their assumption, Equation 3.51 cannot be used to accurately predict the performance of harvesters [30]. By substituting Equation 3.47 into Equation 3.52, the corrected maximum power output in the r -th mode is rewritten as,

$$P_{max} = \frac{F_{mcr}^2}{8c_{mr}} = \frac{\gamma_r^2 m_{mr}}{16\xi_r \omega_r} \ddot{u}_b^2 = \frac{m_{er}}{16\xi_r \omega_r} \ddot{u}_b^2 \quad (3.54)$$

In Chapter 5, a parametric study shows that, if $k^2 Q_m$ is adequately large, the corrected maximum power output given in Equation 3.54 can be used to evaluate the maximum performance directly.

3.3.2 Mass ratio

Based on Equation 3.50, a modal factor, which is designated as mass ratio, is introduced as:

$$N_r = \frac{m_{er}}{m_T} = \frac{\gamma_r^2 m_{mr}}{m_T} \quad (3.55)$$

The mass ratio N is the percentage ratio of the effective mass to the total mass, and the sum of mass ratios of all modes equals 1 ($N \leq 1$). For RC harvesters without tip masses, mass ratios in modes 1, 2 and 3 are approximately 0.61, 0.19 and 0.07, respectively [30]. Obviously, harvester with larger total mass and base motion is able to generate more power. Therefore, normalizing the input and using power density to evaluate the performance is more intuitive. By substituting Equation 3.55 into Equation 3.54, the maximum squared acceleration weighted power density (MSAPD) of harvesters is written as,

$$\text{MSAPD}_{max} = \frac{N_r \rho}{16 \xi_r \omega_r} * 10^{-6} (\text{W s}^4 / \text{cm}^3 \text{ m}^2) \quad (3.56)$$

where ρ is the mass density (kg/m^3). MSAPD is a normalised power density, which is defined as the average power per 1m/s^2 base excitation per cubic centimetre (cm^3). Figure 3.3 presents a parametric study about the maximum MSAPD as a function of $k^2 Q_m$ for different mass ratios ($f=46.8$ Hz, $Q_m=49.5$ and $\rho \approx 7840$ kg/m^3). The results given in this parametric study are determined using DPM with the optimal resistive load. The piezoelectric material is assumed to have stronger or weaker piezoelectric effects and the forcing function is adjusted to ensure that the mass ratio has been correctly represented in DPM. The results show that, for different values of $k^2 Q_m$, mass ratio linearly affects the maximum power density. When $k^2 Q_m > 2$, MSAPD is purely mechanical, and it is simply determined by the magnitude of mass ratio. When $k^2 Q_m < 2$, MSAPD is affected by the simultaneous changes of mass ratio and $k^2 Q_m$. When $k^2 Q_m$ is too small, MSAPD can be significantly decreased. A detailed parametric study is presented in Chapter 5.

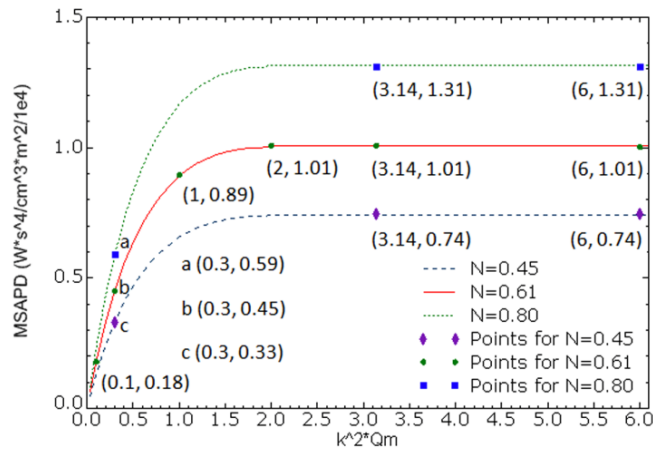


Figure 3.3: Maximum MSAPD as function of $k^2 Q_m$ with different mass ratio N

3.3.3 A modal approach using mass ratio and EMCC

The parametric study presented in Figure 3.3 shows that, the maximum performance of a harvester is affected by mass ratio and $k^2 Q_m$. For configurational study of harvesters, in order to determine the effects of the changes of structure on performance conveniently, damping ratio can be assumed to have a fixed value. For such cases, mass ratio and EMCC can be used as two criteria to evaluate the structural and electromechanical performance of a harvester. Then, a modal approach is introduced using mass ratio and EMCC for

configurational study. In Figure 3.4, a conventional approach (Figure 3.4a) is compared with the modal approach (Figure 3.4b). For the conventional approach, after operating full analysis using DPM to determine the power output, a power output comparison is required and this step needs to be repeated until the configurational performance is surely optimised. For the modal approach, mass ratio and EMCC are used as two filters. The configuration with poor structural and electromechanical performance can be determined without carrying out full analysis using DPM. Besides, using the modal approach is much easier to determine how the change of configuration affects the performance in both mechanical and electromechanical domains.

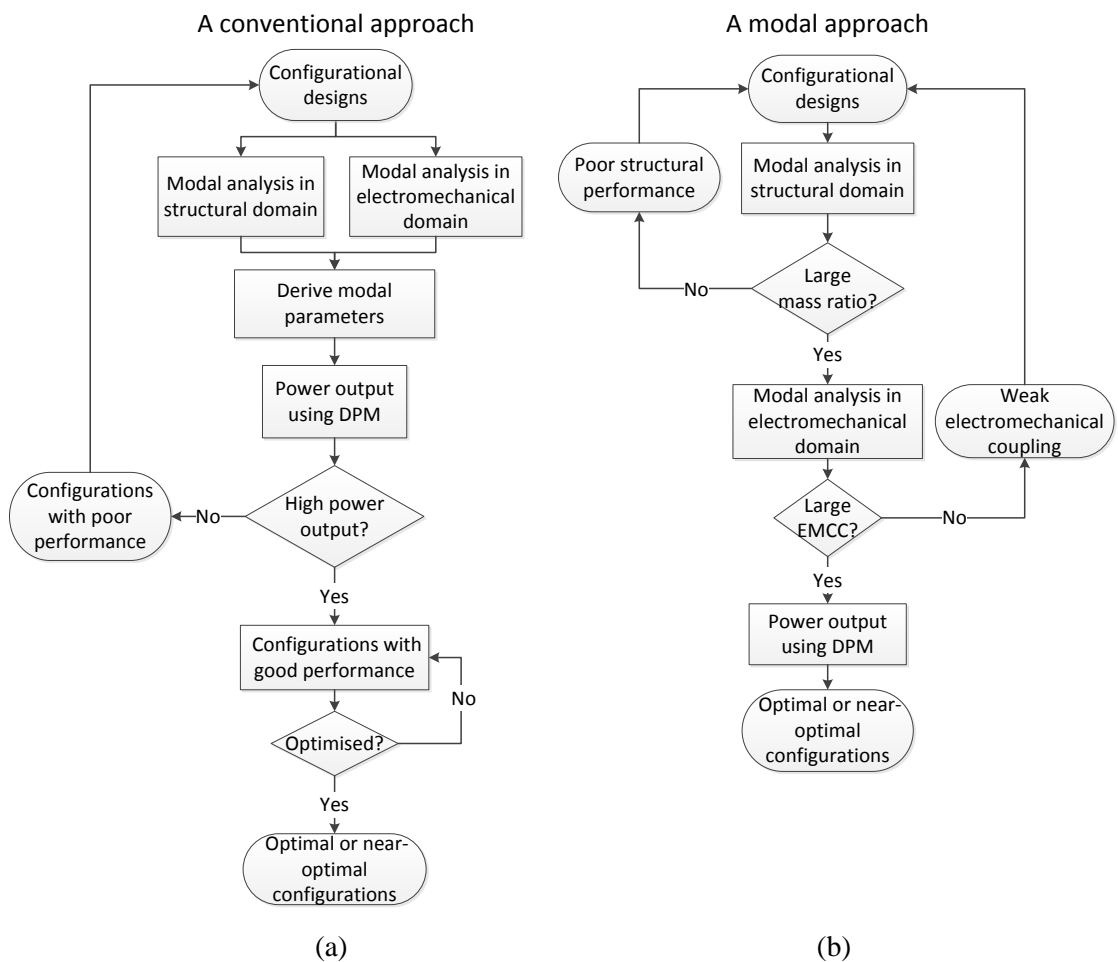


Figure 3.4: Flow charts for configurational designs of vibration energy harvesters; (a) a conventional approach; (b) a modal approach.

3.3.4 Implementation of the modal approach using FEA

The procedures for carrying out the modal approach using FEA simulations can be summarised by the following steps.

Step 1: Run the natural frequency extraction analysis to obtain the short-circuit resonance frequency f_r , the generalized modal mass m_m and the modal participation factor γ_r . The short-circuit condition of a harvester can be realised by fixing the electrical boundary conditions on the electrode surfaces of the piezoelectric layers. Use Equation 3.54 to derive mass ratio N .

Step 2: Run the steady-state dynamics analysis at short-circuit resonance frequency f_r , apply a base excitation to obtain the complex current i_r with a short-circuit condition. Use Equations 3.35 and 3.36 to derive the forcing function F_r and the modal electromechanical coupling factor χ_r , respectively. Then, EMCC k_r can be determined using Equation 3.53.

Step 3: With known mass ratio and EMCC, the structural and electromechanical modal performance in each mode are determined. For the harvester with preferred modal performance, use DPM (Equation 3.28) to derive the power output FRFs with resistive loads around single mode or multiple modes.

3.3.5 A configurational optimization strategy for multi-resonance harvesters

Since the sum of mass ratios of all modes equals 1, if one mode has very large mass ratio, this mode becomes dominant and large power output can be generated. This is preferred when the performance around one resonance frequency needs to be optimised, such as for the investigation of cantilevered beam structures. However, if one mode has too large mass ratio, the remaining modes only have small mass ratios, and eventually these modes generate low power output.

For multi-resonance harvester designs, it is necessary to determine whether the harvester has good broadband performance. A resonance of a harvester can generate very large power output. However, the power output drops rapidly for off-resonance conditions. Therefore, the broadband performance of a harvester should consider both the resonance and off-resonance performances. The capability of a harvester to generate an effective

bandwidth for an acceptable power output level can be evaluated. However, for harvesters with the same effective bandwidth, the broadband performances can still be different.

Figure 3.5 shows normalised power FRFs of different harvesters with approximately the same bandwidth of 31 Hz for a minimal power output of 1×10^{-6} W between 25 Hz to 70 Hz. In Figure 3.5(a), the harvester only generates a very large peak. In Figure 3.5(b), the harvester generates two peaks: one peak is large and the other is small. In Figure 3.5(c), the harvester generates two equal and relatively large peaks. In Figure 3.5(d), the deep notch around the anti-resonance between the two peaks is eliminated. In fact, the harvester with only one very large peak has the worst broadband performance. Firstly, there is only one resonance while the energy of random vibrations is distributed to broadband frequency ranges in real applications. Secondly, the power difference between the peak and the minimal level is too large. For such a case, the generated voltage on devices around the peak can be too high and may eventually damage the electric devices in real application. The broadband performance of the harvester shown in Figure 3.5(b) is similar to the harvester shown in Figure 3.5(a). The second peak is too small to enhance the broadband performance.

The harvester shown in Figure 3.5(c) has good broadband performance since the very large peak is split into two smaller but relatively large peaks. The harvester shown in Figure 3.5(d) has the best broadband performance since the deep notch between the two relatively large peaks is also eliminated. When the harvester has more than two resonance frequencies, the broadband performance should be enhanced even more. Besides, for a harvester with two or more resonances, if any adjacent modes are far away from each other, the broadband performance is also significantly affected. For example, the cantilevered beam harvester cannot generate two close resonance frequencies; its performance is similar to the performance of the harvester shown in Figure 3.5(a).

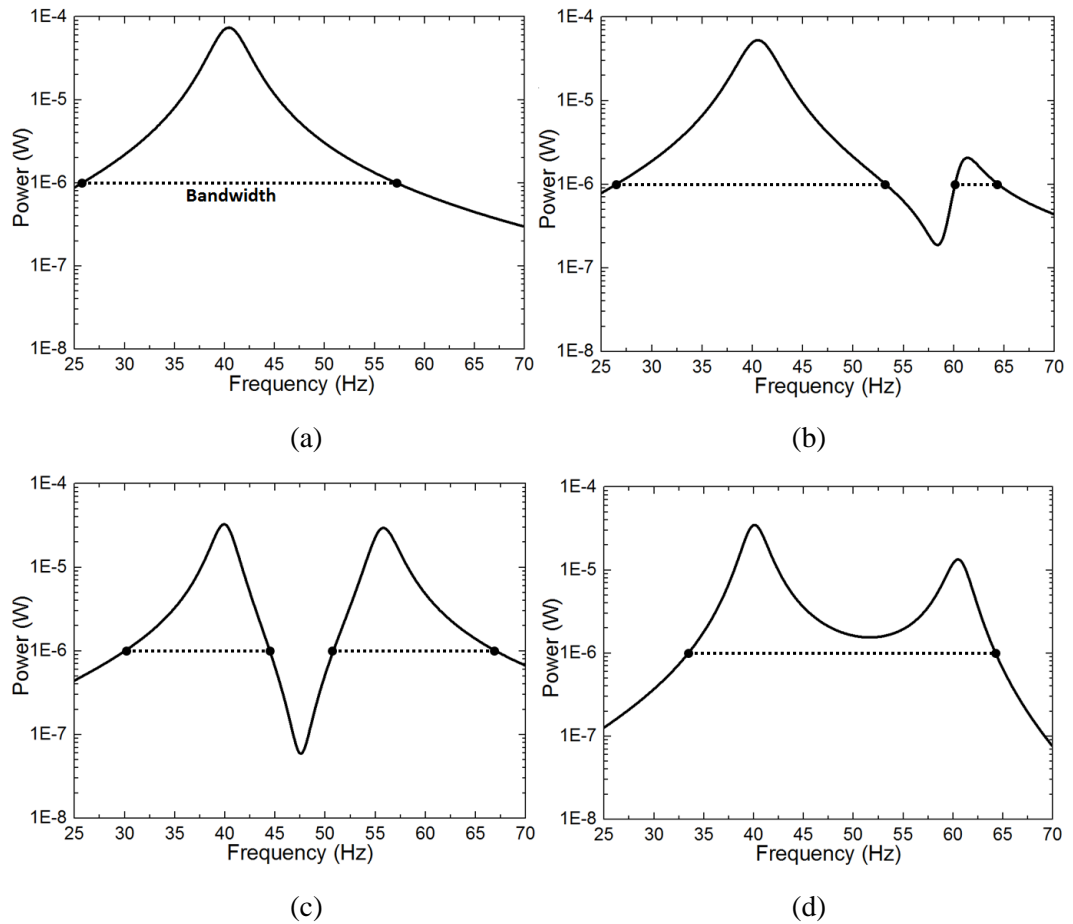


Figure 3.5: Power FRFs of harvesters and broadband performance comparison. (a) single peak (b) one large peak and one small peak; (c) two same peaks; (d) two peaks without anti-resonance

Based on the comparison of the broadband performance in Figure 3.5, in general, harvesters with closer multiple modes and relatively large power in each mode are considered to have good broadband performance. Then, the modal structural performance of a multi-resonance harvester with good broadband performance should be evaluated initially. In particular, the mass ratios of multi-modes should be evenly distributed. A mode with too large mass ratio will generate too large peak and eventually reduce the peaks of other modes. Moreover, the resonance frequencies between each two adjacent modes should be close enough. The modal structural performance of harvesters can be evaluated using the modal approach. Besides, to apply the modal approach using FEA, the natural frequencies and mass ratio can be determined directly using the modal analysis in step 1 whereas the derivation of EMCC required a further step to operate steady-state analysis in step 2. Then, an effective configurational optimisation strategy for multi-resonance harvester designs is developed based on the modal approach. Figure 3.6 shows the flow chart of the optimization strategy. Mass ratios and frequency ratios are used as two criteria

to screen the configurations of harvesters with acceptable mass ratio in each mode and close resonance frequencies between any two adjacent modes. Then, the configurations meet stricter screening criteria will have better structural broadband performance. This strategy obviates the needs to operate full steady-state analysis using FEA and to predict power output using DPM at the first stage. Once the configurations with optimal or near-optimal structural broadband performance have been determined, the further step of the modal approach is to evaluate the EMCC and the full analysis can be operated to predict the power output.

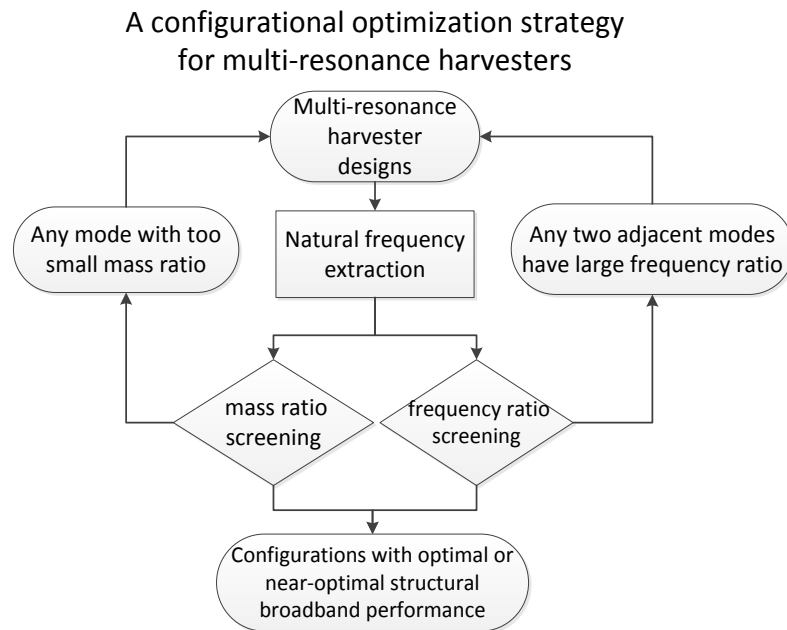


Figure 3.6: Flow chart of the optimization strategy for multi-resonance harvesters

3.4 Summary

In this chapter, the analytical equations and solution for a cantilever bimorph harvester using DPM is presented firstly. The derivations of the required modal parameters of DPM using FEA software is introduced. A corrected SDOF model is presented and the modal participation factor is introduced as the correction factor. Then, using the modal participation factor, a modal factor designated as mass ratio is introduced and it is used in conjunction with EMCC to evaluate the modal structural and electromechanical performance, respectively. Based on this, a modal approach is introduced for configurational study, and a configurational optimization strategy is developed for multi-resonance harvester designs.

CHAPTER 4 RESEARCH OVERVIEW AND CONTRIBUTIONS

4.1 Introduction

This thesis is written in *Alternative Format* in which the research methodologies and findings are presented in the form of published, accepted and submitted academic papers. Thus, each of Chapters 5 to 12 is a published, accepted or submitted journal paper. The main purpose of the research overview is to summarise the overall research contributions of the whole thesis, and to show the coherence and continuity of the study and the rationale for using the alternative format. In addition, the brief summary of each published, accepted or submitted journal paper is presented. The contributions of the authors to the journal papers are also clarified.

4.2 Research overview

In existing harvester designs, many works focus on the optimization of power output directly. The power outputs can be affected by the simultaneous changes of structural behaviour and electromechanical coupling. However, no attempt has been made in previous investigations to analyse the individual effects of these two factors on the output power. Without clearly clarifying the effects from these two factors, the variation or improvement of power output in the published results could be confused when comparing results across several publications. In particular, the modal structural behaviour depends on the vibration modal shape and mass distribution, and it directly affects the forcing function and maximum power output, which has not been stated clearly in existing works.

In this thesis, a criterion referred to as mass ratio is introduced to represent the effects of modal structural behaviour on the power density of harvesters directly. Mass ratio is the ratio of the effective mass to the total mass, and it depends on the modal participation factor. It actually represents how much mass of each mode effectively participates in the

motion and affects the maximum power density linearly. For example, when the piezoelectric and substrate layers have equal length, rectangular cantilevered harvesters of various lengths but without tip masses always have almost the same mode shape and mass ratio. Besides, for cantilevered beam harvesters with tip masses, when the dimensions of the tip masses and beams are slightly changed to control the resonance frequencies, the modal structural behaviour and mass ratio are hardly affected. Many existing works actually optimized power outputs solely based on the optimization of the electromechanical coupling. The effects of the mass ratio were either ignored or not recognised. For multi-resonance harvester designs, to clarify the simultaneous effects of the structural behaviour and electromechanical coupling on the performance becomes more complicated due to the interference of strong vibration coupling. Without clearly clarifying the modal performance of each mode, one or more modes can be dominant while the remaining modes only generate weak performance. This issue can be found in many existing works and the broadband performances of their designed multi-resonance harvesters become limited. Therefore, instead of analysing the power output performance directly, this thesis attempts to clarify the influences of the structural behaviour and electromechanical coupling on the power output performance of harvesters using mass ratio and EMCC, respectively. This is the first work in which mass ratio is defined and used with EMCC to determine the modal performance of both cantilevered beam harvesters and multi-resonance harvesters.

Since the modal performance of the cantilevered beam harvester has not been adequately optimized and the multi-resonance harvesters normally consist of several beam-shaped structures, the investigation of the cantilevered beam harvester is presented firstly in Chapter 5. A parametric study is presented to investigate the effects of mass ratio and EMCC on the power destiny. The design strategy is implemented to optimize the mass ratio and EMCC separately by geometrical variations of the configurations. This is the first work that the modal structural and electromechanical performance of CTC and DTC beam harvesters are clearly determined and compared to the modal performance of RC beam harvesters with different coverage of piezoelectric.

In Chapter 6, a modal approach is introduced based on the design strategy used in Chapter 5. The modal approach uses mass ratio and EMCC as two criteria to evaluate the performance of a harvester. Once the mode has both good value of the mass ratio and

EMCC, high power output can be achieved. The modal approach is also compared with the conventional approach using DPM, which requires deriving the modal parameters in both structural and electromechanical domains. The power output of a harvester with resistive loads is determined using DPM. The conventional approach using DPM can only determine the performance of a harvester after the model has been fully analysed and it requires long computing time. Besides, the conventional approach cannot be used to compare the performance of different harvesters clearly since the simultaneous effects of the structural behaviour and electromechanical coupling on the performance have not been clarified. Because a multi-resonance harvester with good broadband performance requires close resonance frequencies with relative large power output in each mode, a configurational optimization strategy is developed based on the modal approach. The frequency ratio of each two adjacent modes and the mass ratio in each mode are used as the structural screening criteria to screen the configuration with good structural broadband performance. This is the first work in which an effective optimization method has been developed for the configurations of multi-resonance harvesters using FEA. Using the configurational optimization strategy enables easy selection of the configurations with optimal or near-optimal structural broadband performance from hundreds of configurations and it obviates the need to operate full steady-state analysis at the first stage.

A novel two-layer harvester, which consists of two rectangular cantilevered beam layers and a spacer fixed between the two layers to ensure enough space for vibration, is developed in Chapter 6. Two masses are attached on two layers and one of the two masses serves as the spacer. By altering the dimensions of the harvesters and the positions of the masses, two close resonance frequencies with considerable power output in each mode can be generated. Using the configurational optimization strategy, the configurations with optimal or near-optimal structural performance are determined. In Chapter 7, a continuous study for the two-layer harvester is presented. The two-layer harvester using CTC and DTC beams are developed and compared with the harvester using RC beams. Based on the design of the two-layer harvester, the multi-layer harvesters, which consist of up to five layers and which can generate up to five close resonance frequencies, are developed in Chapter 8. The optimal or near-optimal configurations of the three-layer harvesters with two types of setup are determined using the configurational optimization strategy. The multi-layer harvester can effectively improve the power output bandwidth and the selected configuration with good performance can be used for different harvester sizes ranging from

few mm to hundreds of mm with the power ranging from microwatts to milliwatts. In Chapter 9, a novel doubly clamped multi-layer harvester is developed and systematically analysed. Instead of using a cantilevered base, it consists of a doubly clamped base and up to two upper/lower layers and two spacers. By altering the positions of masses, the doubly clamped two-layer and three-layer harvesters can generate three and five close resonance frequencies, respectively, with nearly the same level of power output in each mode. The doubly clamped multi-layer harvester can generate multiple resonance frequencies using fewer components than the cantilevered multi-layer harvesters do.

From Chapter 6 to Chapter 9, the multi-resonance harvesters are developed based on the configurational optimization strategy using FEA. The power outputs FRFs with resistive loads are determined using DPM. In real applications, since the harvesters are developed as power supplies for wireless sensor networks, the alternating current generated from the harvester needs to be converted into direct current by connecting with capacitors or rechargeable batteries. However, the circuit analysis with nonlinear electrical components, such as the storage capacitor, cannot be used in conjunction with conventional harvester models. To overcome the limitation, ECM has been widely used as an alternative analysis technique. However, since the configuration becomes more complicated and the full steady-state analysis in a wider bandwidth is required using FEA, existing FEA-ECM models are difficult to implement for multi-resonance harvester designs and they normally require long computing and processing time. Chapter 10 presents an easily implemented and fully coupled ECM, which transfers the corrected lumped modal parameters to the circuit simulation software SPICE. The lumped modal parameters and the correction factors are derived from the FEA data at resonance frequencies, which obviate the need to operate full steady-state analysis in a wider bandwidth and save analysis time. The FEA-SPICE ECM using corrected lumped modal parameters has been successfully compared with FEA-DPM for power output with resistive load.

An experimental study for the multi-layer harvesters is presented in Chapter 11. The experimental results are compared with the FEA results to validate the modal approach and the configurational optimization strategy. Although the geometrical dimensions and parameters of the harvesters manufactured and tested are slightly different from those of the theoretical models, their structural performances are similar to those of the theoretical models analysed previously. The findings indicate that the configurational optimization

strategy using FEA software can successfully pre-select the configuration with optimal or near-optimal structural performance and such configuration can be directly used to manufacture harvesters, which are guaranteed to have optimal or near optimal experimental performance.

From Chapter 5 to Chapter 11, PZT is used in both simulations and experiments. In fact, without proper and careful design, the harvester using PZT can have limited performance due to the moderate piezoelectricity of the material. Therefore, some researches use high performance piezoelectric materials, such as PMNT, for vibration energy harvesting. However, the high performance materials are normally bonded on conventional beam harvester, which prevents the harvester from generating better broadband performance. In Chapter 12, an experimental comparison between the multi-layer harvesters using PZT and PIMNT is presented. This is the first work in which the high performance PIMNT has been used in multi-resonance harvester and has been compared with the harvester using PZT for the same configuration. The results show that using the high performance PIMNT in conjunction with the multi-layer configuration can tremendously improve the broadband performance in comparison with the cantilevered beam harvester using PZT.

4.3 Outline of published/submitted papers

This section presents the outline of each paper. The title of each paper, names of the authors, the publication details and a brief description of the content of each paper are presented. For all papers presented in this thesis, Xingyu Xiong is the first author and the main contributor to the investigations including model analysis, experimental design and testing, data processing and paper writing. His supervisor Dr S Olutunde Oyadiji is the second author and the corresponding author who provided supervision, suggestion and paper proofreading.

4.3.1 Modal electromechanical optimization of cantilevered piezoelectric vibration energy harvesters by geometric variation

Authors: Xingyu Xiong and S Olutunde Oyadiji

Published in: Journal of Intelligent Material Systems and Structures 25 (10), 1177-1195, 2013

In this paper, cantilevered beam harvesters have been investigated. The first part of the paper presents a parametric study to identify the effects of mass ratio, EMCC and damping ratio on the power density systematically. A design strategy is introduced to investigate mass ratio and EMCC separately using geometric parameter study. The second part presents the detailed optimization of mass ratio and EMCC with geometric parameter study of the cantilevered beam harvesters using the ABAQUS FEA software. The results show that using the full coverage of the piezoelectric layer does not generate the optimal EMCC and using partial coverage of the piezoelectric layer is able to improve the EMCC. Using CTC configuration can decrease the mass ratio significantly. Using DTC configuration and attaching reasonable extra masses can both generate larger mass ratio.

4.3.2 Optimal design of two-layer stacked vibration energy harvesters using a modal approach

Authors: Xingyu Xiong and S Olutunde Oyadiji

Published in: Smart Materials and Structures 23 (3), 035005, 2014

In this paper, two-layer harvesters have been developed. A modal approach using mass ratio and EMCC is introduced to determine the modal performance. The finding indicates that a mode with too large mass ratio can be dominant and it causes the remaining modes to have small mass ratio and poor structural performance. A screening process is introduced to select the configurations with optimal or near-optimal performance. Thereafter, the optimal design of the two-layer harvesters with different configurations has been presented. The results also show that if the base layer is fully covered by the piezoelectric layer, the anti-resonance between two modes can be eliminated. For such a case, if two modes are close enough, a wider bandwidth of power output can be generated.

4.3.3 Tapered two-layer broadband vibration energy harvesters

Authors: Xingyu Xiong and S Olutunde Oyadiji

Submitted to: ASME Journal of Vibration and Acoustics (accepted)

In this paper, two-layer harvesters using CTC and DTC beams have been investigated. The results show that, when the configuration has two layers and one mass, CTC harvesters can achieve better broadband performance than RC harvesters whereas DTC harvesters are

unable to provide close resonance frequencies. When the configuration has two layers and two masses, the broadband performance of DTC harvesters is significantly improved. The findings also indicate that the mode with too large or too small mass ratio will normally have strong or weak EMCC in that mode, and a model with evenly distributed mass ratios in multi-modes can normally generate acceptable EMCC in multi-modes.

4.3.4 A general modal approach for the development of optimal multi-layer stacked vibration energy harvesters

Authors: Xingyu Xiong and S Olutunde Oyadiji

Published in Journal of Sound and Vibration 333 (21), 5386-5411, 2014

In this paper, multi-layer harvesters have been developed. In particular, the configurations of three-layer harvesters are thoroughly optimized. The three-layer harvesters have two different set-ups: either the masses are located on one side of the base layer, or the masses are located on two sides of the base layer. The results show that the two-sided three-layer harvesters have better broadband performance than the one-sided three-layer harvesters. For the four-layer and five-layer harvesters, since the mass positions are too many, typical configurations with good broadband performance are analysed. The finding indicates that the multi-layer harvesters can improve the bandwidth of power output significantly.

4.3.5 Modal optimization of doubly-clamped base-excited multilayer broadband vibration energy harvesters

Authors: Xingyu Xiong and S Olutunde Oyadiji

Published in Journal of Intelligent Material Systems and Structures, doi: 10.1177/1045389X14551433, 2014

In this paper, doubly clamped multi-layer harvesters have been developed. The detailed procedures for carrying out the modal approach and the configurational optimization strategy by FEA simulations are summarised. The optimal designs of the two-layer and three-layer harvesters are presented. The results show that, when the mass positions are close to the centre of the beam layer, the harvester can easily achieve broadband power output once the base layer is a little bit thicker than the upper and lower layers. If the mass

positions become too close to the centre of the beam layer, two of the five modes become inactive due to interference from strong structural coupling. The findings also indicate that using large piezoelectric coverage can significantly decrease the EMCC due to strong self-cancellations.

4.3.6 An equivalent circuit model using corrected lumped modal parameters for multi-resonance piezoelectric vibration energy harvesting

Authors: Xingyu Xiong and S Olutunde Oyadiji

Submitted to: IEEE/ASME Transactions on Mechatronics (under review)

In this paper, fully coupled ECM using corrected lumped modal parameters are developed. The conventional circuit analysis normally uses lumped SDOF model, which oversimplifies the structural modal behaviour. In this paper, the modal participation factor is introduced to correct the modal contribution of each mode to the overall motion. The corrected lumped modal parameters are transferred to the SPICE electrical circuit analysis software to operate circuit simulation. The performances of two-layer and the three-layer harvesters with resistive loads are predicted using ECM and the power output FRFs have been compared with the same models predicted using DPM. Besides, the implementation of the ECM is significantly simplified in comparison with existing ECM.

4.3.7 Design, analysis and experimental validation of the performance of multi-layer stacked vibration energy harvesters

Authors: Xingyu Xiong and S Olutunde Oyadiji

Submitted to: Journal of Sound and Vibration

In this paper, experimental studies of multi-layer harvesters are presented. The power output FRFs of the two-layer and three-layer harvesters with selected configurations are measured and compared with FEA results to validate the configurational optimization strategy. The modal participation factors and EMCC of the two-layer harvesters are derived from the experimental data and they are compared with the same modal parameters derived from FEA data to validate the modal approach. The results of the experimental broadband performances show that the two-layer harvesters can generate 1.5 times wider

bandwidth and the three-layer harvesters can generate 2 times wider bandwidth in comparison with the single layer harvester with a tip mass.

4.3.8 Experimental study of the broadband performance of multi-layer vibration energy harvesters using PZT and PIMNT

Authors: Xingyu Xiong and S Olutunde Oyadiji

Submitted to: Smart Materials and Structures

In this paper, PIMNT and PZT are used on the two-layer and three-layer harvesters with the same configuration for comparisons. The piezoelectric layer is bonded on the top surface of the base layer and it has two types of locations. The first type of piezo-layer is bonded near the clamped end of the base layer. The second type of piezo-layer is bonded between the middle and the free tip of the base layer. The results show that the PIMNT-harvester can generate nearly 10 times larger power output than the PZT-harvester for both resonance and off-resonance conditions. Besides, with the first type of piezo-layer, the PIMNT-harvester can generate more than 3.5 times wider bandwidth than the PZT-harvester. Besides, using the second type of piezo-layer can eliminate the anti-resonance area between two adjacent modes whereas it has not improved the broadband performance.

4.4 Summary

The research overview emphasizes the coherency and continuity of the research investigations presented in all papers. These papers contain innovative and creative ideas and results, which have significantly contributed to the research field of vibration energy harvesting. Currently, three papers presented in Chapters 5, 6 and 8 have been formally published in journals and the remaining papers, which are presented in Chapters 9 to 12, have been submitted for peer review for journal publications. Hence, instead of using *Traditional Format* for the PhD Thesis, the *Alternative Format* is used in this thesis to highlight the original contributions to knowledge.


CHAPTER 5 MODAL ELECTROMECHANICAL OPTIMIZATION OF CANTILEVERED PIEZOELECTRIC VIBRATION ENERGY HARVESTERS BY GEOMETRIC VARIATION

Xingyu Xiong and S Olutunde Oyadiji

Journal of Intelligent Material Systems and Structures 25 (10), 1177-1195, 2013

Modal electromechanical optimization of cantilevered piezoelectric vibration energy harvesters by geometric variation

Xingyu Xiong and S Olutunde Oyadiji

Journal of Intelligent Material Systems and Structures
2014, Vol. 25(10) 1177–1195
© The Author(s) 2013
Reprints and permissions:
sagepub.co.uk/journalsPermissions.nav
DOI: 10.1177/1045389X13502872
jim.sagepub.com


Abstract

The design studies of cantilevered piezoelectric vibration energy harvesters have been focused on the optimization of the power output of rectangular cantilevered beam vibration energy harvesters. However, without clarifying the influences of the modal electromechanical coupling and mechanical behaviour clearly, the power outputs cannot be adequately optimized. In this article, a distributed parameter electromechanical model is used to predict the power output with resistive loads, and the parameters are derived using the finite element method. First, a parametric study is presented to investigate the effects of the two factors on the volumetric power of cantilevered vibration energy harvesters. Then, an optimization strategy is implemented to investigate the modal electromechanical coupling coefficient and mass ratio separately using geometric parameter study. Mass ratio represents the influences of modal mechanical behaviour on the power density directly. The findings indicate that the convergent and divergent tapered cantilevered and rectangular cantilevered beam designs with partial coverage of piezoelectric layer are able to generate higher electromechanical coupling coefficient than conventional rectangular cantilevered designs with full coverage. Besides, using convergent tapered cantilevered designs can actually decrease the power density significantly. Both using divergent tapered cantilevered structures and attaching reasonable extra masses with varied locations on vibration energy harvesters can generate larger power density.

Keywords

Energy harvesting, piezoelectric, electromechanical coupling coefficient, volumetric power

Introduction

In recent years, the possibility of developing self-powered, batteryless wireless sensors and sensor nodes for preventive maintenance strategies has made the small-scale ambient energy harvesting to become a gradually focused research field (Cook-Chennault et al., 2008). In particular, as an attractive option and one of the kinetic energy harvesting implementations, a lot of work has been concentrated on developing the vibration energy harvesters (VEHs) using piezoelectric materials in the last decade (Anton and Sodano, 2007; Roundy et al., 2008). Resonance has been considered as an effective method of energy conversion from the mechanical domain to the electrical domain. Cantilevered structures have become widely used, which normally have resonance frequencies in the range of 100 Hz and produce microwatts (μW) to milliwatts (mW) power output, for the sizes of VEH considered with respect to the natural sizes of wireless sensors and sensor nodes.

The study of cantilevered VEHs has been focused on different aspects with the overall goal being to optimize the performance of existing devices. Many investigations are focused on the geometric parameter designs of rectangular cantilevered (RC) VEHs and investigate the power output directly. Richter et al. (2007) developed models of RC VEHs with different lengths and widths in order to explore how the beam dimensions affected the matching resistance and power output.

Dynamics and Aeroelasticity Expert Group, School of Mechanical, Aerospace and Civil Engineering, The University of Manchester, Manchester, UK

Corresponding author:

S Olutunde Oyadiji, Dynamics and Aeroelasticity Expert Group, School of Mechanical, Aerospace and Civil Engineering, The University of Manchester, Manchester M13 9PL, UK.
Email: s.o.oyadiji@manchester.ac.uk

Results in their study have shown that with the same length, the wider RC VEHs can generate more than twice the power output. Zhu et al. (2010) used the commercial finite element analysis (FEA) code ANSYS to explore the influence of dimensions on the current and power output of RC VEHs, including the length, width and thickness of VEHs as well as tip masses. The study suggested that a wider but shorter beam was preferred since it generated larger current and power output. However, the resonance frequencies in their models were varied, and the base acceleration inputs were incorrectly normalized. Both Song et al. (2009) and Patel et al. (2011) have optimized their design of RC VEHs by changing the geometrical parameters and adding large tip masses to achieve a fixed resonance frequency. The former work used a high-performance piezoelectric single crystal to ensure that the system electromechanical coupling is strong and added a bulky tip mass (7.7 times the beam mass). It was a special design and did not explore the reason for the generation of larger power density when compared with previous works. The latter research of Patel et al. mainly investigated the influence of piezoelectric coverage on the power output. The influences of attaching huge tip masses (nearly 15 times the beam mass) on the maximum power output were ignored.

In fact, in the work carried out for this article, it was found that a VEH with reasonable extra masses (2–5 times) or a divergent tapered cantilevered (DTC) structure can significantly affect the modal mechanical behaviour and also increase the mass ratio. Mass ratio is the ratio of the effective mass to the total mass and depends on the modal participation factor. It represents how much mass effectively participates in the motion and affects the forcing function and maximum power density directly. In most existing works, RC VEHs without tip masses have been extensively investigated. Although the geometrical dimensions of the RC VEHs have been changed, the mass ratios did not change, especially when the substrate and piezoelectric layers have equal length. This is because the modal behaviours of the different RC VEHs are similar. Besides, only slightly changing the dimensions of both VEHs and tip masses, in order to tune the resonance frequency, will hardly affect the mass ratio. Therefore, the variation of the normalized maximum power in most existing works was actually due to the electromechanical coupling conditions. In some previous investigations reported in the literature, the predicted power outputs were affected by the simultaneous changes of electromechanical coupling and mechanical behaviour. There was no attempt made to analyse the individual effects of these two factors on the output power. More importantly, system coupling combined the effects of damping and electromechanical coupling coefficient (EMCC) simultaneously, which also has not been stated clearly in many previous design works.

Some investigations improved the performance of VEHs actually via enhancing the EMCC. Erturk et al. (2009) have analysed the strain distribution of RC VEH with and without tip masses and suggested that the electrodes on the piezoelectric layer should be segmented into several parts in order to avoid self-cancellations in higher modes. Roundy et al. (2005) indicated that a convergent tapered cantilevered (CTC) beam can notably increase energy density of VEH compared with the RC beam due to the contributions of the strain distribution. However, despite the fact that this idea has been used in several researches for special designs, how the CTC design improves the power output has not been adequately analysed. In this article, results show that, first, for a VEH with medium to strong electromechanical coupling, using CTC structure actually generates lower power density than RC and DTC VEHs since it has smaller mass ratio; second, using CTC structure only generates higher EMCC when it has large piezoelectric coverage.

Moreover, Friswell and Adhikari (2010) developed RC VEHs covered with different shapes of piezoelectric layer on the substrate layer. They found that RC VEHs with half coverage of piezoelectric layer generate 2 times power output than full coverage. Bourisli and Al-Ajmi (2010) found that the optimized EMCC of RC VEH in the fundamental mode is achieved with 50%–60% piezoelectric coverage but that it also depends on the thickness ratio of the piezoelectric layer to the substrate layer. Patel et al. (2011) also found that RC VEHs with 60% coverage generate higher power output than full coverage. However, instead of discussing EMCC, Patel et al. showed how the piezoelectric coverage affects the modal backward coupling term and incorrectly concluded that the EMCC did not affect the maximum power. In fact, the variation of power output in their results corresponded to EMCC directly since the system is designed to have weak to medium coupling. In this article, the variations of EMCC with the geometrical dimensions of VEHs are investigated using RC, DTC and CTC structures. Also, how EMCC affects the maximum power is carefully investigated.

Generally, the existing designs and geometric studies of cantilevered VEHs are based on specified parameters and running the mathematical analyses to optimize the power output directly. Without clarifying the effects of the electromechanical coupling and mechanical behaviour carefully, the results could be easily confused when compared with others' results and may not be acceptable when the configurations are different. This article attempts to clarify how these two factors affect the maximum power. A design strategy is developed and suggests that EMCC and mass ratio should be investigated separately in order to optimize the performance of VEHs. In this article, the power outputs are on resistive loads. A Rayleigh damping system has been used and the electrical losses are ignored. Section

‘Vibration energy harvesting model’ of this article is on the presentation of distributed parameter and FEA models; section ‘Performance determination and optimization strategy’ is on the performance determination and design strategy; section ‘Modal electromechanical coupling optimization’ is on the optimization of the EMCC of RC, CTC and DTC VEHs; section ‘Modal mechanical behaviour optimization’ is on the optimization of mass ratio of RC, CTC and DTC VEHs and RC VEHs with extra masses; a summary of the technical findings is presented in section ‘Conclusion’ at the end of this article.

Vibration energy harvesting model

Erturk and Inman (2008a) established a fully coupled distributed parameter electromechanical model (DPM) based on the Euler–Bernoulli beam assumptions and predicted the power output with resistive loads. The analytical model was successfully validated experimentally by themselves and other researchers. However, the analytical model is only valid for the uniform RC VEHs. To overcome the limitations, the well-established approximate engineering solution and the finite element method (FEM) using commercial FEA software packages, such as ABAQUS and ANSYS, have been widely used. The FEM has been theoretically and experimentally validated in the existing works (Patel et al., 2011; Trindade and Benjeddou, 2009; Wu et al., 2012; Yang and Tang, 2009; Zhang, 2010), and it is able to deal with complicated models and derive data conveniently, and it is normally used to perform design studies.

Analytical model

The vibration response can be represented using modal analysis technique, and the absolute transverse displacement relative to the moving base of the beam $u_{rel}(x, t)$ is

$$u_{rel}(x, t) = \sum_{r=1}^{\infty} \phi_r(x) \eta_r(t) \tag{1}$$

where $\phi_r(x)$ and $\eta_r(t)$ are the mass-normalized eigenfunction and the corresponding modal coordinates of the r th mode of the cantilevered beam, respectively. Using Erturk and Inman (2008a, 2011) with the assumption of Euler–Bernoulli beam and negligible external excitation from air damping, the equation governing the modal response of the beam is

$$\frac{d^2 \eta_r(t)}{dt^2} + 2\zeta_r \omega_r \frac{d\eta_r(t)}{dt} + \omega_r^2 \eta_r(t) + \chi_r v(t) = F_r(t) \tag{2}$$

where v is the generated voltage given by the uniform electric field E over the thickness of the piezoelectric

Table 1. Coupling term θ and piezoelectric capacitance C_p of a RC VEH with unimorph and bimorph structures.

	Unimorph	Bimorph	
		Parallel connection	Series connection
θ	$e_{31} b h_{p_{cu}}$	$2e_{31} b h_{p_{cb}}$	$e_{31} b h_{p_{cb}}$
C_p	$\epsilon_{33}^s b L / h_p$	$2\epsilon_{33}^s b L / h_p$	$\epsilon_{33}^s b L / 2h_p$

RC: rectangular cantilevered; VEH: vibration energy harvester. ϵ_{33}^s is the clamped dielectric constant; b is the width of the beam; e_{31} is the piezoelectric constant in stress form; $h_{p_{cu}}$ and $h_{p_{cb}}$ are the distance from the centre of the piezoelectric layer(s) to the neutral axis of the beam for unimorph and bimorph structure, respectively.

layer h_p . ζ_r , ω_r , χ_r and F_r are the damping ratio, angular resonance frequency, modal electromechanical coupling term and modal mechanical forcing term, respectively (Table 1). For the RC VEH with equal length of the substrate and piezoelectric layer, given a harmonic base acceleration $\ddot{u}_b = Y_0 \omega^2 e^{j\omega t}$

$$F_r(t) = -Y_0 \omega^2 e^{j\omega t} m \int_{x=0}^L \phi_r(x) dx \tag{3}$$

$$\chi_r = \int_{x=0}^L \theta \frac{d^2 \phi_r(x)}{dx^2} dx = \theta \left. \frac{d\phi_r(x)}{dx} \right|_{x=L} \tag{4}$$

where m is the mass per unit length of the beam, L is the length of the beam and θ is the coupling term. The equation governing the electrical behaviour is expressed as (Erturk and Inman, 2008a, 2011)

$$\frac{v(t)}{R_l} + C_p \frac{dv(t)}{dt} - \sum_{r=1}^{\infty} \chi_r \frac{d\eta_r(t)}{dt} = 0 \tag{5}$$

where C_p is the piezoelectric capacitance and R_l is the resistive load.

When a harmonic base acceleration $Y_0 \omega^2 e^{j\omega t}$ is applied, the steady-state solution of equation (2) is

$$\eta_r(t) = \frac{F_r - \chi_r v}{\omega_r^2 - \omega^2 + j2\zeta_r \omega_r \omega} e^{j\omega t} \tag{6}$$

The voltage across R_l can be represented by (Erturk and Inman, 2008a, 2011)

$$v(t) = \frac{\sum_{r=1}^{\infty} \frac{j\omega F_r \chi_r}{\omega_r^2 - \omega^2 + j2\zeta_r \omega_r \omega}}{\sum_{r=1}^{\infty} \frac{j\omega \chi_r^2}{\omega_r^2 - \omega^2 + j2\zeta_r \omega_r \omega} + \frac{1}{R_l} + j\omega C_p} e^{j\omega t} \tag{7}$$

Hence, solving equation (7) in the frequency domain gives the complex power simply as $v(j\omega)(v(j\omega)/R_l)^*$. For the assumption that no electric losses have occurred

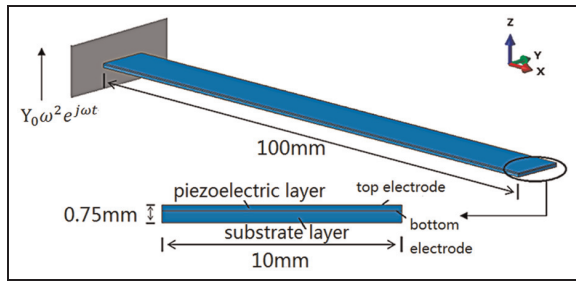


Figure 1. Unimorph rectangular cantilevered beam model A.

Table 2. Properties of the unimorph rectangular cantilever model A.

Parameters	Properties
Beam length, L	100 mm
Beam width, b	10 mm
Thickness of piezoelectric layer, h_p	0.25 mm
Piezoelectric materials	PZT-5A ^a
Density of piezoelectric layer	7750 kg/m ³
Clamped dielectric constant, ϵ_{33}^S	7.3488×10^{-9} F/m
Piezoelectric layer Young's modulus	60.9×10^9 N/m ²
Piezoelectric constant, e_{31}	-5.4 C/m ²
Transverse coupling factor, k_{31}	0.344
Thickness of substrate layer, h_s	0.5 mm
Density of substrate layer	7850 kg/m ³
Substrate layer Young's modulus	200×10^9 N/m ²

PZT: lead zirconate titanate.

^aMorgan Technical Ceramics standard.

with rectifier, the average power output is $|v|^2/2R_l$. The vibration response of the beam relative to its base is

$$u_{rel}(x, t) = \sum_{r=1}^{\infty} \phi_r(x) \frac{F_r - \chi_r v}{\omega_r^2 - \omega^2 + j2\zeta_r \omega_r \omega} e^{j\omega t} \quad (8)$$

Finite element model

When the VEH model is not uniform, the derivations of the eigenfunction $\phi_r(x)$ and coupling terms θ , χ_r and F_r become complicated. Using FEA software packages like ABAQUS and ANSYS are able to derive those parameters conveniently. A unimorph RC VEH model A is developed in ABAQUS and shown in Figure 1. The dimensions and typical material properties are given in Table 2. The substrate layer is clamped at one end and the piezoelectric layer is fixed on it. The base displacement excitation is applied along the z -axis, and the voltage is applied on the top and bottom of the piezoelectric layer.

Using the idea of equivalent circuit model (Yang and Tang, 2009), by letting the applied voltage go to 0 for the short-circuit condition ($v = 0$), applying base excitation at each resonance frequency and deriving the absolute transverse displacement relative to the moving base

from the FEA results, the forcing function F_r can be determined from equation (6) in the frequency domain. For the r th mode

$$F_r = (\omega_r^2 - \omega^2 + j2\zeta_r \omega_r \omega) \eta_r(j\omega_r) = 2\zeta_r \ddot{u}_{rel} \sqrt{m_{mr}} \Big|_{\omega = \omega_r} \quad (9)$$

where m_m is the generalized modal mass associated with the mode and derived from the FEA natural frequency extraction analysis. Normally, $m_m \cong 0.24 mL$ for a uniform RC beam. By replacing $v(t)/R_l$ with $i(t)$ in equation (5), the complex current i_r for the short-circuit condition with base excitation can be derived from the electric displacement D data in FEA results and it is

$$i_r = j\omega \chi_r \eta_r(j\omega_r) = \sum_{r=1}^{\infty} \frac{j\omega F_r \chi_r}{\omega_r^2 - \omega^2 + j2\zeta_r \omega_r \omega} \Big|_{\omega = \omega_r} \quad (10)$$

Then, the modal coupling term χ_r can be determined from equation (10) for multiple modes or any single mode. A proportional damping is used in the simulations. For the r th mode, the damping ratio is defined by

$$\zeta_r = \frac{\alpha_R}{2\omega_r} + \frac{\beta_R \omega_r}{2} \quad (11)$$

where α_R is the mass proportional damping (viscous air damping), which damps the lower frequencies, and β_R is the stiffness proportional damping (strain rate damping), which damps the higher frequencies. In this article, these parameters are defined as $\alpha_R = 4.886$ rad/s and $\beta_R = 1.2433 \times 10^{-5}$ s/rad in most simulation models. In fact, the defined proportional damping is just a convenient method to predict the damping. Indeed, the damping affects the electromechanical coupling and power output significantly. Then, for the real applications, obtaining the damping ratio experimentally is required. With the known ζ_r , F_r and χ_r , the fully coupled voltage and translation responses can be successfully determined from single mode or multiple modes using equations (7) and (8).

Performance determination and optimization strategy

Performance determination

In section 'Vibration energy harvesting model', a DPM has been presented. The voltage and power output with different resistive loads can be generated using equation (7). However, the performance of a VEH cannot be clearly determined unless a specified model has been defined. Generally speaking, maximizing the VEH's power output is the primary objective of design. Guyomar et al. (2009) introduced a criterion to evaluate the maximum average power output of VEH with

resistive load (for standard rectifier interface; no electrical losses with rectifier; optimal load is matched)

$$P_{max} = \begin{cases} \frac{F_m^2}{2c_m} \frac{\pi k^2 Q_m}{(\pi + k^2 Q_m)^2} & \text{when } k^2 Q_m \leq \pi \\ \frac{F_m^2}{8c_m} & \text{when } k^2 Q_m \geq \pi \end{cases} \quad (12)$$

where k is the EMCC; $Q_m = 1/2\zeta$ is the quality factor; F_m and c_m are lumped mechanical force and damping coefficient, respectively. In terms of equation (13), when $k^2 Q_m > \pi$, the power output is maximum and purely mechanical. If $k^2 Q_m < \pi$, the reachable power given by equation (12) is always smaller than the maximum power.

In fact, equations (12) and (13) are based on the assumption of lumped single-degree-of-freedom (SDOF) system and determined by equation (14). Erturk and Inman (2007, 2008b, 2011) discussed the mechanical behaviour and compared the lumped SDOF model with the Euler–Bernoulli beam model and introduced the correction factor of the SDOF model. They found a very good agreement of the relative motion transmissibility (uncoupled) predicted using the Euler–Bernoulli beam model and lumped SDOF model with the correction factor in a wide-frequency band around the resonance. For the fundamental mode in transverse vibration of any RC beam without tip mass, $\gamma \cong 1.566$, once the beam aspect ratio satisfies the Euler–Bernoulli beam assumption. In fact, γ is also called the modal participation factor, which indicates how strongly motion is in the x -, y - or z -direction or rotation about one of these axes is represented in the eigenvector of that mode (SIMULIA Corp, 2010). For a harmonic base motion, the motion and electrical governing equations in lumped SDOF system are

$$\begin{cases} m_m \ddot{z} + c_m \dot{z} + k_m z - \alpha v = F_m \\ C_p \dot{v} + \frac{v}{R_l} - \alpha \dot{z} = 0 \end{cases} \quad (14)$$

The corrected lumped forcing function is

$$F_{mr} = -\gamma_r m_m \ddot{y} \quad (15)$$

and the EMCC and lumped parameters are

$$k^2 = \frac{\alpha_r^2}{k_m C_p + \alpha_r^2} = \frac{\omega_{oc}^2 - \omega_{sc}^2}{\omega_{oc}^2}; \quad (16)$$

$$c_{mr} = 2\zeta_r \sqrt{k_{mr} m_{mr}}; \quad \omega_r = \sqrt{\frac{k_{mr}}{m_{mr}}}$$

and the corrected complex voltage on the resistor is

$$v(j\omega) = \frac{\gamma_r \alpha_r R_l \dot{\omega}^2 m_{mr}}{j\omega R_l \alpha_r^2 + (j\omega c_{mr} - \omega^2 m_{mr} + k_{mr})(1 + j\omega C_p R_l)} \quad (17)$$

where z is the relative displacement related to the base motion y ; $\alpha_r = \chi_r \sqrt{m_{mr}}$ is the lumped coupling factor; m_m is the generalized modal mass; k_m is the effective stiffness; $\omega_{sc} = \omega_r$ is the undamped angular resonance frequency for short-circuit condition of the r th mode and ω_{oc} is the open-circuit angular resonance frequency. By substituting equations (15) and (16) into equation (13), the maximum power can be rewritten as

$$P_{max} = \frac{F_{mr}^2}{8c_{mr}} = \frac{\gamma_r^2 m_{mr}}{16\xi_r \omega_r} \dot{y}^2 = \frac{m_{er}}{16\xi_r \omega_r} \dot{y}^2 \quad (18)$$

where m_e is called the effective mass, which represents the mass participating in the forcing function and motion, and the sum of the effective masses for all modes is the total mass M of the model (SIMULIA Corp, 2010)

$$m_{er} = \gamma_r^2 m_{mr}; \quad \sum_{r=1}^{\infty} m_{er} = M \quad (19)$$

It should be noted that the generalized modal mass m_m in this article is called effective mass by Erturk and Inman. Apparently, a VEH with larger total mass and base motion is able to generate more power. Therefore, normalizing the input and using power density to evaluate the performance are more intuitive. In this article, the mean squared acceleration weighted power density (MSAPD) has been used and defined as the average power per 1 m/s² base excitation per cubic centimetre (cm³). Therefore, the maximum MSAPD can be written as

$$MSAPD_{max} = \frac{N_r \rho}{16\xi_r \omega_r} \times 10^{-6} (\text{Ws}^4/\text{cm}^3 \text{m}^2); \quad N_r = \frac{m_{er}}{M} \quad (20)$$

where ρ is the mass density (kg/m³) and N_r denotes the mass ratio for the r th mode. The mass ratio N is the percentage ratio of the effective mass to the total mass, which depends on the modal participation factor and represents how much mass of each mode effectively participates in the overall motion and the contribution of each mode to the maximum power output. Apparently, the mass ratio of each mode is always smaller than 1 ($N \leq 1$). Table 3 gives the mass ratio of the first four modes of the transverse vibration of RC model A. Obviously, the first mode with the largest N is able to generate greater power than other (higher) modes.

Parametric studies of mass ratio, EMCC and damping

In the first case, the frequency response functions (FRFs) of MSAPD (input normalized power density) around the fundamental mode of transverse vibration determined by DPM (solid curve ‘D’) are compared

Table 3. Mass ratio N in the first four transverse vibration modes of RC model A.

Mode number	f_r (Hz)	m_m ($\times 10^{-3}$ kg)	γ	m_e ($\times 10^{-3}$ kg)	M ($\times 10^{-3}$ kg)	$N = m_e/M$ (%)
1	46.826	1.4616	1.5663	3.5855	5.8625	61.16
2	293.31	1.4622	0.8691	1.1043		18.84
3	821.66	1.4602	0.5112	0.3815		6.507
4	1611.9	1.4549	0.3670	0.1959		3.341

RC: rectangular cantilevered.

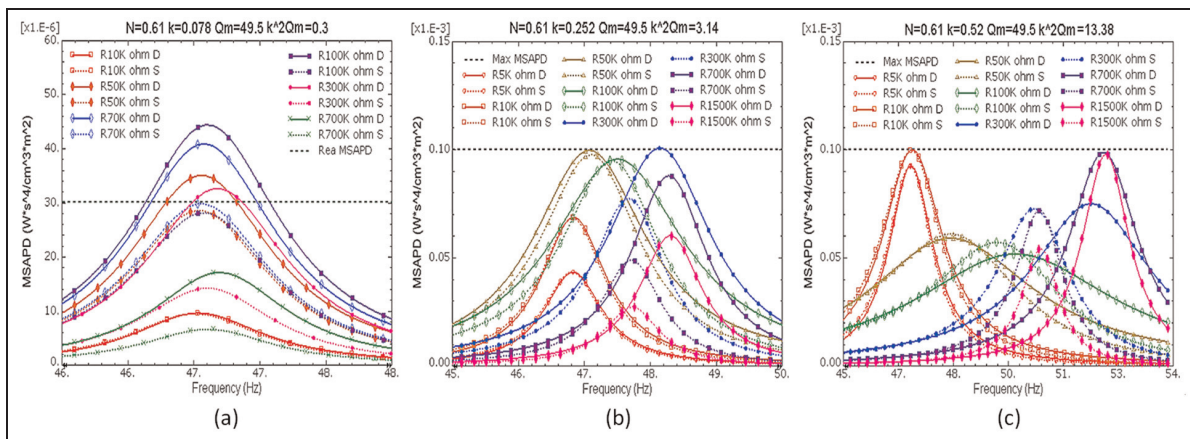


Figure 2. FRFs of the MSAPD with different resistive loads: (a) A with weak coupling; (b) model A and (c) A with strong coupling. FRF: frequency response function; MSAPD: mean squared acceleration weighted power density; DPM: distributed parameter electromechanical model; SDOF: single-degree-of-freedom. Solid curve: DPM; dotted curve: corrected SDOF model; dashed line: maximum MSAPD or reachable MSAPD.

with the results determined by the lumped SDOF model with correction factor (dotted curve ‘S’) in Figure 2. Figure 2(b) is the MSAPD FRFs of unimorph RC VEH model A ($f_1 = 46.83$ Hz, $\zeta_1 = 0.0101$, $\chi_1 = 0.013$ and $F_1 = 5.988 \times 10^{-2}$; $k_1 = 0.252$, $k^2Q_m = 3.14$, $N_1 = 61.2\%$ and $MSAPD_{MAX1} = 0.101$ mW s⁴/cm³ m²). Figure 2(c) is model A with strong coupling ($k_1 = 0.52$, $k^2Q_m = 13.37$) and Figure 2(a) is model A with weak coupling ($k_1 = 0.078$, $k^2Q_m = 0.3$). The dashed line is the maximum MSAPD determined by equation (13) ($k^2Q_m \geq \pi$) or the reachable MSAPD determined by equation (12) ($k^2Q_m < \pi$). In this case, the piezoelectric material is assumed to have stronger or weaker piezoelectric effects but the same structural properties; thus only the coupling term χ_1 is increased or decreased. The results show that when the resistance of the load is low, the two models predict very close responses. When the resistance of the load becomes high, using the lumped SDOF model without back coupling effects has failed to predict the FRFs of MSAPD in comparison with DPM. When $k^2Q_m < \pi$, equation (12) is only able to predict the peak value of the MSAPD determined by the lumped SDOF model, as shown in Figure 2(a). However, a large error can be observed in comparison with the peak value

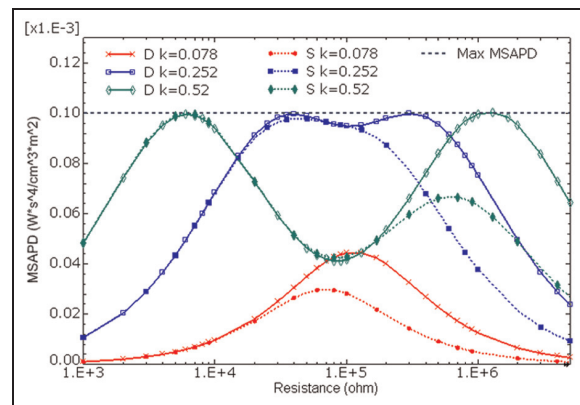


Figure 3. Optimal MSAPD versus resistance using DPM and corrected SDOF with different EMCCs. MSAPD: mean squared acceleration weighted power density; DPM: distributed parameter electromechanical model; SDOF: single-degree-of-freedom.

determined by DPM. When $k^2Q_m \geq \pi$, the maximum power is purely mechanical and equation (13) is able to predict the maximum power correctly. In Figure 3, for different values of k , the optimal values of MSAPD with a range of resistance predicted by the two models

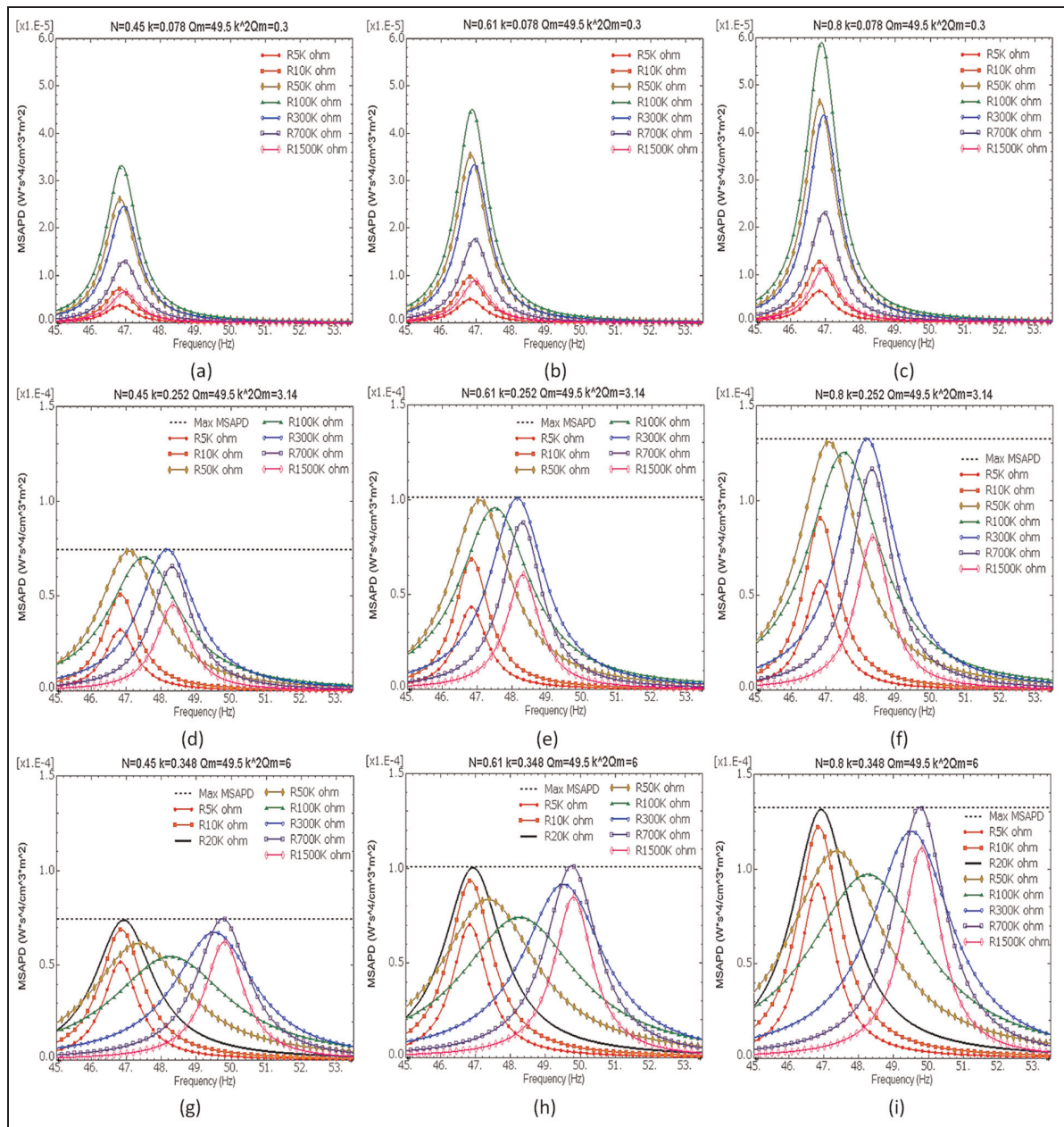


Figure 4. Effects of different mass ratios N to the modal mechanical behaviour and MSAPD FRFs with different coupling conditions: (a, d and g) $N = 45\%$; (b, e and h) $N = 61.2\%$ and (c, f and i) $N = 80\%$. MSAPD: mean squared acceleration weighted power density; FRF: frequency response function.

are given. The results are just as similar as the FRFs of MSAPD. With smaller resistance, the two models generate nearly the same value of MSAPD. Once the resistance becomes larger, the error between two models is also increased. To conclude, DPM is required to generate reliable MSAPD FRFs with different resistive loads, and the reachable MSAPD given by equation (12) will generate errors since it does not consider the back coupling effects.

In the second case, a parametric study is developed in Figure 4 to present the effects of different mass

ratios N on the modal mechanical behaviour and MSAPD FRFs with different coupling conditions. In this case, the forcing function is adjusted based on the parameter of model A (in Figure 4(e)) to ensure the changed mass ratio has been correctly represented in DPM. The results show that, first, increasing the mass ratio can always increase the power density linearly with different coupling conditions and different resistive loads. Second, changing the mass ratio will not affect the system impedance and matched resistive load. Besides, the maximum MSAPD can be determined

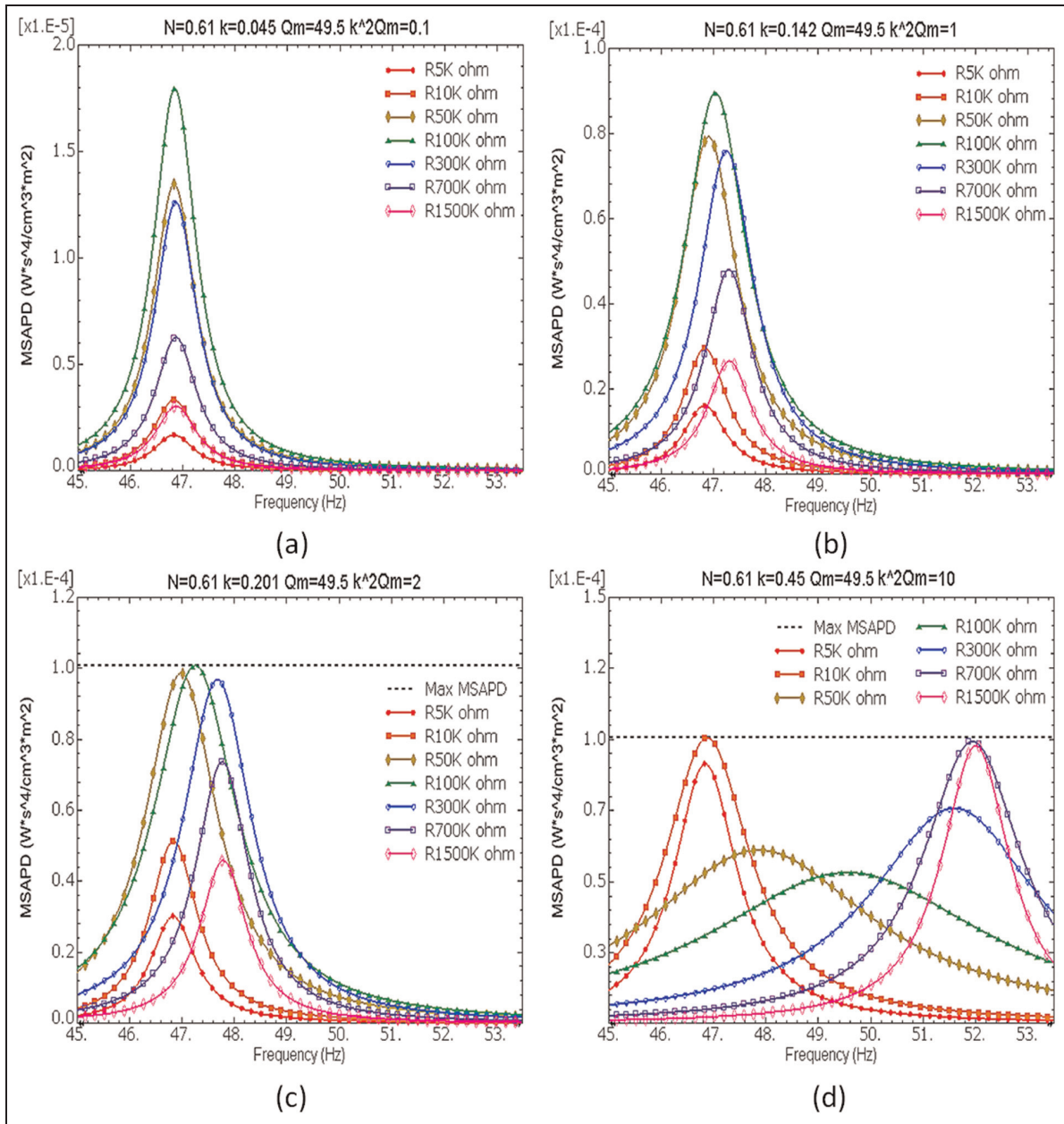


Figure 5. Effects of different EMCCs to electromechanical coupling and MSAPD FRFs: (a) $k = 0.045$, $k^2Q_m = 0.1$; (b) $k = 0.142$, $k^2Q_m = 1$; (c) $k = 0.201$, $k^2Q_m = 2$ and (d) $k = 0.45$, $k^2Q_m = 10$. EMCC: electromechanical coupling coefficient; MSAPD: mean squared acceleration weighted power density; FRF: frequency response function.

directly using mass ratio by equation (20). It means using mass ratio can directly represent the influence of modal mechanical behaviour to the maximum power density. It is evident that a weak coupling system in Figure 4(c) ($k^2Q_m = 0.3$, $N = 80\%$) can generate a much closer MSAPD in comparison with a strong coupling system in Figure 4(g) ($k^2Q_m = 6$, $N = 45\%$). However, the latter one has a wider frequency band due to the stronger electromechanical coupling.

In the third case, the effects of different EMCCs to system electromechanical coupling and MSAPD FRFs

are shown in Figure 5. Including the result given in Figures 2(c) and 4(b), (e) and (h), when $Q_m = 49.5$ and $N = 61.2\%$, the values of k^2Q_m are increased from 0.1, 0.3, 1, 2, 3.14, 6, 10 to 13.38. The results show that, first, the EMCC will not affect the maximum MSAPD when the k^2Q_m is adequately large. In fact, when $k^2Q_m = 2$ (see Figure 5(c)), the maximum MSAPD is already reached by connecting a 100 kΩ resistor, and when k^2Q_m is decreased to 1 (see Figure 5(b)), the reachable peak of MSAPD is only slightly decreased. Second, when k^2Q_m becomes much smaller than 1, the power

density is significantly decreased. Moreover, the impedance of system and the optimal resistance have been changed with different values of k^2Q_m . When k^2Q_m is smaller than 2, the system with an external load around 100 kΩ resistance can attain the highest power density, and it has a resonance frequency, which is always close to the short-circuit resonance frequency. When k^2Q_m is increased, the maximum power density is manifested by two separate peaks, which occur at two separate frequencies. The lower frequency is obtained when an external load around 10 kΩ resistance is connected. The higher frequency is achieved by connecting an external load of higher 700 kΩ resistance. The higher frequency is close to the open-circuit resonance frequency. A larger k^2Q_m can generate a larger frequency shift, which is due to the increase of EMCC. When EMCC becomes too large, the system with an external load of 100 kΩ resistance has a much broader peak that

lies between the two extreme peaks, but its MSAPD is also significantly decreased. However, with the same k^2Q_m , the value of EMCC and damping ratio could be different.

Figures 4 and 5 show the range of the MSAPD FRFs for different resistances, mass ratios and EMCC. Figure 6 shows the maximum MSAPD as function of k^2Q_m for different mass ratios. The points located on the curves in Figure 6 are the maximum MSAPD of the curves in Figures 4 and 5 (except for Figure 5(d)). The results show that mass ratio linearly affects the maximum power density for different values of k^2Q_m . EMCC only affects the maximum MSAPD when the value of k^2Q_m is smaller than 2. When $k^2Q_m > 2$, the maximum MSAPD becomes purely mechanical, and it is simply determined by the mass ratio. When $1 < k^2Q_m < 2$, the decrease of the k^2Q_m slightly reduces the maximum MSAPD. When $k^2Q_m < 1$, the maximum MSAPD can be significantly decreased.

The fourth case is to determine the influence of damping ratio on the electromechanical coupling and MSAPD directly. Figure 7 shows the predicted MSAPD for this case. The cases presented in Figures 5(b) and 7(a) have the same values of $k^2Q_m = 1$ but the value of Q_m for Figure 5(b) ($Q_m = 49.5$) is thrice that of Figure 7(a) ($Q_m = 15.8$). The corresponding values of MSAPD for the same resistance of 100 kW, for example, are about $9e-5$ and $2.9e-5$ for Figures 5(b) and 7(a), respectively. That is, the MSAPD value for Figure 5(b) is thrice that of Figure 7(a). Similarly, Figures 5(c) and 7(b) have the same value of $k^2Q_m = 2$, and for $R = 100$ kW, they have Q_m and MSAPD values of 49.5 and $10e-5$, respectively, for Figure 5(c) and 31.6 and $6.5e-5$, respectively, for Figure 7(b), which gives the same ratio of about 1.5. Also, Figures 4(h) and 7(c) have the same value of $k^2Q_m = 6$, and for $R = 20$ kW, they have Q_m and MSAPD values of 49.5

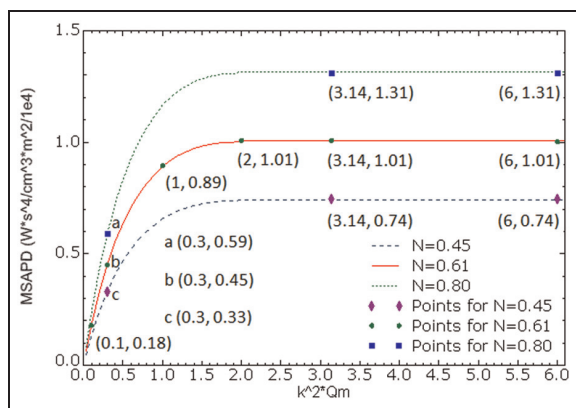


Figure 6. Maximum MSAPD as function of k^2Q_m with different mass ratios N . MSAPD: mean squared acceleration weighted power density.

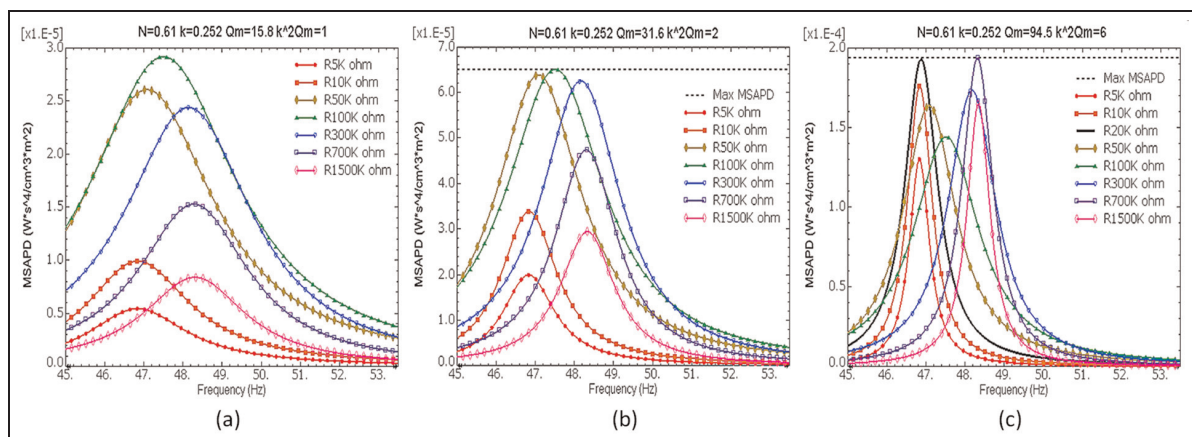


Figure 7. Effects of different damping ratios to the electromechanical coupling and MSAPD FRFs: (a) $Q_m = 15.8$, $\zeta = 0.0316$; (b) $Q_m = 31.6$, $\zeta = 0.0158$ and (c) $Q_m = 94.5$, $\zeta = 0.0053$. MSAPD: mean squared acceleration weighted power density; FRF: frequency response function.

and $1e-4$, respectively, for Figure 4(h) and 94.5 and $1.93e-4$, respectively, for Figure 7(c), which gives the same ratio of about 0.52 . In fact, when the MSAPD is not optimized with smaller or larger resistance, the values of Q_m and MSAPD still give the same ratio compared between each pair of figures. Thus, it can be inferred, first, that for the same value of k^2Q_m , the damping ratio affects the power density linearly. Second, with a specified resonance frequency, only the combined effects of EMCC and damping affect the optimal load. Moreover, since the EMCC is constant in Figure 7, the frequency shifts from the lower frequency to the higher frequency with different k^2Q_m are quite similar. Obviously, a model with a lighter damping is able to generate sharper peaks and higher MSAPD than the one with a heavier damping. But this is at the expense of a reduced frequency bandwidth.

Optimization strategy

From the expressions and case studies given in sections 'Performance determination' and 'Parametric studies of mass ratio, EMCC and damping', with a normalized acceleration input, there are four factors directly affecting the performance of VEHs: mass ratio, EMCC, damping ratio and resonance frequency. The system modal electromechanical coupling depends on the interaction between the EMCC and damping ratio. The effect of modal mechanical behaviour on power density is represented by mass ratio, which indicates how much mass effectively participates in the motion of the particular mode and affects the power density linearly. In fact, when the damping ratio and resonance frequencies are fixed, the mass ratio and EMCC are the two modal factors for the optimization of a VEH. Therefore, the optimization strategy in this article is implemented by two approaches: investigate and optimize the EMCC and mass ratio separately with geometric parameter study. On the one hand, if the EMCC is adequately large and system coupling is certainly strong, the reachable power can be optimized and it will be purely mechanical. On the other hand, for a certain k^2Q_m , the model with a larger mass ratio N can always generate higher power density.

Damping not only significantly affects the maximum power output but also affects the electromechanical coupling. A system with a large EMCC but high damping will let the system coupling become weak. However, damping is already simplified on simulation stage and should not be used to optimize the performance since the mechanism of damping in real applications is not quite clear and hard to control precisely. Besides, the effects from electrical losses, like dielectric losses and losses on electrical components, should also be considered in real applications. Therefore, the investigations of matching resistance to specified models could be meaningless at the design stage, since the

electromechanical coupling of the system combines the effects of damping and EMCC simultaneously. Furthermore, a VEH with a very small damping could be useless, because while it generates high peak power at resonance, it has a narrow band of power output. Thus, the power drops off significantly when the system is running off the resonance frequency.

Therefore, to optimize the power output without clarifying the system modal coupling situation and mechanical behaviour first could make the whole analysis to become inadequate or even useless. However, existing studies of cantilevered VEHs widely ignore this. The improvement or variation to the power output in one study compared with other studies can be easily confused since the influences to the performance of VEHs from these two factors are mixed. Especially, if the investigation of power output did not remove the effect of the resonance frequency or even incorrectly normalized the input, the results will be misleading. For example, instead of dividing the power by the square base acceleration, Zhu et al. (2010) incorrectly normalized the power by dividing it by the base acceleration. Finally, it should be noted that equations (12) and (13) are only valid for the resonance situation with the assumption that optimal loads are always matched. For real applications, the VEHs could easily operate off the resonance and finding a matching load is necessary. Besides, equation (12) did not consider the back coupling effects. Therefore, DPM should always be used to derive the power output FRFs of VEHs, as it will yield correct predictions at resonance as well as off-resonance conditions.

Modal electromechanical coupling optimization

RC beams

Figure 8 shows the variations of the EMCC in the first three modes as a function of the length/width ratio of

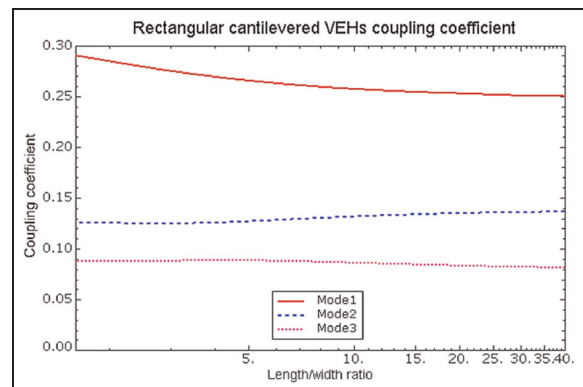


Figure 8. EMCC in the first three modes. VEH: vibration energy harvester; EMCC: electromechanical coupling coefficient.

Table 4. EMCC of the TC VEHs modified from *model A* in the first two modes.

Trapezoidal models		DTC		RC		CTC	
Width (mm)	Clamped end W_1	4	7	10	13	16	19
	Free tip W_2	16	13	10	7	4	1
Width ratio		4	1.86	1	0.54	0.25	0.05
Mode 1 k		0.192	0.225	0.252	0.269	0.285	0.296
Mode 2 k		0.178	0.153	0.132	0.112	0.096	0.087

EMCC: electromechanical coupling coefficient; TC: tapered cantilevered; VEH: vibration energy harvester; DTC: divergent tapered cantilevered; RC: rectangular cantilevered; CTC: convergent tapered cantilevered.

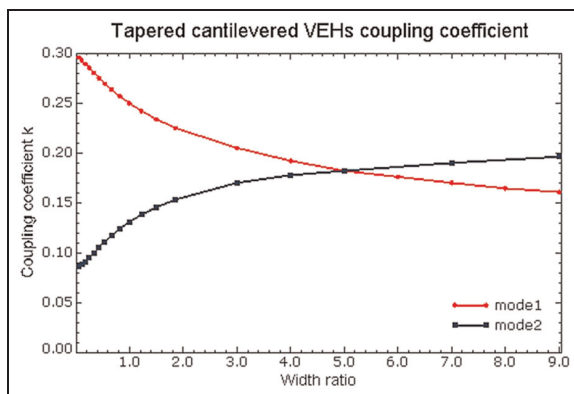


Figure 9. EMCC of the TC VEHs with different width ratios. EMCC: electromechanical coupling coefficient; TC: tapered cantilevered; VEH: vibration energy harvester.

RC unimorph beams. In this case, the thicknesses of substrate and piezoelectric layers are 0.5 and 0.25 mm, respectively. The widths and lengths are altered simultaneously to keep the volume the same as *model A*. The first natural frequencies of VEHs are from 11.65 to 299.5 Hz and they are from 72.99 to 1857.8 Hz for the second mode. It has been found that the first mode has the highest EMCC, and the magnitude of EMCC is much lower in the second and third modes. In fact, the vibration mode shapes of higher modes change the strain distributions along the length of the beam and cause the electric displacement D along the thickness to be partly reversed, and then the total charge is decreased due to self-cancellation. Besides, the shorter

beam with smaller length/width ratio has the stronger coupling. The EMCC can be increased by more than 10% when the length/width ratio is less than 2. When the length/width ratio is too small, the model is more like a plate instead of a cantilevered beam. The results show that when lead zirconate titanate (PZT)-5A ($k_{31} = 0.344$) is used with a typical damping ratio (0.01–0.03) in the first mode, the system can have medium to strong coupling.

Tapered cantilevered beams

In addition to the RC beams, Roundy et al. (2005) indicated that a tapered cantilevered (TC) beam with a larger clamped end and smaller free tip produces a higher strain distribution in the first mode, which is able to increase the power output significantly. Table 4 describes the EMCC of some typical TC models modified from *model A* in the first and second modes, and Figure 9 shows EMCC of TC models as a function of different width ratios (W_2/W_1). The ratio of the free tip to the clamped end is from 0.05 to 9. This results in CTC beams with wider clamped end but narrow free end, and DTC beams with narrower clamped end but wide free tip models, as shown in Figure 10. It is evident that the DTC model has the lower natural frequency and vice versa. For the smallest width ratio of 0.05 in CTC (similar to triangular beam), it has been found that the EMCC is enhanced in the first mode from 0.252 to 0.296 but it is also weakened by almost the same amount in the second mode. On the contrary, the EMCC of DTC with width ratio of 4 in the first mode

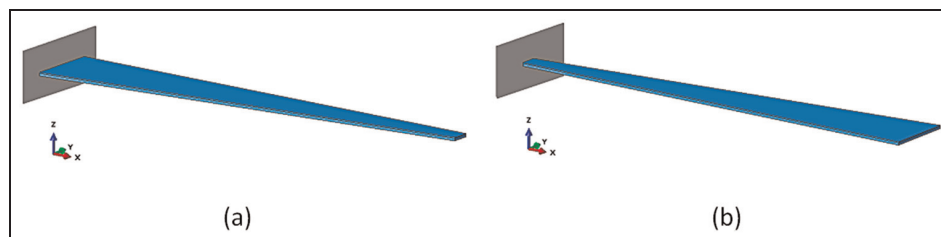


Figure 10. Views of the tapered beams modified from *model A*: (a) convergent (CTC) and (b) divergent (DTC). CTC: convergent tapered cantilevered; DTC: divergent tapered cantilevered.

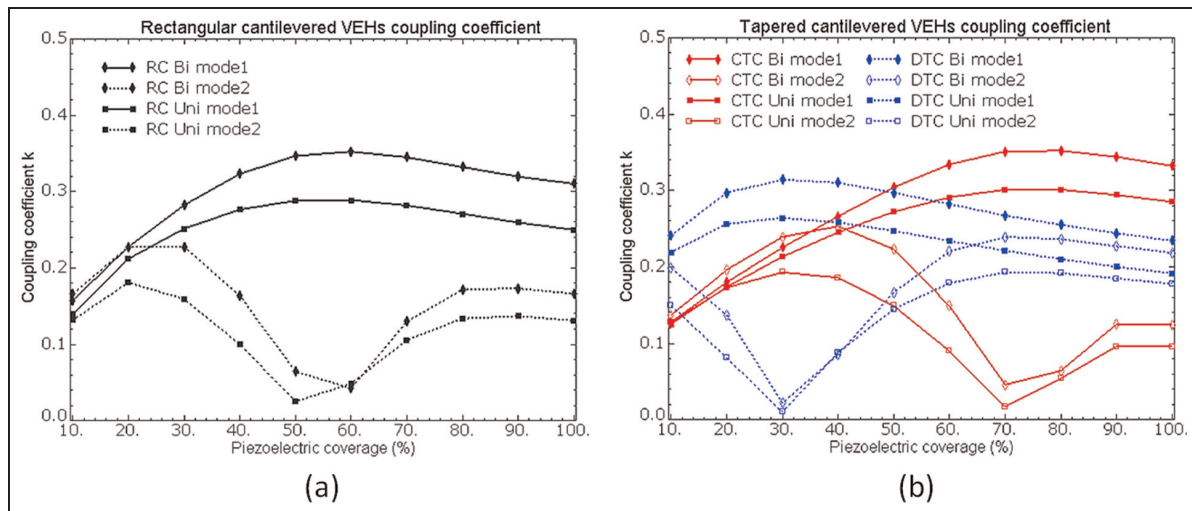


Figure 11. EMCC of cantilevered VEHs in modes 1 and 2 with bimorph and unimorph structures and three width ratio of 0.25 (CTC), 1 (RC) and 4 (DTC) from 10% to 100% piezoelectric coverage: (a) RC, (b) DTC and CTC.

EMCC: electromechanical coupling coefficient; RC: rectangular cantilevered; CTC: convergent tapered cantilevered; DTC: divergent tapered cantilevered; VEH: vibration energy harvester.

is decreased from 0.252 to 0.192 but it is increased from 0.132 to 0.178 in the second mode.

Unimorph and bimorph with varying piezoelectric coverage

Due to the high cost of piezoelectric materials, usually the substrate layer of a VEH is not fully covered by the piezoelectric materials, especially for the larger VEHs with lower resonance frequencies designed for environmental vibrations. Besides, there is another widely used method to enhance the coupling by attaching two piezoelectric layers on both the top and bottom of the substrate layer, which is called the bimorph structure. Three models have been investigated, namely, RC (*model A*), DTC (width ratio of 4) and CTC (width ratio of 0.25) with both unimorph and bimorph structures and different coverages in order to study the effects of coverage on the EMCC. The results are shown in Figure 11. The coverage is defined as the percentage of the surface area of the piezoelectric layer to the surface area of the substrate from the clamped end to the free tip. The results of RC model in Figure 11(a) show that the bimorph structures can generate reasonable enhancement of EMCC in most conditions, which is a maximum of 20% of the EMCC of the unimorph models. With the 50%–70% coverage, both unimorph and bimorph models have the highest EMCC in the first mode, whereas they have the lowest EMCC in the second mode due to the adverse strain distributions which cause the strongest cancellations. The higher EMCC in the second mode occurs within the 20%–30% coverage, while an acceptable k is still produced in the first mode. For instance, the k in the first and

second modes for the bimorph model with 30% coverage are 0.294 and 0.234, respectively. Apparently, using small coverage is able to avoid self-cancellation in the second mode, and it also saves the piezoelectric materials. The model with 100% coverage has the weaker coupling compared with the 60% coverage in the first mode. This is because when the coverage is increased and the area close to the free tip is covered, the significant drop of strain distribution near the free tip causes the increase of the total charge to be relatively less than the increase of the capacitance C_p .

In fact, the CTC structure enhanced the EMCC in the first mode due to the covered area close to the clamped end being larger than the free tip. Similarly, if the piezoelectric coverage of the DTC model is reduced from the free tip, k is increased much more than the increase obtained in the k for a RC model of the same coverage. The results in Table 5 show that the DTC VEH with 30% and 50% piezoelectric coverage and width ratio of 4 is able to produce a much larger k than 100% coverage, and it is even larger than the RC with 100% coverage. However, the CTC with 30% and 50% piezoelectric coverage and width ratio of 0.25 generates a lower k than 100% coverage. Figure 11(b) shows the variations of k of the DTC and CTC VEHs in the first two modes. By comparing with Figure 11(a), it is evident that the highest k of the DTC VEH is the lowest value of k of the three VEHs. However, the DTC VEH requires much smaller coverage to generate its optimized coupling coefficient, which is around 30% for the width ratio of 4 and which will require less piezoelectric materials than RC and CTC models. Generally, the fully covered model does not have the best performance and the piezoelectric

Table 5. EMCC in the first mode for unimorph RC and TC VEHs with 50% and 30% coverages.

Beam type	Width ratio	EMCC with different coverages		
		100%	50%	30%
DTC	4	0.196	0.247	0.264
RC (A)	1	0.252	0.288	0.251
CTC	0.25	0.285	0.272	0.213

EMCC: electromechanical coupling coefficient; RC: rectangular cantilevered; TC: tapered cantilevered; VEH: vibration energy harvester; DTC: divergent tapered cantilevered; CTC: convergent tapered cantilevered.

Table 6. Effects of covered locations of piezoelectric layers on EMCC of RC VEHs with 20% and 50% coverages.

Coverage (%)	Mode	EMCC					
		Distance from clamped base (mm)					
		0	10	20	30	40	50
20	1	0.211	0.160	0.124	0.093	0.066	0.043
	2	0.181	0.021	0.075	0.135	0.161	0.150
50	1	0.288	0.198	0.138	0.094	0.062	0.039
	2	0.025	0.164	0.240	0.249	0.206	0.150

EMCC: electromechanical coupling coefficient; RC: rectangular cantilevered; VEH: vibration energy harvester.

materials should cover the area with large strain and the coverage should be limited. This helps to optimize the system coupling.

Similar work can be found in Patel et al. (2011), which showed the influence of coverage on the back coupling term in unimorph RC VEHs. First, the back coupling term given in their electrical governing equation is not the same as the forward coupling term given in their motion governing equation. In fact, it is allowed to use one equivalent modal coupling term to represent these two different terms (Erturk and Inman, 2011). Second, the EMCC is actually the product of the two coupling terms. In Patel et al.'s article, the back coupling term was only increased rapidly and maximized with a very small coverage and decreased continuously to the full coverage. However, the power output was optimized at 50%–60% coverage (system coupling was designed to be weak to medium in their designs). Therefore, they incorrectly concluded that the variation of coverage to EMCC is not corresponding to the maximum power.

In fact, the covered location of the piezoelectric layer can be different with the same coverage. Table 6 shows the effects of different covered locations on the EMCC of RC VEHs with 20% and 50% coverage. The piezoelectric material location is moved from the clamped base to the free tip. When the piezoelectric material location from the base is more than 20 mm, the EMCC can be optimized in mode 2 because the self-cancellation effect, due to the location of the strain node to the base, is eliminated. However, the EMCC of mode 1 is significantly decreased when the piezoelectric material is not fixed to the base.

Some existing works have focused on enhancing the EMCC using segmentation, which is achieved by separating the piezoelectric layer into two or multiple parts from different strain nodes due to the mode shapes. The segments can be in series or parallel connection with the load to avoid self-cancellation in higher modes. However, the self-cancellation still reappears in mode 1 unless multiple sets of rectifiers are used, which will generate much higher electrical losses in real applications. Furthermore, the findings in section 'Modal mechanical behaviour optimization' indicate that the fundamental mode generates the largest mass ratio, which produces the highest power density. Then, for the optimal designs of cantilevered VEHs, using segmentation to enhance the EMCC in higher modes is not effective.

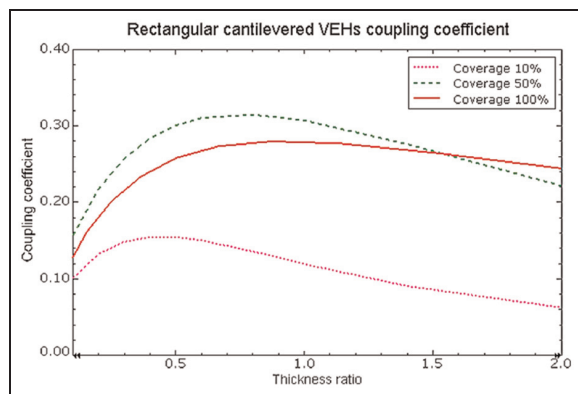
Effect of thickness ratio

In the previous cases, the thicknesses of the piezoelectric and substrate layers are 0.25 and 0.5 mm, respectively. In this section, the thickness of model A is changed in order to determine the effects of thickness ratio on EMCC. Table 7 shows that when the total thickness is changed from 0.3 to 1.5 mm and the thickness ratio of piezoelectric to substrate layer is 0.5, the EMCC is basically constant. Figure 12 shows the variations of the EMCC in the first mode with different coverage and thickness ratios. It shows that the EMCC will be generally strong when the thickness ratio is from 0.4 to 0.9. The model with a smaller coverage is more suitable for the smaller thickness ratio. For example, the EMCC will be maximized when the thickness ratio is 0.4 with

Table 7. EMCC of unimorph RC VEHs with different total thicknesses and thickness ratios of 0.5.

Total thickness (mm)	Thickness ratio	Mode 1 k	Mode 2 k
0.3	0.5	0.253	0.130
0.9	0.5	0.250	0.132
1.5	0.5	0.247	0.134

EMCC: electromechanical coupling coefficient; RC: rectangular cantilevered; VEH: vibration energy harvester.

**Figure 12.** EMCC with different coverage and thickness ratios in the first mode.

EMCC: electromechanical coupling coefficient; VEH: vibration energy harvester.

Table 8. Mass ratio N of the typical rectangular cantilevered VEHs of constant volume in the first three modes.

$L \times W$ (mm)	f_1 (Hz)	N_1 (%)	f_2 (Hz)	N_2 (%)
$L200 \times W5$	11.65	61.28	72.99	18.82
$L100 \times W10$ (A)	46.83	61.16	293.3	18.84
$L66.7 \times W15$	106.3	61.06	664.0	18.92
$L40 \times W25$	299.5	61.09	1858	18.93

VEH: vibration energy harvester.

10% coverage, and it increases to 0.9 with 100% coverage. Moreover, the decreases of the EMCC by changing the thickness ratio with 100% coverage are less than the smaller coverage models, especially when the thickness ratio becomes large. Therefore, for a partly covered VEH, no matter what kinds of materials are used, the thickness of piezoelectric and substrate layers should be carefully chosen to optimize the EMCC.

Modal mechanical behaviour optimization

RC beams

Table 8 presents the mass ratio N of the first two modes of some typical RC models modified from model A by

Table 9. Mass ratio N of the RC VEHs with different volumes and constant natural frequency in the first mode.

f_1 (Hz)	Thickness (mm)	Length (mm)	Width (mm)	N_1 (%)
46.8	0.3	63.4	8	61.1
46.8	1	115.5	10	61.2
46.8	1.5	141.3	15	61.2
46.7	3	200	25	61.3

RC: rectangular cantilevered; VEH: vibration energy harvester.

Table 10. Typical mass ratio N of the TC VEHs modified from A in the first two modes.

Beam type	W_2/W_1	f_1 (Hz)	N_1 (%)	f_2 (Hz)	N_2 (%)
DTC	4	30.66	74.68	256.5	15.22
RC (A)	1	46.83	61.16	293.3	19.85
CTC	0.25	68.64	49.78	334.8	21.04
CTC	0.053	86.93	46.24	381.4	21.12

TC: tapered cantilevered; VEH: vibration energy harvester; DTC: divergent tapered cantilevered; RC: rectangular cantilevered; CTC: convergent tapered cantilevered.

changing the length and width. It shows that the mass ratios of RC beams are constant in each mode and it is frequency independent. For a specified frequency, a RC VEH that operates in the first mode can generate more than 3 times and nearly 10 times maximum MSAPD than the one that operates in the second and third modes, respectively. Another RC case has been developed to find out whether using frequency control technique but totally different dimensions affects the mass ratio. The results in Table 9 show that the mass ratios of the first mode are still nearly identical.

Therefore, since the vibration mode shapes and mass distributions to the modal participation factors of different RC beams in each mode are nearly identical, it results in constant mass ratios of the RC beams. As section 'Performance determination and optimization strategy' shows that the mass ratio determines the maximum power density, analyses of RC VEHs without tip masses in existing works by changing the geometric parameters are not able to determine the influence of the mechanical behaviour, and the optimized power is only affected by variation of EMCC and electromechanical coupling.

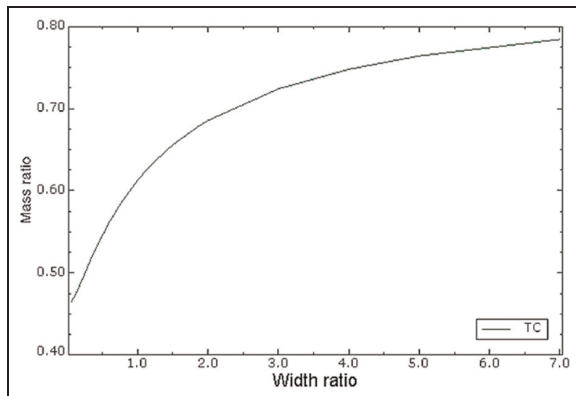
TC beams

Some typical mass ratios N of the TC VEHs modified from RC model A in the first three modes are given in Table 10. The results show that the mass ratio of CTC with width ratio of 0.05 (similar to a triangular beam) in the first mode is reduced from 61.2% to 46.2%. For

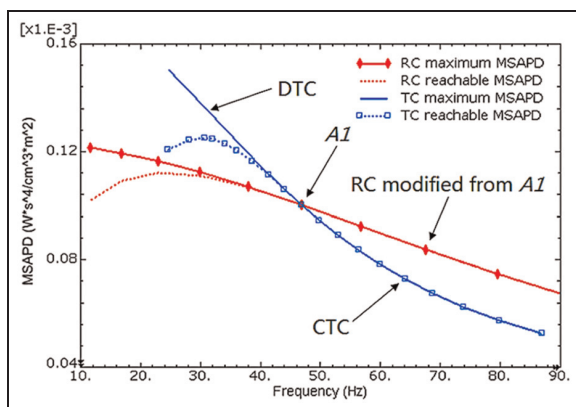
Table 11. Mass ratio N of the TC VEHs with different volumes and same width ratio in the first mode.

f (Hz)	T (mm)	L (mm)	W_1 (mm)	W_2 (mm)	W_2/W_1	N_1 (%)
19.60	0.75	125	3.2	12.8	4.00	74.70
44.23	0.75	83.3	4.8	19.2	4.00	74.64
30.47	3	200	10	40	4.00	74.78

TC: tapered cantilevered; VEH: vibration energy harvester.

**Figure 13.** Relationship between the width ratio and mass ratio of TC models in the first mode.

TC: tapered cantilevered.

**Figure 14.** Comparison of the maximum and reachable MSAPD of the unimorph RC and TC VEHs modified from A with 100% coverage and thickness ratio of 0.5 (the MSAPD only represents the highest power density of the models at their short-circuit resonance frequency).

MSAPD: mean squared acceleration weighted power density; VEH: vibration energy harvester; DTC: divergent tapered cantilevered; CTC: convergent tapered cantilevered; RC: rectangular cantilevered; TC: tapered cantilevered.

the DTC with width ratio of 4, the mass ratio is increased from 61.2% to 74.7%. Table 11 shows the mass ratios of different DTC models with the same width ratio of 4. It is evident that the mass ratios are nearly the same when the width ratio of TC is fixed.

Figure 13 shows the general relationship between the width ratio and mass ratio of TC models for the first mode. Figure 14 shows that although the DTC has more possibility to generate the larger maximum MSAPD due to the higher mass ratio, its lower EMCC (see Figure 9) may eventually reduce the magnitude of the reachable peak of MSAPD when the system coupling becomes weak. In Figure 14, the reachable MSAPD is derived by DPM and the maximum MSAPD is obtained by assuming the MSAPD is always maximized. Besides, when the frequency is lower, the larger damping ratio also affects the system electromechanical coupling and causes the decreases of reachable MSAPD in both RC and TC VEHs. However, a DTC with small piezoelectric coverage can effectively increase the EMCC and generate higher power density. For a system that does not have a weak coupling, the CTC will generate lower power density than RC and DTC since the lower mass ratio and the increased EMCC of CTC will only affect the maximum power slightly.

RC beam with tip masses

Normally, an additional mass will be attached to the VEH to tune the resonance frequency. The extra mass not only increases the volume, but also modifies the mode shape, mass distribution and strain distribution, which eventually affects the VEH performance. Three RC models have been chosen to attach different cubic masses (the same materials as the substrate) to their free tips. The three RC models are based on *model A*; they are named by their length (L) and width (W) as follows: $L100 \times W10$ (*A*), $L66.7 \times W15$ and $L40 \times W25$. The dimensions of the cubic tip masses are from 0.5 to 2.5 cm, and the volumes of tip masses are from 0.125 to 15.625 cm³. Then, the tip mass weight is from 0.98 to 122.7 g and the ratio of the tip mass/beam mass is from 0.17 to 20.9. Moreover, point masses located right on the free tip have been defined in the models using the same magnitudes from 0.98 to 122.7 g for comparisons. Figure 15 shows the $L66.7 \times W15$ beam with 26.5 g tip mass (the dimension is 1.5 cm), while Figure 16 shows the tuned frequencies and modal participation factors of the three beams with different ratios of tip mass/beam mass. Figure 17 shows the variations of the mass ratio with ratio of tip mass/beam mass and frequencies. The results in these figures demonstrate that the tip

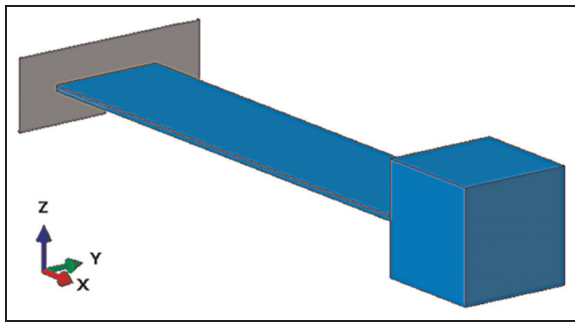


Figure 15. View of the $L66.7 \times W15$ beam with 26.5 g tip mass.

masses effectively enhance the mass ratio in the first mode compared with the RC model without a tip mass.

Figure 16(a) shows that when the ratio of tip mass/beam mass is same, using cubic tip masses generated lower frequencies than using point masses. Generally, when the tip mass/beam mass ratio increases from 0 to 3, Figure 17(a) shows that the mass ratio increases rapidly, while Figure 16(b) shows that the modal participation factor decreases rapidly. When the ratio of tip mass/beam mass is larger than 5, the mass ratios are slightly increased and the modal participation factors of beam models with cubic tip masses are also slightly increased. However, the modal participation factors of beam models with point masses decrease to 1 asymptotically. Similar results of using point mass can be found in Erturk and Inman (2008b). This is because of the differences in the offset distances between the tip of the beams and the centre of mass of the tip masses and the increase in mass moments of inertia of the tip masses. These factors generate adverse effects compared with the responses of the beam models with point masses

located right at the centre of the free tip. If the point mass becomes infinitely large, the model is similar to a mass–spring model and $\gamma \cong 1$. It should be noted that the shorter beam has the smaller mass ratio N compared with the longer beams when the massive tip mass is the same. For example, the N values of the three models with a 13.6 g tip mass (1.2 cm) are 81.5% ($L40 \times W25$), 83.5% ($L66.7 \times W15$) and 84.4% ($L100 \times W10$), for tip mass/beam mass ratio of 2.31. Meanwhile, the same magnitude of the point mass with different RC VEHs generates the same mass ratio. To conclude, the mass ratio of a VEH with a tip mass/beam mass ratio of around 2–5 is increased by 30%–40% in comparison with a RC VEH without tip mass.

Attached masses with varying locations

In real applications, the masses are not always attached right at the tip. It is well known that a mass located at the free tip generates the lowest frequency, and then by relocating the mass position from the tip to the clamped end, the tuned frequency is increased due to the decrease of the effective length of the beam. There is a need to find out the differences in the mass ratio when using lighter tip masses and a heavier mass with altered locations. The $L66.7 \times W15$ RC model with tip masses up to 62.8 g (dimension of 2 cm) can tune the natural frequency from its original value of 106.3–12.68 Hz in the first mode. The mass positions are defined as the percentage of the length from the clamped end to the attached mass (effective length) over the total length of the beam. Thus, the mass position of the tip mass is 100%. In this case, three cubic tip masses of the magnitudes of 7.85, 26.5 and 62.8 g are considered. Each

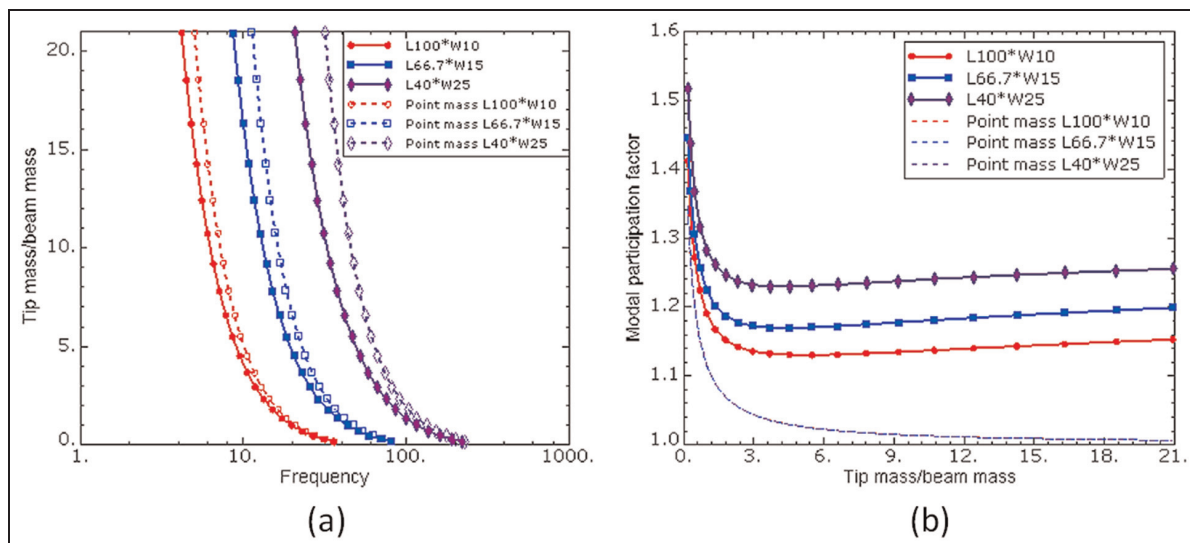


Figure 16. (a) Tuned frequencies and (b) modal participation factors with ratio of tip mass/beam mass in the first mode.

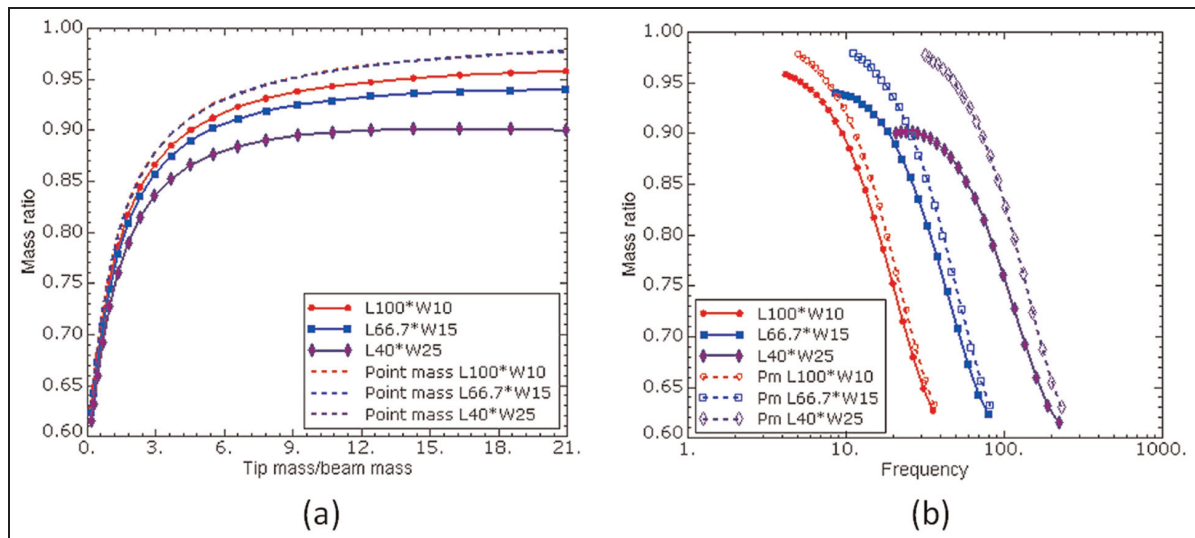


Figure 17. Mass ratio with different tip masses in the first mode: (a) ratio of tip mass/beam mass and (b) mass ratio of FRFs.

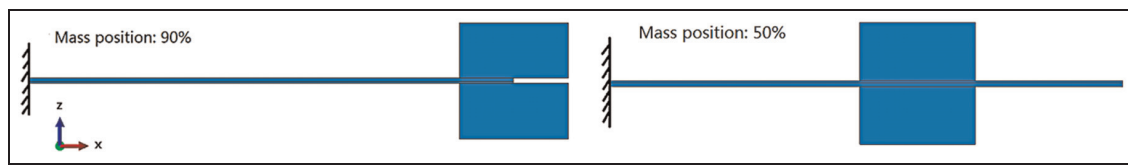


Figure 18. Views of $L66.7 \times W15$ with 26.5 g mass and 90% and 50% mass positions.

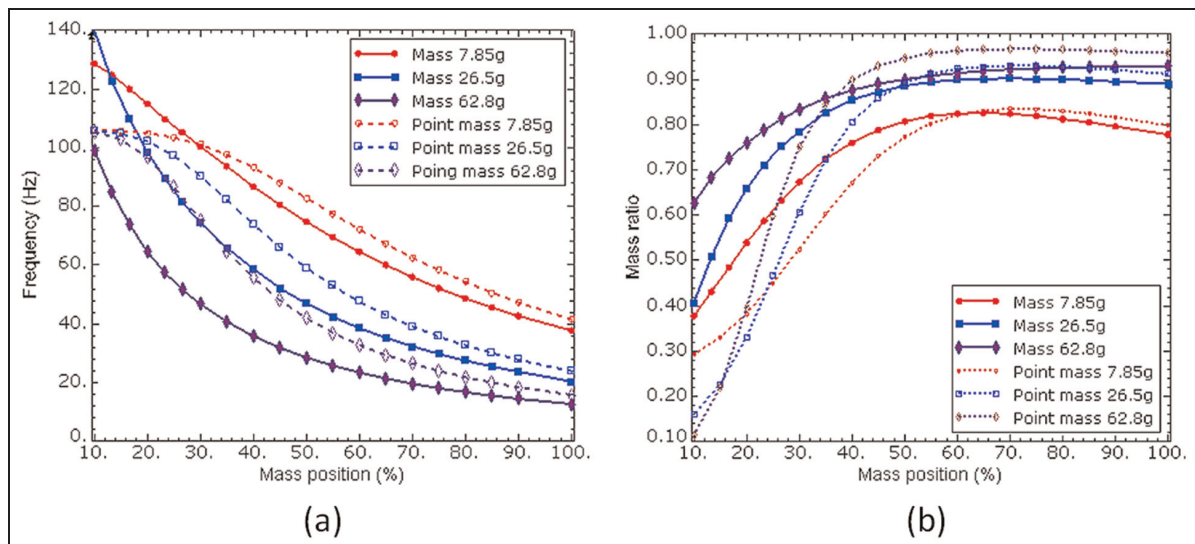


Figure 19. Modal properties of $L66.7 \times W15$ with three different masses and altered mass positions: (a) resonant frequencies and (b) mass ratio.

mass has been split into two equal parts, and they are symmetrically attached on the $L66.7 \times W15$ RC VEH. Figure 18 illustrates VEHs with two equal masses of total magnitude of 26.5 g attached and located at 90%

and 50% mass positions. Moreover, the point masses that have the same magnitudes as the bulky masses and different locations are also used in this case. Figure 19 shows the variations of the mass ratios and resonance

Table 12. Effects of tip masses to the EMCC of RC VEHs in the first mode.

Mass dimension (tip mass/beam mass)	Model A	$L66.7 \times W15$	$L40 \times W25$	Model A 50% coverage	Model A 20% coverage
Without mass (0)	0.252	0.261	0.281	0.288	0.212
1 cm (1.34)	0.278	0.288	0.313	0.272	0.184
1.6 cm (5.48)	0.284	0.295	0.326	0.268	0.181
2 cm (10.7)	0.288	0.300	0.332	0.267	0.179

EMCC: electromechanical coupling coefficient; RC: rectangular cantilevered; VEH: vibration energy harvester.

frequencies with mass position for the $L66.7 \times W15$ beam. Three point masses and three bulky masses are used at the tip of the beam, and their positions are changed from 10% to 100%. When the mass positions are varied from 50% to 100%, this figure shows that the masses can generate acceptable mass ratios. When the mass position is close to the clamped area, the mass ratio is reduced rapidly. Besides, the resonance frequencies of the beam models with bulky masses can become even larger than the original natural frequency of the beam without mass. This is similar to the CTC models with wider clamped ends. Moreover, using lighter masses like 7.85 and 26.5 g at 60%–70% mass positions can even generate more mass ratio in the first mode than simply attaching them to the free tip. This result can be observed with both bulk and point masses. It is evident that for specified frequencies, using heavier masses with different mass positions generates more power density than using smaller tip masses. In real applications, a VEH with a pre-designed tip mass can operate off the desired resonance frequency. This will lead to a significant decrease in the power output due to the offset of the resonance frequency. Therefore, slight adjustments of the mass position to tune the frequency are convenient and necessary.

Effect of extra mass on EMCC

In fact, adding extra masses not only changes the mass ratio but also changes the EMCC. Erturk et al. (2009) stated that the tip masses will change the strain distributions of RC VEHs. The boundary condition is changed from clamped-free to clamped-clamped once the tip mass becomes infinitely large. In addition, the changed strain distribution for beams with tip mass also affects the EMCC. Table 12 briefly shows the effects of tip masses on the EMCC of RC VEHs with full coverage and partial coverage in the first mode. For the full coverage models, the increase in EMCC of the wider model $L40 \times W25$ is greater than for the narrower models. Besides, adding a small tip mass can effectively increase the EMCC, and then using even larger tip masses only generates a small increase of EMCC. For the model A with partial coverages, the EMCC is decreased. Moreover, the decreases of EMCC for beams with 20% coverage are more than the decreases of EMCC for beams with 50% coverage.

Table 13. Effects of moving 7.85 g mass to different positions on the EMCC of model A in the first mode.

Piezoelectric coverage (%)	Without mass	Mass position		
		100% (tip)	70%	50%
100	0.252	0.278	0.242	0.227
50	0.288	0.272	0.291	0.296
20	0.212	0.184	0.214	0.236

EMCC: electromechanical coupling coefficient.

Table 13 shows the effects of moving 7.85 g mass to different positions on the EMCC of model A with different coverages. This table shows that moving the mass from the tip to the centre of the beam, in the full coverage model, causes the EMCC to decrease. When the model has partial coverage, moving the mass will actually decrease the effective length of the beam, and the effective coverage and EMCC are increased. In particular, the EMCC of the model with small coverage can be significantly increased.

Conclusion

This article has presented a systematic parametric analysis of the modal electromechanical coupling and mechanical behaviour of the cantilevered VEHs. The system modal electromechanical coupling combines the effects from EMCC and damping ratio simultaneously. The influences of modal mechanical behaviour to the volumetric power can be represented by the mass ratio, which represents how much mass effectively participates in the motion and affects the forcing function directly. Also, a design strategy is presented to optimize the EMCC and mass ratio separately.

Because of the self-cancellations in the higher modes, the EMCC of the RC models in the first mode is nearly 2 and 3 times larger than in the second and third modes, respectively. A wider and shorter RC VEH can generate 10% more EMCC than the longer and narrower RC VEHs. Also, the partly covered substrate and bimorph structure are able to enhance the EMCC from 10% to 20% and reduce the quantity of piezoelectric materials required as well. Especially, the DTC VEHs are able to generate acceptable EMCC with much smaller coverage

than RC and CTC VEHs. However, the thickness ratio of piezoelectric and substrate layer should be analysed carefully to optimize the EMCC when using different materials. Moreover, using tip masses can increase the EMCC of the VEHs with full coverage by more than 10%. For the VEHs with limited coverage, moving masses from the tip to the centre of the beam is able to decrease the effective length of the beam and increase the EMCC by more than 25%.

For a certain modal coupling condition, optimizing the mass ratio and using large density materials are able to enhance the power density effectively. For the RC models without tip mass, the mass ratio in each mode is constant, and in the first mode, it is nearly 3 times and 10 times larger than in the second and third modes, respectively. This implies that the VEH operating in the first mode has the highest performance. Moreover, the VEHs with extra masses can increase mass ratio and power density by more than 40%. Using DTC structure can increase the mass ratio of 20%. However, using CTC structure will decrease the mass ratio by more than 20%.

Declaration of conflicting interests

The authors declared no potential conflicts of interest with respect to the research, authorship, and/or publication of this article.

Funding

This research received no specific grant from any funding agency in the public, commercial or not-for-profit sectors.

References

- Anton SR and Sodano HA (2007) A review of power harvesting using piezoelectric materials (2003–2006). *Smart Materials and Structures* 16: R1–R21.
- Bourisli RI and Al-Ajmi MA (2010) Optimization of smart beams for maximum modal electromechanical coupling using genetic algorithms. *Journal of Intelligent Material Systems and Structures* 21: 907–914.
- Cook-Chennault KA, Thambi N and Sastry AM (2008) Powering MEMS portable devices – a review of non-regenerative and regenerative power supply systems with special emphasis on piezoelectric energy harvesting systems. *Smart Materials and Structures* 17: 043001.
- Erturk A and Inman DJ (2007) On mechanical modeling of cantilevered piezoelectric vibration energy harvesters. In: *Proceedings of IDETC/CIE*, Las Vegas, NV, 4–7 September.
- Erturk A and Inman DJ (2008a) A distributed parameter electromechanical model for cantilevered piezoelectric energy harvesters. *Journal of Vibration and Acoustics* 130: 041002.
- Erturk A and Inman DJ (2008b) On mechanical modeling of cantilevered piezoelectric vibration energy harvesters. *Journal of Intelligent Material Systems and Structures* 19: 1311–1325.
- Erturk A and Inman DJ (2011) *Piezoelectric Energy Harvesting*. John Wiley & Sons, Chichester, UK.
- Erturk A, Tarazaga PA, Farmer JR, et al. (2009) Effect of strain nodes and electrode configuration on piezoelectric energy harvesting from cantilevered beams. *Journal of Vibration and Acoustics* 131: 011010-1–011010-11.
- Friswell MI and Adhikari S (2010) Sensor shape design for piezoelectric cantilever beams to harvest vibration energy. *Journal of Applied Physics* 108: 014901-1–014901-6.
- Guyomar D, Sebald G, Pruvost S, et al. (2009) Energy harvesting from ambient vibrations and heat. *Journal of Intelligent Material Systems and Structures* 20: 609–624.
- Patel R, McWilliam S and Popov AA (2011) A geometric parameter study of piezoelectric coverage on a rectangular cantilever energy harvester. *Smart Materials and Structures* 20: 085004.
- Richter B, Twiefe J, Sattel T, et al. (2007) Design method for piezoelectric bending generators in energy harvesting systems. In: *Active and passive smart structures and integrated systems*, 19–22 March 2007, San Diego, CA, Proc. of SPIE, Vol. 6525: 652504-1–652504-11.
- Roundy S, Leland ES, Baker J, et al. (2005) Improving power output for vibration-based energy scavengers. *IEEE Pervasive Computing* 4: 28–36.
- Roundy S, Wright PK and Rabaey J (2008) A study of low level vibrations as a power source for wireless sensor nodes. *Computer Communications* 26: 1131–1144.
- SIMULIA Corp (2010) *Abaqus Theory Manual in ABAQUS 6.10 Documentations*. Available at: <http://www.3ds.com/products-services/simulia/>
- Song HJ, Choi YT, Wang G, et al. (2009) Energy harvesting utilizing single crystal PMN-PT material and application to a self-powered accelerometer. *Journal of Mechanical Design* 131: 091008-1–091008-8.
- Trindade MA and Benjeddou A (2009) Effective electromechanical coupling coefficients of piezoelectric adaptive structures: critical evaluation and optimization. *Mechanics of Advanced Materials and Structures* 16: 210–223.
- Wu H, Tang LH, Yang YW, et al. (2012) A novel two-degrees-of-freedom piezoelectric energy harvester. *Journal of Intelligent Material Systems and Structures* 24: 357–368.
- Yang YW and Tang LH (2009) Equivalent circuit modeling of piezoelectric energy harvesters. *Journal of Intelligent Material Systems and Structures* 20: 2223–2235.
- Zhang L (2010) *Analytical modeling and design optimization of piezoelectric bimorph energy harvester*. Dissertation, The University of Alabama, USA.
- Zhu MZ, Worthington E and Tiwari A (2010) Design study of piezoelectric energy-harvesting devices for generation of higher electrical power using a coupled piezoelectric-circuit finite element method. *IEEE Transactions on Ultrasonics, Ferroelectrics, and Frequency Control* 57(2): 427–437.

CHAPTER 6 OPTIMAL DESIGN OF TWO-LAYER STACKED VIBRATION ENERGY HARVESTERS USING A MODAL APPROACH

Xingyu Xiong and S Olutunde Oyadiji

Smart Materials and Structures 23 (3), 035005, 2014

Optimal design of two-layer vibration energy harvesters using a modal approach

Xingyu Xiong and S Olutunde Oyadiji

Dynamics and Aeroelasticity Expert Group, School of Mechanical, Aerospace and Civil Engineering,
The University of Manchester, M13 9PL, UK

E-mail: s.o.oyadiji@manchester.ac.uk

Received 5 July 2013, revised 27 November 2013

Accepted for publication 20 December 2013

Published 3 February 2014

Abstract

Piezoelectric vibration energy harvesters (VEHs) with two-layer structures are developed. The attached masses are used to tune the frequencies and as spacers between the two layers. By changing the dimensions of the layers and masses and relocating the positions of the masses, the VEHs can generate close resonance frequencies and considerable power output. The modal approach is introduced to determine the modal performance using the mass ratio and the modal electromechanical coupling coefficient, where the mass ratio represents the influence of the modal mechanical behaviour on the power density directly, and the modal parameters required are derived using the finite element method. The findings indicate that a mode with too large mass ratio will cause the remaining modes to have small mass ratios and poor performance. Then, a screening process for the identification of the configurations of VEHs with optimal or near-optimal performance is developed using the modal approach. This procedure facilitates the selection of VEH configurations with close resonances and favourable values of mass ratio initially before carrying out full analysis. Furthermore, the approach can be used to develop VEHs of different sizes ranging from a few millimeters to hundreds of millimeters with the power ranging from microwatts to milliwatts.

Keywords: energy harvesting, piezoelectric, multiple resonances, modal performance, optimization

(Some figures may appear in colour only in the online journal)

1. Introduction

In the field of preventive maintenance, there is currently the need for self-powered, batteryless wireless sensors and sensor nodes. This has led to the development of small-scale ambient energy harvesting into a new research field. A lot of work has been concentrated on developing vibration energy harvesters (VEHs) using piezoelectric materials in the last decade [1]. Resonance has been considered as an effective method of energy conversion from the mechanical domain to the electrical domain. However, conventional VEHs are mainly designed to operate around the fundamental mode. The higher modes, with much higher resonance frequencies, are far away from the first mode and they generate much lower levels of power output in comparison with the first

mode. However, the applicable vibration sources from the environment are normally random and variant within a lower frequency range. Therefore, conventional designs using one mode have limited performance and can be ineffective. To overcome this limitation, many researchers have focused on different aspects with the overall goal being to optimize the broadband power output capability [2], using, for example, a resonance tuning technique [3, 4], a nonlinear system with magnets [5–7], and multi-resonance designs.

For multi-resonance systems, designs with arrays of beams have been widely reported in the literature. Ferrari *et al* [8] carried out an experiment with an array of three cantilevered VEHs. The resonance frequencies could be tuned conveniently by altering the lengths of the beams and by attaching different tip masses. Qi *et al* [9] developed a

multi-resonance VEH with an array of cantilevered beams connected to a clamped–clamped beam. In their designs, the piezoelectric material only covered the common base and the resonances were generated by the common base and sub-branches. Apparently, the structure with an array of beams can generate very close resonance frequencies. However, for each resonance, normally just one part of the VEH is active and the remaining parts of the VEH are almost silent (inactive). Thus, the piezoelectric material is not effectively used, which leads to weak electromechanical coupling, and the power density is also decreased significantly.

Another popular design of multi-resonance system can be realized by attaching two or more masses to one cantilevered beam VEH. Lee *et al* [10], Ou *et al* [11] and Zhou *et al* [12] developed dual mass VEHs. In their designs, the cantilevered beam is segmented into two parts by attaching one mass to the middle of the beam, and the other mass to the free tip. Then, the model can generate two resonances. However, only when the mass attached to the middle of the beam is much heavier than the mass attached to the free tip can the two resonances be close enough. Wu *et al* [13] have modified the two mass VEH by splitting the cantilevered beam into separate parallel narrow cantilevered beams with a gap between them. An additional beam is located in the gap with one end clamped to the free ends of the original beams and the other end orientated towards the clamped ends of the original beams. The two resonances can be much closer with lighter masses. Chen *et al* [14] improved the design using up to nine masses to segment the cantilevered beam into ten cells, which generate a wider frequency range of broadband power output. However, a thin but very long beam and heavier masses are required to decrease the central resonance frequency and expand the frequency band, which limits the applicability of the design. In addition, the optimal power output of the VEH with nine masses is only slightly increased in comparison with the same cantilevered VEH but without the additional masses. Thus, the addition of nine masses sacrifices the power density significantly. Some other multi-resonance system designs can also be found in the literature. Erturk *et al* [15] developed an L-shaped VEH, in which the second resonance frequency can be two times higher than the first resonance frequency. Karami and Inman [16] developed a zigzag VEH with up to 11 sub-branches. However, the resonances are still far away from each other, which limits the ability of the VEH to produce broadband power output. Generally, the design objective of a multi-resonance system is to achieve close resonance frequencies with nearly the same power output level but also large values of the power output in each mode. The number of resonances should be limited because it not only improves the ability of the VEH to produce broadband power output, but it also significantly affects the power density.

The main contributions of this paper include the following. Firstly, a novel optimization strategy using a modal approach is introduced. The design strategy initially evaluates the modal structural aspects using the mass ratio. Then, a modal filter is developed to select the configurations with better mechanical performance in multiple modes. Use of the design strategy obviates the need to run the full analysis at the first stage and it

is more effective and convenient for general multi-resonance structural designs of vibration energy harvesters (VEHs) in comparison with conventional methods. Secondly, the modal approach is also introduced to determine how the maximum power density of VEHs has been affected by the modal response. The power output is normally affected by the electrical and mechanical behaviours of VEHs simultaneously. However, there has been no attempt made to analyse the individual effects of the mechanical behaviour on the output power for multi-resonance designs. In some optimization investigations reported in the literature, the predicted power outputs were affected by the simultaneous changes of electromechanical coupling and mechanical behaviour. When comparing the results from one work to other works, the results can be easily confused and may not be acceptable when the configurations are different.

The third contribution of the paper is the development and optimization of a novel two-layer VEH based on the modal approach and design strategy. The design combines the concepts and benefits of array of beams and two mass models simultaneously. The first two modes are generated from the interaction between the base layer and the upper layer. Extra masses are attached to tune the resonance frequencies and one of the masses also serves as a spacer to bond the two layers together and ensure enough space for vibration. The two-layer VEH can easily generate close resonance frequencies and considerable power output in the two modes. There is no need to attach heavy masses or to carefully choose the length of the beam in comparison with previous double mass designs. In particular, the positions of masses are moveable in order to achieve broadband power output for different requirements, without the need to change any component dimensions. The optimal and near-optimal mass positions can be considered as non-dimensional factors which can be directly used for different scales with different ranges of frequency and power output. The two-layer VEH can eliminate the anti-resonance between the first and second modes once the base layer is fully covered by the piezoelectric material. Then, the capability for broadband power output can be effectively improved.

The paper is organized as follows: a general distributed electromechanical parameter model and the determination of the parameters using finite element analysis (FEA) software (section 2); performance determination of VEHs for single layer and multiple layer structures using a modal approach and the corresponding frequency response functions of power density (section 3); analyses of the two-layer VEHs and implementation of a screening process for optimal designs (section 4); factors affecting the performance of the two-layer VEHs (section 5) and the concluding section at the end of the paper.

2. Vibration energy harvesting model

The steady-state linear vibration response of a structure subjected to continuous harmonic excitation can be represented using the modal analysis technique. The absolute displacement

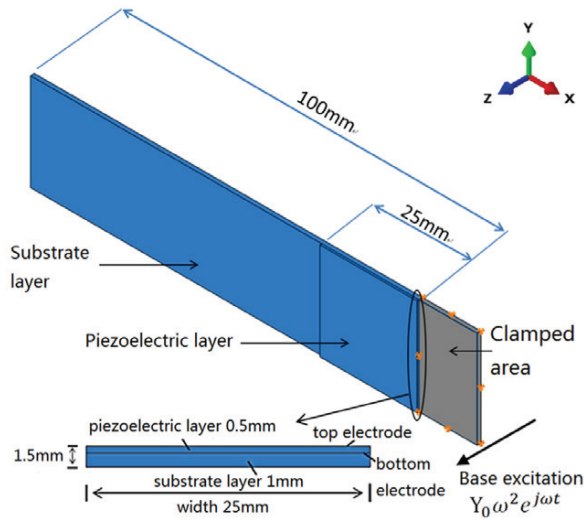


Figure 1. Cantilevered VEH model 1LM0.

of the transverse vibration relative to the moving base of the VEH model at time t can be given by

$$u_{\text{rel}}(t) = \sum_{r=1}^{\infty} \phi_r \eta_r(t) \quad (1)$$

where ϕ_r and $\eta_r(t)$ are the mass-normalized eigenfunction and the corresponding modal coordinates of the r th mode of the VEH, respectively. The equations governing the vibration modal response and electrical behaviour of the VEH model with a resistive load are given as [17, 18]

$$\frac{d^2 \eta_r(t)}{dt^2} + 2\zeta_r \omega_r \frac{d\eta_r(t)}{dt} + \omega_r^2 \eta_r(t) + \chi_r v(t) = F_r(t) \quad (2)$$

$$\frac{v(t)}{R_1} + C_p \frac{dv(t)}{dt} - \sum_{r=1}^{\infty} \chi_r \frac{d\eta_r(t)}{dt} = 0 \quad (3)$$

where v is the generated voltage given by the uniform electric field E over the thickness of the piezoelectric layer h_p ; ζ_r , ω_r , χ_r and F_r are the damping ratio, angular resonance frequency, modal electromechanical coupling term and modal mechanical forcing term, respectively; C_p is the piezoelectric capacitance and R_1 is the resistive load. The steady-state solution of equation (2) is

$$\eta_r(t) = \frac{F_r - \chi_r v}{\omega_r^2 - \omega^2 + j2\zeta_r \omega_r \omega} e^{j\omega t} \quad (4)$$

When the VEH model is not a uniform beam, the derivations of the eigenfunction ϕ_r , coupling term χ_r , and F_r become complicated. Using FEA software packages like ABAQUS and ANSYS, it is possible to derive these parameters conveniently. A typical cantilevered VEH model A is developed in ABAQUS and shown in figure 1. The dimensions and typical material properties are given in table 1. The substrate layer is clamped at one end and the piezoelectric layer is fixed on the clamped end. The base displacement excitation is applied along the

Table 1. Properties of the VEH model A.

Parameter	Property
Beam length/width	100 mm/25 mm
Thickness of piezoelectric layer	0.5 mm
Length of piezoelectric layer	25 mm
Thickness of substrate layer	1 mm
Piezoelectric material	PZT-5A ^a
Density of piezoelectric layer	7750 kg m ⁻³
Clamped dielectric constant ϵ_{33}^S	7.3488×10^{-9} F m ⁻¹
Piezoelectric layer Young's modulus	60.9×10^9 N m ⁻²
Piezoelectric constant e_{31}	-5.4 C m ⁻²
Transverse coupling factor k_{31}	0.344
Density of substrate layer	7850 kg m ⁻³
Substrate layer Young's modulus	200×10^9 N m ⁻²
Structural damping	0.04

^a Morgan Technical Ceramics standard.

z -axis and the voltage is applied on the top and bottom of the piezoelectric layer. Using the idea of the equivalent circuit method [19], by letting the applied voltage go to zero for the short-circuit condition ($v = 0$), applying harmonic base excitation $\ddot{u}_b = Y_0 \omega^2 e^{j\omega t}$ at each resonance frequency and deriving the absolute displacement relative to the moving base from the FEA results, the forcing function F_r can be determined from equation (4) in the frequency domain. For the r th mode

$$F_r = (\omega_r^2 - \omega^2 + j2\zeta_r \omega_r \omega) \eta_r(j\omega_r) = 2\zeta_r \ddot{u}_{\text{rel}} \sqrt{m_{\text{mr}}} |_{\omega=\omega_r} \quad (5)$$

where m_m is the generalized modal mass associated with the mode and derived from the FEA natural frequency extraction analysis. By replacing $v(t)/R_1$ with $i(t)$ in equation (3), the complex current i_r for the short-circuit condition with base excitation can be derived from the electric displacement D data in the FEA results and it is

$$i_r = j\omega \chi_r \eta_r(j\omega_r) = \sum_{r=1}^{\infty} \frac{j\omega F_r \chi_r}{\omega_r^2 - \omega^2 + j2\zeta_r \omega_r \omega} \Big|_{\omega=\omega_r} \quad (6)$$

Then, the modal coupling term χ_r can be determined from equation (6) for multiple modes or any single mode. The voltage across R_1 can be represented by [17, 18]

$$v(t) = \frac{\sum_{r=1}^{\infty} \frac{j\omega F_r \chi_r}{\omega_r^2 - \omega^2 + j2\zeta_r \omega_r \omega}}{\sum_{r=1}^{\infty} \frac{j\omega \chi_r^2}{\omega_r^2 - \omega^2 + j2\zeta_r \omega_r \omega} + \frac{1}{R_1} + j\omega C_p} e^{j\omega t} \quad (7)$$

Hence, solving equation (7) in the frequency domain gives the complex power simply as $v(j\omega) \left(\frac{v(j\omega)}{R_1} \right)^*$. From the assumption that no electric losses occur when a rectifier is used, the average power output is $|v|^2 / 2R_1$. In this paper, for convenience of analysis, structural damping is used and defined as 0.04 and the corresponding damping ratio is 0.02. Indeed, the damping affects the power output significantly. Then, for real applications, it is required to obtain the damping ratio experimentally.

3. Performance determination using a modal approach

3.1. A modal approach and the concept of mass ratio

From section 2, the voltage and power output frequency response functions (FRFs) of a VEH with different resistive loads can be generated by the distributed parameter (electromechanical) model (DPM), which is based on the Bernoulli–Euler beam assumption. However, the performance, in particular the maximum power of a VEH, cannot be clearly determined using the DPM unless a specified model has been defined.

Erturk and Inman [20, 21] compared the Bernoulli–Euler beam model with the lumped single degree-of-freedom (SDOF) model, and derived a correction factor γ which enables the SDOF model to be used. They found very good agreement of the relative motion transmissibility predicted using the Bernoulli–Euler beam model and the SDOF model with the correction factor in a wide frequency band around the resonance. In fact, the correction factor γ is also called the modal participation factor, which indicates how strongly motion in the x -, y - or z -direction or rotation about one of these axes is represented in the eigenvector of that mode [22]. However, in their works, the comparison using the correction factor only involved purely structural responses without predicting the electrical output results. Guyomar *et al* [23] used an SDOF model including the electromechanical coupling to determine the normalized power in different rectifier interfaces with resistive loads. They introduced a modal electromechanical criterion $k^2 Q_m$ to evaluate the maximum average power output (for a standard rectifier interface with no electrical losses; optimal load is matched):

$$P_{\max} = \frac{F_m^2}{2c_m} \frac{\pi k^2 Q_m}{(\pi + k^2 Q_m)^2} \quad \text{when } k^2 Q_m \leq \pi \quad (8)$$

$$P_{\max} = \frac{F_m^2}{8c_m} \quad \text{when } k^2 Q_m \geq \pi \quad (9)$$

where k is the modal electromechanical coupling coefficient (EMCC); $Q_m = 1/2\zeta$ is the quality factor; F_m and c_m are the lumped mechanical force and damping coefficient, respectively. In terms of equation (9), when $k^2 Q_m > \pi$, the power output is maximum and purely mechanical. If $k^2 Q_m < \pi$, the reachable power given by equation (8) is always smaller than the maximum power. Figure 2 shows the ratio of the reachable power to the maximum power as a function of $k^2 Q_m$. However, in Guyomar's work, the modal participation factor was not considered when using the lumped SDOF model. Besides, since the back coupling from resistance is ignored in equations (8) and (9), the electromechanical coupling cannot be fully involved in their prediction in comparison with using the DPM.

In this paper, a modal approach based on the lumped SDOF model is developed to evaluate the resonance performance and maximum power output, which includes both the corrected structural response and the electromechanical coupling. A modal structural criterion named the mass ratio N is introduced; it depends on the modal participation factor

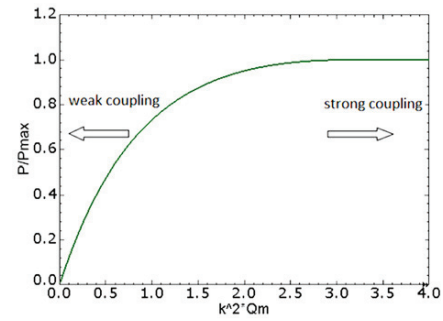


Figure 2. Ratio of the reachable power to the maximum power as a function of $k^2 Q_m$.

γ , which represents the influence of the modal mechanical behaviour on the power density directly.

For a harmonic base motion, the motion and electrical governing equations in the lumped SDOF system are

$$\begin{aligned} m_m \ddot{z} + c_m \dot{z} + k_m z - \alpha v &= F_m \\ C_p \dot{v} + \frac{v}{R_l} - \alpha \dot{z} &= 0. \end{aligned} \quad (10)$$

The corrected lumped forcing function is

$$F_{mr} = -\gamma_r m_m \ddot{y}; \quad (11)$$

the EMCC and lumped parameters are

$$\begin{aligned} k^2 &= \frac{\alpha_r^2}{k_m C_p + \alpha_r^2} = \frac{\omega_{oc}^2 - \omega_{sc}^2}{\omega_{oc}^2}; \\ c_{mr} &= 2\zeta_r \sqrt{k_{mr} m_{mr}}; \quad \omega_r = \sqrt{k_{mr} / m_{mr}} \end{aligned} \quad (12)$$

and the corrected complex voltage on the resistor is

$$v(j\omega) = \frac{\gamma_r \alpha_r R_l j \omega^2 m_{mr}}{j\omega R_l \alpha_r^2 + (j\omega c_{mr} - \omega^2 m_{mr} + k_{mr})(1 + j\omega C_p R_l)} \quad (13)$$

where z is the relative displacement related to the base motion y ; $\alpha_r = \chi_r \sqrt{m_{mr}}$ is the lumped coupling factor; m_m is the generalized modal mass; k_m is the effective stiffness and $\omega_{sc} = \omega_r$ is the undamped angular resonance frequency for short-circuit condition of the r th mode; ω_{oc} is the open-circuit angular resonance frequency. By substituting equations (11) and (12) into equation (9), the maximum power can be rewritten as

$$P_{\max} = \frac{F_{mr}^2}{8c_{mr}} = \frac{\gamma_r^2 m_{mr}}{16\xi_r \omega_r} \ddot{y}^2 = \frac{m_{er}}{16\xi_r \omega_r} \ddot{y}^2. \quad (14)$$

m_e is called the effective mass which represents the mass participating in the forcing function and motion and the sum of the effective masses for all modes is the total mass M of the whole model [22]:

$$m_{er} = \gamma_r^2 m_{mr}; \quad \sum_{r=1}^{\infty} m_{er} = M. \quad (15)$$

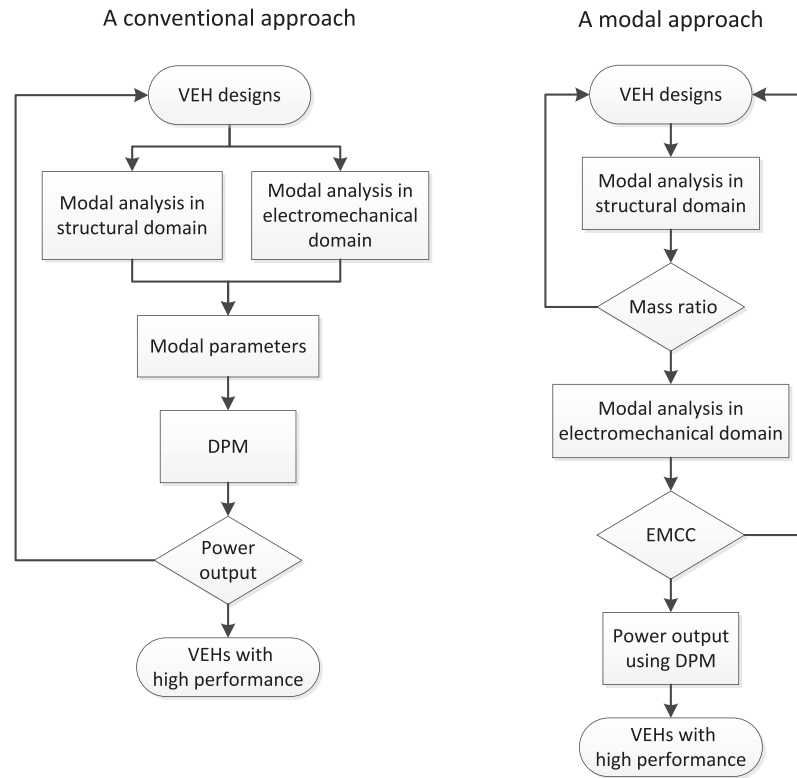


Figure 3. Flow charts comparing conventional and modal approaches to determine the performance of VEHs.

Then, a modal structural criterion which is termed the mass ratio is introduced as

$$N_r = \frac{\gamma_r^2 m_{mr}}{M} = \frac{m_{er}}{M}. \quad (16)$$

N_r denotes the mass ratio for the r th mode. The mass ratio N is the percentage ratio of the effective mass to the total mass, which depends on the modal participation factor and represents how much mass of each mode effectively participates in the overall motion and the contribution of each mode to the maximum power output. Apparently, the mass ratio of each mode is always smaller than 1 ($N \leq 1$). This is because any structure with multiple degrees of freedom cannot behave like a simple mass–spring–damper model ($m_m = M$ and $\gamma = 1$). In fact, the mass ratio N represents the effect of the modal mechanical behaviour on the forcing function and it linearly affects the power density. It should be noted that the generalized modal mass m_m in this paper is called the effective mass by Erturk and Inman [20, 21]. Apparently, a VEH with larger total mass and base motion is able to generate more power. Therefore, normalizing the input and using the power density to evaluate the performance is more intuitive. In this paper, the mean squared acceleration weighted power density (MSAPD), which is defined as the average power per 1 m s^{-2} base excitation per cubic centimetre (cm^3), has been used. Therefore, the maximum MSAPD can be written as

$$\text{MSAPD}_{\max} = \frac{N_r \rho}{16 \xi_r \omega_r} \times 10^{-6} \text{ (W s}^4 \text{ cm}^{-3} \text{ m}^{-2}) \quad (17)$$

where ρ is the mass density (kg m^{-3}). For a specified resonance frequency and damping ratio, the modal mechanical performance of the VEH model in terms of the maximum power density can be evaluated using the mass ratio directly. Then, a modal approach is developed, which uses the mass ratio and EMCC as two assessment factors to evaluate the modal mechanical and electromechanical performance. Figure 3 shows flow charts that compare the conventional approach to the modal approach of VEH performance evaluation. The modal approach avoids the need to carry out full analysis using the DPM at the first stage. Case studies using the modal approach and the DPM to determine the performance of VEHs are given in section 3.2.

3.2. Performance determination of VEHs

3.2.1. Evaluation of the resonance performance of a single layer VEH. A single layer VEH is simply a single cantilevered VEH. Table 2 shows the modal performance of the first four modes of the transverse vibration of the VEH model 1LOM (see figure 1). Obviously, the first mode with the largest $N_1 = 52.3\%$ is able to generate the largest maximum MSAPD. The first mode has the highest k , but the value of $k^2 Q_M = 1.5$ is smaller than π ($Q_M = 25$), and then its reachable MSAPD is slightly smaller than the maximum MSAPD. Due to the effects of the smaller N and the higher f , the maximum MSAPD in the higher modes is decreased significantly. Besides, since the EMCC in higher modes is also decreased, the reachable

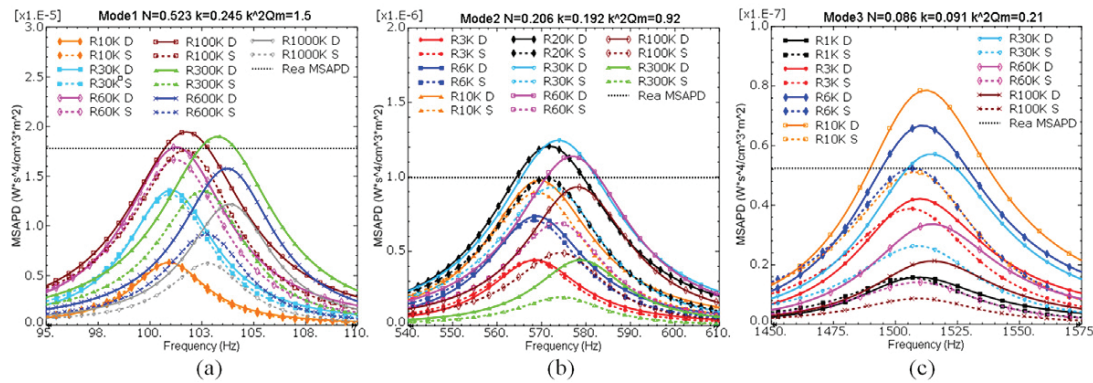


Figure 4. FRFs of the MSAPD with different resistive loads of model A; solid curve: distributed parameter model (D); dashed curve: corrected SDOF model (S); dotted line: reachable MSAPD for (a) mode 1; (b) mode 2; (c) mode 3.

Table 2. Modal performance of the first four transverse vibration modes of VEH model 1L0M.

Mode No.	f_r (Hz)	m_m ($\times 10^{-3}$ kg)	γ	m_e ($\times 10^{-3}$ kg)	M ($\times 10^{-3}$ kg)	$N = m_e/M$ (%)	k	$k^2 Q_M$	Reachable MSAPD ^a	Maximum MSAPD ^a
1	100.9	4.53	1.595	11.53	22.05	52.3	0.245	1.50	1.78×10^{-5}	2.02×10^{-5}
2	568.3	4.94	0.960	4.55		20.6	0.192	0.92	9.95×10^{-7}	1.42×10^{-6}
3	1506.9	4.85	0.626	1.90		8.6	0.091	0.21	5.21×10^{-8}	2.23×10^{-7}
4	2932.3	4.47	0.465	0.97		4.4	0.008	0.00	1.11×10^{-10}	5.84×10^{-8}

^a Units: $W s^4 cm^{-3} m^{-2}$.

MSAPD becomes even much smaller than the maximum MSAPD.

In figure 4, the frequency response functions (FRFs) of the MSAPD (input normalized power density) around the resonance frequency of each mode of transverse vibration determined by the DPM (solid curve ‘D’) are compared with the results determined by the lumped SDOF model with correction factor (dashed curve ‘S’). The FRFs of the DPM are determined using multiple modes for accuracy. The dotted line is the reachable MSAPD determined by equation (8) ($k^2 Q_M < \pi$). The results show that when the resistance of the load is low, the two models predict very close responses. When the resistance of the load becomes high, using the lumped SDOF model without back coupling effects has failed to predict accurately the FRFs of the MSAPD in comparison with the DPM. When $k^2 Q_M < \pi$, equation (8) is only able to predict the peak value of the MSAPD determined by the lumped SDOF model.

However, a large error can be observed in comparison with the peak value determined by the DPM, which is higher than the peak value generated by the lumped SDOF model. To be specific, the higher modes with smaller $k^2 Q_M$ generate greater errors. Thus, the DPM is required to generate reliable MSAPD FRFs with different resistive loads and the reachable MSAPD given by equation (8) will generate errors since it does not consider the back coupling effects. Besides, the maximum MSAPD of model 1L0M cannot be reached for each mode due to the inadequate EMCC. In fact, for the first two modes, the peaks of the MSAPD are already close to the maximum MSPAD when $k^2 Q_M \geq 0.92$ (see table 2).

In figure 5, the piezoelectric material is assumed to have stronger piezoelectric effects but the same structural properties in the first mode, thus only the coupling term χ_1 and EMCC k_1 are increased. Obviously, when $k^2 Q_M \geq \pi$ (see figures 5(b) and (c)), the maximum power is purely mechanical and using the mass ratio N and equation (16) it is possible to predict the maximum power density directly. In fact, when $k^2 Q_M = 2.16$ (see figure 5(a)), the maximum MSAPD is already reached by connecting a 100 k Ω resistor. When $k^2 Q_M$ is increased, the maximum power density is manifested by two separate peaks which occur at two separate frequencies. A larger $k^2 Q_M$ can generate a larger frequency shift, which is due to the increase of EMCC. The higher frequency is close to the open-circuit resonance frequency. Additionally, the lumped SDOF model is not able to predict the frequency shift correctly; it under predicts.

3.2.2. Evaluation of a two-layer VEH. The second mode of a single layer VEH is normally far away from the first mode, which limits the ability to produce broadband power output. Table 3 shows the values of N and k of the two-layer model 2L1MT75 (the configuration and dimensions are given in sections 4.1 and 4.2). The first two modes have close resonance frequencies and their EMCCs are nearly the same. Then, the maximum power density around the first two modes is basically determined by the values of N and resonance frequencies. The second mode has the largest value of $N_2 = 83.4\%$ and the rest of the modes have much smaller values of N since the sum of N for all modes equals 100%, and N_2 is more than 7 times larger than N_1 . Besides, the resonance frequency

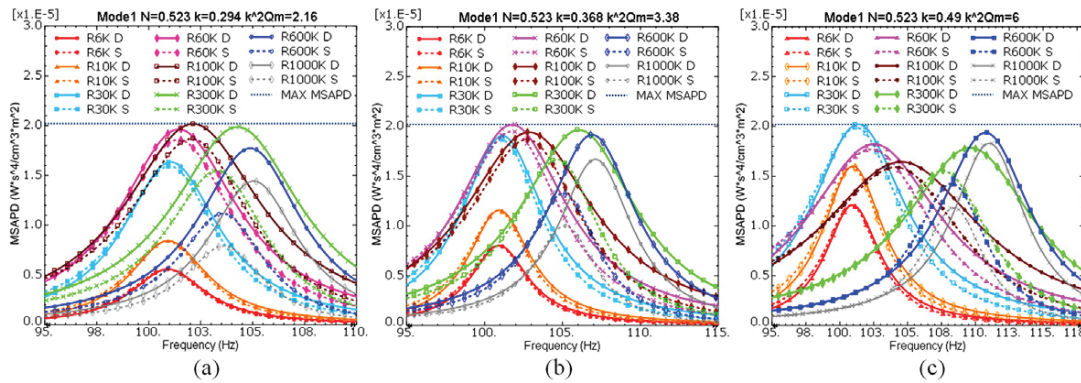


Figure 5. Increase of EMCC to the MSAPD FRFs around the first mode. (a) $k = 0.294$; (b) $k = 0.368$; (c) $k = 0.49$.

Table 3. Modal performance of the first three transverse vibration modes of model 2L1MT75.

Mode No.	f_r (Hz)	m_m ($\times 10^{-3}$ kg)	γ	m_e ($\times 10^{-3}$ kg)	M ($\times 10^{-3}$ kg)	$N = m_e/M$ (%)	k	$k^2 Q_M$
1	25.6	71.29	0.557	22.14	188.86	11.7	0.186	0.87
2	38.2	75.22	1.447	157.43		83.4	0.181	0.82
3	716.4	6.77	0.759	3.91		2.1	0.186	0.86

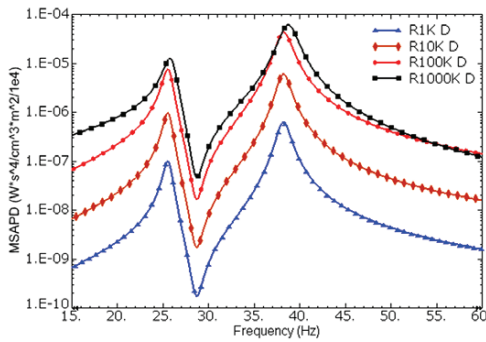


Figure 6. MSAPD FRFs of the model 3L3MP090 with different resistive loads.

of the second mode is nearly 1.5 times higher than the first mode. Therefore, in figure 6, the predicted MSAPD FRFs using the DPM with different resistive loads show that the second mode can generate nearly 5 times more power density than the first mode. Generally, if the multi-resonance VEH has close resonance frequencies, for a specified acceleration input, using the mass ratio and EMCC it is possible to predict the resonance performance conveniently.

To conclude, no matter what the configuration of the VEH, whether a single or multiple cantilevered beam structure, the modal mechanical performance can be determined directly using N , which affects the power density linearly. The values of the EMCC and $k^2 Q_M$ represent the modal electromechanical coupling condition. Then, the performance of a VEH model can be clearly determined using the modal approach and the corresponding FRFs of the MSAPD in multiple modes. In particular, the natural frequencies and mass ratio can be determined directly using the modal analysis in the FEA software. However, the determination of the coupling term

and EMCC require running full steady-state analysis in the FEA software and using the DPM in the post-processing (see equation (6)).

4. Optimization of two-layer VEHs using the modal approach

4.1. Configurations of two-layer VEHs

Figure 7 illustrates two typical examples. Figure 7(a) is the model 2L2MP09, which has two layers (2L) and two extra masses (2M). Figure 7(b) is the model 2L1MP0, which has two layers and one mass (1M). The masses are designed to be movable to different positions, and they also serve as spacers to separate the two layers of beams. The positions of the masses from the free tip to the clamped end are identified as Pmn where m and n denote the positions of masses M_{+1} and M_{+2} and are identified by numbers from 0 to 9. For example, the configuration in figure 7(a) is P09 and the configuration in figure 8 is P39. The base layer is actually the model 1L0M as given in figure 1, which has a 25 mm \times 25 mm \times 0.5 mm piezoelectric layer attached near the root. The dimensions of the second layer (L_{+1}) are 100 mm \times 25 mm \times 1 mm, and the dimensions of each mass are 10 mm \times 25 mm \times 10 mm.

4.2. Optimization of a two-layer VEH with one mass

In this section, the VEH models with two layers and one mass are discussed. The first case is model 2L1MP0 with different thicknesses for L_{+1} , which are changed from 0.3 to 7.5 mm. Table 4 gives the resonance frequencies, mass ratios and EMCCs. Figure 9(a) shows the MSAPD FRFs of models with thicknesses from 0.3 to 1 mm, and figure 9(b) shows the MSAPD FRFs of models with thicknesses from 1 to 7.5 mm. It should be noted that all the MSAPD FRFs given in section 4

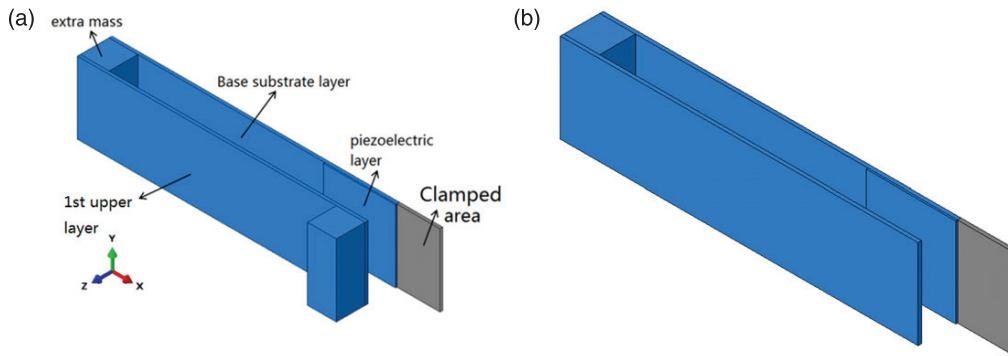


Figure 7. Two-layer VEHs: (a) two layers with two masses (2L2MP09); (b) two layers with one mass (2L1MP0).

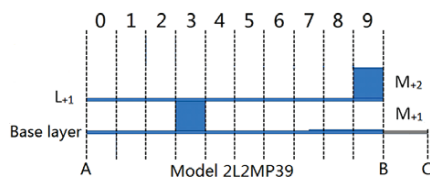


Figure 8. Numbering of mass positions: model 2L2MP39 has two layers and two masses, and the locations of the masses are 3 and 9, respectively; A = tip of base layer; BC = clamped length of base layer.

are already optimized by connecting the optimal resistive load. The results in table 4 show that when the thickness of L_{+1} is 0.4 or 0.5 mm, the two modes are close. When the thickness of L_{+1} is decreased from 0.4 to 0.3 mm, the second mode still has the same resonance frequency but the EMCC of the model becomes much smaller. This is because L_{+1} becomes too light and the L_{+1} layer just locally vibrates, which hardly affects the base layer. Thus, the strain on the piezoelectric layer becomes very small. Since the values of N and k for mode 1 of the 0.4 and 0.3 mm models are both too small, the first mode is not manifested in the MSAPD FRFs shown in figure 9(a).

When L_{+1} becomes thicker, the two modes became well separated and there is a significant interval between their resonance frequencies. Also, the magnitude of the MSAPD trough at the anti-resonance frequency between the two modes becomes deeper. The peak value of the MSAPD for each mode depends on the values of N and k . There is a regular pattern that when N and k are increased in one mode, then they are decreased in the other mode. In figure 9(b), when L_{+1} becomes thicker than 2.5 mm, the two modes become closer again. However, when it is too thick, the mass ratio in the two modes cannot be evenly distributed, and then the second mode generates much higher power density than the first mode.

Therefore, the design objective of the multi-layer VEH in this paper is to determine a good configuration of the VEH model that will provide close enough multiple modes and evenly distributed mass ratio and EMCC. Any mode that has too large N and k will cause the rest of the modes to have poor performance. If the interval between two modes becomes too large, the anti-resonance can also affect the broadband power output.

The second case is the model 2L1MP0 with different thicknesses of M_{+1} , which are changed from 3 to 20 mm. Obviously, in table 5 and figure 10, the model with a thicker mass generates a lower resonance frequency in the first mode and the resonance frequency of the second mode is barely affected. This is because M_{+1} is attached to the base layer and it tunes the resonance frequency generated by the base layer but L_{+1} is hardly affected. Besides, the thicker mass generates larger N in the first mode. However, since the mass also serves as a spacer between the two layers, its thickness cannot be too small. The limitation of the thickness of the mass in its role as a spacer to the amplitude of vibration will be discussed in section 5.3.

The third case is the model 2L1MP0 with different lengths of L_{+1} , which are changed from 50 to 140 mm. Figure 11(a) shows the MSAPD FRFs of models with lengths from 50 to 100 mm, and figure 11(b) shows the MSAPD FRFs of the model with lengths from 100 to 140 mm. Apparently, when L_{+1} is shorter than 100 mm, the interval between the first two modes becomes larger and the resonance frequencies of the first mode are barely affected. This is because the effective mass of L_{+1} applied on the tip of the base layer is much lighter than M_{+1} , and the change in length of L_{+1} only causes a slight change to the overall dynamic mass of the first mode. When L_{+1} becomes longer and heavier, the resonance frequencies of the two modes are both decreased and the interval between them becomes smaller, but the N and k of the first mode are also significantly decreased as shown in table 6. Then, the model 2L1ML11 has a better performance in this case.

4.3. Optimization of a two-layer VEH with two masses

4.3.1. Change in the thickness of the mass M_{+2} . In this section, the model 2L2MP09 with different thicknesses of M_{+2} is discussed. M_{+1} with mass position 0 is constantly 10 mm thick. Figure 12(a) shows the MSAPD FRFs of models with thicknesses of M_{+2} from 0 mm (2L1M) to 7 mm, and figure 12(b) shows models with thicknesses of M_{+2} from 7 to 20 mm. In figure 12(a), when M_{+2} becomes thicker, the two modes are closer, and the mass ratio and EMCC are decreased in the first mode as shown in table 7. The first mode is barely activated when the second mass is 7 mm thick.

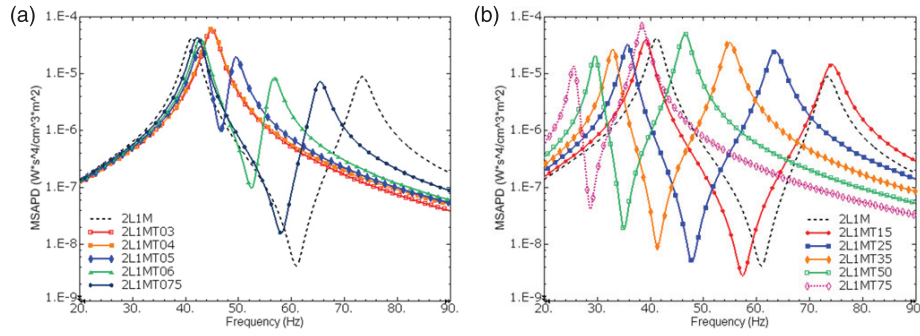


Figure 9. MSAPD FRFs of the model 2L1MP0 with different thicknesses of L_{+1} .

Table 4. Modal performance of the model 2L1MP0 with different thicknesses of L_{+1} .

Model (2L1MP0)	Thickness of L_{+1} (mm)	Mode 1			Mode 2		
		$f1$ (Hz)	$N1$ (%)	$k1$	$f2$ (Hz)	$N2$ (%)	$k2$
2L1MT03	0.3	30.23	4.5	0.002	44.50	69.6	0.225
2L1MT04	0.4	39.17	0.2	0.034	44.50	75.0	0.222
2L1MT05	0.5	42.66	38.2	0.203	49.15	38.1	0.117
2L1MT06	0.6	42.51	48.6	0.216	56.35	29.0	0.092
2L1MT075	0.75	41.91	50.0	0.218	65.04	29.6	0.096
2L1M	1	40.84	47.9	0.218	72.96	34.6	0.112
2L1MT15	1.5	38.85	42.4	0.216	73.63	43.9	0.134
2L1MT25	2.5	35.50	33.2	0.211	62.99	56.5	0.150
2L1MT35	3.5	32.80	26.4	0.206	54.52	65.1	0.159
2L1MT50	5	29.57	19.2	0.198	46.24	74.2	0.168
2L1MT75	7.5	25.59	11.7	0.186	38.18	83.4	0.181

Table 5. Modal performance of the model 2L1MP0 with different thicknesses of M_{+1} .

Model	Thickness of M_{+1} (mm)	Mode 1			Mode 2		
		$f1$ (Hz)	$N1$ (%)	$k1$	$f2$ (Hz)	$N2$ (%)	$k2$
2L1M M03	3	55.34	28.8	0.210	73.89	49.7	0.135
2L1M M04	4	52.42	33.3	0.214	73.63	45.9	0.127
2L1M M05	5	49.88	36.9	0.216	73.51	42.9	0.122
2L1M	10	40.84	47.9	0.218	72.96	34.6	0.112
2L1M M11	11	39.51	49.3	0.218	72.86	33.6	0.112
2L1M M15	15	35.14	53.6	0.217	72.31	30.8	0.112
2L1M M20	20	31.07	56.8	0.215	71.38	29.0	0.115

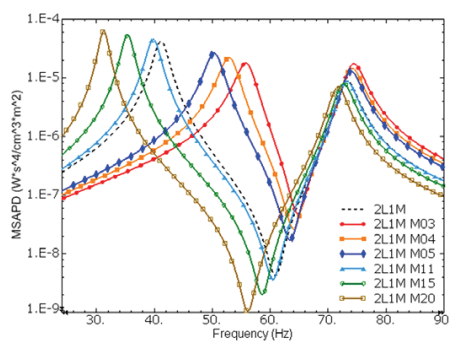


Figure 10. MSAPD FRFs of model 2L1MP0 with different thicknesses of M_{+1} .

However, the anti-resonance between the two modes also disappears. In figure 12(b), when M_{+2} is thicker than 7 mm, the interval between the two modes is increased again and

the anti-resonance re-appears before the first mode. This is because the phase angle of the motion and current of the first mode has been reversed, and the sign of the coupling term χ_1 has become minus. The phase angle of the current will also be reversed when the piezoelectric coverage is increased; this will be discussed in section 5.1.

4.3.2. Model screening for optimal VEHs. In this section, VEH models (2L2M) with different mass positions are investigated. Since the possible combinations of the mass positions are too many, the structural modal approach is used initially to screen the VEHs with close resonance frequencies and the preferred values of mass ratio. This was varied by computing the first two resonance frequencies of 2L2M with M_{+1} and M_{+2} located at varying positions using FEA modal analysis in the ABAQUS FE code.

Figures 13(a) and (b) show the contours of the computed resonance frequencies while figures 13(d) and (e) show the

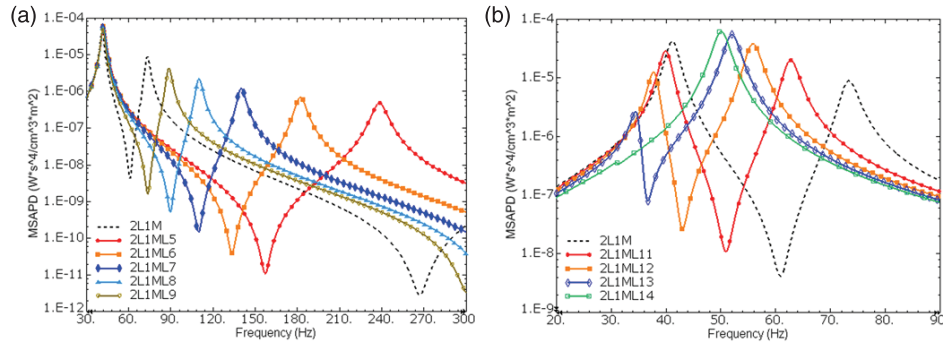


Figure 11. MSAPD FRFs of the model 2L1MP0 with different lengths of L_{+1} .

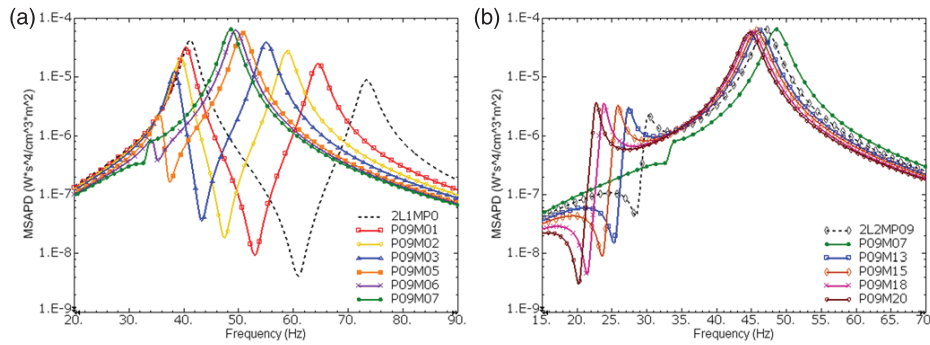


Figure 12. MSAPD FRFs of the model 2L2MP09 with different thicknesses of the second mass.

Table 6. Modal performance of the model 2L1MP0 with different lengths of L_{+1} .

Model	Length of L_{+1} (mm)	Mode 1			Mode 2		
		f_1 (Hz)	N_1 (%)	k_1	f_2 (Hz)	N_2 (%)	k_2
2L1ML5	50	41.85	73.1	0.229	236.37	9.3	0.131
2L1ML6	60	41.77	71.5	0.229	180.93	10.6	0.114
2L1ML7	70	41.72	68.7	0.229	139.30	13.3	0.103
2L1ML8	80	41.62	64.3	0.227	109.45	17.8	0.099
2L1ML9	90	41.38	57.8	0.225	88.16	24.5	0.102
2L1M	100	40.84	47.9	0.218	72.96	34.6	0.112
2L1ML11	110	39.73	33.2	0.204	62.33	49.6	0.136
2L1ML12	120	37.69	15.6	0.178	55.43	67.4	0.168
2L1ML13	130	34.65	3.3	0.141	51.54	79.8	0.196
2L1ML14	140	31.14	0.0	0.021	49.58	83.3	0.213

mass ratios of the first two modes. Figures 13(c) and (f) show the ratio of the resonance frequencies (f_2/f_1) and the ratio of the mass ratios (N_2/N_1), respectively. From figures 13(c) and (f), it is seen that a smaller value of f_2/f_1 means a smaller interval between the two modes and a favourable value of N_2/N_1 means that the mass ratio of each mode is neither too large nor too small. A good design of the 2L2M VEH is defined in this paper as that for which $f_2/f_1 \leq 2$ and $0.25 \leq N_2/N_1 \leq 4$. The contour plots in figures 13(c) and (f) show the regions where the favourable values of f_2/f_1 and N_2/N_1 are located.

Then, a screening process is developed to select the mass positions with the favourable values of f_2/f_1 and N_2/N_1 . This is done by combining figures 13(c) and (f) to produce a combined favourable region as shown in figure 14. The mass

positions in the overlapped area covered by diagonally crossed lines have both smaller f_2/f_1 and favourable N_2/N_1 , which give better mechanical performance. A general procedure for optimal design of the two-layer VEH is illustrated in figure 15. Since a lot of configurations have poor modal mechanical performance, instead of performing the full electromechanical analysis directly, using a modal approach to screen the VEHs initially is much more convenient, straightforward, quicker and cheaper to implement in terms of computing and analysis time.

As the mass positions with better mechanical performance are determined, two cases are developed to discuss some typical models. In table 8 and figure 16, the position of M_{+1} is 0. When the position of M_{+2} is changed from 2 to 6, the value of f_2/f_1 is close to 2 or smaller than 2 and the mass

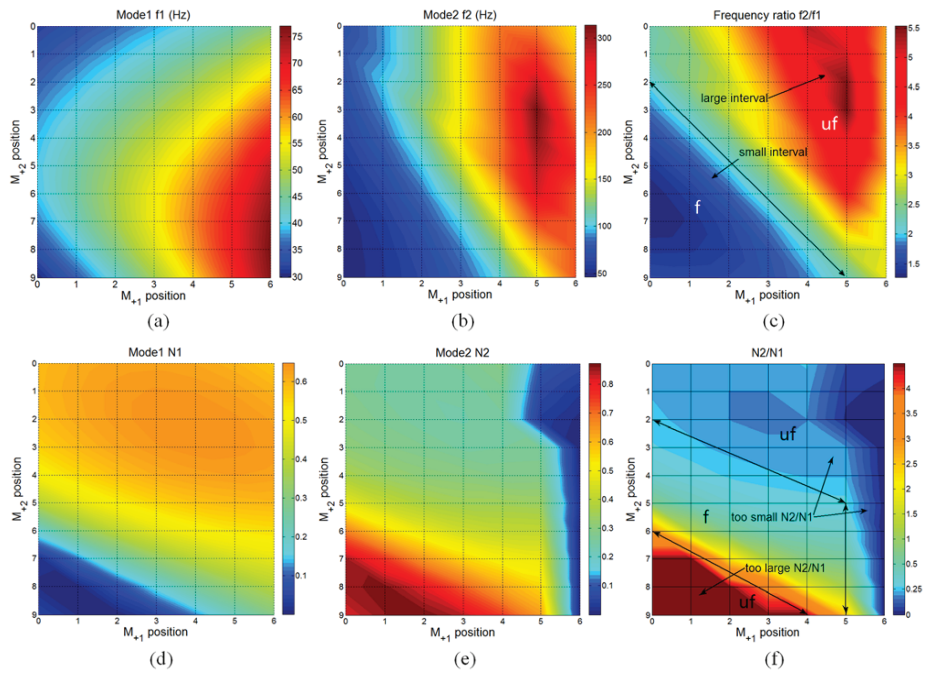


Figure 13. Contours of the resonance frequencies and mass ratios of the first two modes with different mass positions M_{+1} and M_{+2} : (a) and (b) resonance frequencies of modes 1 and 2; (d) and (e) mass ratios of modes 1 and 2; (c) and (f) plots of f_2/f_1 and N_2/N_1 ; *f: favourable region; uf: unfavourable region.

Table 7. Modal performance of the model 2L2MP09 with different thicknesses of M_{+2} .

Model	Thickness of M_{+2} (mm)	Mode 1			Mode 2		
		f_1 (Hz)	N_1 (%)	k_1	f_2 (Hz)	N_2 (%)	k_2
2L1MP0	0	40.84	47.9	0.218	72.96	34.6	0.112
P09 M01	1	40.16	37.0	0.209	64.11	45.9	0.129
P09 M02	2	39.30	25.7	0.196	58.44	57.5	0.147
P09 M03	3	38.27	15.4	0.179	54.64	68.3	0.166
P09 M05	5	35.84	2.5	0.137	50.26	81.9	0.197
P09 M06	6	34.55	0.3	0.092	49.01	84.5	0.207
P09 M07	7	33.30	0.1	0.060	48.10	85.0	0.214
P09	10	29.93	4.5	0.084	46.50	81.6	0.226
P09 M13	13	27.21	10.6	0.069	45.61	76.5	0.231
P09 M15	15	25.69	14.2	0.062	45.17	73.3	0.232
P09 M18	18	23.75	19.1	0.056	44.61	69.2	0.234
P09 M20	20	22.64	20.5	0.053	44.26	68.0	0.234

Table 8. Modal performance of the model 2L2M with different mass positions of M_{+2} .

Model (2L2M)	Mode 1			Mode 2			f_2/f_1	N_2/N_1
	f_1 (Hz)	N_1 (%)	k_1	f_2 (Hz)	N_2 (%)	k_2		
P00	31.59	59.2	0.218	72.23	27.0	0.110	2.29	0.46
P01	33.65	59.5	0.222	77.94	27.6	0.115	2.32	0.46
P02	35.62	58.5	0.226	73.47	28.6	0.106	2.06	0.49
P03	37.38	55.8	0.227	67.92	31.2	0.100	1.82	0.56
P04	38.79	50.3	0.226	61.58	36.7	0.100	1.59	0.73
P05	39.62	39.2	0.219	55.25	47.7	0.113	1.39	1.22
P06	39.35	18.9	0.220	50.09	67.8	0.103	1.27	3.59
P07	37.16	1.6	0.129	47.32	84.9	0.198	1.27	53.06
P08	33.60	0.9	0.092	46.54	85.4	0.219	1.39	90.05
P09	29.93	4.5	0.084	46.50	81.6	0.226	1.55	17.94

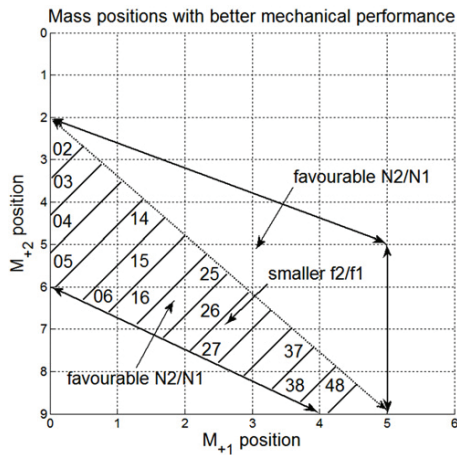


Figure 14. Determination of the mass positions with better mechanical performance. The area covered by the diagonally crossed lines is the overlapped area with both smaller f_2/f_1 (in figure 13(c)) and favourable N_2/N_1 (in figure 13(f)).

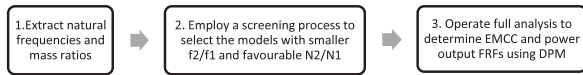


Figure 15. A general procedure for optimal design of the two-layer VEH.

ratio is more evenly distributed. When the position of M_{+2} is smaller than 2, the value of f_2/f_1 is slightly larger than 2. When the position of M_{+2} is larger than 6, the values of N and k of the first mode are decreased significantly. Then, the first mode becomes barely activated until the phase of the first mode has been changed to that of the model with mass position 9. But even at P09, the mass ratio of mode 1 is still very small compared to the mass ratios for positions P00 to P06. Therefore, the preferred positions are chosen from P02 to P06.

In table 9 and figure 17, some other models with preferred mass positions are given, in which the positions of M_{+1} and M_{+2} are varied simultaneously. Since the effective length of the base layer is decreased, the EMCCs in the two modes are increased and the resonance frequency of the first mode is increased. However, the resonance frequency of the second

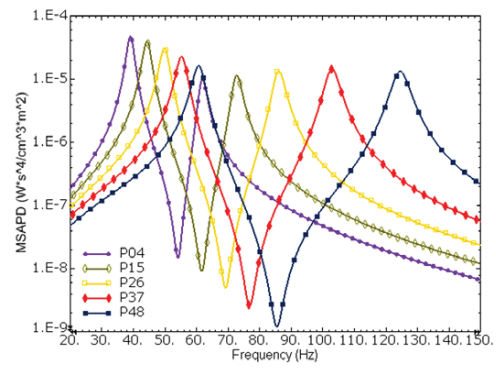


Figure 17. MSAPD FRFs of the model 2L2M with different mass positions.

mode is also increased significantly, and then the interval between the two modes becomes larger. Besides, the value of N_2/N_1 is also increased. Apparently, all the mass positions in this case can provide relatively small intervals between the two modes and evenly distribute the mass ratio.

The original thickness of the two masses of model 2L2M is 10 mm. In table 10 and figure 18, the thicknesses of the two masses are varied simultaneously from 5 to 20 mm with the mass positions P05 and P09. The results show that, for different thicknesses (and magnitudes) of the masses, the masses with the same position generate similar responses with only slight changes in the values of f_2/f_1 and N_2/N_1 . Thus, P05 still generates favourable f_2/f_1 and N_2/N_1 and P09 always generates very large values of N_2/N_1 . Specifically, the thinner masses can generate smaller values of f_2/f_1 and the resonance frequencies are higher. This shows the robustness of the optimization of the mass positions using the modal approach.

4.4. Varying mass positions for smaller and larger systems

In fact, the mass positions can be considered as dimensionless factors. Then, the designs of the two-layer VEHs with different mass positions can be used in different systems. In this section, two models are developed for a smaller system and a larger system. The dimensions of the model for a smaller system are given as base and first upper layer: 15 mm × 4 mm ×

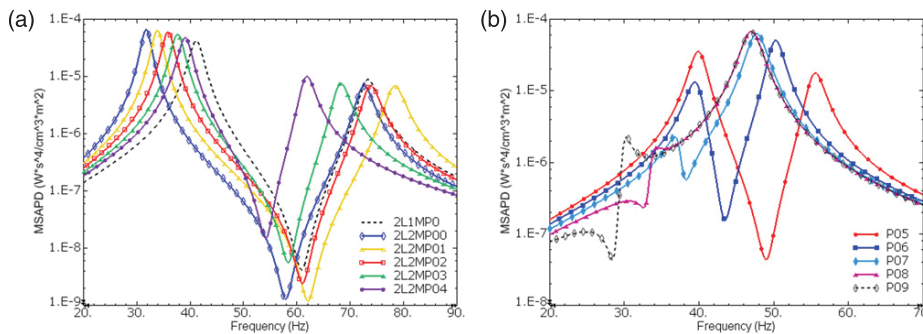


Figure 16. MSAPD FRFs of the model 2L2M with different mass positions of the second mass.

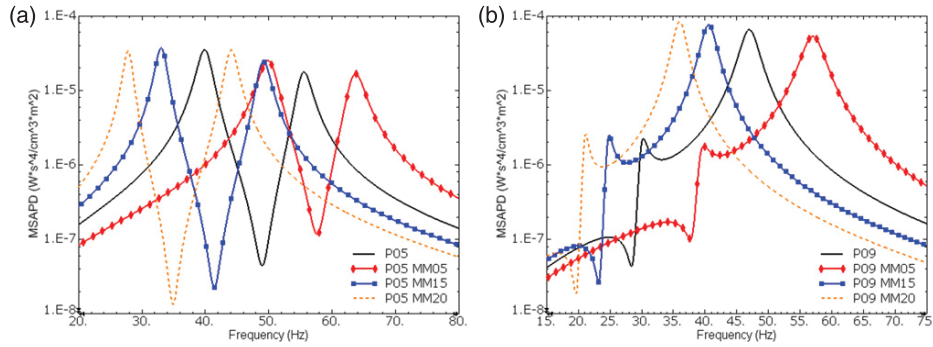


Figure 18. MSAPD FRFs of the model 2L2M with different thicknesses of the two masses. (a) 2L2MP05; (b) 2L2MP09.

Table 9. Modal performance of the model 2L2M with different mass positions.

Model (2L2M)	Mode 1			Mode 2			$f2/f1$	$N2/N1$
	$f1$ (Hz)	$N1$ (%)	$k1$	$f2$ (Hz)	$N2$ (%)	$k2$		
P04	38.79	50.3	0.226	61.58	36.7	0.100	1.59	0.73
P15	43.92	46.7	0.232	72.33	41.2	0.115	1.65	0.88
P26	49.29	40.7	0.236	85.42	48.0	0.134	1.73	1.18
P37	54.61	33.3	0.239	101.90	55.9	0.152	1.87	1.68
P48	59.83	26.3	0.244	123.14	62.4	0.161	2.06	2.37

Table 10. Modal performance of the model 2L2M with different thicknesses of the two masses.

Model	Masses' thickness (mm)	Modal Performance							
		$f1$ (Hz)	$N1$ (%)	$k1$	$f2$ (Hz)	$N2$ (%)	$k2$	$f2/f1$	$N2/N1$
P05 MM05	5	49.50	35.2	0.220	63.28	48.0	0.116	1.28	1.37
P05	10	39.62	39.2	0.219	55.25	47.7	0.113	1.39	1.22
P05 MM15	15	32.90	35.6	0.211	48.94	53.4	0.125	1.49	1.50
P05 MM20	20	27.74	29.6	0.201	43.88	60.8	0.140	1.58	2.05
P09 MM05	5	39.19	2.9	0.084	56.27	79.9	0.229	1.44	27.37
P09	10	29.93	4.5	0.084	46.50	81.6	0.226	1.55	17.94
P09 MM15	15	24.65	4.8	0.087	40.24	83.1	0.222	1.63	17.26
P09 MM20	20	21.00	4.4	0.092	35.75	84.3	0.217	1.70	19.03

0.1 mm; piezoelectric layer: 4 mm × 4 mm × 0.05 mm; masses: 1.5 mm × 4 mm × 1.5 mm. The dimensions of the model for a larger system are given as base and first upper layer: 500 mm × 100 mm × 8 mm; piezoelectric layer: 150 mm × 100 mm × 3 mm; masses: 50 mm × 100 mm × 50 mm. Thus, the aspect ratios of the two models are different. The length and thickness of the masses are 1/10 of the length of the base layers.

In table 11 and figure 19, the modal performance and power output (due to 1 m s⁻² base excitation) of the two models with typical mass positions ‘P05’, ‘P09’, ‘P26’ and ‘P29’ are given. Obviously, the larger model has much lower resonance frequencies and the smaller model has higher resonance frequencies. For the preferred mass positions ‘P05’ and ‘P26’ identified in figure 14, the responses of the two models are quite similar and the values of $f2/f1$ and $N2/N1$ are only slightly different. For the mass positions ‘P09’ and ‘P29’, the differences of the mass ratio between the two models become a little bit larger, but the values of $f2/f1$ and the

corresponding responses are still similar. Therefore, it is shown that the mass positions ‘P09’ and ‘P29’ always have poor performance in different systems with different dimensions or scales of models. The designs with favourable mass positions have good agreement in different systems, and they can be used from lower frequency to higher frequency with the power range from microwatts to milliwatts.

5. Factors affecting the performance of a two-layer VEH

5.1. Effect of varying the piezoelectric coverage

In the previous sections, the piezoelectric layer that has been used has a constant length of 25 mm and it only covers the root of the base layer. In table 12 and figure 20, two-layer VEH models with different piezoelectric coverages are presented. Firstly, the length of the piezoelectric layer of model 2L1M has been increased from 25 mm (PL25) to 90 mm (PL90),

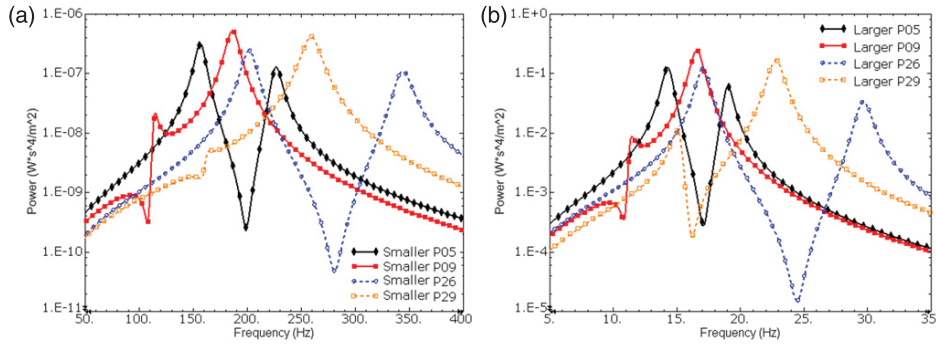


Figure 19. MSAPD FRFs of the model 2L2M with different mass positions in a smaller and a larger system. (a) Smaller system; (b) larger system.

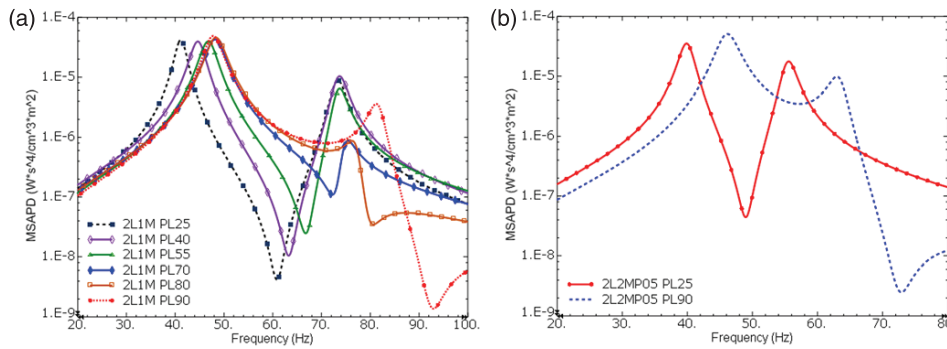


Figure 20. MSAPD FRFs of the two layer models with different piezoelectric coverages. (a) 2L1MP0; (b) 2L2MP05.

Table 11. Modal performance of the model 2L2M with different mass positions in a smaller and a larger system.

Model	f_1 (Hz)	N_1 (%)	k_1	f_2 (Hz)	N_2 (%)	k_2	f_2/f_1	N_2/N_1
Smaller P05	155.31	43.5	0.231	225.18	45.8	0.114	1.45	1.05
Smaller P09	113.72	6.0	0.078	183.37	82.5	0.236	1.61	13.71
Smaller P26	200.05	42.5	0.249	341.48	48.3	0.135	1.71	1.14
Smaller P29	161.46	0.3	0.058	254.66	89.3	0.239	1.58	267.05
Larger P05	14.14	37.1	0.220	18.91	47.7	0.102	1.34	1.29
Larger P09	11.29	2.6	0.096	16.34	81.6	0.219	1.45	31.32
Larger P26	16.80	41.5	0.234	29.50	45.5	0.110	1.76	1.10
Larger P29	15.08	3.7	0.171	22.56	82.1	0.187	1.50	22.09

which is considered as full coverage since the effective length of the base layer is 90 mm (mass position 0). The EMCC of the first mode is increased significantly and reaches the peak value when the length of the piezoelectric layer is increased to 70 mm, and then the EMCC is slightly decreased for full coverage. However, the EMCC of the second mode has been changed irregularly. When the length of the piezoelectric layer is increased to 40 mm, the EMCC is slightly increased, and then, it becomes very small until the length is 90 mm.

In fact, the decrease of the EMCC in the first mode is due to the drop of the strain distribution near the free tip, which causes the increase of the total charge to be relatively less than the increase of the piezoelectric capacitance. However, the decrease of the EMCC in the second mode is due to self-cancellations of the current. This is due to the strain distribution along the length of the beam which causes the electric

displacement D along the thickness to be partly reversed. Figures 21(a) and (b) illustrate the first two modes' shapes and the corresponding electric displacement distributions of model 2L1M PL90 in the $X-Z$ plane. The lengths and directions of the vector arrows on the beam indicate the distributed values and directions of D . Therefore, when the length of the piezoelectric layer is between 70 and 80 mm, the current in the second mode is almost cancelled and the EMCC becomes very weak. When the model is fully covered, the EMCC starts to increase again. However, the phase of the total current in the second mode is changed at this stage and the sign of the coupling term χ_2 becomes negative. Therefore, in figure 20(a), the anti-resonance between the first two modes is eliminated. The model 2L2M with 90 mm long piezoelectric layer has a similar response, as shown in figure 20(b).

Table 12. Modal performance and coupling terms of two layer models with different piezoelectric coverages.

Model	Piezo-layer length (mm)	f_1 (Hz)	N_1 (%)	k_1	χ_1	f_2 (Hz)	N_2 (%)	k_2	χ_2	f_2/f_1	N_2/N_1
2L1M PL25	25	40.84	47.9	0.218	5.51×10^{-3}	72.96	34.6	0.112	4.95×10^{-3}	1.79	0.72
2L1M PL40	40	44.02	45.4	0.263	9.12×10^{-3}	73.21	36.3	0.117	6.57×10^{-3}	1.66	0.80
2L1M PL55	55	46.26	47.2	0.290	1.25×10^{-2}	73.33	34.5	0.085	5.59×10^{-3}	1.59	0.73
2L1M PL70	70	47.29	52.0	0.300	1.50×10^{-2}	74.72	29.8	0.023	1.75×10^{-3}	1.58	0.57
2L1M PL80	80	47.31	55.3	0.297	1.59×10^{-2}	77.16	26.7	0.027	-2.25×10^{-3}	1.63	0.48
2L1M PL90	90	46.92	57.5	0.289	1.62×10^{-2}	81.45	24.6	0.084	-7.85×10^{-3}	1.74	0.43
2L2MIP05 PL25	25	39.62	39.2	0.219	5.36×10^{-3}	55.25	47.7	0.113	3.79×10^{-3}	1.39	1.22
2L2MIP05 PL90	90	45.36	57.0	0.282	1.52×10^{-2}	63.13	29.2	0.119	-8.64×10^{-3}	1.39	0.51

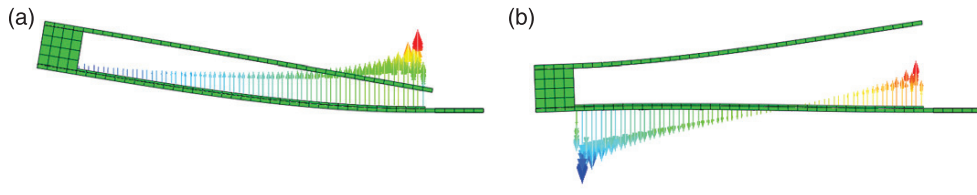


Figure 21. Electrical displacement mode shapes of model 2L1M.

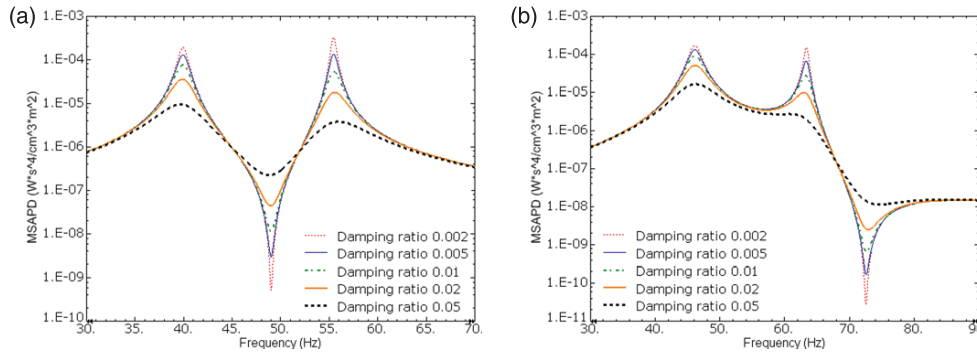


Figure 22. MSAPD FRFs with different damping ratios. (a) 2L2MP05 PL25; (b) 2L2MP05 PL90.



Figure 23. Relative displacement between the two layers.

5.2. Effect of structural damping

The effects of different levels of structural damping have been analysed in this section. Firstly, the value of the damping ratio can directly affect the coupling criterion $k^2 Q_M$. With a larger damping, the system coupling becomes weaker, and vice versa. Secondly, the damping ratio also directly affects the mechanical forcing function and the magnitude of the maximum power. In figure 22, the damping ratio is changed from 0.002 to 0.5. Figure 22(a) shows the MSAPD FRFs of model 2L2MP05 PL25 and figure 22(b) shows the MSAPD FRFs of model 2L2MP05 PL90. Apparently, with different damping ratios, the magnitude of the power density around each mode is significantly affected. The model with small damping ratio can generate a high peak value of the power density. However, the magnitude of the power density around the anti-resonance with small damping is also greatly decreased. Meanwhile, the magnitude of the MSAPD off the resonance and anti-resonance is not significantly affected. Therefore, no matter how small or large the damping is, a model without anti-resonance between the two modes will help to enhance the ability for broadband power output.

5.3. Effect of vibration magnitude

The designs of the two-layer VEHs use M_{+1} as spacers. Apparently, the mass must be thick enough to ensure that

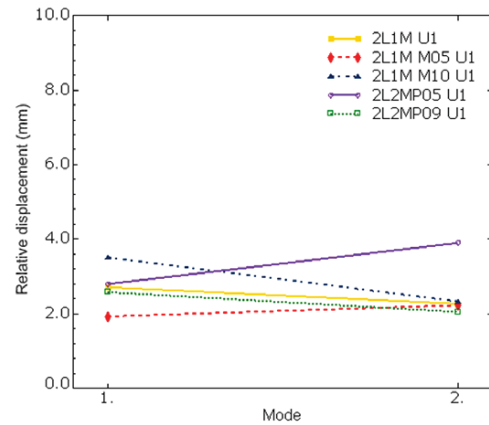


Figure 24. Relative displacement between the two layers under 9.81 m s^{-2} base excitation.

the vibration space between the two layers is adequately large. Figure 23 illustrates the relative displacement $U1$, which is the relative displacement between the bottom surface of L_{+1} and the top of the base layer. When the VEH is stationary, $U1$ equals 0 mm. When the system is oscillated, $U1$ should be smaller than the thickness of mass M_{+1} , which is 10 mm here. In figure 24, under a 9.81 m s^{-2} ($1g$) base excitation, the $U1$ values of some typical models are shown. The results show that all models have enough space for vibration of L_{+1} for a relatively strong 9.81 m s^{-2} base excitation. Since the original damping ratio is 0.02, for a system with a very small damping ratio like 0.005, the relative displacement would be 4 times larger. Then, a thicker mass M_{+1} or a smaller base excitation would be required. Normally, for a smaller base excitation like

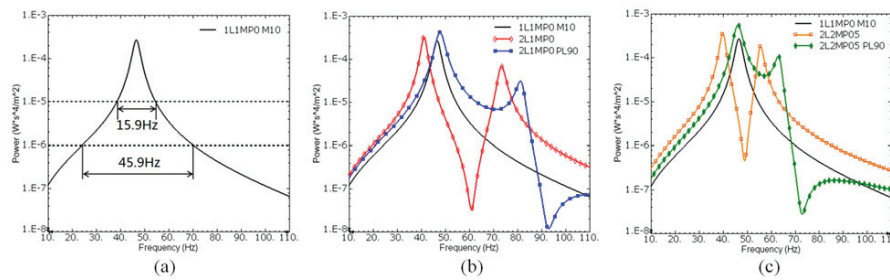


Figure 25. FRFs and the broadband ability of the power output with 1 m s^{-2} base excitation. (a) Single cantilevered VEH with tip mass 1L1M M10; (b) 2L1M; (c) 2L2M.

Table 13. Comparison of the bandwidths of the two-layer models.

Minimal power (W)	Frequency range (Hz)				
	1L1MP0 M10	2L1MP0	2L1MP0 PL90	2L2MP05	2L2MP05 PL90
10^{-5}	15.9	22.2	33.1	24.8	31.0
10^{-6}	45.9	62.7	65.4	66.3	48.2

5 m s^{-2} , all models can operate satisfactorily without reaching the vibration amplitude limit.

5.4. Effect of operating off-resonance and broadband power output

In the above sections, the MSAPD is used since it can present the effect of the mass ratio of each mode on the power density directly. When the mass ratio is nearly evenly distributed, the two-layer VEH can generate the same or even a higher level of power output around each mode in comparison with the first mode of a single layer VEH. Then, by combining the two modes together, a broadband power output can be achieved. In figure 25, the power output FRFs with 1 m s^{-2} base excitation of five models are given. Model 1L1MP0 M10 is the single layer model 1LOM with mass M_{+1} attached at mass position 0 (free tip). In figure 25(a), the frequency range of a defined minimal power output of 10^{-6} W of model 1L1MP0 M10 is 45.9 Hz, and the frequency range of a defined power output which is ten times higher than the minimal power output, that is 10^{-5} W , is 15.9 Hz. Table 13 gives the frequency ranges of the two different levels of the minimal power output. Model 2L1MP0 PL90 can generate more than 2 times the frequency range of the 10^{-5} W power output and nearly 1.5 times the frequency range of the 10^{-6} W power output of model 1L1MP0. However, model 2L2MP05 PL90 has a narrower frequency band for the 10^{-6} W power output than model 2L1MP0 PL90. This is because the value of f_2/f_1 is smaller than it is for model 2L1MP0 (see table 12). Therefore, the interval between the two modes should not be too small, as it might affect the off-resonance performance and generate a narrower broadband.

6. Conclusion

In this paper, two-layer VEHs have been developed. A modal approach using the mass ratio and the EMCC is developed

to predict the resonance performance of the VEHs. It has been found that a mode with too large a mass ratio will make the rest of the modes have small mass ratios and poor performance. Meanwhile, if the interval between two modes becomes too large, the anti-resonance can also significantly affect the performance. Therefore, the design objective of the two-layer VEH is to determine a good configuration for the VEH model so that it can have modes that are close enough and evenly distributed mass ratios. The modal frequencies can be tuned and the mass ratios distributed by changing the dimensions of the layers and masses. However, the modal frequencies and mass ratios can be more easily varied by simply relocating the mass positions in the VEH model.

A screening process has been developed using the structural modal approach to filter the mass positions with favourable values of the frequency ratio f_2/f_1 and ratio of mass ratios N_2/N_1 . A good mass position has a smaller interval between the two modes and the mass ratio of each mode is neither too large nor too small. Since many configurations have poor modal mechanical performance, using a modal approach to screen the VEHs can remove the need to carry out the full electromechanical analysis on all possible configurations. Instead, only the screened configurations that have favourable mass positions are subjected to full electromechanical analysis.

Furthermore, if the base layer is fully covered by the piezoelectric layer, the phase of the current in the second mode can be reversed and the sign of the coupling term becomes negative. Then, the anti-resonance between the first two modes can be eliminated, which provides a wider band of power output. However, if the interval between the first two modes becomes too small, the broadband power output can also be narrower. Also, the structural damping mainly affects the performance around the resonances and anti-resonances. In addition, since the mass M_{+1} is used as a spacer, its thickness should be carefully chosen when the magnitude of the vibration is very large or the damping is quite small.

References

- [1] Anton S R and Sodano H A 2007 A review of power harvesting using piezoelectric materials (2003–2006) *Smart Mater. Struct.* **16** R1–R21
- [2] Tang L, Yang Y and Soh C K 2010 Toward broadband vibration-based energy harvesting *Intell. Mater. Syst. Struct.* **21** 1867–97
- [3] Roundy S and Zhang Y 2005 Toward self-tuning adaptive vibration based micro-generators *Proc. SPIE* **5649** 373–84
- [4] Zhu D, Roberts S, Tudor J and Beeby S 2008 Closed loop frequency tuning of a vibration-based microgenerator *Proc. Power MEMS + microEMS (Sendai, Nov. 9–12)* pp 229–32
- [5] Erturk A, Hoffmann J and Inman D J 2009 A piezomagnetoelastic structure for broadband vibration energy harvesting *Appl. Phys. Lett.* **94** 254102
- [6] Ferrari M, Ferrari V, Guizzetti M, Ando B, Baglio S and Trigona C 2010 Improved energy harvesting from wideband vibrations by nonlinear piezoelectric converters *Sensors Actuators A* **162** 425–31
- [7] Tang L, Yang Y and Soh C K 2012 Improving functionality of vibration energy harvesters using magnets *Intell. Mater. Syst. Struct.* **23** 1433–49
- [8] Ferrari M, Ferrari V, Guizzetti M, Marioli D and Taroni A 2008 Piezoelectric multifrequency energy converter for power harvesting in autonomous microsystems *Sensors Actuators A* **142** 329–35
- [9] Qi S F, Shuttleworth R, Oyadiji S O and Wright J 2010 Design of a multiresonant beam for broadband piezoelectric energy harvesting *Smart Mater. Struct.* **19** 094009
- [10] Lee S, Youn B D and Jung B C 2009 Robust segment-type energy harvester and its application to a wireless sensor *Smart Mater. Struct.* **18** 095021
- [11] Ou Q, Chen X, Gutschmidt S, Wood A and Leigh N 2012 An experimentally validated double-mass piezoelectric cantilever model for broadband vibration-based energy harvesting *Intell. Mater. Syst. Struct.* **23** 117–25
- [12] Zhou W, Penamalli G R and Zuo L 2012 An efficient vibration energy harvester with a multi-mode dynamic magnifier *Smart Mater. Struct.* **21** 015014
- [13] Wu H, Tang L H, Yang Y W and Soh C K 2012 A novel two-degrees-of-freedom piezoelectric energy harvester *Intell. Mater. Syst. Struct.* **24** 357–68
- [14] Chen Z S, Yang Y M, Lu Z M and Luo Y T 2013 Broadband characteristics of vibration energy harvesting using one-dimensional phononic piezoelectric cantilever beams *Physica B* **410** 5–12
- [15] Erturk A, Hoffmann J and Inman D J 2009 Modeling of piezoelectric energy harvesting from an L-shaped beam mass structure with an application to UAVs *Intell. Mater. Syst. Struct.* **20** 529–44
- [16] Karami M A and Inman D J 2011 Analytical modeling and experimental verification of the vibrations of the zigzag microstructure for energy harvesting *J. Vib. Acoust.* **133** 011002
- [17] Erturk A and Inman D J 2008 A distributed parameter electromechanical model for cantilevered piezoelectric energy harvesters *J. Vib. Acoust.* **130** 041002
- [18] Erturk A and Inman D J 2011 *Piezoelectric Energy Harvesting* (New York: Wiley) 978-1-1199-9135-9
- [19] Yang Y W and Tang L H 2009 Equivalent circuit modeling of piezoelectric energy harvesters *Intell. Mater. Syst. Struct.* **20** 2223
- [20] Erturk A and Inman D J 2007 Mechanical considerations for modeling of vibration-based energy harvesters *IDETC/CIE (Las Vegas, NV, Sept. 4–7)*
- [21] Erturk A and Inman D J 2008 On mechanical modeling of cantilevered piezoelectric vibration energy harvesters *Intell. Mater. Syst. Struct.* **19** 1311
- [22] SIMULIA Corp 2010 *Abaqus Theory Manual in ABAQUS 6.10 Documentations*
- [23] Guyomar D, Sebald G, Pruvost S, Lallart M, Khodayari A and Richard C 2009 Energy harvesting from ambient vibrations and heat *Intell. Mater. Syst. Struct.* **20** 609–24

CHAPTER 7 TAPERED TWO-LAYER BROADBAND VIBRATION ENERGY HARVESTERS

Xingyu Xiong and S Olutunde Oyadiji

ASME Journal of Vibration and Acoustics (accept)

Tapered Two-layer Broadband Vibration Energy Harvesters

Xingyu Xiong and S Olutunde Oyadiji*
School of Mechanical, Aerospace and Civil Engineering,
The University of Manchester, M13 9PL, UK

ABSTRACT

Two-layer piezoelectric vibration energy harvesters (VEHs) using convergent and divergent tapered structures have been developed for broadband power output. The VEHs consist of a base cantilevered beam which is attached to an upper beam by a spacer to develop a two-layer configuration. Two masses are attached to each layer to tune the resonance frequencies of each VEH and one of these masses also serves as the spacer. By varying the positions of the masses, the convergent and divergent tapered VEHs can generate close resonance frequencies and considerable power output in the first two modes. A broadband VEH design strategy is introduced based on a modal approach, which determines the modal performance using mass ratio and modal electromechanical coupling coefficient (EMCC). The required modal parameters are derived using the finite element method. Mass ratio represents the influence of the modal mechanical behaviour on the power density directly. Since the dominant mode causes the remaining modes to have smaller mass ratios, smaller EMCC and poor performance, the design strategy involves the selection of the VEH configurations with close resonances and favourable values of mass ratio initially, and deriving the EMCC and power density of those selected configurations.

Keywords: vibration energy harvesters; piezoelectric energy harvesting; multiple resonances; broadband; modal performance.

1. INTRODUCTION

There is currently a need to develop self-powered, batteryless wireless sensor and sensor nodes for structural health monitoring. This has led to the need for harvesting small-scale ambient energy becoming a central issue [1]. Vibration energy harvesting using piezoelectric materials has become a popular technique which has good potential to provide sufficient power [2]. Vibration energy harvesters (VEHs) can convert mechanical strain energy into electrical energy based on the piezoelectric effect. However, the conventional beam-shaped VEHs have limited bandwidth, which is ineffective in real applications.

* Corresponding author. Tel: 00 44 161 275 4348 Fax: 00 44 161 275 3844
E-mail address: s.o.oyadiji@manchester.ac.uk

Therefore, broadband techniques are being developed in order to achieve relatively large power output in a wider frequency bandwidth. Nonlinear VEHs with magnet, resonance tuning technique and multi-resonance designs are widely reported in existing literatures [3]. In particular, multi-resonance VEHs normally contains multiple beam parts, which can generate close resonance frequencies in multiple modes [4-12].

As a typical multi-resonance design, VEHs contain array of beams that can effectively expand the bandwidth of the power output [4-7]. VEHs with array of beams normally have several individual cantilevered beams, which are electrically connected in series or in parallel. The resonance frequency of each cantilevered beam can be easily tuned to generate close vibration modes. However, when the number of cantilevered beams is increased, the power density could be significantly reduced. This is because when the VEH is working around one mode, the corresponding cantilevered part is active, and the remaining parts are almost passive. Besides, since a large part of the piezoelectric materials is bonded to the passive cantilevered beams, the electromechanical coupling in each mode is also decreased. Some researchers developed two-mass VEHs [8, 9]. Two extra masses are attached on one cantilevered beam. One mass is attached to the centre of the beam and another is attached to the free tip. The two masses separate the cantilevered beam into two parts; the interaction of vibration from the two parts can generate two resonance frequencies. However, in order to generate enough close resonances, a heavy mass is normally required to be attached to the centre of the beam, but this makes one vibration mode to be easily dominant. The uneven power output can eventually affect the broadband performance. Erturk et al. [10] developed an L-shaped VEH in which the second resonance frequency can be two times higher than the first resonance frequency. Xiong and Oyadiji [11] developed a two-layer VEH consisting of a base rectangular cantilevered (RC) beam that is connected to an upper RC beam by a spacer. Two masses are attached to each layer to tune the resonance frequencies of the VEH and one of these masses also serves as the spacer. By varying the positions of the masses, the VEH can generate close resonance frequencies and considerable power output in the first two modes. Some researches indicated that using tapered cantilevered beams can notably affect the performance of VEHs compared with using RC beams due to the different mass and strain distributions [12, 13]. Therefore, it is also necessary to analysis the performance of two-layer VEHs using tapered beams.

In this paper, two-layer VEHs using convergent tapered cantilevered (CTC) beams and divergent tapered cantilevered (DTC) beams are well designed using a broadband VEH design strategy. This is based on a modal approach which determines the modal performance of the VEHs based on two modal factors: mass ratio and electromechanical coupling coefficient. In particular, mass ratio represents the influence of the modal mechanical behaviour on the power density of each mode. Using the design strategy can select configurations with close resonances and good modal performance in multiple modes can be selected.

The performances of VEHs using tapered beams are compared with VEHs using rectangular beams in both the mechanical and electrical domains. This paper contains five sections: section 2 is on the brief introduction of VEH modelling using a general distributed electromechanical parameter model (DPM) with the utilization of finite element analysis (FEA); section 3 is on the introduction of a broadband VEH design strategy; section 4 is on the implementation of the design strategy for the tapered two-layer VEH designs; the last section presents the conclusions of this paper.

2. VIBRATION ENERGY HARVESTER MODELLING

The modal analysis technique can be used to represent the steady-state linear vibration response of a VEH model which is subjected to continuous harmonic excitation. The displacement of the transverse vibration relative to the moving base of the VEH at time t is:

$$u_{rel}(t) = \sum_{r=1}^{\infty} \phi_r \eta_r(t) \quad (1)$$

where ϕ_r is the mass-normalised eigenfunction and $\eta_r(t)$ is the corresponding modal coordinates of the r^{th} mode. Erturk and Inman established an analytical model for cantilevered VEHs based on the Euler-Bernouli beam assumptions and used the DPM to predict the power output of VEHs with resistive loads [14]. The governing equations of the modal vibration response and electrical behaviour of the VEH model with a resistive load are given as:

$$\frac{d^2 \eta_r(t)}{dt^2} + 2\zeta_r \omega_r \frac{d\eta_r(t)}{dt} + \omega_r^2 \eta_r(t) + \chi_r v(t) = F_r(t) \quad (2)$$

$$\frac{v(t)}{R_l} + C_p \frac{dv(t)}{dt} - \sum_{r=1}^{\infty} \chi_r \frac{d\eta_r(t)}{dt} = 0 \quad (3)$$

where $\eta_r(t)$ is the corresponding modal coordinates of the r^{th} mode, v is the generated voltage, ζ_r is the damping ratio, ω_r is angular resonance frequency, χ_r is the modal electromechanical coupling term, F_r is the modal mechanical forcing term, C_p is the piezoelectric capacitance and R_l is the resistive load. The steady state solution of Eq.(2) is:

$$\eta_r(t) = \frac{F_r - \chi_r v}{\omega_r^2 - \omega^2 + j2\zeta_r \omega_r \omega} e^{j\omega t} \quad (4)$$

The voltage across R_l can be represented by:

$$v(t) = \frac{\sum_{r=1}^{\infty} \frac{j\omega F_r \chi_r}{\omega_r^2 - \omega^2 + j2\zeta_r \omega_r \omega}}{\sum_{r=1}^{\infty} \frac{j\omega \chi_r^2}{\omega_r^2 - \omega^2 + j2\zeta_r \omega_r \omega} + \frac{1}{R_l} + j\omega C_p} e^{j\omega t} \quad (5)$$

The complex power in the frequency domain is $v(j\omega) \left(\frac{v(j\omega)}{R_l}\right)^*$ and the average power output is $|v|^2/2R_l$

(ignore electric losses). The vibration response of the beam relative to its base is:

$$u_{rel}(x, t) = \sum_{r=1}^{\infty} \phi_r(x) \frac{F_r - \chi_r v}{\omega_r^2 - \omega^2 + j2\zeta_r \omega_r \omega} e^{j\omega t} \quad (6)$$

When the VEH model is not an uniform beam, the derivation of the eigenfunction and other modal parameters can be complicated and tedious. FEA software packages like ABAQUS and ANSYS can be used to solve the eigenvalue problem and derive the modal parameters. By letting the applied voltage to be zero ($v = 0$) on the top and bottom surface of the piezoelectric layer in the FEA simulation, the forcing function F_r at each resonance frequency with a vertical harmonic base excitation $\ddot{u}_b = Y_0 \omega^2 e^{j\omega t}$ can be determined in the frequency domain from Eq. (4) using the absolute displacement data derived from the FEA results. For the r^{th} mode:

$$F_r = (\omega_r^2 - \omega^2 + j2\zeta_r \omega_r \omega) \eta_r(j\omega_r) = -j2\zeta_r \ddot{u}_{rel} \sqrt{m_{mr}} \Big|_{\omega=\omega_r} \quad (7)$$

where m_m is the generalized modal mass. By substituting $v(t)/R_l$ with $i(t)$ in Eq. (3):

$$i = \sum_{r=1}^{\infty} j\omega \chi_r \eta_r(j\omega_r) = \sum_{r=1}^{\infty} \frac{j\omega F_r \chi_r}{\omega_r^2 - \omega^2 + j2\zeta_r \omega_r \omega} \Big|_{\omega=\omega_r} \quad (8)$$

Once the electrical current is derived from the FEA simulation, the modal coupling term χ_r can be determined from Eq. (8) for multiple modes or any specified mode. Structural damping is used and defined as 0.04 in this paper ($\zeta_r = 0.02$) for the convenience of modal analysis. For the real applications, the damping ratio needs to be obtained experimentally.

3. DESIGN STRATEGY BASED ON A MODAL APPROACH

In order to analyse the performance of VEH thoroughly and present the frequency response of the maximum power output with the optimal load, the frequency-by-frequency steady-state analysis is always required by the conventional method. However, the conventional method cannot efficiently determine the optimal performance of a VEH as it will require too many computations which will take too much time. Also, it is hard to find out how the change of configuration affects the performance in both mechanical and electromechanical domains which the conventional method is used. Therefore, design strategy is developed in this section for the optimal design of multi-resonance VEHs. The strategy is based on a modal approach, which determines the modal mechanical and electromechanical performance of VEHs using mass ratio and modal electromechanical coupling coefficient (EMCC) as performance variables.

Erturk and Inman [15] introduced a correction factor γ to improve the accuracy of the single degree-of-freedom (SDOF) model for analysing VEH performance. The correction factor γ is also called the modal participation factor, which indicates how strongly motion in the x -, y - or z -direction or rotation

about one of these axes is represented in the eigenvector of that mode [16]. Erturk and Inman only analysed the purely structural responses using the correction factor. Guyomar et al. [17] introduced a modal electromechanical criterion $k^2 Q_m$ to evaluate the maximum average power output based on the SDOF system, where k is the EMCC and $Q_m = 1/2\zeta$ is the quality factor. However, in Guyomar's work, the effect of the modal participation factor on the power output has not been accurately represented in multiple degrees of freedom systems. Xiong and Oyadiji [18] analysed the modal performance of cantilevered VEHs with RC, CTC and DTC structures and considered both the corrected structural response and the electromechanical coupling. In their work, a modal structural criterion named mass ratio N was introduced, which depends on the modal participation factor γ and represents the influence of the modal mechanical behaviour on the power density directly. In particular, a parametric study has been presented using DPM to determine the influences of EMCC and mass ratio on the power density around the resonance frequency.

In this paper, the mean squared acceleration weighted power density (MSAPD), which is defined as the average power due to 1m/s^2 base excitation per cubic centimetre (cm^3) of VEH, has been used. A parametric study about the maximum MSAPD as a function of $k^2 Q_m$ for different mass ratios (for a VEH with $f=46$ Hz, $Q_m=25$ and $\rho \approx 7840$ kg/m^3) is given in **Fig 1**. The results show that, for different values of $k^2 Q_m$, mass ratio linearly affects the maximum power density. EMCC only affects the maximum MSAPD when the value of $k^2 Q_m$ is smaller than 2. Therefore, using mass ratio and EMCC can directly determine the modal structural and electromechanical performance of VEHs, respectively.

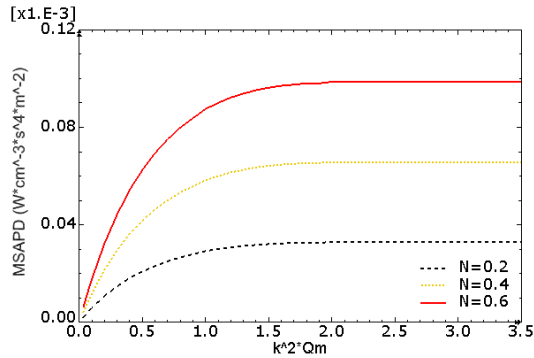


Fig 1: Parametric study of maximum MSAPD as function of $k^2 Q_m$ for different mass ratio N

For a harmonic base motion, the motion and electrical governing equations for lumped SDOF system are:

$$\begin{cases} m_m \ddot{z} + c_m \dot{z} + k_m z - \alpha v = F_m \\ C_p \dot{v} + \frac{v}{R_l} - \alpha \dot{z} = 0 \end{cases} \quad (9)$$

where z is the relative displacement related to the base motion y ; m_m , c_m and k_m are the generalized modal mass, damping coefficient and stiffness, respectively; $F_m = -\gamma m_m \ddot{y}$ is the corrected lumped forcing function; $\alpha = \chi \sqrt{m}$ is the lumped coupling factor and EMCC $k^2 = \alpha^2 / (k_m C_p + \alpha^2)$. Using

Guyomar's assumption [17], when $k^2 Q_m$ is large enough, the maximum power output is only affected the mechanical characteristics and the maximum power of the r^{th} mode can be rewritten as:

$$P_{max} = \frac{F_{mr}^2}{8c_{mr}} = \frac{\gamma_r^2 m_{mr}}{16\zeta_r \omega_r} \dot{y}^2 = \frac{m_{er}}{16\zeta_r \omega_r} \dot{y}^2 \quad (10)$$

where m_e is called the effective mass which represents the mass participating in the forcing function and motion and the sum of the effective masses for all modes is the total mass M of the whole model [16]:

$$m_{er} = \gamma_r^2 m_{mr}; \quad \sum_{r=1}^{\infty} m_{er} = M \quad (11)$$

Then, a modal structural criterion which is termed mass ratio is introduced as:

$$N_r = \frac{m_{er}}{M} = \frac{\gamma_r^2 m_{mr}}{M} \quad (12)$$

The maximum MSAPD can be written as:

$$MSAPD_{max} = \frac{N_r \rho}{16\xi_r \omega_r} * 10^{-6} (W s^4 / cm^3 m^2) \quad (13)$$

The mass ratio N is the percentage ratio of the effective mass to the total mass, and the sum of mass ratios of all modes equals 1 ($N \leq 1$). It represents how much mass of each mode effectively participates in the overall motion and linearly affects the power density. Apparently, if one mode has too large mass ratio, the remaining modes have small mass ratios. It should be noted that the generalized modal mass m_m in this paper is called effective mass by Erturk and Inman [15]. Multi-resonance VEHs should have close resonance frequencies and considerable power output in multiple modes. By FE modal analysis, ω_r , m_m and the modal participation factor γ can be easily derived. The design strategy uses mass ratio and frequency ratio as the first filter to select the VEH configurations which have close resonances and favourable values of mass ratio. These selected configurations have optimal or near-optimal structural broadband performance. Then, a steady-state analysis is carried out at the resonance frequencies of these selected configurations. With the displacements and the current data derived from FE analysis, EMCC can be easily derived using Eq.8. The optimal power output of the configurations with relatively strong EMCC will be derived eventually using DPM, and these configurations will have much better broadband performance than the remaining configurations. The flow chart of the design strategy is given by **Fig 2**.

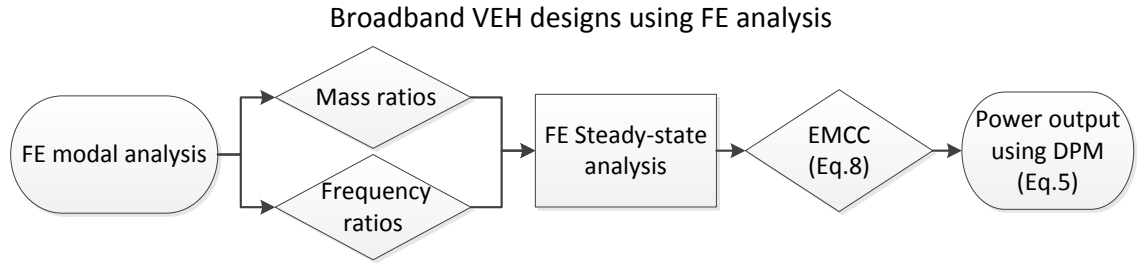


Fig 2: Flow charts of the broadband VEH design strategy using FEA software

4. Design of tapered two-layer VEHs

4.1 Two-layer, one-mass tapered VEH

In this section, the tapered two-layer VEHs with one extra mass is developed. **Fig 3** illustrates a two-layer CTC VEH *CTC3-IMP0*. The two-layer tapered VEH consists of a base layer CTC beam and an upper beam CTC beam. The piezoelectric layer is bonded on the base beam near the clamped end. The dimensions of the tapered two-layer VEHs are given in **Table 1**. In particular, the dimensions of the base and upper layers are same. A CTC VEH has a wider clamped end and a narrower free tip while a DTC VEH has a narrower clamped end and a wider free tip. The free tip to clamped end taper ratio is altered from 1/4 (CTC) to 4 (DTC) while the sum of the two widths is fixed to 50mm. The surface of the piezoelectric layer is fixed at 6.25 cm². Therefore, DTC and CTC VEHs have the same volume (ignored the clamped area) and the same piezoelectric coverage. The material properties in the FEA simulation are given in **Table 2**.

Table 1: Dimensions of tapered two-layer VEHs

Base/ upper layer length/ thickness	100/ 1 mm	
Sum of the two widths	50 mm	
Taper ratio (Free tip to clamped end)	CTC4	1/4
	CTC3	1/3
	CTC2	1/2
	RC	1
	DTC2	2
	DTC3	3
	DTC4	4
Thickness of piezoelectric layer	0.5 mm	
Surface of piezoelectric layer	6.25 cm ²	
Mass length/ width/ thickness	10/ 25/ 10 mm	

Table 2: Materials properties

Piezoelectric materials	PZT-5A*
Density of piezoelectric layer	7750 kg/m ³ *
Clamped dielectric constant ϵ_{33}^s	7.349x10 ⁻⁹ F/m*
Piezoelectric layer	60.9x10 ⁹ N/m ² *
Young's modulus	
Piezoelectric constant e_{31}	-5.4 C/m ² *
Transverse coupling factor k_{31}	0.344
Density of structural layer/ mass	7850 kg/m ³
Structural layer/ mass	200x10 ⁹ N/m ²
Young's modulus	

*PZT-5A: Morgan Technical Ceramics standard

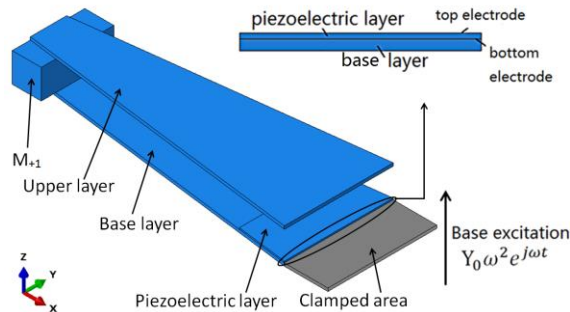


Fig 3: Structure of two-layer tapered VEH; two-layer with one mass *CTC3-IMP0*

The masses, which also serve as spacers, can be located at different positions along the length of the beam in order to tune the resonance frequencies. Since the lengths of the base and upper layers are both 100 mm and the length of the mass is 10 mm, the mass positions are divided into ten parts from the free tip to the clamped end of the base layer, and they are identified by a number from 0 to 9 as shown in **Fig 4**. The mass positions are designated as PMN , where M and N denote the positions of masses M_{+1} and M_{+2} . For example, the mass positions are $P0$ in **Fig 3(b)** and $P07$ in **Fig 4**. The CTC and DTC VEH designations are structured as “Taper ratio, number of masses (1M or 2M) and mass positions”, e.g., $CTC3-IMP0$ (see **Fig 3**) and $DTC3-2MP09$ (see **Fig 7**).

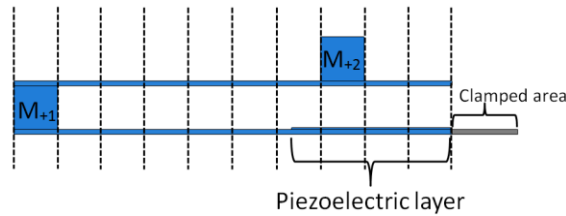


Fig 4: Numbering of mass positions; $P07$: the position of M_{+1} is 0 and M_{+2} is 7.

For the two-layer, one-mass VEH, since the area near the clamped end has been occupied by the piezoelectric layer, the position of M_{+1} is only varied from 0 to 5. **Fig 5(a)** and **5(b)** show the contours of the natural frequencies of the first and second modes, respectively. When M_{+1} is moved from 0 to 5, the VEH generates higher natural frequencies. **Fig 5(c)**, **5(d)** and **5(e)** show the frequency ratio f_2/f_1 , mass ratio N_1 and N_2 , respectively. The results show that, when N_1 is too large, N_2 becomes too small, and DTC models normally have large N_1 but small N_2 . The CTC models with mass position 0 to 2 can generate close natural frequencies in the first two modes. Based on the design strategy, frequency ratio and mass ratio are used as two filters, and the screening criteria are specified as frequency ratios < 2 and mass ratios > 0.1 . By means of these screening criteria, the number of VEH configurations is reduced from 35 to 9. The selected configurations are located in the shaded area of **Fig 5(f)**. The results show that, except for $CTC4-IMP0$ which has too small N_1 , CTC models with mass position $P0$ to $P2$ have optimal structural broadband performance.

Table 2 shows the modal performance of the two-layer, one-mass tapered VEHs with mass positions $P0$ including the mass ratio, frequency ratio and EMCC. Apparently, DTC models have large N_1 and k_1 while their N_2 and k_2 are small. When the taper ratio is decreased from 4 to $1/4$, N_1 and k_1 are both decreased while N_2 and k_2 are both increased, and f_2/f_1 is decreased. **Fig 6** shows the MSAPD FRFs with optimal loads for these configurations. $CTC4-IMP0$ has close resonance frequencies but the peak value of the MSAPD of the first mode is too small. The peak values of MSAPD of DTC models in the second modes are also too small and the large gap between the two modes generates a deeper trough

around the anti-resonance area, which also significantly affects the broadband performance. To conclude, for tapered two-layer VEHs with one mass, CTC models are able to provide better broadband power output than RC and DTC models.

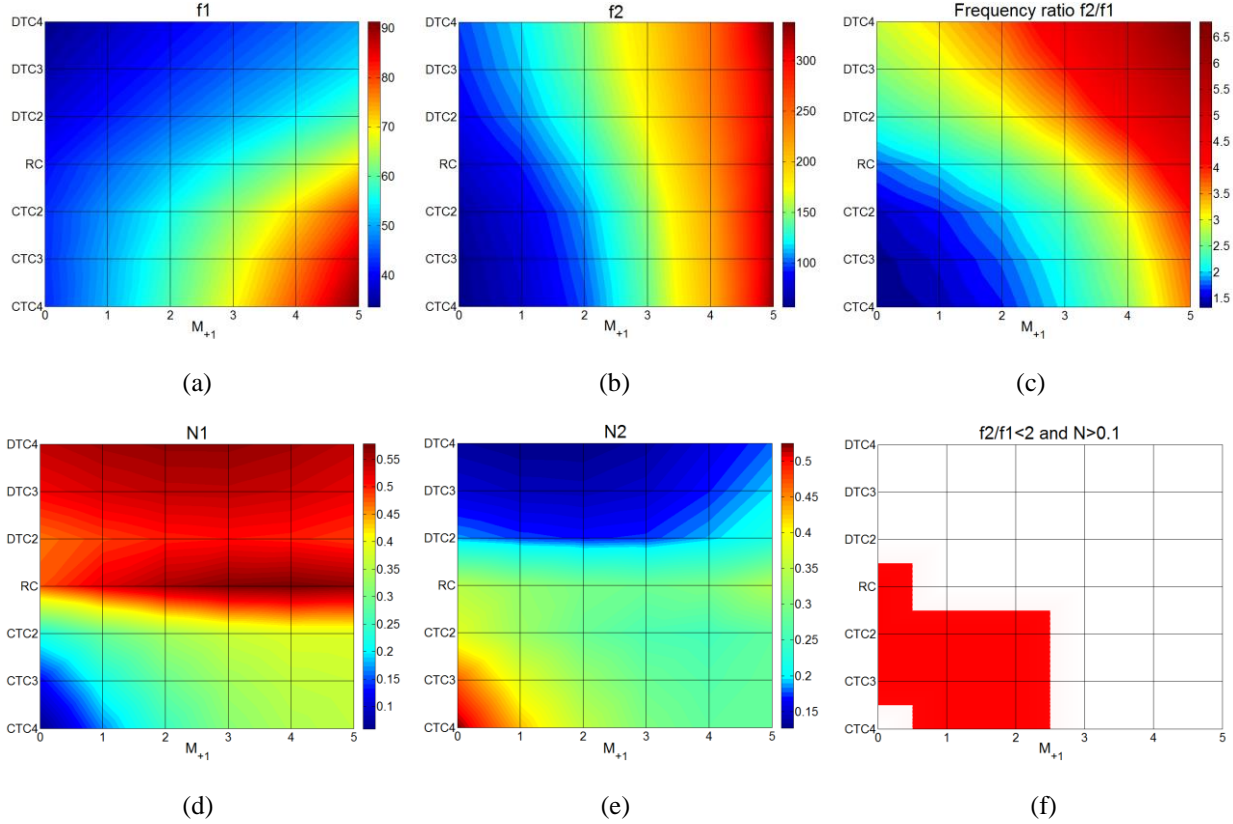


Fig 5: Modal structural performance and screening results of tapered two-layer VEH with one mass. (a)-(b): f_1 and f_2 ; (c) frequency ratio f_2/f_1 ; (d)-(e): N_1 and N_2 ; (f) screening results when $f_2/f_1 < 2$ and $N > 0.1$.

Table 2: Modal performance of one mass tapered VEHs with mass positions P0

Models	f_1	f_2	N_1	N_2	f_2/f_1	k_1	k_2
<i>CTC4</i>	42.47	56.31	7.8%	69.3%	1.33	0.119	0.153
<i>CTC3</i>	42.89	58.57	16.3%	61.7%	1.37	0.145	0.143
<i>CTC2</i>	42.66	62.76	29.4%	50.1%	1.47	0.175	0.129
<i>RC</i>	40.84	72.96	47.9%	34.6%	1.79	0.218	0.112
<i>DTC2</i>	37.79	84.87	61.6%	24.5%	2.23	0.252	0.093
<i>DTC3</i>	35.46	91.81	67.9%	20.2%	2.59	0.261	0.073
<i>DTC4</i>	33.62	96.27	71.6%	17.7%	2.86	0.261	0.056

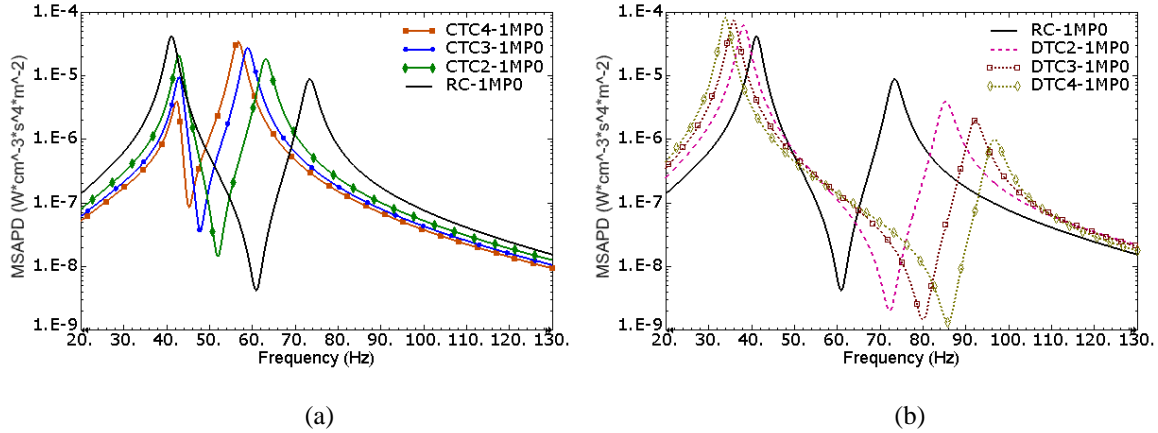


Fig 6: MSAPD FRFs of two-layer, one-mass VEH with mass position P0; (a): CTC models; (b) DTC models.

4.2 Two-layer, two-mass tapered VEH

In this section, the tapered two-layer VEHs with two masses is developed. **Fig 7** illustrates a typical divergent model *DTC3-2MP09*. The second mass M_{+2} is attached to the upper layer DTC beam. In this case, the position of M_{+1} is varied from 0 to 5 and the position of M_{+2} is varied from 0 to 9. Then, for 7 taper ratios, the total number of configurations with different mass positions and different taper ratios are 420. For such a large number of configurations, the use of the design strategy to exclude the unwanted configurations with poor structural performance becomes far more efficient. **Fig 8** shows the modal structural performance using 3D slices. In particular, **Fig 8(a)** and **8(b)** show the natural frequencies of the first and second mode, respectively. **Fig 8(c)**, **8(d)** and **8(e)** show the frequency ratio f_2/f_1 , mass ratio N_1 and N_2 , respectively.

In this case, two sets of screening criteria are specified, namely (a) frequency ratios < 2 and mass ratios > 0.05 , (b) frequency ratios < 1.5 and mass ratios > 0.2 . The results of applying these two sets of screening criteria are shown by the shaded regions of **Fig 9(a)** and **9(b)**. Obviously, the second set of screening criteria is stricter than the first set of screening criteria. The numbers of the selected configurations using the first and second sets of screening criteria are 106 and 19, respectively, as shown in **Table 3**. These selected configurations using the second set of screening criteria have much better structural performance for broadband power output. Compared Fig 9(a) with Fig 5(f), it can be deduced that 35 two-mass DTC models meet the screening criteria whereas none of the one-mass DTC models meet these same criteria. Therefore, DTC models with two masses can generate a good structural broadband performance in comparison with DTC models with one mass. However, CTC models still contain more preferred configurations than DTC, and the smaller taper ratios CTC3 and CTC4 models show the best structural performance, as can be clearly seen in Table 3. When the position of M_{+1} is 0, the configurations can easily generate good structural broadband performance. Interestingly, for the stricter

screening results, when the taper ratio is decreased from 4 to 1/4, the optimal or near optimal mass positions are also altered from P08 to P02.

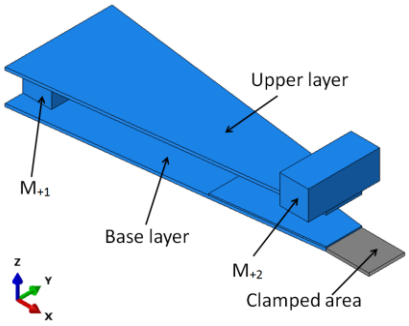


Fig 7: Tapered two-layer VEHs with two masses: model *DTC3-2MP09*

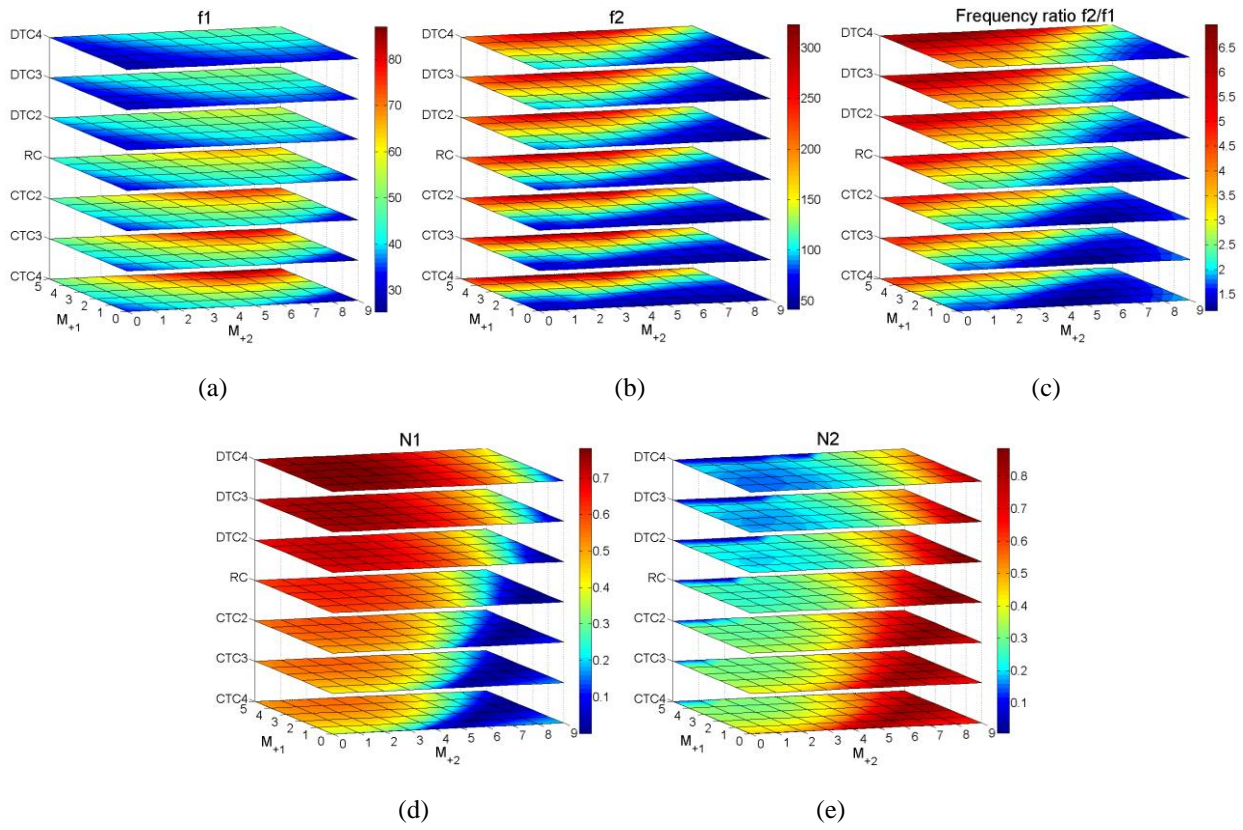


Fig 8: Modal structural performance of tapered two-layer VEH with two masses. (a)-(b): f_1 and f_2 ; (c) frequency ratio f_2/f_1 ; (d)-(e): N_1 and N_2 ;

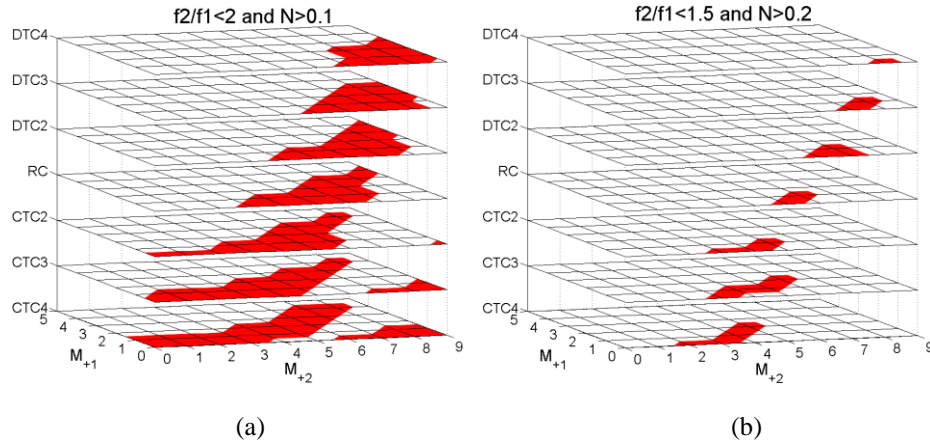


Fig 9: Screening results of tapered two-layer VEH with two masses. a) $f_2/f_1 < 2$ and $N > 0.1$; (b) $f_2/f_1 < 1.5$ and $N > 0.2$

Table 3: Number of selected configurations which satisfy screening criteria sets 1 and 2.

Models	Taper ratio	Number of configurations	
		$f_2/f_1 < 2$	$f_2/f_1 < 1.5$
		$N > 0.1$	$N > 0.2$
<i>CTC4</i>	54.37	23	4
<i>CTC3</i>	53.47	20	4
<i>CTC2</i>	53.31	15	3
<i>RC</i>	55.25	13	2
<i>DTC2</i>	54.28	13	3
<i>DTC3</i>	49.71	12	2
<i>DTC4</i>	44.93	10	1
Total		106	19

Table 4 shows the modal performance of some selected VEHs with optimal performance. In particular, DTC models still generate larger k_1 than CTC models, and k_2 are always smaller than k_1 for all models. **Fig 10(a)** and **10(b)** show the MSAPD FRFs with optimal loads for these configurations. The FRFs of the CTC models are very close to these of the RC model. The FRFs of DTC models are slightly shifted to a lower frequency when the taper ratio is increased.

Table 5 and **Fig 10 (c)** show the modal performance and MSAPD FRFs with optimal loads of some typical models with mass position P09. *CTC2-2MP09* and *CTC4-2MP09* have met the first set of screening criteria. However, due to the very small k_1 in these models, the amplitudes of the MSAPD around the first mode are significantly reduced. For the CTC models with mass position P09, the

anti-resonance trough between the first two modes has disappeared. This is because the phase of the current has changed. Besides, *DTC2-2MP09* has very small N1 and the peak of the MSAPD in the first mode has almost disappeared. In fact, there is a regular pattern that the mode has a too large or a too small mass ratio will normally have strong or weak EMCC. **Fig 11** shows the contours of the variations of the mass ratio and EMCC of the configurations with mass positions from P00 to P09. Apparently, the distributions of the mass ratio and EMCC in each mode have a fairly close agreement. In general, the models with evenly distributed mass ratios in multi-modes normally have acceptable EMCC, and these models eventually generate relatively large power output in multi-modes. If these modes are close enough, the broadband power output can be achieved. Furthermore, in real applications, when the input becomes large, the dominant vibration mode, which has large mass ratio and strong EMCC, can actually generate very large strain. This could reduce the lifecycle of the VEH or even damage the VEH.

Table 4: Modal performance of some selected two-layer, two-mass tapered VEHs

Models	f1	f2	N1	N2	f2/f1	k1	k2
<i>CTC4-2MP02</i>	38.33	54.37	31.8%	51.1%	1.42	0.160	0.118
<i>CTC3-2MP03</i>	40.12	53.47	31.7%	51.8%	1.33	0.170	0.117
<i>CTC2-2MP04</i>	40.84	53.31	32.6%	52.0%	1.31	0.185	0.117
<i>RC-2MP05</i>	39.62	55.25	39.2%	47.7%	1.39	0.219	0.113
<i>DTC2-2MP06</i>	36.94	54.28	42.6%	46.7%	1.47	0.248	0.103
<i>DTC3-2MP07</i>	34.55	49.71	36.7%	54.0%	1.44	0.251	0.103
<i>DTC4-2MP08</i>	32.17	44.93	25.4%	65.9%	1.40	0.242	0.116

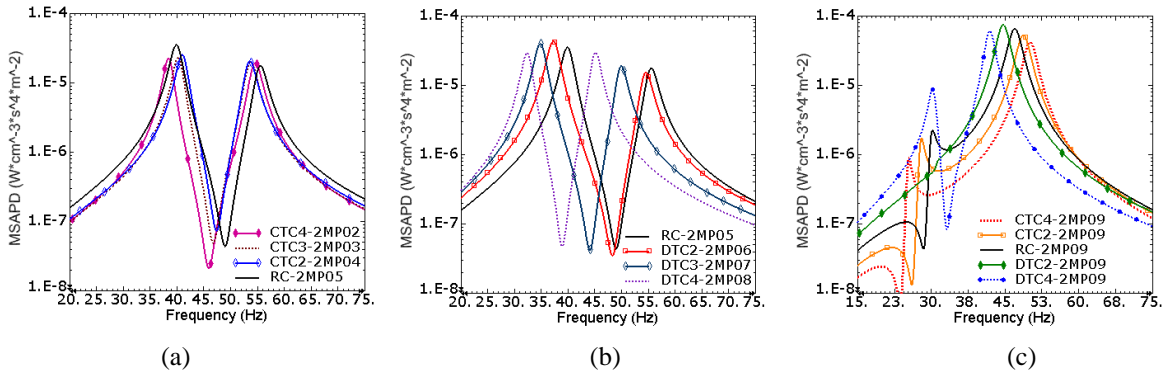


Fig 10: MSAPD FRFs of tapered two-layer VEH with two masses; (a): typical CTC models; (b): typical DTC models; (c): models with mass position P09

Table 5: Modal performance of two masses tapered VEHS with mass position P09

Models	f1	f2	N1	N2	f2/f1	k1	k2
<i>CTC4</i>	25.30	49.70	19.9%	62.3%	1.96	0.026	0.190
<i>CTC2</i>	27.80	48.29	12.7%	71.2%	1.74	0.046	0.208
<i>RC</i>	29.93	46.50	4.5%	81.6%	1.55	0.084	0.226
<i>DTC2</i>	31.01	44.19	0.01%	88.7%	1.43	0.025	0.223
<i>DTC4</i>	30.32	41.68	7.3%	83.8%	1.37	0.206	0.166

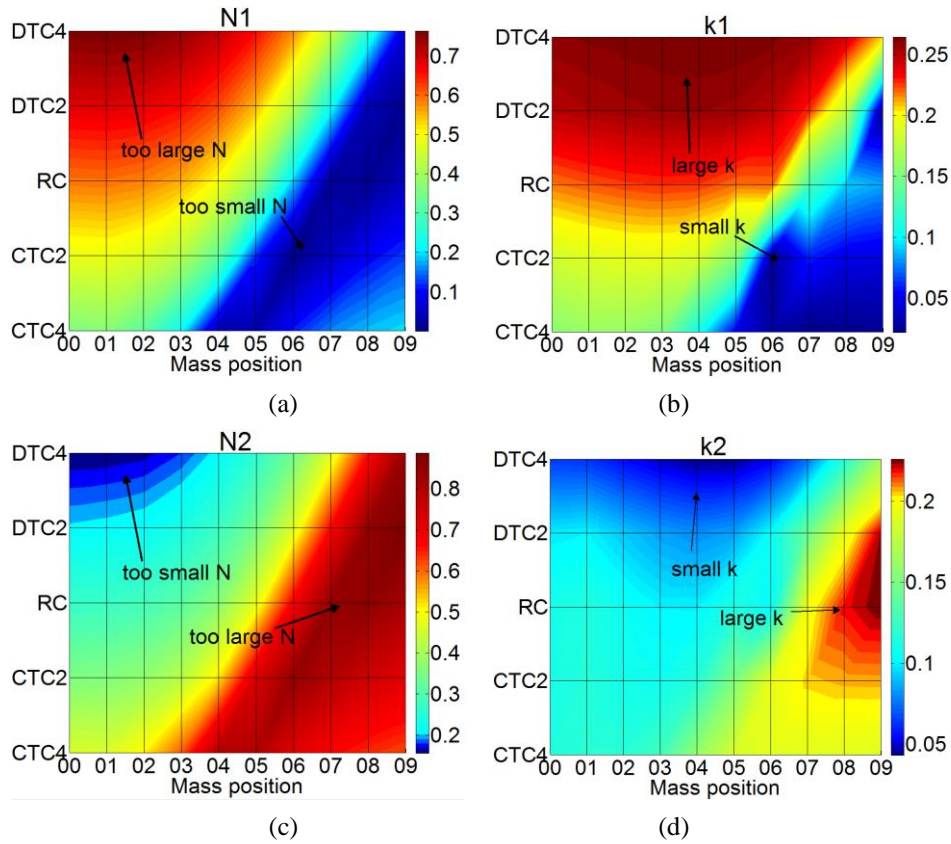


Fig 11: Mass ratio and EMCC of the configurations with mass positions from P00 to P09. (a)-(b): N1 and k1; (c)-(d): N2 and k2.

In all the above cases, the surface area of the piezoelectric is fixed at 6.25 cm^2 , which gives partial piezoelectric coverage. In **Table 6**, the modal performance data of typical tapered models with partial and full piezoelectric coverage are given. For models with full coverage, because the 10 mm free tip has been occupied by M_{+1} , the length of the piezoelectric layer has been increased to 90 mm in DTC and CTC models (*PLmax*). The results show that, for DTC models, there are very slight variations in the values of k1 and k2 between the models with partial and full coverage. For CTC models, especially *CTC4-2MP02-PLmax*, k1 is increased significantly while k2 is decreased significantly. **Fig 12** illustrates

the first two mode shapes and the corresponding electric displacement distributions of model *CTC4-2MP02-PLmax* and *DTC4-2MP08-PLmax*. The lengths and directions of the vector arrows on the beam indicate the distributed values and directions of the electric displacement. When the base is fully covered, the strain distributions along the length of the base cause the electric displacement along the thickness to be partly reversed. After the self-cancellation, the phase of the total current in the second mode is changed and the sign of the coupling term becomes negative (see **Table 5**). However, as the taper ratio in *CTC4-2MP02-PLmax* is too small, the area near the free tip with reversed current becomes smaller. This eventually causes a very strong cancellation in mode 2.

Table 6: Comparisons of the modal performance of typical models with partial and full piezoelectric coverage

Models	f2/f1	N1 (%)	N2 (%)	k1	k2	χ_1 (*10 ⁻³)	χ_2 (*10 ⁻³)
DTC4-2MP08	1.40	25.4	65.9	0.242	0.116	4.83	3.16
DTC4-2MP08-PLmax	1.34	22.6	66.6	0.238	0.118	9.08	-6.48
DTC2-2MP07	1.39	39.2	47.7	0.227	0.144	5.09	4.28
DTC2-2MP07-PLmax	1.48	42.5	42.1	0.266	0.104	12.32	-6.35
CTC2-2MP03	1.36	45.1	43.8	0.192	0.107	4.64	3.77
CTC2-2MP03-PLmax	1.39	57.0	29.2	0.304	0.078	17.63	-6.05
CTC4-2MP02	1.40	54.5	28.9	0.160	0.118	3.74	3.89
CTC4-2MP02-PLmax	1.28	38.9	42.0	0.317	0.004	18.97	0.27

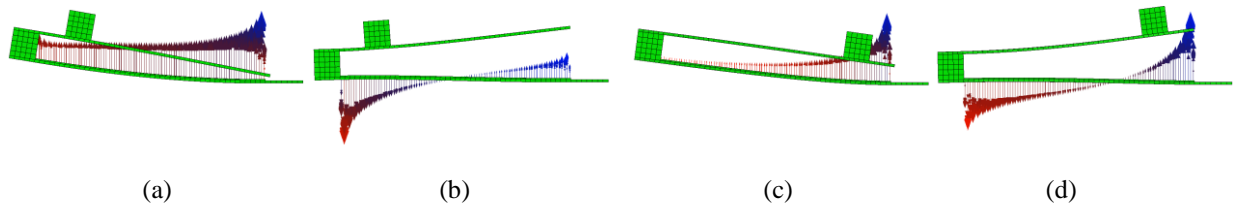


Fig 12: Electrical displacement mode shapes. (a)-(b): mode 1 and 2 of *CTC4-2MP02-PLmax*; (c)-(d): mode 1 and 2 of *DTC4-2MP08-PLmax*

Fig 13 shows the corresponding MSAPD FRFs of the models with fully covered piezoelectric layer. Except for *CTC4-2MP02-PLmax*, the anti-resonance trough between mode 1 and mode 2 is basically eliminated in the remaining models. This phenomenon can effectively enhance the broadband performance of VEHs.

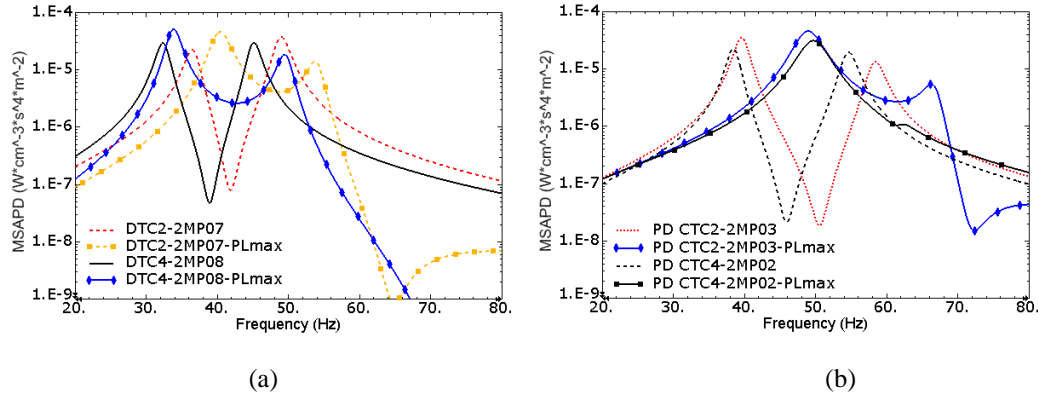


Fig 13: MSAPD FRFs of typical tapered VEH with full piezoelectric coverage; (a) DTC models; (b) CTC models.

4.3 Effect of structural damping

In all the above cases, the damping ratio was fixed to 0.02. In fact, the value of the damping ratio can directly affect the coupling criterion $k^2 Q_M$ and the mechanical response simultaneously. Therefore, the effects of different levels of structural damping have been analysed in this section. In **Fig 14**, damping ratio is varied from 0.002 to 0.05 in *DTC2-2MP07* and the corresponding full piezoelectric coverage model. The figure shows that, the use of smaller damping ratio generates sharper responses not only around the resonances, but also around the anti-resonances. However, the magnitude of the MSAPD off the resonance peak and the anti-resonance troughs cannot be significantly affected by changing the damping ratio. The models without anti-resonance troughs between two modes have effectively enhanced broadband performance.

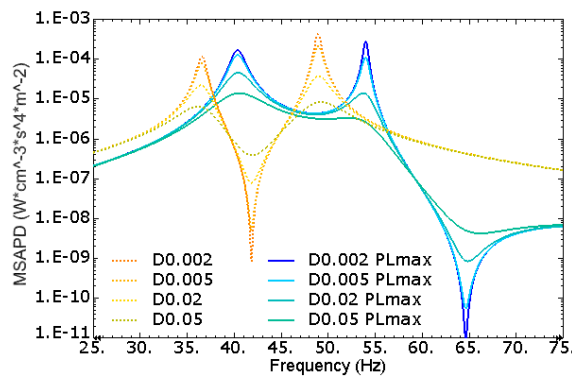


Fig 14: MSAPD FRFs of *DTC2-2MP07* with different damping ratios.

5. CONCLUSIONS

This paper has developed CTC and DTC two-layer stacked VEHS to achieve broadband power output in

the first two modes by varying the mass positions. For the configuration with one mass, the CTC model can successfully achieve broadband power output while the DTC model fails to provide close resonance frequencies. For the configuration with two masses, the broadband performances of the DTC models are significantly improved. Furthermore, except for the CTC model with too small taper ratio, when the base layer is fully covered with the piezoelectric layer, the anti-resonance between two modes can be eliminated. Besides, the power density off the resonance cannot be significantly affected by changing the damping ratio. The results also indicate that the mode with too large or too small mass ratio will normally generate strong or weak EMCC. The VEHs with evenly distributed mass ratios normally generate acceptable EMCC in multi-modes. Therefore, to design a multi-resonance broadband VEH, using the introduced design strategy to select the VEH configurations with close resonances and acceptable values of mass ratio initially can be very effective and convenient.

REFERENCES

- [1] N. S. Hudak and G. G. Amatuucci, "Small-scale energy harvesting through thermoelectric, vibration, and radio frequency power conversion," *Journal of Applied Physics*, 103(10), 101301, 2008.
- [2] S.R. Anton, and H. A. Sodano, "A review of power harvesting using piezoelectric materials (2003-2006)," *Smart Materials and Structures*, 16(3), R1, 2007.
- [3] L. Tang, Y. Yang, and C. K. Soh, "Toward broadband vibration-based energy harvesting," *Intell. Mater. Syst. Struct.*, 21(18), 1867-1897, 2010.
- [4] M. Ferrari, V. Ferrari, M. Guizzetti, D. Marioli, and A. Taroni, "Piezoelectric multifrequency energy converter for power harvesting in autonomous microsystems," *Sensors and Actuators A: Physical*, 142(1), 329-335, 2008.
- [5] S.Qi, R.Shuttleworth, S.O.Oyadiji and J.Wright, Design of a multiresonant beam for broadband piezoelectric energy harvesting. *Smart Materials and Structures* (2010) 19: 094009.
- [6] W. Wang, T. Yang, X. Chen and X.Yao, "Vibration energy harvesting using a piezoelectric circular diaphragm array," *IEEE Trans. Ultrason. Ferroelectr. Freq. Control*, 59(9), 2022-2026, 2012
- [7] M. F. Lumentut, L. A. Francis and I. M. Howard, "Analytical techniques for broadband multielectromechanical piezoelectric bimorph beams with multifrequency power harvesting," *IEEE Trans. Ultrason. Ferroelectr. Freq. Control*, 59(11), 2555-2568, 2012
- [8] Zhou, W., Penamalli, G. R., and Zuo, L., "An efficient vibration energy harvester with a multi-mode dynamic magnifier," *Smart Materials and Structures*, 21(1), 015014, 2012.
- [9] Ou, Q., Chen, X., Gutschmidt, S., Wood, A., Leigh, N., and Arrieta, A. F., "An experimentally validated double-mass piezoelectric cantilever model for broadband vibration-based energy harvesting," *Intell. Mater. Syst. Struct.*, 23(2), 117-126, 2012.
- [10] A. Erturk, J. Hoffmann and D.J. Inman, "Modeling of piezoelectric energy harvesting from an L-shaped beam mass structure with an application to UAVs," *Intell. Mater. Syst. Struct.* 20: 529-544, 2009.
- [11] X. Xiong and S. O. Oyadiji, "Optimal design of two-layer vibration energy harvesters using a modal approach,"

Smart Materials and Structures, 23(3), 035005, 2014.

[12] S. Roundy, E. S. Leland, J. Baker, E. Carleton, E. Reilly, E. Lai, B. Otis, J. M. Rabaey, P. K. Wright and V. Sundararajan, "Improving Power Output for Vibration-based Energy Scavengers," IEEE Pervasive Computing, 4:28-36, 2005.

[13] S. Mehraeen, S. Jagannathan and K. A. Corzine, "Energy harvesting from vibration with alternate scavenging circuitry and tapered cantilever beam," Industrial Electronics, IEEE Transactions on, 57(3), 820-830, 2010.

[14] A. Erturk, and D. J. Inman, "A Distributed Parameter Electromechanical Model for Cantilevered Piezoelectric Energy Harvesters," Journal of Vibration and Acoustics, 130(4), 041002, 2008.

[15] A. Erturk, and D. J. Inman, "On Mechanical Modeling of Cantilevered Piezoelectric Vibration Energy Harvesters," Intell. Mater. Syst. Struct., 19, 1311, 2008.

[16] SIMULIA Corp., "Abaqus Theory Manual in ABAQUS 6.10 Documentations," www.simulia.com, 2010.

[17] D. Guyomar, G. Sebald, S. Pruvost, M. Lallart, A. Khodayari and C. Richard, "Energy harvesting from ambient vibrations and heat," Intell. Mater. Syst. Struct., 20(5), 609–624, 2009.

[18] X. Xiong and S. O. Oyadiji, "Modal electromechanical optimization of cantilevered piezoelectric vibration energy harvesters by geometric variation," Intell. Mater. Syst. Struct., DOI:1045389X13502872, 2013.

CHAPTER 8 A GENERAL MODAL APPROACH FOR THE DEVELOPMENT OF OPTIMAL MULTI-LAYER STACKED VIBRATION ENERGY HARVESTERS

Xingyu Xiong and S Olutunde Oyadiji

Journal of Sound and Vibration 333 (21), 5386-5411, 2014



Contents lists available at ScienceDirect

Journal of Sound and Vibration

journal homepage: www.elsevier.com/locate/jsvi



A general modal approach for the development of optimal multi-layer stacked vibration energy harvesters



Xingyu Xiong, S. Olutunde Oyadiji*

School of Mechanical, Aerospace and Civil Engineering, The University of Manchester, Manchester M13 9PL, UK

ARTICLE INFO

Article history:

Received 30 October 2013

Received in revised form

28 April 2014

Accepted 21 May 2014

Handling Editor: M.P. Cartmell

Available online 20 June 2014

ABSTRACT

Piezoelectric vibration energy harvesters with multi-layer stacked structures have been developed. They consist of multi-layer beams, of zigzag configurations, with rigid masses attached between the beams. The rigid masses, which also serve as spacers, are attached to each layer to tune the frequencies of the harvester. Close resonance frequencies and considerable power output can be achieved in multiple modes by varying the positions of the masses. A modal approach is introduced to determine the modal performance conveniently using the mass ratio and the modal electromechanical coupling coefficient, and the required modal parameters are derived using the finite element method. Mass ratio represents the influence of modal mechanical behaviour on the power density. Since the modes with larger mass ratios cause the remaining modes to have smaller mass ratios and lower power densities, a screening process using the modal approach is developed to determine the optimal or near-optimal performance of the harvesters when altering mass positions. This procedure obviates the need for full analysis by pre-selecting the harvester configurations with close resonances and favourable values of mass ratio initially. Furthermore, the multi-layer stacked designs using the modal approach can be used to develop harvesters with different sizes with the power ranging from microwatts to milliwatts.

© 2014 Elsevier Ltd. All rights reserved.

1. Introduction

In the last decade, self-powered, batteryless wireless sensors for preventive maintenance have attracted considerable attention in the research field, which has led to a need for the investigation of small-scale ambient energy harvesting. The development of vibration energy harvesters using piezoelectric materials has become an attention-grabbing topic recently [1]. Resonances, especially in the fundamental mode, have been considered as an effective way of energy conversion from the mechanical domain to the electrical domain. However, the resonance frequencies of higher modes are normally far away from the first mode, and the higher modes generate much lower level of power output compared with the fundamental mode. In addition, in real applications, the environmental vibration sources are normally random within a lower frequency range. Therefore, the performance of conventional harvester designs is limited since only the fundamental mode is effectively used. In particular, conventional harvester designs have poor off-resonance performance. To overcome this limitation, different strategies have been proposed. This includes incorporating broadband power output capability in

* Corresponding author. Tel.: +44 161 275 4348; fax: +44 161 275 3844.

E-mail address: s.o.oyadiji@manchester.ac.uk (S.O. Oyadiji).

harvesters [2], for example by resonance tuning technique [3,4], design of nonlinear harvesters with magnets [5–7], and multi-resonance designs.

For the multi-resonance systems, harvesters with array of beams have been investigated by some researchers. Ferrari et al. [8] electrically connected three cantilevered harvesters together and tuned the resonance frequencies by altering the lengths of beams and attaching different tip masses. Qi et al. [9] physically combined an array of cantilevered beams to a clamped–clamped beam in order to develop a multi-resonance system. In their design, the resonances are generated by both the common base and an array of branches while the piezoelectric material only covered the common base. On the one hand, structures with array of beams can generate very close resonance frequencies. On the other hand, normally just one part of the harvester is active for each resonance, and the rest are almost silent (inactive). Thus, since the piezoelectric material cannot be effectively used, the electro-mechanical coupling becomes weak, and the power density is also decreased significantly.

Moreover, by attaching two or more masses on one beam produces a multi-resonance system. Lee et al. [10], Ou et al. [11] and Zhou et al. [12] both developed dual mass harvesters. In their designs, two masses are attached on a cantilevered beam. One mass is attached to the middle of the beam, which segments the beam into two parts. The other mass is attached to the free tip. Apparently, the model can generate two resonances. However, in order to generate enough close resonances, the mass attached to the middle of the beam needs to be much heavier than the mass attached to the free tip. Wu et al. [13] developed a modified dual mass harvester. They divided a cantilevered beam into two parallel narrower cantilevered beams with a gap between them. An additional beam is clamped to the free ends of the two original beams in the gap and the free end pointing to the clamped ends of the original beams. The modified model can generate much closer resonances with lighter masses. Chen et al. [14] designed a multi-mass system with up to 9 masses attached on a cantilevered beam, which separated the beam into 10 segments. Then, a wider frequency range of broadband power output can be achieved. However, the design has limited applicability since the beam is very thin but also too long. Besides, only using heavier masses can effectively decrease the central resonance frequency and expand the frequency band. In addition, the power density of the harvester with 9 masses is significantly reduced. The optimal power is only increased slightly in comparison with a cantilevered harvester of length equal to the length of a segment of the 9-mass cantilevered beam but without additional mass.

There are some other harvester designs with multi-resonances that have been reported. An L-shaped harvester has been developed by Erturk et al. [15]. In their design, the resonance frequency of the 2nd mode can be two times higher than the resonance frequency of the 1st mode. A zigzag harvester has been developed by Karami and Inman [16]. The model is clamped at one end and has up to 11 sub-branches. However, the resonances are far away from each other, and a large number of the modes are barely active, which limit the capability for broadband power output.

In general, a good multi-resonance design should achieve not only close resonance frequencies but also considerable power output in each mode. However, too many resonances can also significantly affect the power density. In this paper, harvesters with up to 5 layers of stacked beam structures have been developed. The design integrates the advantages from the array of beams and dual-mass models simultaneously. The model can easily control the resonances and the level of power density by relocating the masses, and provide broadband power output in a lower frequency range. Particularly, a modal approach is introduced to determine the resonance performance of the multi-resonance models intuitively. Then, a screening process is developed using the modal approach, which simplifies the optimization of designs and avoids operating full analyses at the first stage. This paper contains six sections: Section 2 is on the introduction of a general distributed electromechanical parameter model and the determination of the parameters using finite element analysis (FEA) software; Section 3 is on the use of mass ratio and a modal approach to determine the performance of harvesters; Section 4 is on the implementation of a screening process for optimal designs of the multi-layer stacked harvesters; Section 5 is the analyses of the factors affecting performance of the multi-layer stacked harvesters and the concluding section is at the end of the paper.

2. Vibration energy harvesting model

The modal analysis technique can be used to represent the steady-state linear vibration response of a structure which is subjected to continuous harmonic excitation. The absolute displacement of the transverse vibration relative to the moving base of the harvester model at time t is

$$u_{\text{rel}}(t) = \sum_{r=1}^{\infty} \phi_r \eta_r(t) \quad (1)$$

where ϕ_r and $\eta_r(t)$ are the mass-normalised eigenfunction and the corresponding modal coordinates of the r th mode of the harvester, respectively. The governing equations of the vibration modal response and electrical behaviour of the harvester model with a resistive load are given as [17,18]

$$\frac{d^2 \eta_r(t)}{dt^2} + 2\zeta_r \omega_r \frac{d\eta_r(t)}{dt} + \omega_r^2 \eta_r(t) + \chi_r v(t) = F_r(t) \quad (2)$$

$$\frac{v(t)}{R_l} + C_p \frac{dv(t)}{dt} - \sum_{r=1}^{\infty} \chi_r \frac{d\eta_r(t)}{dt} = 0 \quad (3)$$

where v is the generated voltage given by the uniform electric field E over the thickness of the piezoelectric layer; ζ_r , ω_r , χ_r and F_r are the damping ratio, angular resonance frequency, modal electromechanical coupling term and modal mechanical forcing term, respectively; C_p is the piezoelectric capacitance and R_l is the resistive load. The steady-state solution of Eq. (2) is

$$\eta_r(t) = \frac{F_r - \chi_r v}{\omega_r^2 - \omega^2 + j2\zeta_r \omega_r \omega} e^{j\omega t} \tag{4}$$

For the harvester model which is not an uniform beam, deriving the eigenfunction ϕ_r , coupling term χ_r , and F_r is complicated. However, FEA software packages like ABAQUS and ANSYS can be used to derive those parameters conveniently. In Fig. 1, a single layer harvester model with a mass attached to the free tip is developed in ABAQUS. Table 1 gives the dimensions and material properties of the model. The piezoelectric layer is fixed near the clamped end of the beam. Using the idea of equivalent circuit method [19], by letting the applied voltage on top and bottom of the piezoelectric layer to be zero ($v = 0$), the forcing function F_r at each resonance frequency with a vertical harmonic base excitation $\ddot{u}_b = Y_0 \omega^2 e^{j\omega t}$ can be determined in the frequency domain from Eq. (4) using the absolute displacement data in the FEA results. For the r th mode:

$$F_r = (\omega_r^2 - \omega^2 + j2\zeta_r \omega_r \omega) \eta_r(j\omega_r) = 2\zeta_r \ddot{u}_{rel} \sqrt{m_{mr}} \Big|_{\omega = \omega_r} \tag{5}$$

where m_m is the generalized modal mass associated with the mode and derived from the FEA natural frequency extraction analysis. The complex current i_r generated due to base excitation (when $v = 0$) can be derived from the electric displacement D data in the FEA results. By substituting $v(t)/R_l$ with $i(t)$ in Eq. (3):

$$i_r = j\omega \chi_r \eta_r(j\omega_r) = \sum_{r=1}^{\infty} \frac{j\omega F_r \chi_r}{\omega_r^2 - \omega^2 + j2\zeta_r \omega_r \omega} \Big|_{\omega = \omega_r} \tag{6}$$

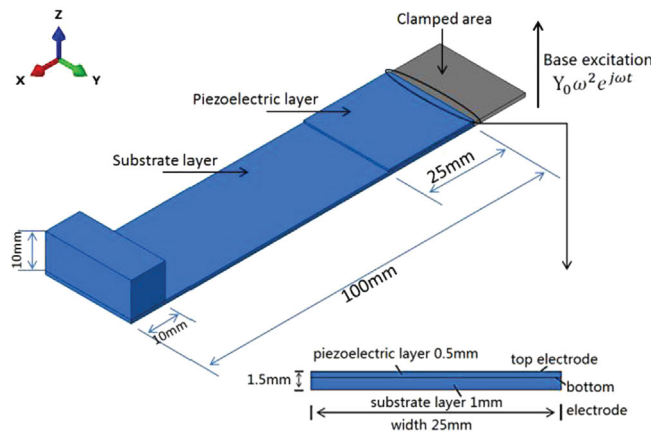


Fig. 1. Harvester model 1L1M.

Table 1
Properties of the harvester model 1L1M.

Parameters	Properties
Beam length/width/thickness	100/25/1 mm
Mass length/width/thickness	25/10/10 mm
Thickness of piezoelectric layer	0.5 mm
Length of piezoelectric layer	25 mm
Piezoelectric materials	PZT-5A ^a
Density of piezoelectric layer	7750 kg/m ^{3a}
Clamped dielectric constant ϵ_{33}^c	7.349×10^{-9} F/m ^a
Piezoelectric layer Young's modulus	60.9×10^9 N/m ^{2a}
Piezoelectric constant e_{31}	-5.4 C/m ^{2a}
Transverse coupling factor k_{31}	0.344 ^a
Density of substrate layer/mass	7850 kg/m ³
Substrate layer/mass Young's modulus	200×10^9 N/m ²
Structure damping	0.04

^a Morgan Technical Ceramics standard.

Then, the modal coupling term χ_r can be determined from Eq. (6) for multiple modes or any single mode. The voltage across R_l can be represented by [17,18]

$$v(t) = \frac{\sum_{r=1}^{\infty} (j\omega F_r \chi_r / (\omega_r^2 - \omega^2 + j2\zeta_r \omega_r \omega))}{\sum_{r=1}^{\infty} (j\omega \chi_r^2 / (\omega_r^2 - \omega^2 + j2\zeta_r \omega_r \omega)) + (1/R_l) + j\omega C_p} e^{j\omega t} \tag{7}$$

Hence, the complex power in the frequency domain is $v(j\omega)(v(j\omega)/R_l)^*$ and the average power output is $|v|^2/2R_l$ (ignore electric losses). In this paper, for the convenience of the analysis, structural damping is used and defined as 0.04 and damping ratio is constant 0.02. Indeed, the damping affects the power output significantly. Therefore, for the real applications, the damping ratio needs to be obtained experimentally.

3. Performance determination using a modal approach

3.1. A modal approach

In Section 2, the distributed parameter (electromechanical) model (DPM) is based on the Bernoulli–Euler beam assumption. However, the conventional method using DPM always requires full analysis which involves frequency-by-frequency steady-state analysis of the model in order to determine the frequency response of the output power. But the full analysis cannot be carried out to directly determine the performance of a harvester, especially the maximum power, unless a specified model has been defined. A flow chart of the conventional method is illustrated in Fig. 2(a).

Guyomar et al. [20] introduced a modal electromechanical criterion $k^2 Q_m$ to evaluate the maximum average power output by using a lumped single degree-of-freedom (sdf) model (for standard rectifier interface with no electrical losses; optimal load is matched):

$$P_{\max} = \frac{F_m^2}{2c_m} \frac{\pi k^2 Q_m}{(\pi + k^2 Q_m)^2} \quad \text{when } k^2 Q_m \leq \pi \tag{8}$$

$$P_{\max} = \frac{F_m^2}{8c_m} \quad \text{when } k^2 Q_m \geq \pi \tag{9}$$

where k is the modal electromechanical coupling coefficient (EMCC); $Q_m = 1/2\zeta$ is the quality factor; F_m and c_m are lumped mechanical force and damping coefficient, respectively. If $k^2 Q_m > \pi$, the power output given by Eq. (9) is maximum and purely mechanical. When $k^2 Q_m < \pi$, the reachable power given by Eq. (8) is always smaller than the maximum power. However, in Guyomar's work, using the lumped sdf model cannot accurately represent the modal mechanical behaviour in multiple degrees of freedom systems. Besides, the electromechanical coupling cannot be fully involved in Eqs. (8) and (9) in comparison with using DPM because the back coupling has been ignored. Erturk and Inman [21,22] introduced a correction factor γ to improve the accuracy of the sdf model. In their work, the relative motion transmissibility predicted using the sdf model with the correction factor has a very good agreement with the relative motion transmissibility predicted using the Bernoulli–Euler beam model in a wide frequency band around the fundamental resonance. In fact, the correction factor γ , which is also called the modal participation factor, indicates how strongly motion in the x -, y - or z -direction or rotation about one of these axes is represented in the eigenvector of that mode [23]. However, Erturk and Inman only analysed the purely structural responses using the correction factor; the effects on the electrical behaviour and power output have been ignored.

Xiong and Oyadiji [24] analysed the modal performance of cantilevered harvesters and considered both the corrected structural response and the electromechanical coupling. In their work, a modal structural criterion named mass ratio N was

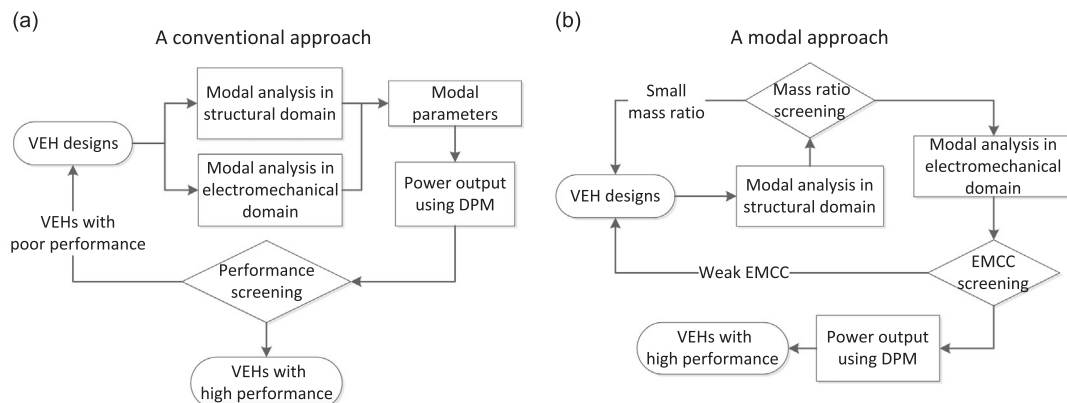


Fig. 2. Flow charts comparing (a) a conventional approach, and (b) a modal approach to determine the performance of harvesters.

introduced, which depends on the modal participation factor γ . In particular, a parametric study has been presented using DPM to determine the influences of EMCC and mass ratio on the performance around the resonance frequency. Essentially, mass ratio represents the influence of the modal mechanical behaviour on the power density directly. The expression of mass ratio will be presented in the next section.

In this paper, a general modal approach is developed to evaluate the resonance performance of harvesters conveniently. In the flow charts given by Fig. 2, the conventional approach (Fig. 2a) has been compared with the modal approach (Fig. 2b) of harvester performance evaluation. Instead of carrying out full analysis using DPM directly to determine performance of harvesters in the conventional approach, the modal approach can avoid full analysis at the first stage by using two modal criteria, namely: mass ratio and EMCC, as two assessments factors.

3.2. Mass ratio and EMCC

For harmonic base excitation, the motion and electrical governing equations of a harvester using a lumped sdof model are:

$$\begin{cases} m_m \ddot{z} + c_m \dot{z} + k_m z - \alpha v = F_m \\ C_p \dot{v} + \frac{v}{R_i} - \alpha \dot{z} = 0 \end{cases} \quad (10)$$

The corrected lumped forcing function with the modal participation factor γ is

$$F_{mr} = -\gamma_r m_m \ddot{y} \quad (11)$$

and the EMCC k and lumped parameters are:

$$k^2 = \frac{\alpha_r^2}{k_m C_p + \alpha_r^2}; \quad c_{mr} = 2\zeta_r \sqrt{k_{mr} m_{mr}}; \quad \omega_r = \sqrt{k_{mr}/m_{mr}} \quad (12)$$

where z is the relative displacement related to the base motion y ; $\alpha_r = \chi_r \sqrt{m_{mr}}$ is the lumped coupling factor; m_m is the generalized modal mass; k_m is the effective stiffness. By substituting Eqs. (11) and (12) into Eq. (9), the maximum power can be rewritten as

$$P_{\max} = \frac{F_{mr}^2}{8c_{mr}} = \frac{\gamma_r^2 m_{mr}}{16\zeta_r \omega_r} \dot{y}^2 = \frac{m_e}{16\zeta_r \omega_r} \dot{y}^2 \quad (13)$$

Here m_e is called the effective mass which represents the mass participating in the forcing function and motion. It should be noted that the generalized modal mass m_m in this paper is called effective mass by Erturk and Inman [20,21]. The sum of the effective masses for all modes is the total mass M of the whole model [23]:

$$m_{er} = \gamma_r^2 m_{mr}; \quad \sum_{r=1}^{\infty} m_{er} = M \quad (14)$$

Then, mass ratio is defined as

$$N_r = \frac{\gamma_r^2 m_{mr}}{M} = \frac{m_{er}}{M} \quad (15)$$

N_r denotes the mass ratio for the r th mode. The mass ratio N is the percentage ratio of the effective mass to the total mass, which depends on the modal participation factor and represents how much mass of each mode effectively participates in the overall motion and the contribution of each mode to the maximum power output. In fact, the mass ratio N represents the effect of the modal mechanical behaviour on the forcing function, and it linearly affects the power density [24]. The mass ratio of each mode is always smaller than 1 ($N_r < 1$) for structures with multiple degrees of freedom.

Apparently, a harvester with a relatively large total mass and base motion is able to generate more power. Therefore, using power density and normalizing the output to evaluate the performance is more intuitive. In this paper, the mean squared acceleration weighted power density (MSAPD), which is defined as the average power per 1 m/s^2 base excitation per cubic centimetre (cm^3), has been used. By substituting Eq. (15) into Eq. (13), the maximum MSAPD can be written as

$$\text{MSAPD}_{\max} = \frac{N_r \rho}{16\zeta_r \omega_r} \times 10^{-6} (\text{Ws}^4/\text{cm}^3 \text{ m}^2) \quad (16)$$

where ρ is the mass density (kg/m^3). When the material density, resonance frequency and damping ratio are known, the maximum power density is simply determined by mass ratio. However, when the electromechanical coupling is not sufficiently strong, the EMCC can also significantly affect the power density. Fig. 3 shows the maximum MSAPD of harvesters as a function of $k^2 Q_m$ for different mass ratios (resonance frequency 46 Hz and $Q_m = 25$). The results are determined using DPM with the optimal resistive load. The results show that, for different values of $k^2 Q_m$, mass ratio always linearly affects the maximum power density. EMCC only affects the maximum MSAPD when the value of $k^2 Q_m$ is smaller than 2. Therefore, the modal approach is developed using mass ratio and EMCC to evaluate the modal mechanical and electromechanical performance of harvesters.

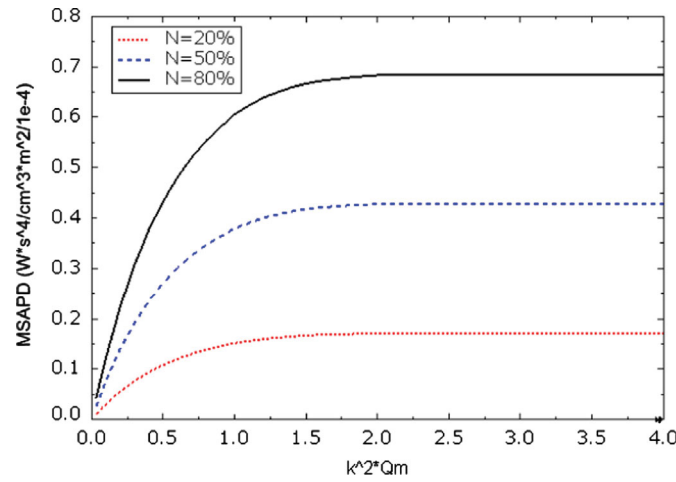


Fig. 3. Maximum MSAPD as function of k^2Q_m for different mass ratio N .

Table 2
Modal parameters of the first four transverse vibration modes of harvester model *1L1M*.

Mode no.	f_r (Hz)	m_m ($\times 10^{-3}$ kg)	γ	m_e ($\times 10^{-3}$ kg)	M ($\times 10^{-3}$ kg)	$N=m_e/M$ (%)	k	k^2Q_m
1	45.996	21.22	1.181	29.61	41.67	71.06	0.226	1.28
2	418.40	10.18	0.711	5.15		12.37	0.194	0.94
3	1094.9	9.67	0.468	2.11		5.07	0.127	0.40
4	2137.7	8.29	0.388	1.25		3.0	0.028	0.02

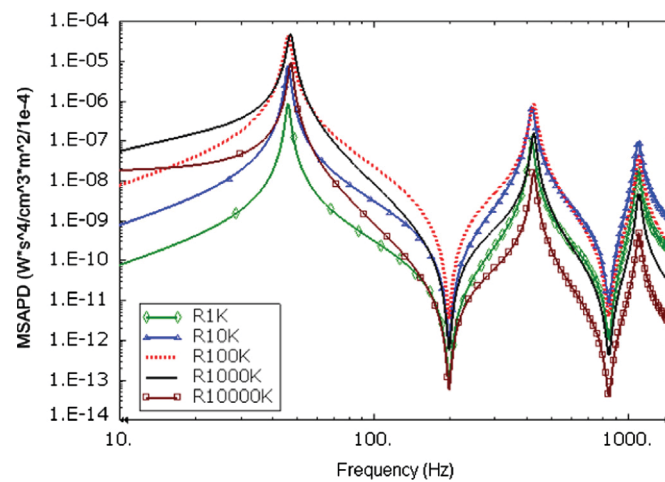


Fig. 4. MSAPD FRFs of the model *1L1M* with different resistive loads.

3.3. Performance determination of harvesters using the modal approach

3.3.1. Evaluation of single layer harvester

Table 2 shows the modal data of the first four modes of the transverse vibration of the single layer harvester model *1L1M* (see Fig. 1), which is simply a cantilevered beam with tip mass. The modal parameters f_r , m_m , γ and m_e were obtained from a modal finite element analysis of the harvester. The parameter k was derived using the DPM model. Fig. 4 shows the predicted frequency response functions (FRFs) of the MSAPD using DPM with different resistive loads. Obviously, the first mode has the lowest resonance frequency, strongest EMCC and largest mass ratio. Then, the first mode is able to generate the greatest power density. Because of the effects of the smaller N , weaker k and the much higher f , the MSAPD in the higher modes are decreased significantly. Besides, the single layer harvester cannot produce broadband power output since the higher modes are far away from the first mode.

3.3.2. Evaluation of multi-layer harvester

For the initial demonstration of the use of the modal approach for the performance evaluation of a multi-layer harvester, the three-layer stacked harvester model 3L3MP090, which the corresponding 3D view is shown in Fig. 13(a), is analysed. This harvester is analysed in greater details in Section 4.2. Table 3 shows the values of N and k of the harvester were derived using the modal approach and DPM. In the first three modes, 3L3MP090 has much closer resonance frequencies in the first three modes in comparison with the single layer model 1L1M. The differences of the EMCC between each mode of the three-layer harvester are also smaller. Then, the power density of 3L3MP090 around the first three modes is basically determined by the values of mass ratios and resonance frequencies. In particular, the second mode has the largest $N_2=73.7$ percent, and the rest of the modes have much smaller N due to the fact that the sum of N for all modes equals 100 percent. For example, N_2 is more than 12 times and nearly 6 times larger than N_1 and N_3 , respectively. In Fig. 5, the predicted MSAPD FRFs using DPM with different resistive loads show that the second mode can generate more than 7 times power density than the first and third modes. Generally, for a specified acceleration input, it is straightforward and convenient to use the mass ratio and EMCC to predict the modal performance of each mode even when the model has close resonance frequencies. Thus, the performance of a harvester model can be clearly determined by predicting the corresponding FRFs of MSAPD in multiple modes.

Table 3
Modal parameters of the first three transverse vibration modes of model 3L3MP090.

Mode no.	f_r (Hz)	$m_m (\times 10^{-3} \text{ kg})$	γ	$m_e (\times 10^{-3} \text{ kg})$	$M (\times 10^{-3} \text{ kg})$	$N=m_e/M$ (%)	k	$k^2 Q_m$
1	20.9	41.03	0.419	7.20	120.17	6.0	0.128	0.41
2	35.1	50.02	1.330	88.53		73.7	0.133	0.44
3	53.8	35.71	0.608	13.20		11.0	0.158	0.63
4	303.1	40.12	0.249	2.48		2.1	0.114	0.32

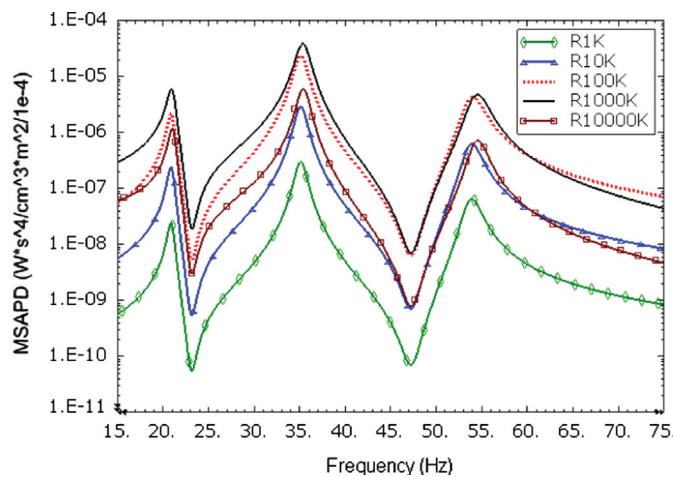


Fig. 5. MSAPD FRFs of the model 3L3MP090 with different resistive loads.

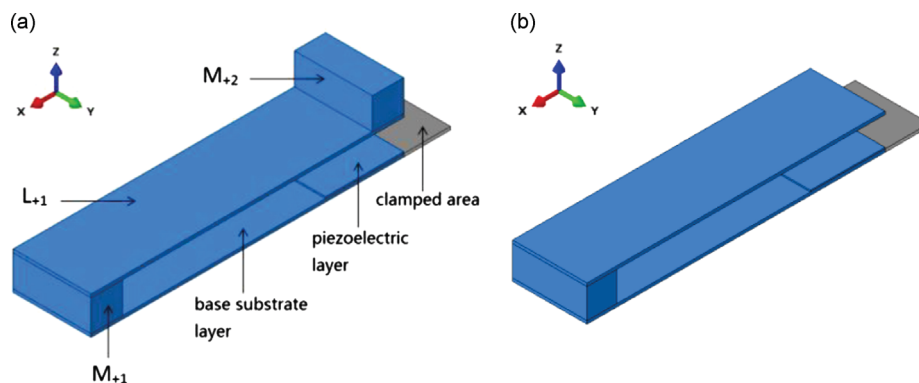


Fig. 6. Two-layer stacked harvesters: (a) two layers with two masses (2L2MP09) and (b) two layers with one mass (2L1MP0).

4. Performance evaluation of multi-layer stacked vibration energy harvesters

4.1. Two-layer stacked harvester

4.1.1. Configurations of two-layer stacked harvester

In this section, two-layer stacked harvesters are developed. Fig. 6 illustrates two typical examples. Fig. 6(a) is the model 2L2MP09, which has two layers (2L) and two extra masses (2M). Fig. 6(b) is the model 2L1MP0, which has two layers (2L) and one mass (1M). The masses are designed to be movable to different positions. The masses also serve as spacers to separate the two layers of the model. The positions of the masses from the free tip to the clamped end are identified as $Pabc-def$, where a , b and c denote the positions of masses M_{+1} , M_{+2} and M_{+3} on the upper half and d , e and f denote the positions of masses M_{-1} , M_{-2} and M_{-3} on the lower half by numbers from 0 to 9. For instance, the mass positions of Fig. 6(a) and (b) are P09 and P0, respectively, and the mass position of Fig. 7 is P392-071. The single (base) layer attached with mass M_{+1} is actually the model 1L1M as given in Fig. 1. A $25 \times 25 \times 0.5 \text{ mm}^3$ piezoelectric layer has been bonded near the clamped end of

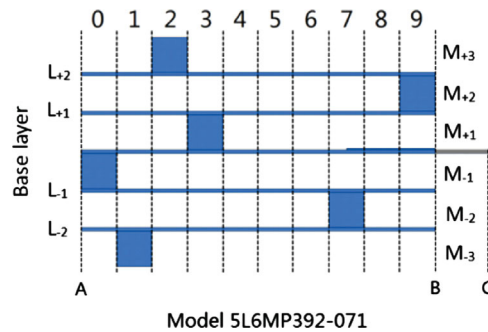


Fig. 7. Numbering of mass positions; model 5L6MP392-071 has 5 layers and 6 masses, four layers are separately located on the opposite sides of the base layer and the locations of masses on the upper half is 392 and the lower half is 071. A=tip of base layer; BC=clamped length of base layer.

Table 4
Modal performance of the model 2L1M with different mass positions of M_{+1} .

Models (2L1M)	Mode 1			Mode 2		
	$f1$ (Hz)	$N1$ (%)	$k1$	$f2$ (Hz)	$N2$ (%)	$k2$
P0	40.84	47.9	0.218	72.96	34.6	0.112
P1	45.68	52.2	0.229	92.30	31.6	0.117
P2	50.98	55.4	0.239	120.24	29.5	0.124
P3	56.74	57.3	0.249	162.06	28.6	0.135
P4	63.00	57.8	0.260	226.94	29.6	0.149
P5	70.07	56.8	0.274	325.82	33.9	0.161
P6	79.02	54.7	0.342	407.19	27.8	0.109

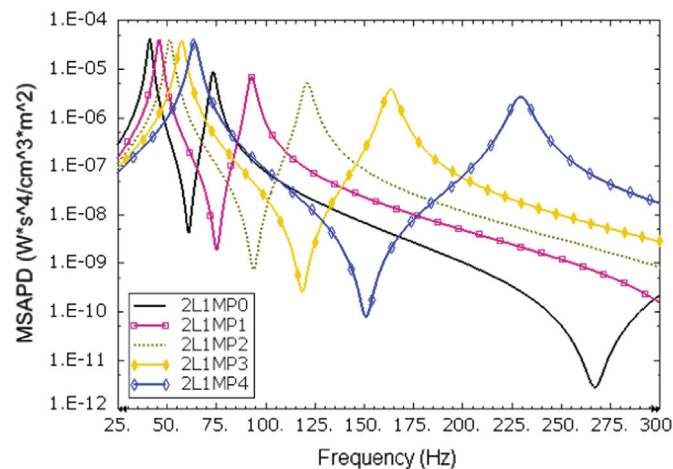


Fig. 8. MSAPD FRFs of the model 2L1M with different mass positions of M_{+1} .

the base layer. The dimension of the layer stacked on the base layer is $100 \times 25 \times 1 \text{ mm}^3$, and the dimension of each mass is $10 \times 25 \times 10 \text{ mm}^3$.

4.1.2. Performance of two layers with one mass (model 2L1M)

It should be noted that all the MSAPD FRFs given in Section 4 are derived using DPM and optimized by connecting the optimal resistive load. The performance of the 2L1M with different mass positions is presented in this section. The location of M_{+1} is varied from 0 to 6 since positions 7–9 are occupied by the piezoelectric layer. Table 4 shows the modal performance of 2L1M with different mass positions. Apparently, when the mass position is 0, the difference between the first two natural frequencies is the smallest. When the mass is relocated from 0 to 6, the first natural frequency is increased, but the second natural frequency is increased much more than the first natural frequency. Then, the difference between the two natural frequencies becomes larger. Besides, the EMCC in the first mode is also increased. This is due to the fact that the effective length of the base layer is decreased, and the piezoelectric coverage is increased. The same phenomenon has been observed in the single cantilevered beam harvester model when relocating an extra mass from the free tip to the clamped end [24]. Fig. 8 shows MSAPD FRFs of 2L1M with mass positions varied from 0 to 4. When the gap between two modes

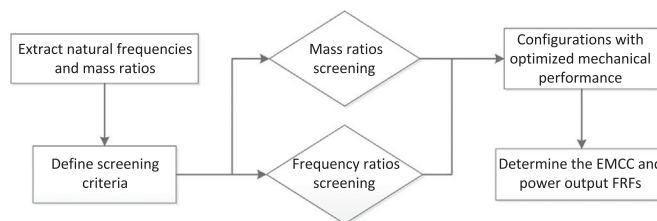


Fig. 9. A general procedure for the mechanical performance optimization using the modal approach.

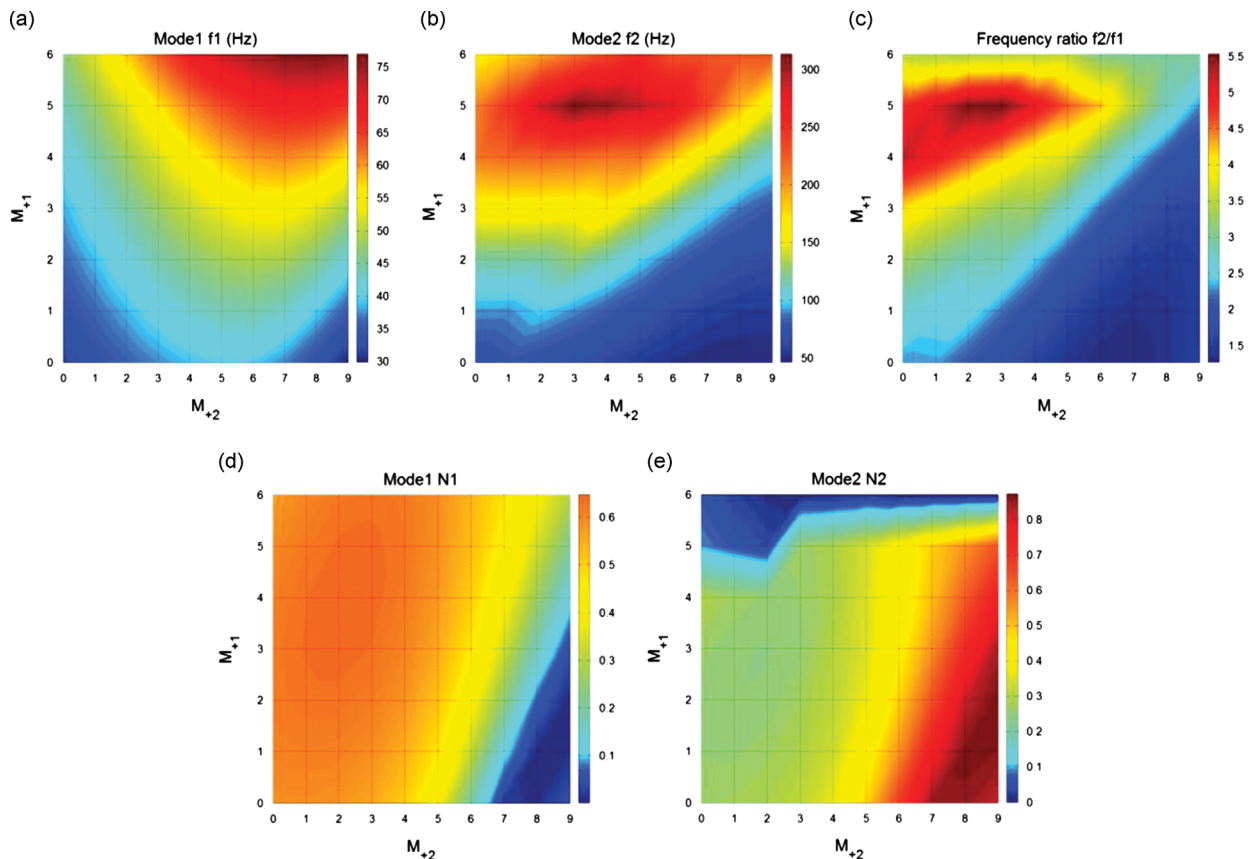


Fig. 10. Contour of the resonance frequencies and mass ratio of the first two modes with different mass positions of M_{+1} and M_{+2} : (a) and (b) resonance frequencies of modes 1 and 2; (d) and (e) mass ratios of modes 1 and 2; (c) and (f) the values of $f2/f1$ and $N2/N1$.

becomes larger, the magnitude of the MSAPD at the anti-resonance frequency between the two modes becomes lower, which significantly affects the capability for broadband power output.

Since the sum of mass ratios for all modes equals 1 (Eqs. (14) and (15)), the mode with the larger mass ratio will cause the remaining modes to have smaller mass ratio and lower power density. Therefore, the main objective for designing the stacked multi-layers harvester in this paper is to determine a good mass position that will provide close enough multiple modes, evenly distributed mass ratio and strong enough EMCC.

4.1.3. Performance of two layers with two masses (model 2L2M)

Although, the modal approach can be used to evaluate the modal performance conveniently, the full steady-state analysis is still required to derive the coupling term and EMCC (see Eq. (6)). The natural frequencies and mass ratio can be determined directly using the modal FE analysis. Then, a screening process based on the modal approach is developed to determine the optimal or near-optimal modal mechanical performance of the harvesters when altering mass positions. This procedure obviates the need for full analysis by determining the harvester configurations with close resonances and favourable values of mass ratio initially (see Fig. 9).

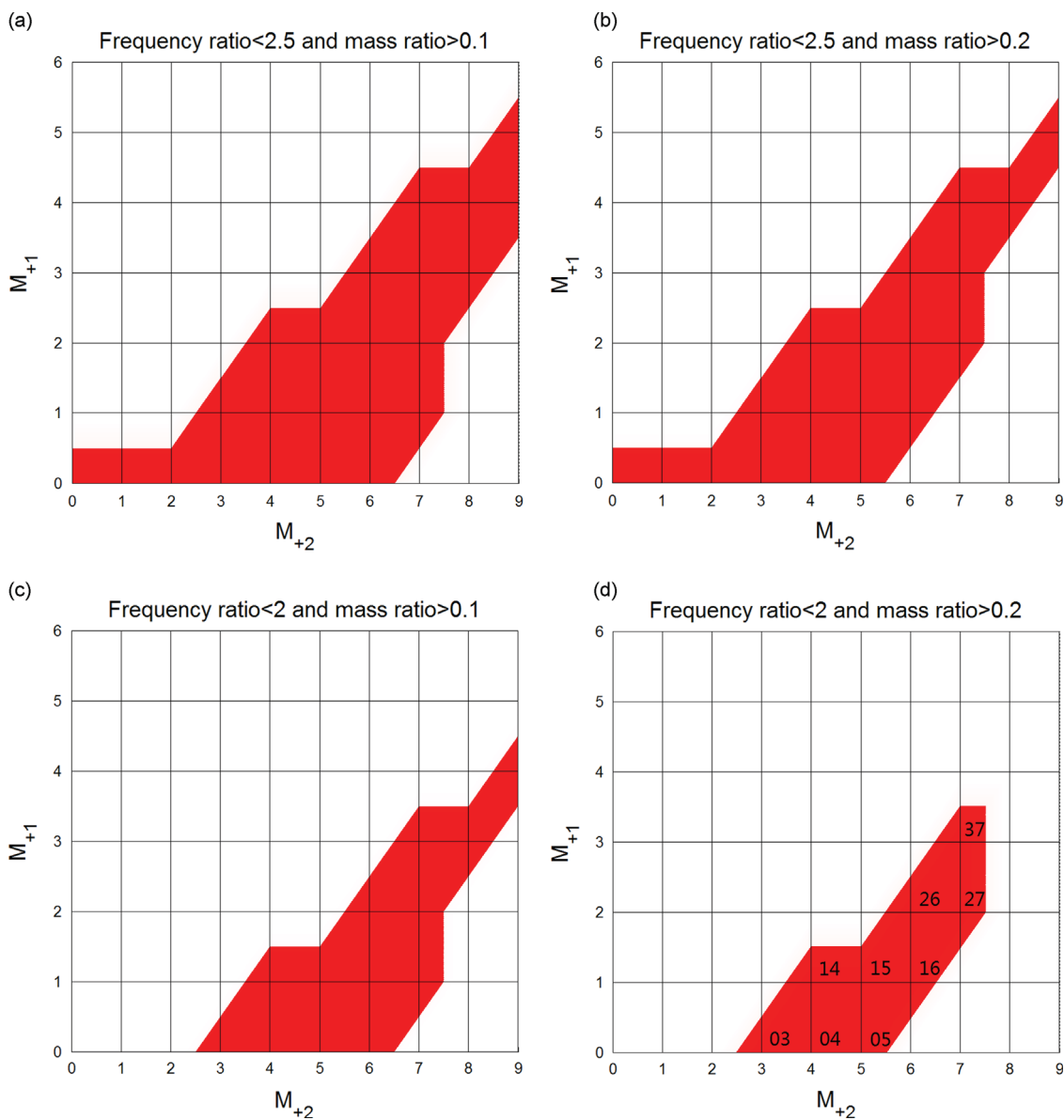


Fig. 11. Determination of the mass positions of model 2L2M with better mechanical performance. The shaded area is where the mass position meets the screening criteria: (a) $f_2/f_1 < 2.5$ and $N > 0.1$; (b) $f_2/f_1 < 2.5$ and $N > 0.2$; (c) $f_2/f_1 < 2$ and $N > 0.1$; and (d) $f_2/f_1 < 2$ and $N > 0.2$.

In this section, the case of model 2L2M with different mass positions (M_{+1} and M_{+2}) is presented. The location of M_{+1} is varied from 0 to 6 (in order to avoid attaching the mass on the area covered by piezoelectric material) and the location of M_{+2} is varied from 0 to 9. Fig. 10(a) and (b) show the contours of the resonance frequencies while Fig. 10(d) and (e) shows the mass ratio of the first two modes. Fig. 10(c) shows the contour of the frequency ratio f_2/f_1 . It is obvious that a smaller f_2/f_1 means a smaller interval between two modes.

Since the combinations of the mass positions are 70, deriving all configurations by running full analysis is tedious. Thus, the screening process is used to select the mass positions with the preferred values of frequency ratio and mass ratio as shown in Fig. 11. The screening criteria of the frequency ratio are specified as $f_2/f_1 < 2$ or $f_2/f_1 < 2.5$. The screening criteria of the mass ratio are specified as $N > 0.2$ or $N > 0.1$ in both modes. Therefore, there are four screening results due to the different combinations of the screening criteria. The mass positions with better mechanical performance are located in the shaded area. Obviously, the more strict screening results contain the less acceptable mass positions. In particular, changing the specified frequency ratio affects the number of the acceptable mass positions more intensely than changing the specified

Table 5
Modal performance of the model 2L2M with mass positions of M_{+2} .

Models (2L2M)	Mode 1			Mode 2			f_2/f_1
	f_1 (Hz)	$N1$ (%)	k_1	f_2 (Hz)	$N2$ (%)	k_2	
P03	37.38	55.8	0.227	67.92	31.2	0.100	1.82
P04	38.79	50.3	0.226	61.58	36.7	0.100	1.59
P05	39.62	39.2	0.219	55.25	47.7	0.113	1.39
P15	43.92	46.7	0.232	72.33	41.2	0.115	1.65
P26	49.29	40.7	0.236	85.42	48.0	0.134	1.73
P37	54.61	33.3	0.239	101.90	55.9	0.152	1.87

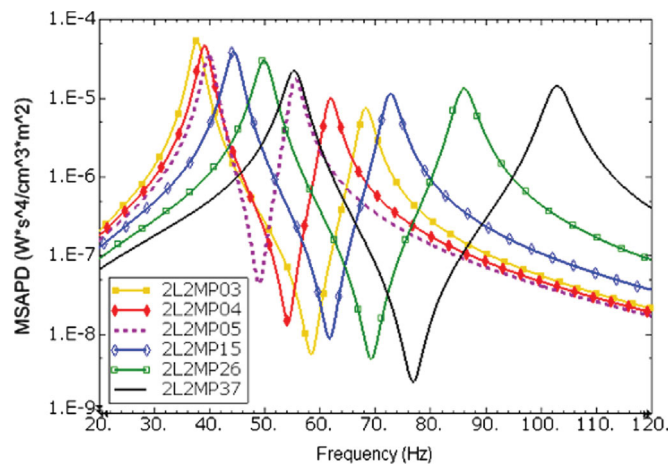


Fig. 12. MSAPD FRFs of the model 2L2M with different mass positions.

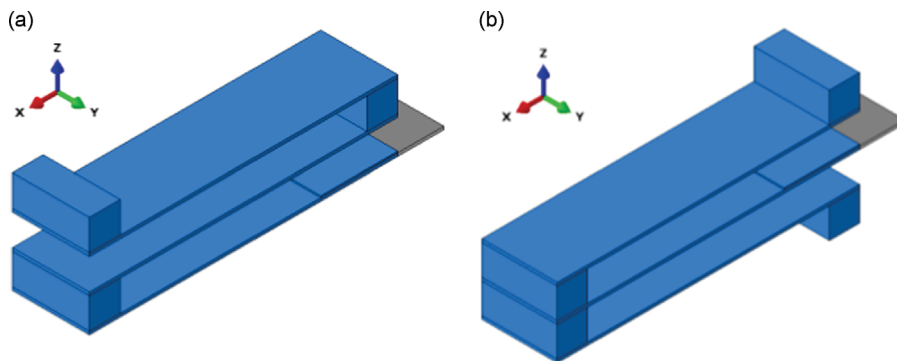


Fig. 13. Three-layer stacked harvester models: (a) model 3L3MP090 (one-sided stacked layers) and (b) model 3L4MP09-09 (two-sided stacked layers).

mass ratio. Fig. 11(d) shows the limited mass positions with much better mechanical performance than the rest of the screened results. The names of mass positions have also been annotated on the shaded area. As the screening results have shown, a lot of configurations have poor modal mechanical performance. Instead of operating full analyses, using the modal approach to screen the harvesters initially is much more convenient, straightforward, quicker and cheaper to implement in terms of computing and analysis time.

Having determined the mass positions with better mechanical performance, some of the corresponding models are now analysed in full in order to demonstrate their performance. In Table 5, when the position of M_{+1} is 0 and the position of M_{+2} is varied from 3 to 5, f_1 is only slightly increased, but f_2 is decreased significantly. Then, the value of f_2/f_1 becomes smaller while the mass ratios are evenly distributed. When the positions of M_{+1} and M_{+2} are varied simultaneously (P15, P26 and P37), the value of f_2/f_1 becomes larger since f_2 is increased much more than f_1 and the mass ratios are still evenly distributed. Fig. 12 shows the MSAPD of the 6 models with preferred mass positions given in Table 5. The figure shows that the results of the full analysis using DPM confirm to the results of the modal approach shown in Table 5.

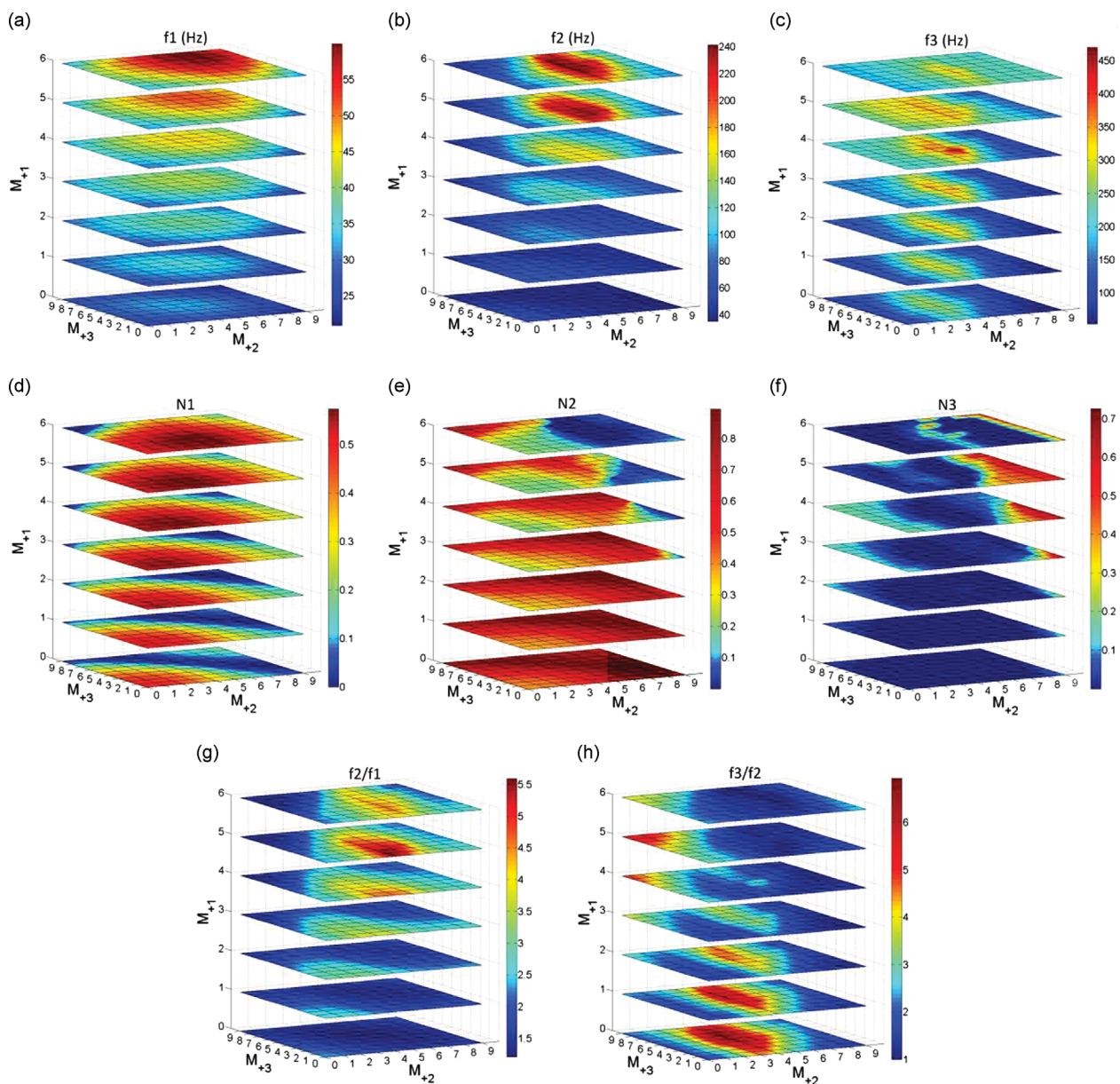


Fig. 14. Contour slices of the resonance frequencies and mass ratio of the first three modes with different mass positions of M_{+1} , M_{+2} and M_{+3} of model 3L3M. (a), (b) and (c) Resonance frequencies of modes 1, 2 and 3; (d), (e) and (f) mass ratios of modes 1, 2 and 3; (g) and (h) the values of f_2/f_1 and f_3/f_2 .

4.2. Three-layer stacked harvester

4.2.1. Configurations of three-layer stacked harvester

In Section 4.1, several analyses of the two-layer stacked harvesters are developed. In particular, f_r and N_r can be easily varied by simply relocating the mass positions. In this section, the harvesters with three stacked layers are developed. Fig. 13 illustrates two examples. Fig. 13(a) shows model 3L3MP090 which has three layers and three masses located on one side of the base layer. Fig. 13(b) shows the model 3LAMP09-09 which has three layers and four masses. Two of the layers and four masses are symmetrically located about the base layer. For harvesters with more than two stacked layers, the dimensions of extra layers and masses are the same as those of the two-layer stacked harvesters.

4.2.2. Performance of one-sided three-layer stacked harvester

In this section, the case of one-sided three-layer model 3L3M with different mass positions (M_{+1} , M_{+2} and M_{+3}) is presented. The location of M_{+1} is varied from 0 to 6 and the locations of M_{+2} and M_{+3} are both varied from 0 to 9. Then, the total number of the mass positions is 700 in this case. Fig. 14(a)–(c) shows the slices of the contours of the resonance

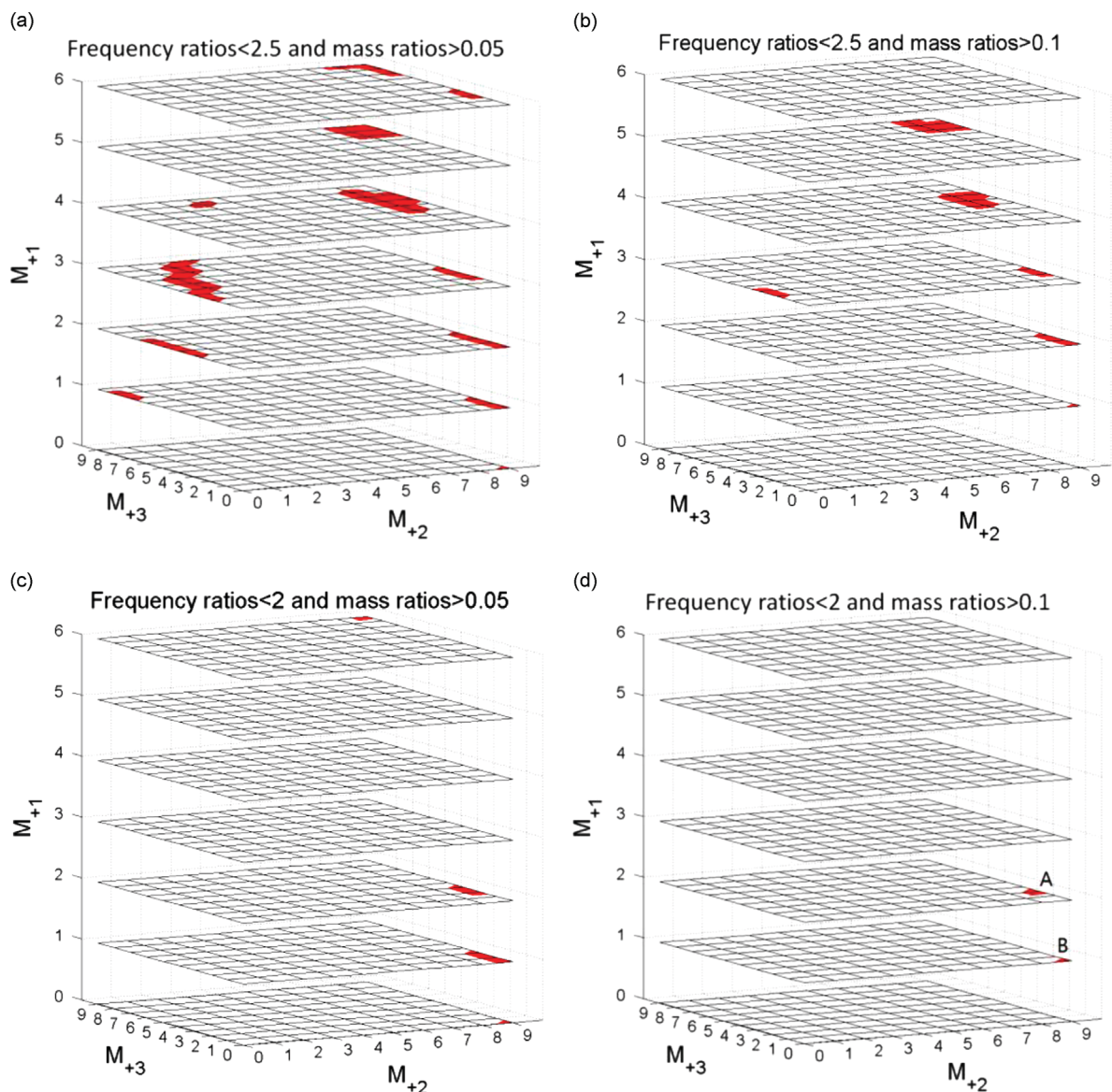


Fig. 15. Determination of the mass positions with better mechanical performance of model 3L3M. The area covered by red colour is the mass position meets the screening criteria for both smaller frequency ratio and larger mass ratio: (a) $f_2/f_1 < 2.5$ and $N > 0.05$; (b) $f_2/f_1 < 2.5$ and $N > 0.1$; (c) $f_2/f_1 < 2$ and $N > 0.05$; and (d) $f_2/f_1 < 2$ and $N > 0.1$. A: P292; B: P190.

frequencies while Fig. 14(d)–(f) shows the slices of the contours of mass ratios of the first three modes of model 3L3M with different mass positions. Fig. 14(g) and (h) shows the slices of the contours of the frequency ratios given by f_2/f_1 and f_3/f_2 .

In this case, it is much harder to determine the mass positions with better performance than in the 2L2M case. The screening process is executed using the modal approach and the screening results are obtained as shown in Fig. 15. The screening criteria of the frequency ratios are specified as $f_2/f_1 < 2$ or $f_2/f_1 < 2.5$, which the screening criteria of the mass ratio are specified as $N > 0.1$ or $N > 0.05$ in all three modes. However, compared with the total number of all mass positions, the preferred mass positions are quite limited. For example, there are only 7 mass positions that meet the criteria (frequency ratio < 2 and mass ratio > 0.05) in Fig. 15(c), and Fig. 15(d) shows that only two mass positions P190 and P292 meet the stricter criteria (frequency ratio < 2 and mass ratio > 0.1).

Table 6 and Fig. 16 show modal performance data and the MASPD of those typical models, respectively. However, there is always one mode that has a much larger mass ratio than the rest of the modes in model 3L3M. Thus, the capability for broadband power output cannot be fully optimized for the one-sided three-layer stacked harvester.

4.2.3. Performance of two-sided three-layer stacked harvester ($M_{+1}=0$)

In this section, the case of the two-sided three-layer model 3L4M with different mass positions (M_{+1} is fixed at 0) is presented. Since there are four masses attached on the model, when the position of M_{+1} is fixed at 0, there are 700 combinations for the remaining three mass positions. The location of M_{-1} is varied from 0 to 6 and the locations of M_{+2} and M_{-2} are both varied from 0 to 9. Fig. 17(a)–(c) shows the slices of the contours of the resonance frequencies while Figs. 17(d, e) and Fig. 14(f) show the slices of the contours of the mass ratios of the first three modes of 3L4M with different mass positions. Fig. 17(g) and (h) shows the slices of the contours of the frequency ratios given by f_2/f_1 and f_3/f_2 . The screening results which are shown in Fig. 18 were obtained using the same screening criteria as those used in the 3L3M case. Obviously, the number of the preferred mass positions is much larger than the number in the 3L3M case. For example, there are only 2 mass positions that meet the stricter criteria (frequency ratio < 2 and mass ratio > 0.1) for the model 3L3M in Fig. 15(d), whereas, Fig. 18(d) shows that there are 20 mass positions that meet the same criteria for the model 3L4M ($M_{+1}=0$).

Table 7 and Fig. 19 show modal performance data and the corresponding MASPD of typical models, respectively. When the masses are symmetrically attached, e.g., model P09-09, the first and third modes are barely active. When the mass positions are unsymmetrical, the model has better performance. For example, model P06-39 can be considered as two layers with mass positions “P06” and “P39” connected in parallel on two sides of the base layer. The results in this section show that model 3L4M with unsymmetrical attached masses is able to generate a good distribution of the mass ratio of the first three modes, which enhances the capability for broadband power output in comparisons with model 3L3M. Further modal

Table 6
Modal performance of the three layers models with different mass positions.

Models	f_1 (Hz)	$N1$ (%)	k_1	f_2 (Hz)	$N2$ (%)	k_2	f_3 (Hz)	$N3$ (%)	k_3	f_2/f_1	f_3/f_2
P190	22.02	11.4	0.139	42.94	64.2	0.118	58.45	15.7	0.178	1.95	1.36
P191	24.013	9.1	0.143	42.835	70.3	0.133	60.505	11.8	0.164	1.78	1.41
P192	25.921	6.0	0.143	42.805	77.1	0.151	63.230	8.1	0.147	1.65	1.48
P292	27.642	12.8	0.158	53.688	65.1	0.129	68.219	13.9	0.172	1.94	1.27
P293	29.786	9.6	0.161	53.569	74.0	0.152	71.447	8.2	0.150	1.80	1.33
P699	52.701	14.3	0.256	103.210	6.2	0.165	181.290	61.4	0.078	1.96	1.76

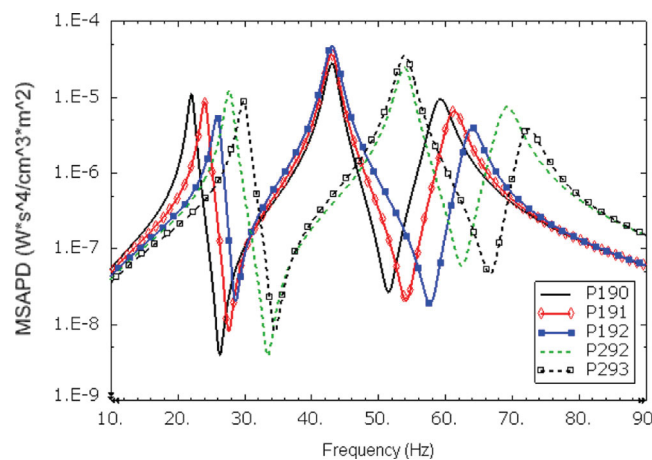


Fig. 16. MASPD FRFs of the three layers models with different mass positions.

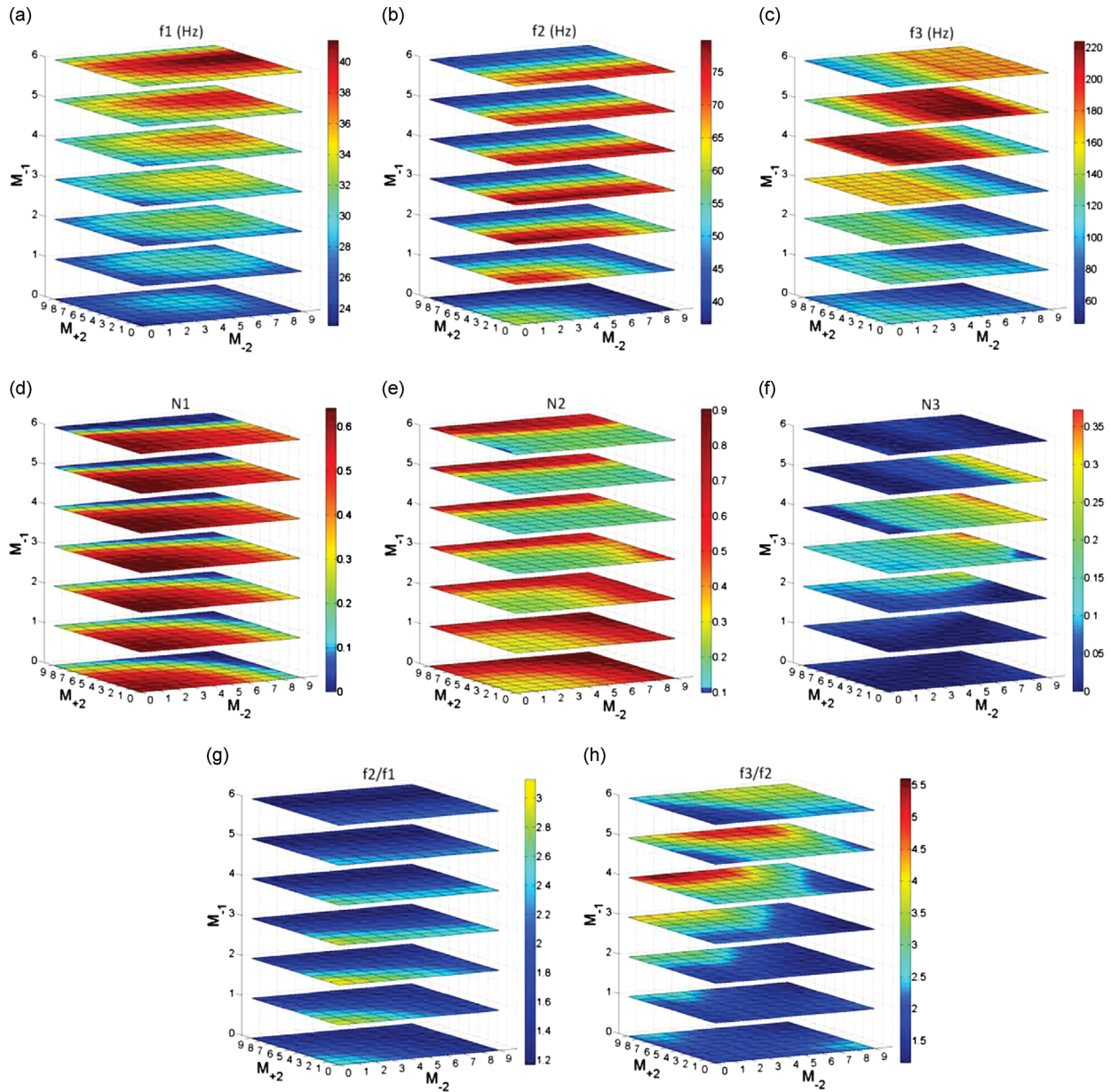


Fig. 17. Contour slices of the resonance frequencies and mass ratio of the first three modes with different mass positions of M_{+2} , M_{-1} and M_{-2} of model 3L4M ($M_{+1}=0$): (a), (b) and (c) resonance frequencies of modes 1, 2 and 3; (d), (e) and (f) mass ratios of modes 1, 2 and 3; (g) and (h) the values of f_2/f_1 and f_3/f_2 .

data and screening results for model 3L4M with mass position $M_{+1}=3$ and $M_{+1}=6$ can be found in [Appendix A](#) at the end of this paper.

4.3. Four- and five-layer stacked harvester

In this section, the four- and five-layer stacked models are developed. When the model has more than three layers, the combinations of mass positions are too many. Thus, only some typical mass positions with better performance have been presented in this section. [Fig. 20](#) illustrates the configuration of model 4L5MP090-09, which is the two-sided four-layer stacked harvester with four layers and five masses.

In fact, once the one-sided model has more than three layers, e.g., model 4L4MP0909 and 5L5MP09090, it becomes harder to evenly distribute the mass ratio to each mode (see [Tables 8](#) and [9](#)) by simply altering the mass positions. Then, a dominant mode which has a very large mass ratio causes the rest of the modes to have poor performance or to be inactive. However, the two-sided model with unsymmetrically located masses can easily generate a better mass ratio distribution.

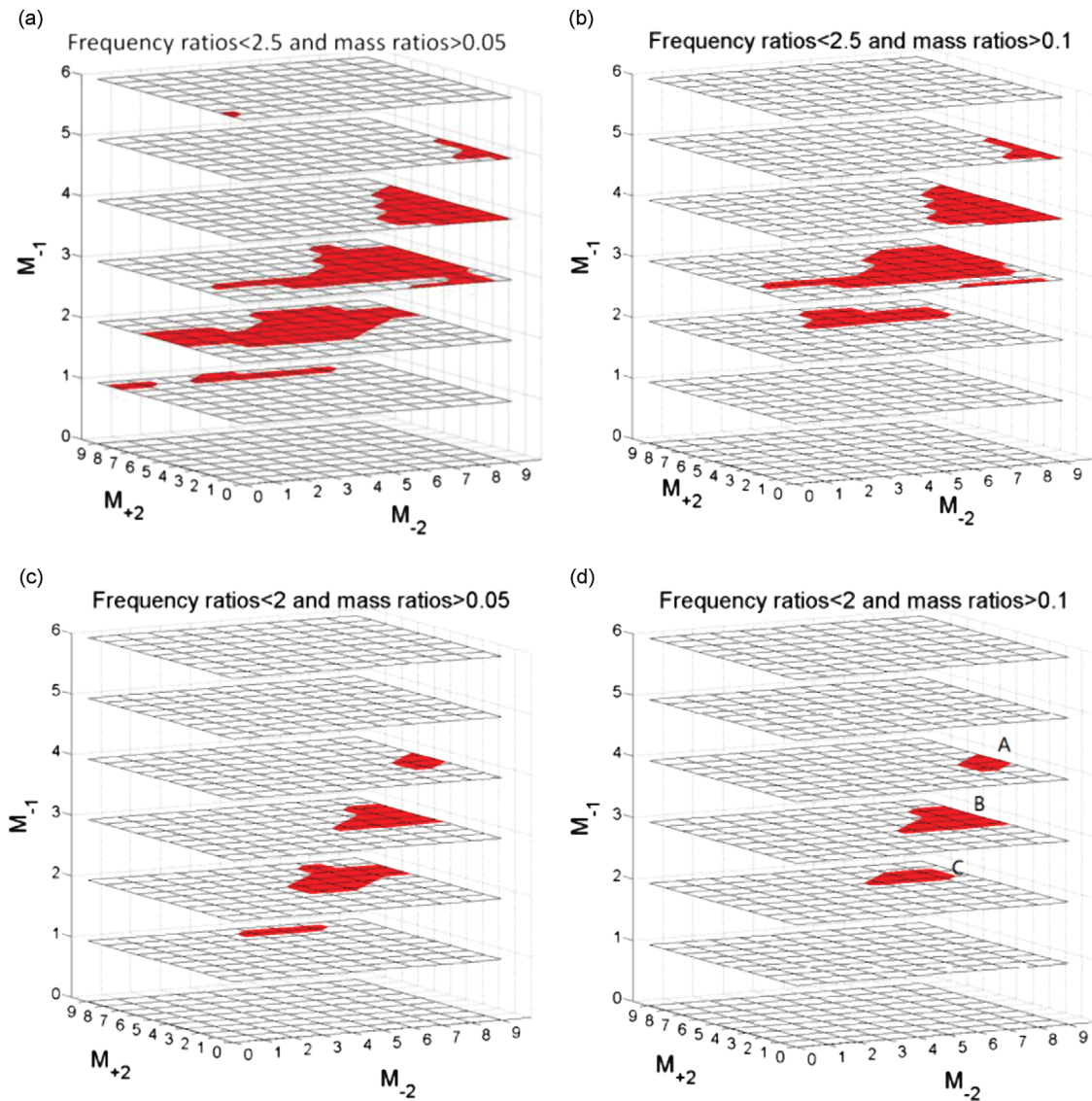


Fig. 18. Determination of the mass positions with better mechanical performance of 3L4M ($M_{+1}=0$): (a) $f_2/f_1 < 2.5$ and $N > 0.05$; (b) $f_2/f_1 < 2.5$ and $N > 0.1$; (c) $f_2/f_1 < 2$ and $N > 0.05$; and (d) $f_2/f_1 < 2$ and $N > 0.1$. A: P03-48, P04-48, P04-49 and P05-49 and B: P04-36, P04-37, P04-38, P04-39, P05-37, P05-38, P05-39, P06-38, P06-39, P07-38 and P07-39; C: P06-26, P06-27, P06-28, P07-27 and P07-28.

Table 7
Modal performance of model 3L4M with typical mass positions.

Models	f_1 (Hz)	N_1 (%)	k_1	f_2 (Hz)	N_2 (%)	k_2	f_3 (Hz)	N_3 (%)	k_3	f_2/f_1	f_3/f_2
P09-09	23.27	1.5	0.102	36.97	90.7	0.222	45.79	0.0	0.011	1.59	1.24
P04-39	32.77	29.5	0.223	61.85	46.7	0.126	78.70	16.1	0.094	1.89	1.27
P05-39	33.32	25.6	0.220	56.23	42.2	0.112	77.25	24.5	0.114	1.69	1.37
P06-39	33.50	19.7	0.214	50.51	42.3	0.112	76.38	30.2	0.125	1.51	1.51
P06-28	32.11	20.8	0.208	50.01	60.8	0.144	71.65	11.2	0.082	1.56	1.43
P05-38	34.11	33.6	0.228	56.53	35.4	0.099	89.89	23.9	0.118	1.66	1.59
P04-48	35.57	41.9	0.242	62.48	22.0	0.076	123.79	29.0	0.132	1.76	1.98

Table 8 and Fig. 21 show modal performance data and the corresponding MASPD of model 4L5M with typical mass positions, respectively. In particular, the natural frequencies of the model with mass position P090-09 are very close, but N_2 is too large and N_1 and N_3 are too small. By altering the masses to unsymmetrical locations, N_1 , N_3 and N_4 and the MASPD of these three modes are significantly increased, e.g., model P391-09. By relocating the position of M_{+1} from 3 to 2, the interval between

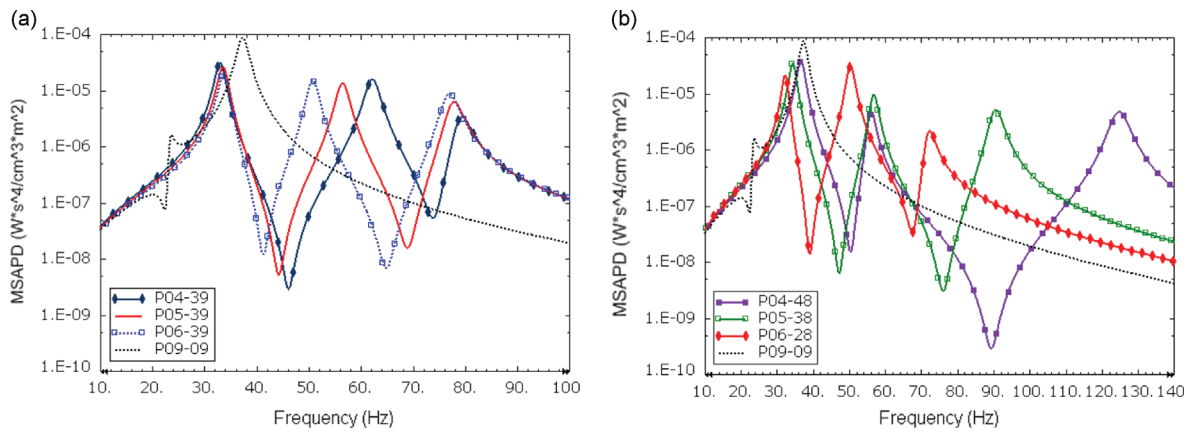


Fig. 19. MSAPD FRFs of the three layers models 3LAM with typical mass positions.

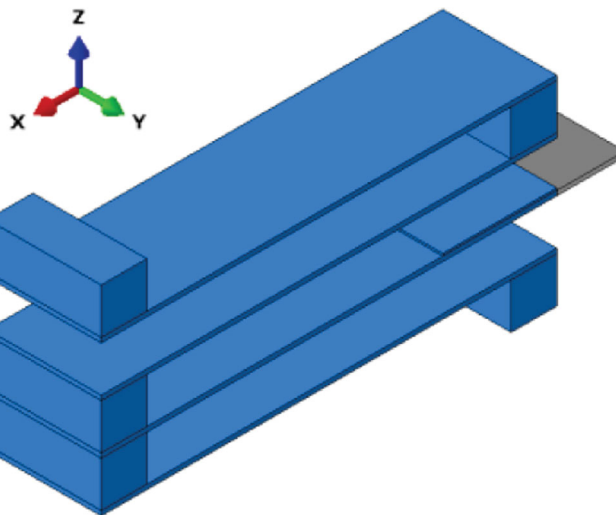


Fig. 20. Four-layer stacked harvester model 4L5MP090-09.

Table 8
Modal performance of the four-layer stacked harvester with typical mass positions.

Models	f_1 (Hz)	N_1 (%)	k_1	f_2 (Hz)	N_2 (%)	k_2	f_3 (Hz)	N_3 (%)	k_3	f_4 (Hz)	N_4 (%)	k_4
P0909	15.54	1.1	0.079	27.80	82.5	0.166	44.07	0.2	0.048	57.53	9.0	0.144
P090-09	18.80	2.7	0.132	30.86	77.9	0.149	39.87	10.4	0.123	49.65	2.9	0.077
P291-09	22.32	9.6	0.166	35.94	39.7	0.085	49.96	30.2	0.183	57.58	14.9	0.058
P391-09	23.59	13.3	0.178	35.05	30.5	0.065	52.36	16.0	0.157	72.41	34.5	0.126

Table 9
Modal performance of the five-layer stacked harvester with typical mass positions.

Models	f_1 (Hz)	N_1 (%)	k_1	f_2 (Hz)	N_2 (%)	k_2	f_3 (Hz)	N_3 (%)	k_3	f_4 (Hz)	N_4 (%)	k_4	f_5 (Hz)	N_5 (%)	k_5
P09090	12.01	1.3	0.094	22.91	80.6	0.122	35.84	3.0	0.107	52.89	3.3	0.043	57.17	6.1	0.138
P090-090	16.67	7.0	0.146	29.14	84.6	0.173	29.69	0.0%	0.014	47.06	0.0%	0.028	49.34	3.5	0.100
P392-070	21.49	22.3	0.193	35.80	26.7	0.095	46.93	22.6	0.115	68.15	9.9	0.020	76.83	14.0	0.122
P392-071	22.36	22.6	0.197	36.41	30.0	0.092	47.74	18.6	0.117	70.18	18.0	0.066	80.85	6.2	0.102

the third and fourth mode in model *P291-09* becomes smaller, but the mass ratio and EMCC of the fourth mode are also decreased simultaneously.

The modal performance data and the corresponding MASPD of some typical five-layer stacked models are given in Table 9 and Fig. 22, respectively. With symmetric mass positions, the third and fourth modes in model *P090-090* have very small mass ratio and weak EMCC. Then, the two modes are inactive in the MASPD FRFs. By unsymmetrically altering the mass positions, the model *P392-070* has much better performance, but the fourth mode still has small mass ratio and weak EMCC. Then, by altering the position of M_{-3} from 0 to 1, the MASPD of model *P329-071* (the configuration is given in Fig. 7) around the fourth mode is increased 10 times while the MASPD around the fifth mode is only decreased 2 times. In fact, when the number of the layers stacked on two sides of the base layer are the same, e.g., model *3L4M* (1 layer on each side) and *5L6M* (2 layers on each side), good performance can be achieved when the combination of the mass positions on one side is similar to the other side but in an unsymmetrical configuration. For example, model *P05-38* and *P392-071* can generate better distributions of the modal frequencies and mass ratios.

4.4. Altering mass positions for smaller and larger systems

In all the above cases, the designs of the multi-layer stacked harvesters with different mass positions have specified dimensions. In fact, the designs with different mass positions can be used at different scales and the mass positions can be considered as dimensionless factors. In this section, two models are developed for a small system and a large system, respectively. The dimensions of the model for a smaller system are given as: substrate layers: $15 \times 4 \times 0.1 \text{ mm}^3$; piezoelectric layer: $4 \times 4 \times 0.05 \text{ mm}^3$; masses: $1.5 \times 4 \times 1.5 \text{ mm}^3$. The dimensions of the model for a large system are given as: substrate

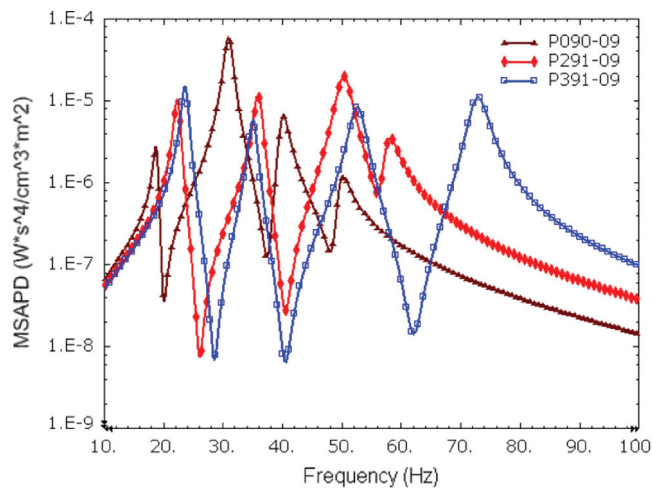


Fig. 21. MASPD FRFs of the four layers models with unsymmetrical mass positions.

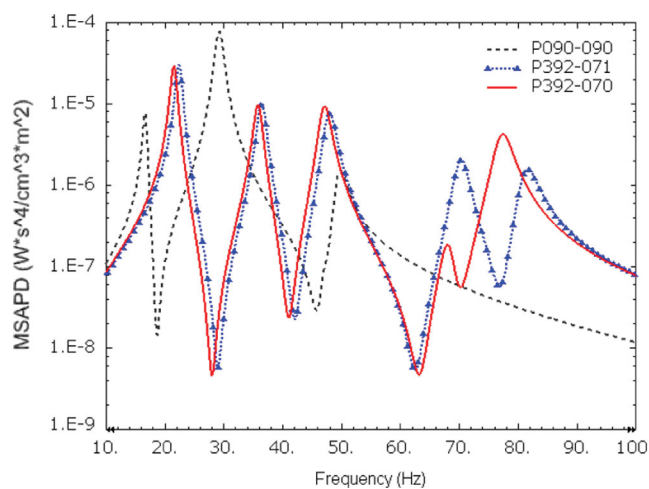


Fig. 22. MASPD FRFs of the five layers models *5L6M* with unsymmetrical mass positions.

layer: $500 \times 100 \times 8 \text{ mm}^3$; piezoelectric layer: $150 \times 100 \times 3 \text{ mm}^3$; masses: $50 \times 100 \times 50 \text{ mm}^3$. Obviously, the length and thickness of the masses are always 1/10 of the length of the base layers, but the aspect ratios of the substrate layer and piezoelectric layer in the two models are different. In Table 10 and Fig. 23, the modal performance and power output (1 m/s^2 base excitation) of the two models with two typical mass positions “P06-39” and “P391-09” are given. Obviously, the large model has much lower resonance frequencies and the small model has higher resonance frequencies. The values of the mass ratios are only slightly different. The values of the frequency ratios between each two modes and the corresponding responses are still similar. Therefore, the designs with preferred mass positions can be used for system with different sizes, frequency ranges and power outputs from lower frequency to higher frequency with the power range from microwatts to milliwatts.

5. Factors affecting performance of two-layer stacked harvester

5.1. Effect of full coverage of piezoelectric layer

In above sections, a same 25 mm long piezoelectric layer has been used and it only covers the root of the base layer. In Table 11 and Fig. 24, the modal performance data and the corresponding MASPD of the 3 and 4 layers stacked models with full piezoelectric coverage are given. The length of the piezoelectric layer has been increased from 25 mm (PL25) to 80 mm in 3L3MP190 (PL80) or 70 mm in 4L5MP291-09 (PL70). The lengths 80 mm and 70 mm of the piezoelectric layer are considered as full coverage since the effective lengths of the base layer are 80 mm and 70 mm (mass position $M_{+1} = 1$ and

Table 10

Modal performance of the harvester models in a smaller and a larger system with different mass positions.

Models	$f1$ (Hz)	$N1$ (%)	$k1$	$f2$ (Hz)	$N2$ (%)	$k2$	$f3$ (Hz)	$N3$ (%)	$k3$	$f4$ (Hz)	$N4$ (%)	$k4$
Small P06-39	131.29	17.60	0.22	201.73	45.60	0.122	287.53	30.20	0.128			
Small P391-09	91.24	11.60	0.18	134.26	31.60	0.067	205.42	17.20	0.169	279.64	34.80	0.128
Large P06-39	11.92	24.10	0.221	17.65	40.40	0.093	28.27	26.80	0.101			
Large P391-09	8.57	16.70	0.187	13.04	30.20	0.058	18.7	15.80	0.147	25.66	30.90	0.097

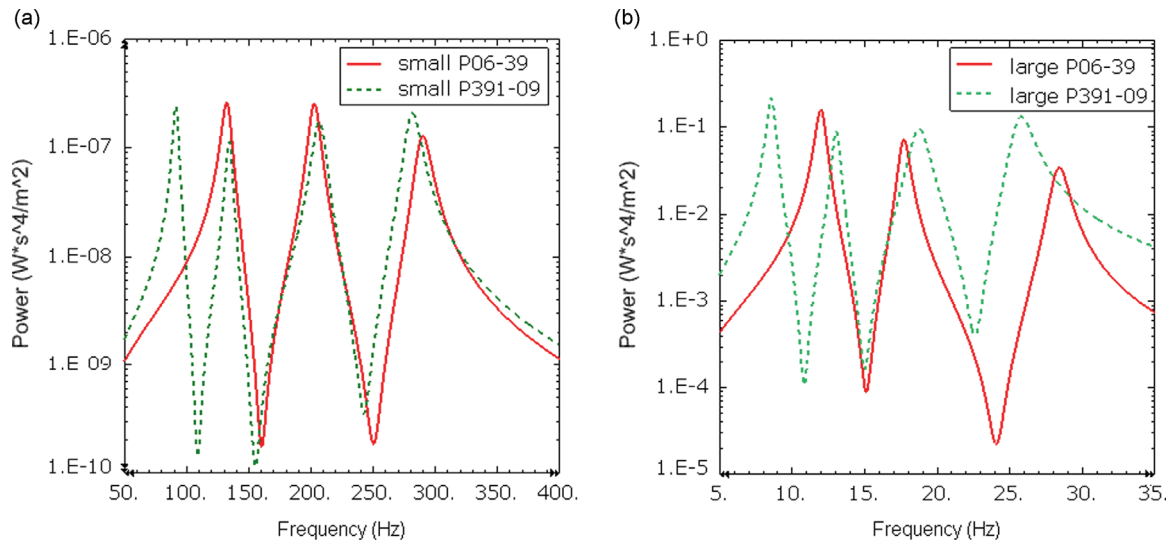


Fig. 23. MASPD FRFs of a small and large harvester models with different mass positions: (a) small harvester and (b) large harvester.

Table 11

Modal performance of three and four layers models with full piezoelectric coverage.

Models	$f1$ (Hz)	$N1$ (%)	$k1$	$f2$ (Hz)	$N2$ (%)	$k2$	$f3$ (Hz)	$N3$ (%)	$k3$	$f4$ (Hz)	$N4$ (%)	$k4$
3L3MP190 PL25	22.02	11.4	0.139	42.94	64.2	0.118	58.45	15.7	0.178			
3L3MP190 PL80	24.28	14.1	0.212	46.88	62.5	0.034	61.82	13.9	0.228			
4L5MP291-09 PL25	22.32	9.6	0.166	35.94	39.7	0.085	49.96	30.2	0.183	57.58	14.9	0.058
4L5MP291-09 PL70	25.49	13.8	0.258	37.11	30.1	0.036	51.41	33.7	0.169	61.16	16.0	0.083

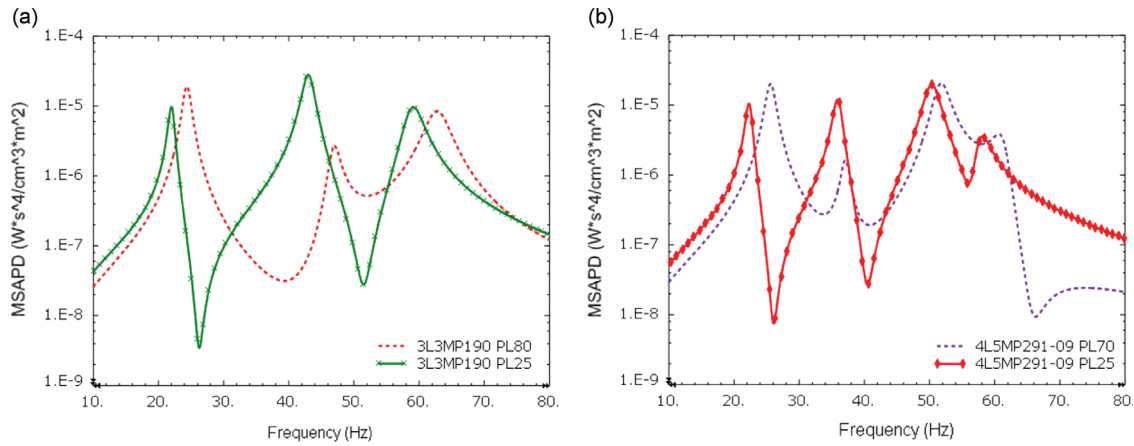


Fig. 24. MSAPD FRFs of three and four layer models with different piezoelectric coverage: (a) three layers and (b) four layers.

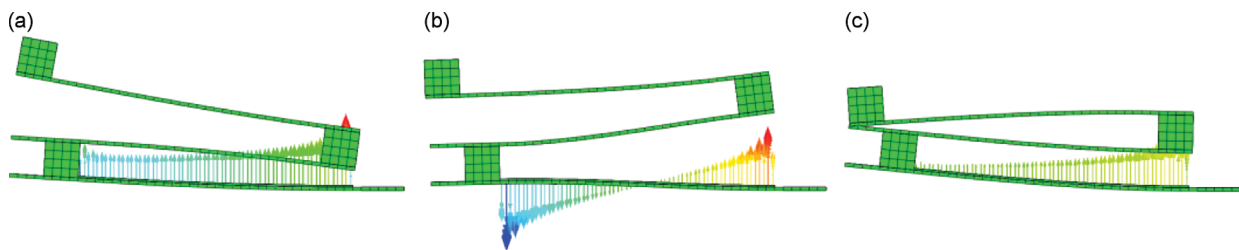


Fig. 25. Electrical displacement mode shapes of model 3L3MP190: (a) mode 1; (b) mode 2; and (c) mode 3.

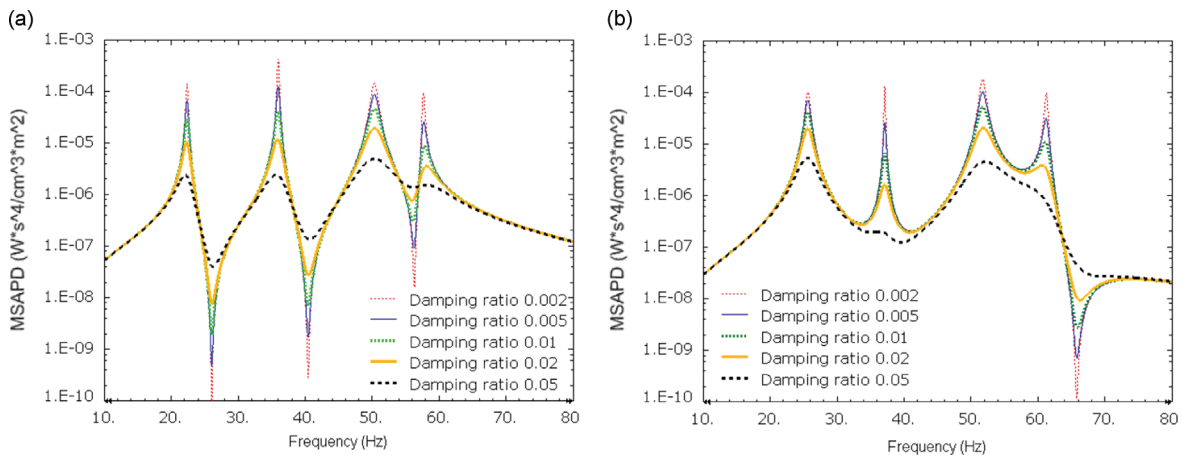


Fig. 26. MSAPD FRFs with different damping ratios: (a) 2L2MP05 PL25 and (b) 2L2MP05 PL70.

$M_{+1}=2$). The results show that the EMCC of the first mode is increased significantly. However, the EMCC of the second mode becomes weaker. In fact, the decrease of the EMCC in the second mode is due to the self-cancellations of the current. It is because the strain distributions along the length of the beam cause the electric displacement D along the thickness to be partly reversed. Fig. 25(a)–(c) illustrates the first three mode shapes and the corresponding electric displacement distributions of model 3L3MP190 in the x – z plane. The lengths and directions of the vector arrows on the beam indicate the distributed values and directions of D . Therefore, when the model is fully covered, the current in the second mode is largely cancelled by itself and the EMCC becomes weak. Meanwhile, the phase of the total current in the second mode is changed at this stage and the sign of the coupling term becomes negative. Therefore, Fig. 24(a) shows that the anti-resonance between mode 2 and mode 3 is basically eliminated. However, the anti-resonance between modes 1 and 2 is not effectively enhanced due to the weak EMCC. The model 4L5MP291-09 with 70 mm long piezoelectric layer has a similar

response as shown in Fig. 24(b). Normally, when the interval between two modes is not too large, full piezoelectric coverage can effectively enhance the off-resonance performance.

5.2. Effect of structural damping

The value of the damping ratio can directly affect the coupling criterion k^2Q_M and the mechanical response simultaneously. Then, the magnitude of the maximum power can be significantly affected when the damping ratio has been changed. In Fig. 26, damping ratio is varied from 0.002 to 0.05. Fig. 26(a) shows the MSAPD FRFs of model 4L5M291-09 PL25 and Fig. 26(b) shows the MSAPD FRFs of model 4L5M291-09 PL70. Apparently, the magnitude of the power density around each mode is significantly affected when the damping ratio has been changed. Using a smaller damping ratio can generate sharper responses not only around resonance, but also around anti-resonance. However, the magnitude of the MSAPD off the resonance cannot be significantly affected by changing the damping ratio. Apparently, a model without anti-resonance between two adjacent modes will help to enhance the capability for broadband power output.

5.3. Effect of the vibration amplitude

The designs of the multi-layer stacked harvesters use masses primarily to alter the natural frequencies and secondarily as spacers. The space between two adjacent layers needs to be adequately large. Therefore, the thickness of the mass should be carefully chosen. Fig. 27 illustrates the relative displacements $U1$, $U2$, $L1$ and $L2$ in a 5-layer stacked harvester model. In particular, $U1$ is the relative displacement between the top of the base layer and the bottom surface of the 1st upper layer (L_{+1}). $U2$ is the relative displacement between the top of L_{+1} and the bottom surface of L_{+2} . $L1$ is the relative displacement between the bottom surface of the base layer and the top of the 1st lower layer (L_{-1}). $L2$ is the relative displacement between the bottom surface of L_{-1} and the top of L_{-2} . When the harvester is stationary, all the relative displacements are 0 mm. When the system is oscillated, all the relative displacements should be smaller than the thickness of the mass, which is 10 mm. If any relative displacement is larger than 10 mm, the two layers will actually touch together. In Fig. 28, under a 9.81 m/s^2 (1 g) base excitation, the relative displacements of some typical models are given, and the results show that all models have enough space for all relative displacements. Since the original damping ratio is 0.02, thicker masses or smaller base excitation are required for the system with a smaller damping ratio like 0.01, which can generate 2 times larger relative

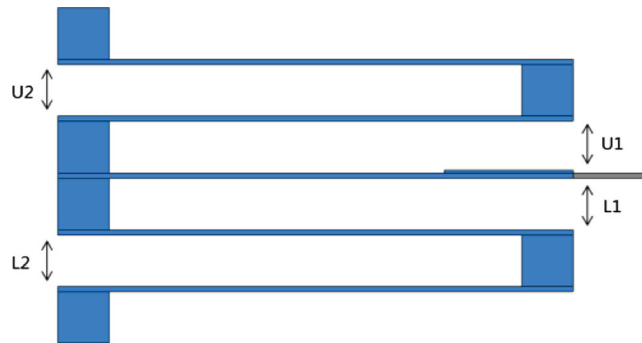


Fig. 27. Relative displacements between each two layers.

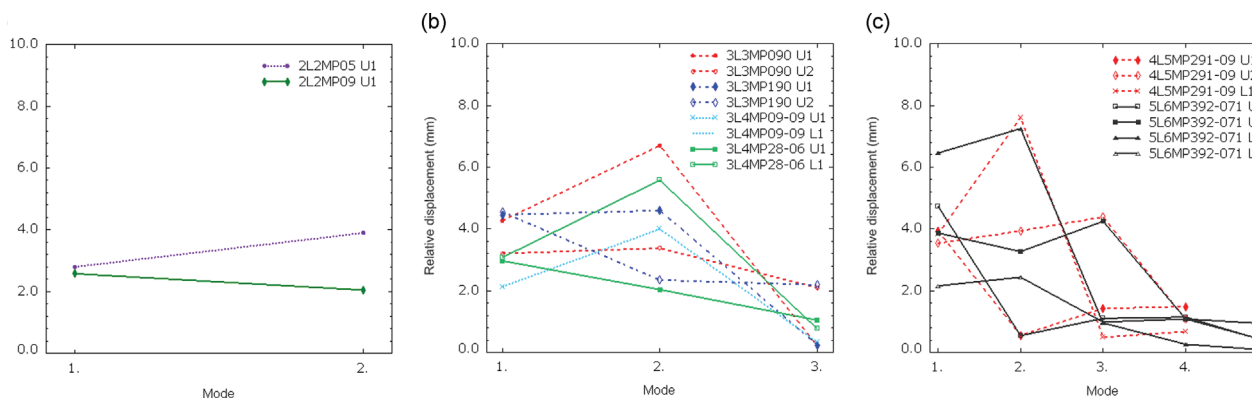


Fig. 28. Relative displacements between each two layers with under 9.81 m/s^2 base excitation.

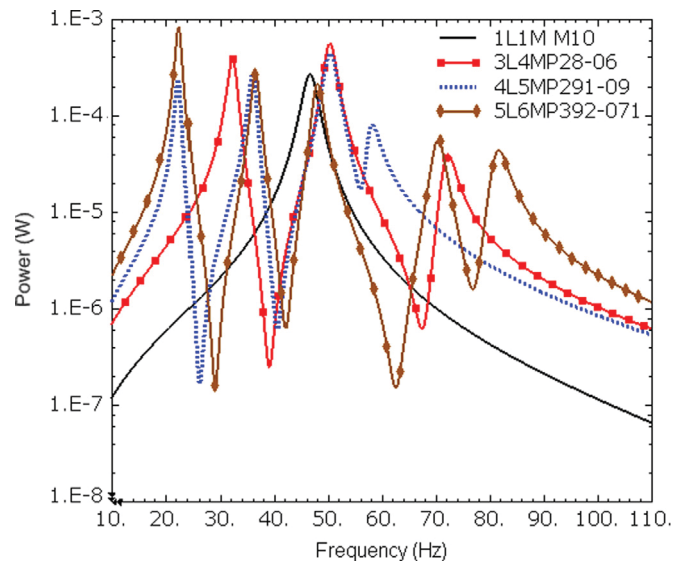


Fig. 29. FRFs and the broadband capability of the power output with 1 m/s^2 base excitation.

Table 12
Comparison of bandwidth of two-layer stacked models.

Minimal power (W)	Frequency range (Hz)				
	1L1M	2L1M	3LAMP28-06	4L5MP291-09	5L6MP392-071
10^{-5}	15.9	22.2	33.7	36	39
10^{-6}	45.9	62.7	84.3	83.9	96.5

displacement. Normally, for a smaller base excitation like 2 m/s^2 , all models can operate without reaching the vibration amplitude limit.

5.4. Effect of operating off-resonance and broadband power output

In fact, the multi-layer stacked harvester can generate the same or even higher level of the power output around each mode in comparison with the first mode of a single layer harvester. Then, the broadband power output can be achieved by combining multiple modes together. In Fig. 29, the power output FRFs from 10 Hz to 110 Hz (100 Hz frequency range) with 1 m/s^2 base excitation of some typical models are given. Table 12 gives the frequency ranges of the two different levels of the minimal power output in those typical models. In particular, the frequency range of the minimal power output 10^{-6} W of model 1L1M is 45.9 Hz, and the frequency range of a ten times higher minimal power output 10^{-5} W of model 1L1M is 15.9 Hz. Using the multi-layer stacked harvester designs can significantly increase the frequency ranges, for instance, Model 3LAMP28-06 can generate 2.1 times frequency range of 10^{-5} W power output and more than 1.8 times frequency range of 10^{-6} W power output than model 1L1M. The five layers model 5L6MP392-071 can generate more than 2 times frequency ranges for both two levels of the minimal power output in comparison with model 1L1M. When the number of the layers is increased, the capability of broadband power output is enhanced.

6. Possibilities for nonlinear responses

In this section, the possibilities for nonlinear harvester responses and considerations for linear versus nonlinear analysis in designing multi-layer stacked harvesters are briefly discussed.

For the designs of multi-resonance harvesters, harvesting energy from several modes efficiently is not easy. In some existing works [9,12,25], one or some modes of these harvesters are easily dominant and produce very large power output, which eventually reduces the performance around other modes. This actually significantly affects the broadband performance and it is clearly due to the lack of proper design of the harvester configurations. This paper focuses on the determination of the modal structural characteristics of multi-resonance harvesters and introduced an effective approach to select the configurations with better structural performance in multimode in order to enhance the broadband performance. Since the modal characteristics of a harvester is unique, once its best performance in linear system with harmonic vibration is enhanced due to the improvement of

modal behaviour, its performance in other more complicated conditions should also be enhanced simultaneously. Therefore, for the current work, the aim of using linear analysis is to identify the configurations of multi-layer stacked harvesters with the optimal or near optimal broadband performance. It should be noted that the optimisation in this paper is configurational whereas linear-versus-nonlinear consideration is dynamics or phenomenological optimisation.

It is also well known that, with high vibration amplitude and large deflection, the harvesters can behave nonlinearly [2,18]. In order to operate the harvesters in the linear regime, a relatively small input and a relatively large damping are required. For the multi-layer harvesters presented in this paper, there is a limitation of vibration due to the thickness of the masses, and the actual space for vibration can be even smaller because some adjacent layers oscillate out of phase. To achieve large deflections and, hence, nonlinear response, thicker masses should be used. However, too large deflections can reduce the lifecycle or even damage the devices especially for relatively brittle monolithic piezoelectric devices, such as piezoelectric ceramic PZT patches, which are used for simulations in this article. Indeed, giving the freedom, a multi-layer harvester could operate with such large deflections that its behaviour could stretch from the linear to the nonlinear range. However, in this case, the thickness of masses must be increased to enable large deflections. Also, flexible piezoelectric composite devices, such as the piezoelectric fibre composite devices and the 1-3 and 0-3 piezoelectric composite devices, should be used to avoid damage. However, these piezoelectric composite devices sacrifice the coupling coefficient, which also significantly affect the performance of harvesters. Ultimately, provision of nonlinear analysis of the multi-layer harvesters is desirable. This is suitable for future studies following the use of linear analysis to select the optimal configurations of the multi-layer harvesters.

The main motivation for designing a nonlinear harvester in some existing works is that the nonlinear harvester has good performance on a wider frequency range than a linear harvester around a single vibration mode [2]. Cammarano et al. [26] state that this is only true if the nonlinear harvester operates in the upper branch region of the nonlinear behaviour. However, the systematic studies of the broadband performance comparison between the nonlinear harvesters and the equivalent linear harvesters with the optimized load are barely given in these works. Also, Cammarano et al. [26] found that the nonlinear harvester exhibits wider bandwidth (3 dB bandwidths for the maximum power) only if the damping is small enough and the nonlinearity is sufficiently high. Furthermore, high nonlinearities require high vibration amplitude and large deflection. Cammarano et al. [26] argue that if the bandwidth is defined such that it avoids operation of the nonlinear harvester in the multiple solution regions, this will amount to effectively assuming that the harvester operates always in the lower solution branch. But, in this condition, the maximum power output of the linear harvester is always significantly higher. In order to maintain the same maximum power for both the linear and the nonlinear system, the damping level of the linear device has to be increased. The result of this is that the bandwidth of the linear harvester increases. Thus, using this definition, the bandwidth of the nonlinear device is always narrower than that of the linear device. Therefore, from the recent work by Cammarano et al. [26], it is clear that to achieve fully nonlinear behaviour of the harvester requires that other conditions be met.

7. Conclusions

In this paper, the multi-layer stacked harvesters have been developed. Initially, a modal approach is developed to evaluate the resonance performance of the harvesters using mass ratio and EMCC as the performance criteria. Mass ratio represents the influences of modal mechanical response to the volumetric power output directly. The system modal electromechanical coupling combines the effects of EMCC and damping ratio simultaneously. Any mode with a too large mass ratio will cause the remaining modes to have small mass ratios and poor performance. Besides, the anti-resonance can significantly affect the capability for broadband power output if the modes are far away from each other. Therefore, the multi-layer stacked harvesters can be optimized by determining good configurations such that models can have close enough modes and evenly distributed mass ratio. The modal frequencies can be tuned and the mass ratios distributed by simply varying the mass positions in the stacked harvester model. However, for the model which has more than 2 layers, the combinations of the different mass positions become too many. Therefore, a screening process is developed based on the modal approach to select the preferred mass positions with larger mass ratio in each mode and close enough modes without performing full DPM analyses. The results show that the designs with preferred mass positions can be used to predict the performance of harvesters of different sizes from low to high frequency ranges and power ranges from microwatts to milliwatts.

The thickness of the masses should be carefully chosen as they are served as spacers. The model with more than two layers can effectively enhance the capability for broadband power output. If the base layer is fully covered with the piezoelectric layer, the phase of the current in higher modes can be reversed and the sign of the coupling term becomes negative. Then, the anti-resonance between each two modes can be eliminated and the capability for broadband power output is enhanced.

Appendix A

A1. Two-sided stacked three-layer model 3LAM ($M_{+1}=3$)

See Figs. A1 and A2.

A2. Two-sided stacked three-layer model 3LAM ($M_{+1}=6$)

See Figs. A3 and A4.

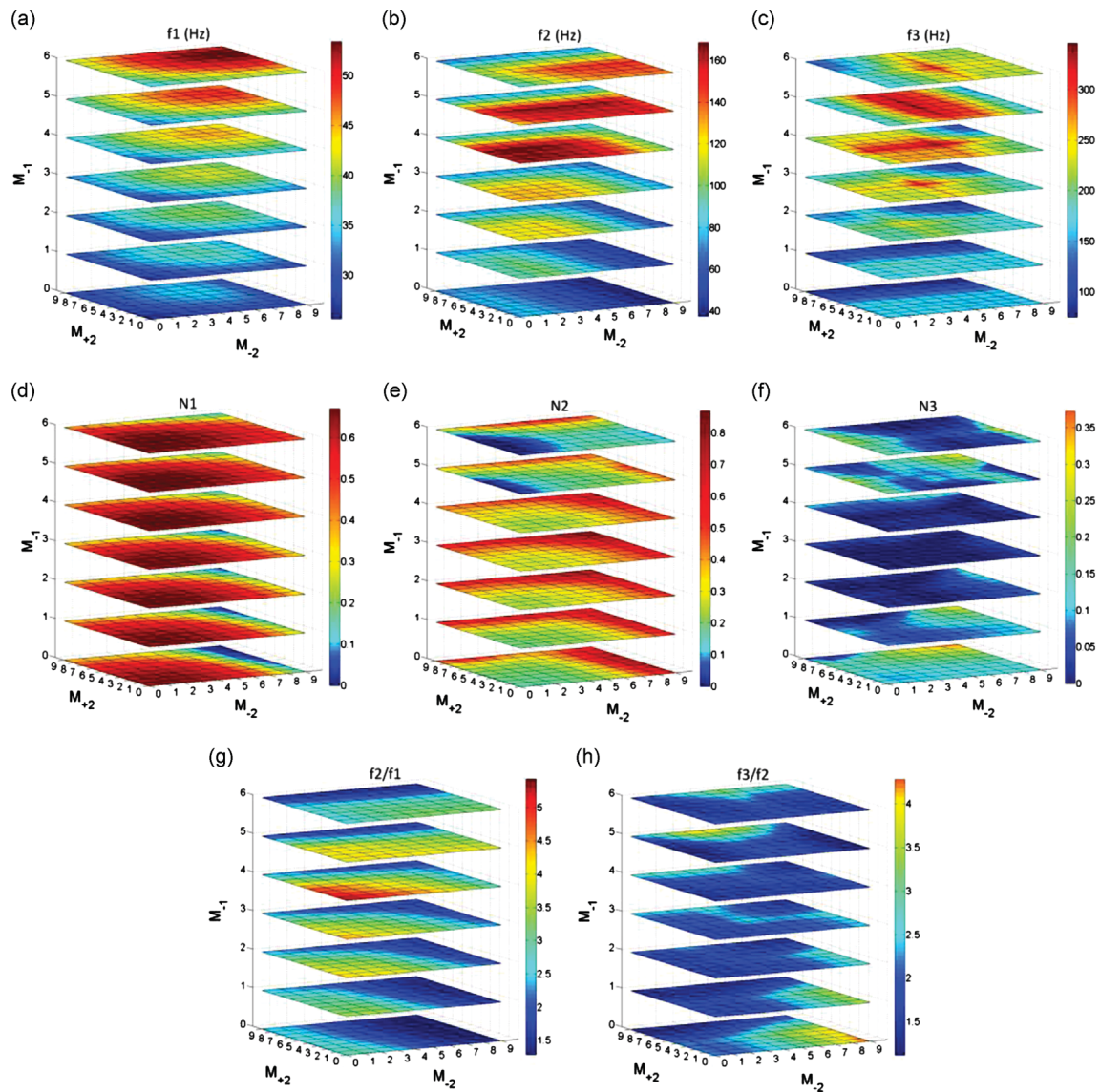


Fig. A1. Model 3L4M with different mass positions of M_{+2} , M_{-1} and M_{-2} ($M_{+1}=3$): (a), (b) and (c) resonance frequencies of modes 1, 2 and 3; (d), (e) and (f) mass ratios of modes 1, 2 and 3; (g) and (h) f_2/f_1 and f_3/f_2 .

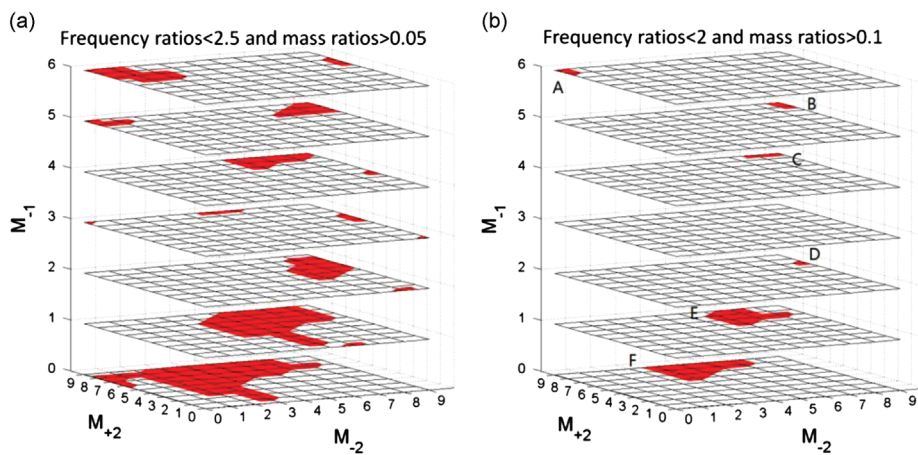


Fig. A2. Determination of the mass positions with better mechanical performance of 3L4M ($M_{+1}=3$): (a) $f_2/f_1 < 2.5$ and $N > 0.05$; (b) $f_2/f_1 < 2$ and $N > 0.1$. A: P38-60 and P39-60 and B: P38-59 and P39-59; C: P39-48 and P39-49; D: P37-29; E: P36-16, P37-16, P37-17, P37-18, P38-16, P38-17 and P39-17; F: P36-04, P37-04, P37-05, P38-04, P38-05, P38-06, P38-07, P39-04, P39-05, P39-06 and P39-07.

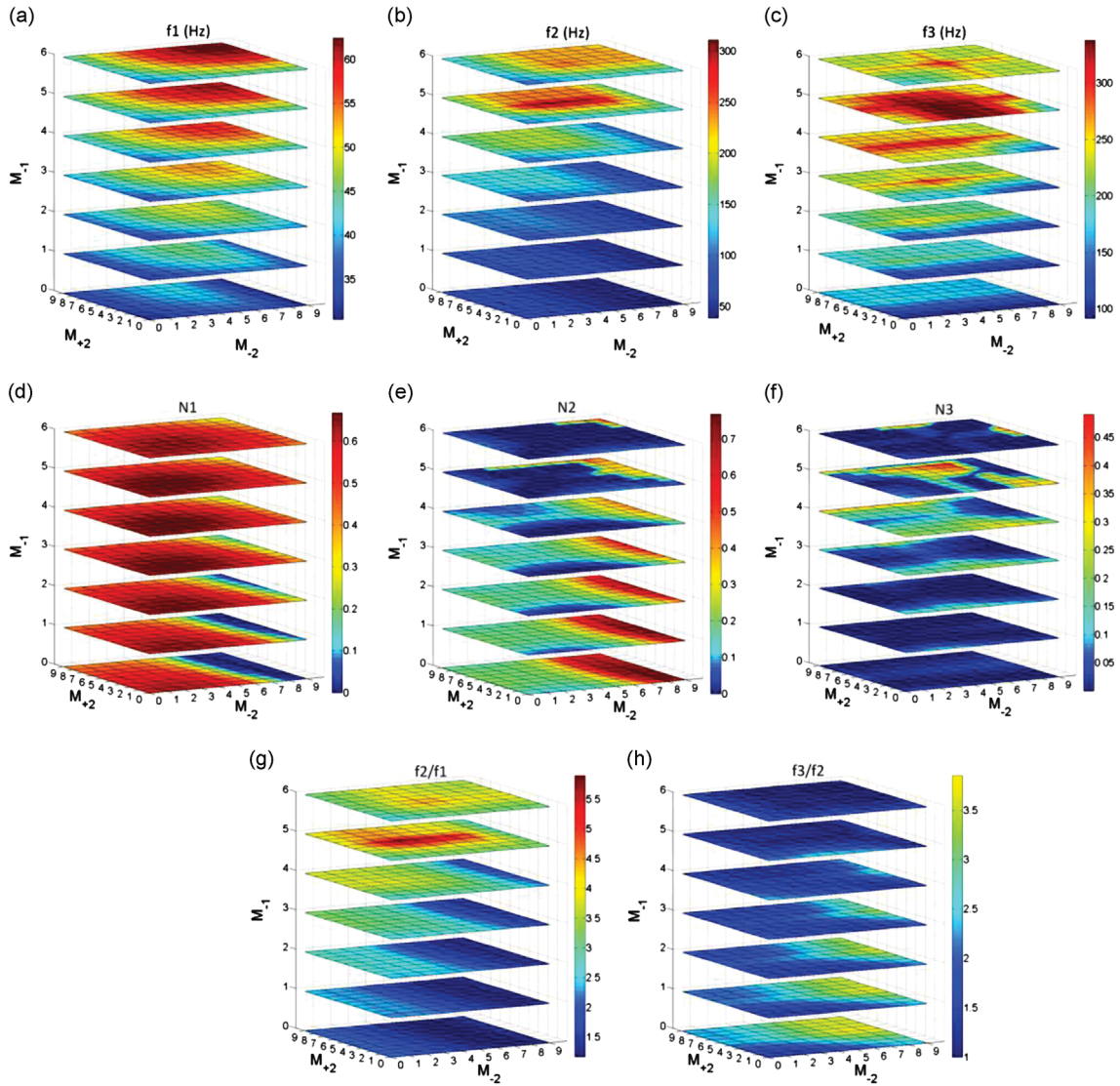


Fig. A3. Model 3LAM with different mass positions of M_{+2} , M_{-1} and M_{-2} ($M_{+1}=6$): (a), (b) and (c) resonance frequencies of modes 1, 2 and 3; (d), (e) and (f) mass ratios of modes 1, 2 and 3; (g) and (h) f_2/f_1 and f_3/f_2 .

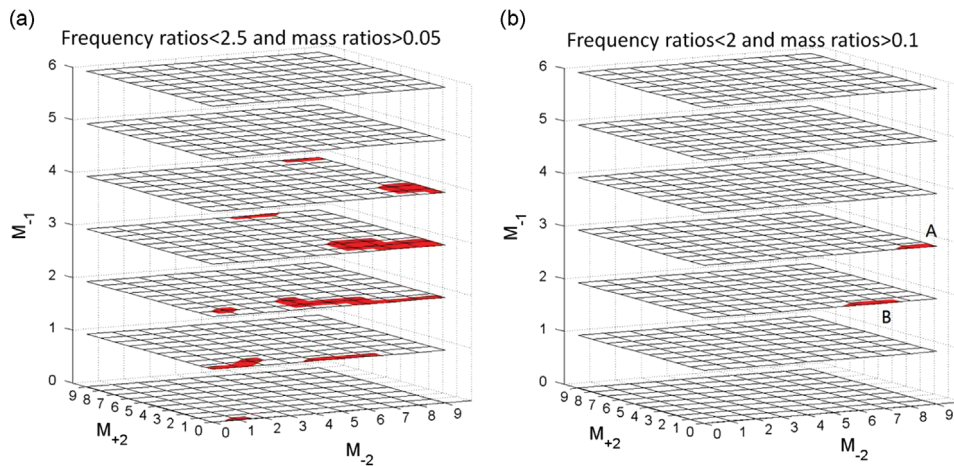


Fig. A4. Determination of the mass positions with better mechanical performance of 3LAM ($M_{+1}=3$): (a) $f_2/f_1 < 2.5$ and $N > 0.05$ and (b) $f_2/f_1 < 2$ and $N > 0.1$. A: P60-38 and P60-39 and B: P60-26 and P60-27.

References

- [1] S.R. Anton, H.A. Sodano, A review of power harvesting using piezoelectric materials (2003–2006), *Smart Materials and Structures* 16 (2007) R1–R21.
- [2] L. Tang, Y. Yang, C.K. Soh, Toward broadband vibration-based energy harvesting, *Journal of Intelligent Materials Systems and Structures* 21 (2010) 1867–1897.
- [3] S. Roundy, Y. Zhang, Toward self-tuning adaptive vibration based micro-generators, *Proc. SPIE 5649, Smart Structures, Devices, and Systems II* (2005) 373–384.
- [4] D. Zhu, S. Roberts, J. Tudor, S. Beeby, *Closed loop frequency tuning of a vibration-based microgenerator*, Proceedings of the PowerMEMS, Sendai, Japan, 2008, 229–232.
- [5] A. Erturk, J. Hoffmann, D.J. Inman, A piezomagnetoelastic structure for broadband vibration energy harvesting, *Applied Physics Letters* 94 (2009) 254102.
- [6] M. Ferrari, V. Ferrari, M. Guizzetti, B. Ando, S. Baglio, C. Trigona, Improved energy harvesting from wideband vibrations by nonlinear piezoelectric converters, *Sensors and Actuators A* 162 (2010) 425–431.
- [7] L. Tang, Y. Yang, C.K. Soh, Improving functionality of vibration energy harvesters using magnets, *Journal of Intelligent Materials Systems and Structures* 23 (2012) 1433–1449.
- [8] M. Ferrari, V. Ferrari, M. Guizzetti, D. Marioli, A. Taroni, Piezoelectric multifrequency energy converter for power harvesting in autonomous microsystems, *Sensors and Actuators A* 142 (2008) 329–335.
- [9] S. Qi, R. Shuttleworth, S.O. Oyadiji, J. Wright, Design of a multiresonant beam for broadband piezoelectric energy harvesting, *Smart Materials and Structures* 19 (2010) 094009.
- [10] S. Lee, B.D. Youn, B.C. Jung, Robust segment-type energy harvester and its application to a wireless sensor, *Smart Materials and Structures* 18 (2009) 095021.
- [11] Q. Ou, X. Chen, S. Gutschmidt, A. Wood, N. Leigh, An experimentally validated double-mass piezoelectric cantilever model for broadband vibration-based energy harvesting, *Journal of Intelligent Materials Systems and Structures* 23 (2012) 117–125.
- [12] W. Zhou, G.R. Penamalli, L. Zuo, An efficient vibration energy harvester with a multi-mode dynamic magnifier, *Smart Materials and Structures* 21 (2012) 015014.
- [13] H. Wu, L. Tang, Y. Yang, C.K. Soh, A novel two-degrees-of-freedom piezoelectric energy harvester, *Journal of Intelligent Materials Systems and Structures* 24 (2013) 357–368.
- [14] Z.S. Chen, Y.M. Yang, Z.M. Lu, Y.T. Luo, Broadband characteristics of vibration energy harvesting using one-dimensional phononic piezoelectric cantilever beams, *Physica B* 410 (2013) 5–12.
- [15] A. Erturk, J. Hoffmann, D.J. Inman, Modeling of piezoelectric energy harvesting from an L-shaped beam mass structure with an application to UAVs, *Journal of Intelligent Materials Systems and Structures* 20 (2009) 529–544.
- [16] M.A. Karami, D.J. Inman, Analytical modeling and experimental verification of the vibrations of the zigzag microstructure for energy harvesting, *Journal of Vibration and Acoustics* 133 (2011) 011002-1.
- [17] A. Erturk, D.J. Inman, A distributed parameter electromechanical model for cantilevered piezoelectric energy harvesters, *Journal of Vibration and Acoustics* 130 (2008) 041002.
- [18] A. Erturk, D.J. Inman, *Piezoelectric Energy Harvesting*, John Wiley & Sons, Chichester, 2011.
- [19] Y. Yang, L. Tang, Equivalent circuit modeling of piezoelectric energy harvesters, *Journal of Intelligent Materials Systems and Structures* 20 (2009) 2223–2235.
- [20] D. Guyomar, G. Sebald, S. Pruvost, M. Lallart, A. Khodayari, C. Richard, Energy harvesting from ambient vibrations and heat, *Journal of Intelligent Materials Systems and Structures* 20 (2009) 609–624.
- [21] A. Erturk and D.J. Inman, Mechanical considerations for modeling of vibration-based energy harvesters. IDETC/CIE September 4–7, 2007.
- [22] A. Erturk, D.J. Inman, On mechanical modeling of cantilevered piezoelectric vibration energy harvesters, *Journal of Intelligent Materials Systems and Structures* 19 (2008) 1311–1325.
- [23] SIMULIA Corp, Abaqus Theory Manual in ABAQUS 6.10 Documentations. 2010.
- [24] X. Xiong, S.O. Oyadiji, Modal electromechanical optimization of cantilevered piezoelectric vibration energy harvesters by geometric variation, *Journal of Intelligent Materials Systems and Structures* 25 (2014) 1177–1195.
- [25] M.A. Karami, D.J. Inman, Electromechanical modeling of the low-frequency zigzag micro-energy harvester, *Journal of Intelligent Material Systems and Structures* 22 (3) (2011) 271–282.
- [26] A. Cammarano, S.A. Neild, S.G. Burrow, D.J. Inman, The bandwidth of optimized nonlinear vibration-based energy harvesters, *Smart Materials and Structures* 23 (5) (2014) 055019.

CHAPTER 9 MODAL OPTIMIZATION OF DOUBLY-CLAMPED BASE-EXCITED MULTILAYER BROADBAND VIBRATION ENERGY HARVESTERS

Xingyu Xiong and S Olutunde Oyadiji

Journal of Intelligent Material Systems and Structures, doi: 10.1177/1045389X14551433,
2014

Modal Optimization of Doubly-clamped Base-excited Multilayer Broadband Vibration Energy Harvesters

Xingyu Xiong and S Olutunde Oyadiji *

School of Mechanical, Aerospace and Civil Engineering,
The University of Manchester, M13 9PL, UK

Abstract

Piezoelectric vibration energy harvesters (VEHs) with doubly-clamped base-excited multilayer structures have been developed. The VEHs consist of stacked H-shaped configurations including up to three beams and two extra masses. One beam is doubly-clamped as a base layer. The extra masses are attached between the base layer and the other two beams to connect them together. By altering mass positions and the thickness of the base layer, the VEHs can generate considerable power output in up to five modes of vibrations. An optimization strategy is established for multi-resonance broadband VEHs designs. The strategy is based on a modal approach, which can determine the modal performance of VEHs using mass ratio and electromechanical coupling coefficient. In particular, mass ratio is used to represent the influence of modal mechanical behaviour on the power density. The design strategy is executed by selecting the multilayer configurations with close resonances and preferred values of mass ratios in multiple modes. These configurations have optimal or near optimal structural performance for broadband power output. The finite element method and a distributed electromechanical parameter model are used to derive the required modal parameters and power output with resistive loads.

Keywords: vibration energy harvesters; piezoelectric energy harvesting; broadband; multiple resonances; optimization

1. Introduction

In recent years, in order to develop self-powered, batteryless wireless sensor and sensor nodes for structural health monitoring, the topic of harvesting small-scale ambient energy has attracted much attention in the research field (Hudak and Amatucci, 2008). As a developing technique with good potential to provide sufficient power, vibration energy harvesting using piezoelectric materials has been widely studied in the last decade (Anton and Sodano, 2007). The vibration energy harvesters (VEHs) can convert mechanical strain energy into electrical energy around vibration modes based on the piezoelectric effect. In real applications, since the sources of environmental vibration are normally random within the lower frequency range, the conventional beam VEHs are limited and ineffective. In order to achieve relatively large power output in a wider frequency bandwidth, broadband techniques are developed, such as magnet VEHs with nonlinear behaviours, resonance tuning technique, and multi-resonance designs (Tang et al., 2010). In particular, the configurations of multi-resonance VEHs are normally designed to contain multiple beam parts, which can generate close resonance frequencies in multiple modes.

* Corresponding author. Tel: 00 44 161 275 4348 Fax: 00 44 161 275 3844

E-mail address: s.o.oyadiji@manchester.ac.uk

As a classic multi-resonance design, VEHs with array of beams have simple configurations and can effectively expand the frequency bandwidth and power output. Ferrari et al. (2008), Xue et al. (2008), Song et al. (2009), Lumentut et al. (2012) theoretically or experimentally developed VEHs with several individual cantilevered beams and tuned the resonance frequency of each cantilevered beam to generate close vibration modes. In their designs, the cantilevered VEHs are only electrically connected. Obviously, the resonance frequencies of these VEHs can be easily controlled to generate very close resonance frequencies. However, only one cantilevered part is active, and the remaining parts of the VEH are almost passive in each mode. Besides, when the number of beams is increased, the electromechanical coupling is decreased due to the fact that a large part of the piezoelectric materials is bonded to the passive cantilevered beams. Eventually, the power density could be significantly reduced. Qi et al. (2010) improved the array of beams design by developing a comb-shaped VEH, which physically connected cantilevered beams to a clamped-clamped beam. The resonances are generated by the interaction between the common base and other cantilevered parts while the piezoelectric material only covered the common base. However, in their design, the power output generated from some cantilevered parts is much smaller than others due to weaker vibration and electromechanical coupling, and the vibration mode mainly generated by the base is far away from the modes generated by the cantilevered parts.

Instead of using multiple cantilevered parts, some researchers developed two-mass VEHs (Ou et al., 2012; Zhou et al., 2012). In their designs, two extra masses are attached on one cantilevered beam. For example, one mass is attached on the centre of the beam, and another is attached on the free tip. The cantilevered beam is divided into two or more parts by the masses, and these parts can generate different resonance frequencies. However, the mass attached to the middle of the beam normally needs to be much heavier than the mass attached to the free tip in order to generate enough close resonances, and one vibration mode can easily behave dominantly. Wu et al. (2013) improved the two-mass design by dividing a cantilevered beam into two parallel narrower cantilevered beams with a gap between them. An additional beam is clamped to the free ends of the two original beams and lies within the space created between the two original beams, with its free end pointing to the clamped ends of the original beams. Their model can generate closer resonances with lighter masses compared with typical two-mass designs. There are also some other multi-resonance designs that have been reported. For example, Erturk et al. (2009) developed an L-shaped VEH, which can generate two close resonance frequencies. Karami and Inman (2011) developed a zigzag VEH, which has up to 11 sub-branches. However, in existing multi-resonance designs, due to the complexity of the configurations, some modes can be far away from others, and some modes are barely active, which limit the capability for broadband power output. A good broadband VEH design requires not only close resonance frequencies, but also relatively large power output in multi-modes.

In this paper, an optimization strategy is introduced initially for multi-resonance broadband VEHs designs. The strategy is based on a modal approach, which can determine the modal performance of the VEHs using mass ratio and electromechanical coupling coefficient. The mass ratio is a modal factor, which is used to represent the influence of the modal mechanical behaviour on the power density of each mode. The optimisation process selects the configurations with optimal or near-optimal structural performance for broadband power output. The selected configurations have close resonances and preferred values of mass

ratios in multiple modes. For multi-resonance VEH designs with complex structures, the strategy is more effective and convenient than conventional methods since there is no need to run full analysis to determine the maximum power output in multiple modes at the first stage.

Furthermore, a novel multilayer VEH is developed and optimized based on the design strategy. The design of the multilayer VEH contains the advantages of the array of beams and the two-mass designs simultaneously. The transverse vibration modes are generated from the interaction between the doubly-clamped base beam and the other two beams. Two extra masses, which divide the other two beams into four cantilevered parts, also serve as spacers to vertically bond the three beams together and ensure enough space for vibration. Thus, the array of beams consists of the cantilevered parts and the base beam. Besides, the piezoelectric materials are only bonded on the base beam near the two clamped ends. The multilayer VEH can easily generate close resonance frequencies and considerable power output in up to five modes. Especially, the positions of masses are moveable. In comparison with previous two-mass designs, there is no need to attach heavy masses or to choose the dimensions of beams carefully in order to achieve broadband power output. Moreover, the configurations with optimal and near-optimal mass positions can be directly used for different scales with different ranges of frequency and power output.

This paper contains six sections: section 2 is on the brief introduction of a general distributed electromechanical parameter model with the utilization of finite element analysis (FEA) software; section 3 is on the introduction of a modal approach to determine the modal performance of VEHs; section 4 is on the implementation of the modal approach and the structural screening sub-process for the design optimization of the multilayer VEHs; section 5 is the analyses of the factors affecting performance of the multilayer VEHs while section 6 contains discussions on the potential effects of large vibration amplitudes. The conclusions of this paper are presented in section 7.

2. Vibration energy harvester modelling

2.1 A distributed parameter electromechanical model

In order to represent the steady-state linear vibration response of a VEH model which is subjected to continuous harmonic excitation, the modal analysis technique can be used and the absolute displacement of the transverse vibration relative to the moving base of the VEH at time t is:

$$u_{rel}(t) = \sum_{r=1}^{\infty} \phi_r \eta_r(t) \quad (1)$$

where ϕ_r is the mass-normalised eigenfunction and $\eta_r(t)$ is the corresponding modal coordinates of the r^{th} mode. Erturk and Inman (2008a) established an analytical model for cantilevered VEHs based on the Euler-Bernouli beam assumptions and using a fully coupled distributed electromechanical parameter model to predict the power output of VEHs with resistive loads. The governing equations of the vibration modal response and electrical behaviour of the VEH model with a resistive load can be written as:

$$\frac{d^2 \eta_r(t)}{dt^2} + 2\zeta_r \omega_r \frac{d\eta_r(t)}{dt} + \omega_r^2 \eta_r(t) + \chi_r v(t) = F_r(t) \quad (2)$$

$$\frac{v(t)}{R_l} + C_p \frac{dv(t)}{dt} - \sum_{r=1}^{\infty} \chi_r \frac{d\eta_r(t)}{dt} = 0 \quad (3)$$

where v is the generated voltage over the thickness of the piezoelectric layer; ζ_r is the damping ratio, ω_r is angular resonance frequency; χ_r is the modal electromechanical coupling term; F_r is the modal mechanical forcing term; C_p is the piezoelectric capacitance and R_l is the resistive load. The steady-state solution of Eq. 2 is:

$$\eta_r(t) = \frac{F_r - \chi_r v}{\omega_r^2 - \omega^2 + j2\zeta_r \omega_r \omega} e^{j\omega t} \quad (4)$$

The voltage across R_l can be represented by:

$$v(t) = \frac{\sum_{r=1}^{\infty} \frac{j\omega F_r \chi_r}{\omega_r^2 - \omega^2 + j2\zeta_r \omega_r \omega}}{\sum_{r=1}^{\infty} \frac{j\omega \chi_r^2}{\omega_r^2 - \omega^2 + j2\zeta_r \omega_r \omega} + \frac{1}{R_l} + j\omega C_p} e^{j\omega t} \quad (5)$$

Then, the complex power in the frequency domain is $v(j\omega)(\frac{v(j\omega)}{R_l})^*$ and the average power output is $|v|^2/2R_l$ (ignore electrical losses). The vibration response of the beam relative to its base is:

$$u_{rel}(x, t) = \sum_{r=1}^{\infty} \phi_r(x) \frac{F_r - \chi_r v}{\omega_r^2 - \omega^2 + j2\zeta_r \omega_r \omega} e^{j\omega t} \quad (6)$$

However, when the VEh model is not an uniform beam, the derivation of the eigenfunction and other modal parameters can be complicated and tedious. To overcome the limitations, finite element analysis (FEA) software packages like ABAQUS and ANSYS are widely used at the design stage. Existing works have theoretically and experimentally proved that FEA simulation can be employed as a useful tool to provide good guidelines for the linear VEh designs (Lee et al., 2009; Berdy et al., 2012; Zhou et al., 2012; Patel, 2013; Wu et al. 2013).

2.2 Finite element analysis

For the eigenvalue extraction analysis, the equation solved by the FEA software is:

$$[M]\ddot{\underline{u}} + [K]\underline{u} = 0 \quad \text{or} \quad (-\omega^2[M] + [K])\underline{U} = 0 \quad (7)$$

where $[M]$ is the mass matrix, $[K]$ is the stiffness matrix, \underline{u} is the vector of nodal displacements and \underline{U} is the eigenvector, which is the vibration mode shape. The FEA software solves the eigenvalue problem to determine the undamped angular natural frequencies ω_r , the generalised modal mass m_m and the modal participation factor γ associated with each mode.

For the piezoelectric analysis, the system equations solved by the FEA software are:

$$[M]\ddot{\underline{u}} + [C]\dot{\underline{u}} + [K]\underline{u} + [X]\underline{\varphi} = \underline{P} \quad (8)$$

$$\underline{Q} + [X]\underline{u} - [D]\underline{\varphi} = 0 \quad (9)$$

where $[C]$ is the damping matrix, $[X]$ is the piezoelectric coupling matrix, $[D]$ is the dielectric stiffness matrix, $\underline{\varphi}$ is the vector of nodal electric potential, \underline{P} is the mechanical force vector and \underline{Q} is the electrical charge vector. By operating the steady-state analysis, the FEA software can determine the nodal displacements, potentials gradients and electrical flux densities.

In Figure 1, a doubly-clamped single layer VEH model which has an extra mass attached is shown and subsequently developed in ABAQUS. Table 1 gives the dimensions and material properties of the model. The piezoelectric layer is divided into two patches and fixed near the two clamped areas of the beam. To determine the forcing function F_r at each resonance frequency with a vertical harmonic base excitation $\ddot{u}_b = Y_0 \omega^2 e^{j\omega t}$, letting the voltage over the thickness of the piezoelectric layer to be zero in FEA simulations (i.e. $v = 0$ in Eq. 4), then, for the r^{th} mode:

$$F_r = (\omega_r^2 - \omega^2 + j2\zeta_r \omega_r \omega) \eta_r(j\omega_r) = 2\zeta_r \ddot{u}_{rel} \sqrt{m_{mr}} \Big|_{\omega=\omega_r} \quad (10)$$

Thus, F_r can be determined using the absolute displacement data derived in the FEA results from the natural frequency extraction analysis. By substituting $v(t)/R_l$ with $i(t)$ in Eq. 3 ($v = 0$):

$$i_r = j\omega \chi_r \eta_r(j\omega_r) = \sum_{r=1}^{\infty} \frac{j\omega F_r \chi_r}{\omega_r^2 - \omega^2 + j2\zeta_r \omega_r \omega} \Big|_{\omega=\omega_r} \quad (11)$$

The complex current i_r generated due to base excitation can be derived from the electrical flux densities data in the FEA results. Then, the modal coupling term χ_r can be determined from Eq. 11 for multiple modes or any single mode. In order to analyse the performance of broadband VEHs conveniently, structural damping or loss factor is used and defined as 0.04 in this paper, which gives the modal damping ratio as $\zeta_r = 0.02$. Since the damping affects the power output significantly, for the real applications, the damping ratio needs to be obtained experimentally.

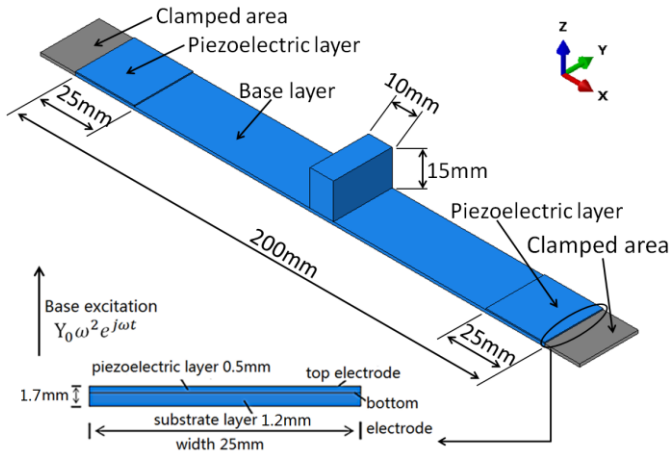


Figure 1: Doubly-clamped single layer model *ILIMA0*

Table 1: Properties of the VEH model *ILIMA0*

Parameters	Properties
Beam length/width/thickness	200/25/1.2 mm
Mass length/width/thickness	25/10/15 mm
Thickness of piezoelectric layer	0.5mm
Length of one piezoelectric plate	25mm
Piezoelectric materials	PZT-5A*
Density of piezoelectric layer	7750kg/m ³ *
Clamped dielectric constant ϵ_{33}^S	7.349x10 ⁻⁹ F/m*
Piezoelectric layer Young's modulus	60.9x10 ⁹ N/m ² *
Piezoelectric constant e_{31}	-5.4C/m ² *
Transverse coupling factor k_{31}	0.344*
Density of substrate layer/mass	7850kg/m ³
Substrate layer/mass Young's modulus	200x10 ⁹ N/m ²
Structure damping	0.04

*Morgan Technical Ceramics standard

3. Performance determination using a modal approach

3.1 Determination of modal performance

To determine the performance of VEHs, the full analysis using the distributed electromechanical parameter model (DPM) is required by the conventional method, which presents frequency response of the output power by carrying out frequency-by-frequency steady-state analysis. However, the conventional method cannot directly determine the optimal performance of a VEH unless the model has been thoroughly analysed, and the optimal load has been determined. In the conventional method, it is also hard to find out how the change of configuration affects the performance electromechanically in general VEH designs.

Guyomar et al. (2009) predicted the maximum average power output directly using a modal electromechanical criterion $k^2 Q_m$. Their prediction was based on a lumped single degree-of-freedom (SDOF) model (standard rectifier interface; no electrical losses; matched optimal load):

$$P_{max} = \frac{F_m^2}{2c_m} \frac{\pi k^2 Q_m}{(\pi + k^2 Q_m)^2} \quad \text{when } k^2 Q_m \leq \pi \quad (12)$$

$$P_{max} = \frac{F_m^2}{8c_m} \quad \text{when } k^2 Q_m \geq \pi \quad (13)$$

where k is the modal electromechanical coupling coefficient (EMCC); $Q_m = 1/2\zeta$ is the quality factor; F_m and c_m are lumped mechanical force and damping coefficient, respectively. If $k^2 Q_m > \pi$, the power output given by Eq. (13) is maximized and purely mechanical due to the strong electromechanical coupling of the system. When $k^2 Q_m < \pi$, reachable power given by Eq. (12) is always smaller than the maximum power. However, in Guyomar's work, the modal mechanical behaviour has not been accurately represented in multiple degrees of freedom systems. Besides, in comparison with using DPM, the electromechanical coupling cannot be fully involved in Eq. (12) and (13) because the back coupling has been ignored. Erturk and Inman (2008b) introduced a correction factor γ to improve the accuracy of the SDOF model. In their work, the relative motion transmissibility predicted using the SDOF model with the correction factor has a very good agreement with the relative motion transmissibility predicted using the Bernoulli-Euler beam model in a wide frequency band around the fundamental resonance. In fact, the correction factor γ , which is also called the modal participation factor, indicates how strongly motion in the x -, y - or z -direction or rotation about one of these axes is represented in the eigenvector of that mode (SIMULIA, 2010). However, Erturk and Inman only analysed the purely structural responses using the correction factor; the effects on the electrical behaviour and power output have been ignored.

Xiong and Oyadiji (2013) analysed both the modal structural and electromechanical performance of cantilevered VEHs using mass ratio and EMCC. In particular, a parametric study has been presented using DPM to determine the influences of mass ratio and EMCC on the power output around the resonance frequency. In their work, as a modal structural criterion depends on the modal participation factor γ , mass ratio is introduced to represent the influence of the modal mechanical behaviour on the power density directly. In the lumped SDOF model, the motion and electrical governing equations of a VEH with harmonic base excitation are given by:

$$\begin{cases} m_m \ddot{z} + c_m \dot{z} + k_m z - \alpha v = F_m \\ C_p \dot{v} + \frac{v}{R_l} - \alpha \dot{z} = 0 \end{cases} \quad (14)$$

where z is the relative displacement related to the base motion y ; α , m_m and k_m are the lumped coupling factor, generalized modal mass and effective stiffness, respectively. The corrected lumped forcing function with the modal participation factor γ for the r^{th} mode is:

$$F_{mr} = -\gamma_r m_{mr} \dot{y} \quad (15)$$

and the EMCC k and lumped parameters for the r^{th} mode are:

$$k^2 = \frac{\alpha_r^2}{k_{mr} C_p + \alpha_r^2}; \quad \alpha = \chi \sqrt{m_{mr}}; \quad c_{mr} = 2\zeta_r \sqrt{k_{mr} m_{mr}}; \quad \omega_r = \sqrt{k_{mr}/m_{mr}} \quad (16)$$

By substituting Eqs. (15) and (16) into Eq. (13), the maximum power can be rewritten as:

$$P_{max} = \frac{F_{mr}^2}{8c_{mr}} = \frac{\gamma_r^2 m_{mr}}{16\xi_r \omega_r} \dot{y}^2 = \frac{m_{er}}{16\xi_r \omega_r} \dot{y}^2 \quad (17)$$

m_e is called the effective mass which represents the mass participating in the forcing function and motion. It should be noted that the generalized modal mass m_m in this paper is called effective mass by Erturk and Inman (2008b). The sum of the effective masses for all modes is the total mass m_T of the whole model (SIMULIA, 2010):

$$m_{er} = \gamma_r^2 m_{mr}; \quad \sum_{r=1}^{\infty} m_{er} = m_T \quad (18)$$

Then, mass ratio for the r^{th} mode is defined as:

$$N_r = \frac{\gamma_r^2 m_{mr}}{m_T} = \frac{m_{er}}{m_T} \quad (19)$$

The mass ratio N is the percentage ratio of the effective mass to the total mass. It depends on the modal participation factor and represents how much mass of each mode effectively participates in the overall motion and represents the effect of the modal mechanical behaviour on the forcing function. The mass ratio is always smaller than 1 for structures with multiple degrees of freedom. In fact, the mass ratio linearly affects the power density (Xiong and Oyadiji, 2013). In this paper, the mean squared acceleration weighted power density (MSAPD), which is defined as the average power per 1m/s^2 base excitation per cubic centimetre (cm^3), has been used. By substituting Eq. (15) into Eq. (13), the maximum MSAPD can be written as:

$$\text{MSAPD}_{max} = \frac{N_r \rho}{16\xi_r \omega_r} * 10^{-6} (\text{W s}^4 / \text{cm}^3 \text{ m}^2) \quad (17)$$

where ρ is the mass density (kg/m^3). Figure 2 shows the maximum MSAPD as a function of $k^2 Q_m$ for different mass ratios (for a VEH with $f=46$ Hz, $Q_m=25$ and $\rho \approx 7840$ kg/m^3). The results given in this parametric study are determined using DPM with the optimal resistive load. The piezoelectric material is assumed to have stronger or weaker piezoelectric effects and the forcing function is also adjusted to ensure that the mass ratio has been correctly represented in DPM. The results show that, for different values of $k^2 Q_m$, mass ratio always linearly affects the maximum power density. EMCC only affects the maximum MSAPD when the value of $k^2 Q_m$ is smaller than 2. Therefore, using mass ratio and EMCC can directly evaluate the modal structural and electromechanical performance of VEHs, respectively, without the need of carrying out full analysis.

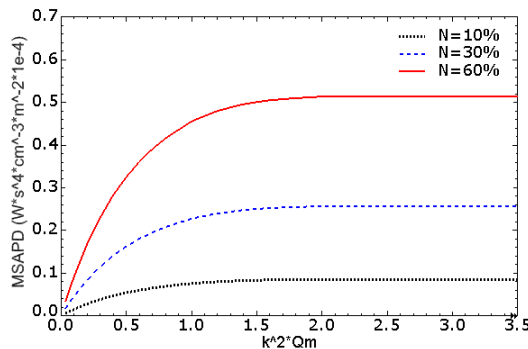


Figure 2: Parametric study of maximum MSAPD as function of $k^2 Q_m$ for different mass ratio N

3.2 A modal approach

In this paper, a modal approach, which is based on the two modal criteria, mass ratio and EMCC, is introduced for multi-resonance broadband VEH designs. In Figure 3, a conventional approach for general VEH designs (Figure 3a) is compared with the modal approach (Figure 3b). Instead of directly carrying out full analysis using DPM to determine performance of VEHs, the modal approach uses mass ratio and EMCC as two filters. Using the modal approach is much easier to determine how the change of configuration affects the performance in both mechanical and electromechanical domains. Since a VEH with good broadband performance requires both close resonance frequencies and relatively large power output in multi-modes, the modal approach using two modal performance filters becomes more efficient than the conventional approach for broadband VEH designs.

Although, the modal performance of VEHs can be evaluated using the modal approach, the full steady-state analysis is still required to derive the electromechanical coupling term and EMCC (see Eq.11). The natural frequencies and mass ratio are determined directly using the modal analysis in FEA software. Then, a structural screening sub-process of the modal approach is used to determine the optimal or near-optimal modal mechanical performance of the broadband VEHs. This sub-process selects the VEH configurations with close resonances and favourable values of mass ratio initially as shown in Figure 3 (c).

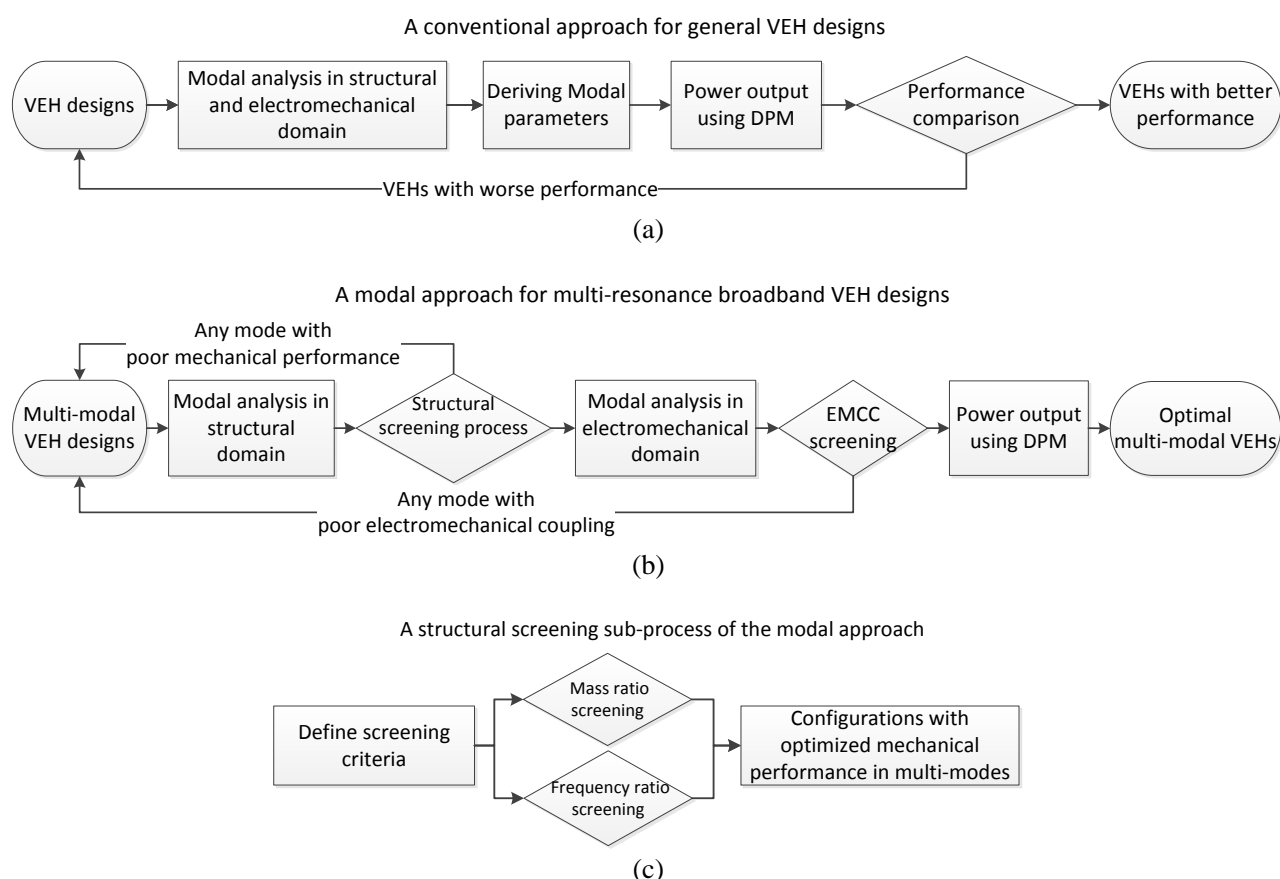


Figure 3: Flow charts of (a) a conventional approach for general VEH designs, (b) a modal approach for broadband VEH designs, and (c) a structural screening sub-process of the modal approach.

3.3 Implementation of the modal approach

The procedures for carrying out the modal approach by FEA simulations can be summarised by the

following steps.

Step 1: Run the natural frequency extraction analysis to obtain the short circuit resonance frequency f_r , generalized modal mass m_m and the modal participation factor γ . Use Eq. 19 to derive mass ratio N .

Step 2: Run the steady-state dynamics analysis at each natural frequency, apply a base excitation to obtain the complex current i with a short-circuit condition. Use Eqs 10, 11 and 16 to derive the forcing function F_r , modal electromechanical coupling factor χ , and the EMCC k , respectively.

Step 3: With known mass ratio and EMCC, the structural and electromechanical modal performance in each mode are determined. For the VEH with preferred modal performance, use DPM (Eq. 5) to derive the power output FRFs with resistive loads around single mode or multiple modes.

For the configurational optimization of multi-resonance VEHs, the structural screening process (see Figure 3c) is operated after step 1 without the need to carry out the steps 2 and 3 for each configuration unless the configuration with optimal or near-optimal structural broadband performance is determined.

3.4 Modal performance determination of model *1L1MA0* using the modal approach

Table 2 shows the modal data of the first four transverse vibration modes of the model *1L1MA0* (see Figure 1), which is simply a doubly-clamped beam VEH with a rigid mass. The modal parameters f_r , m_m , γ and m_e were obtained from the FEA natural frequency extraction analysis. The EMCC k was derived from the FEA steady-state analysis using the DPM model. Figure 4 shows the predicted frequency response functions (FRFs) of the MSAPD using DPM with different resistive loads. The table and figure show that the 1st mode has the lowest resonance frequency, strongest EMCC and largest mass ratio. Therefore, the first mode can generate the greatest power density. However, since the 2nd mode has very small N and very weak k , the peak of the FRF of the MSAPD near the 2nd modes disappears. The peak of the MSAPD of the 3rd mode is decreased significantly in comparison with the MSAPD peak of the 1st mode due to the much higher resonance frequency and the significant decrease of N and k . Obviously, the doubly-clamped single layer VEH cannot produce broadband power output. Firstly, the higher modes are far away from the first mode. Secondly, the modal performances of the higher modes are much worse than the modal performance of the first mode. In order to produce relatively large power output in a wider frequency range, a typical broadband VEH requires close resonance frequencies and evenly distributed mass ratios and acceptable EMCC in multi-modes.

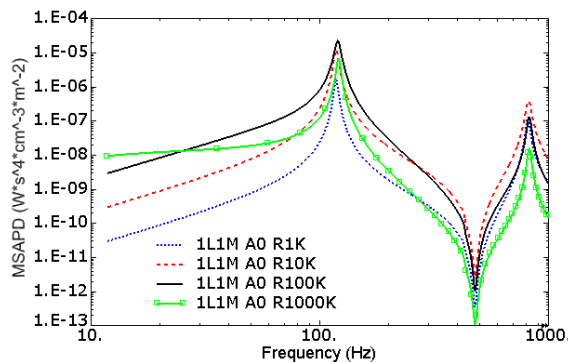


Figure 4: MSAPD FRFs of the model *1L1MA0* with different resistive loads.

Table 2: Modal parameters of the first four transverse vibration modes of VEH model *1L1MA0*

Mode No.	f_r (Hz)	m_m ($\times 10^{-3}$ kg)	γ	m_e ($\times 10^{-3}$ kg)	m_r ($\times 10^{-3}$ kg)	$N=m_e/M$	k	$k^2 Q_m$
1	118.0	46.50	1.138	60.21	81.38	73.98%	0.219	1.204
2	430.2	21.80	0.019	0.008		0.009%	0.006	0.000
3	811.5	16.95	0.707	8.478		10.42%	0.169	0.718
4	1174	17.39	0.095	0.166		0.192%	0.018	0.008

4. Optimal design of doubly-clamped multilayer VEHs

4.1 Modal performance determination of a doubly-clamped two-layer VEH

For the initial demonstration of the use of the modal approach for the broadband VEH designs, a doubly-clamped two-layer VEH model *A0-BT12* is analysed in comparison with *1L1MA0*. The configuration of model *A0-BT12* is given in Figure 5. The details of the dimensions and configurations of doubly-clamped two-layer VEHs are given in section 4.2. Table 3 shows the resonance frequencies, mass ratio and EMCC in the first four modes. In the first three modes, model *A0-BT12* has much closer resonance frequencies in comparison with the single layer model *1L1MA0*. In addition, the mass ratio distributions of *A0-BT12* are more even than *1L1MA0*. Therefore, the design of a broadband VEH, *A0-BT12* will have a much better structural performance than *1L1MA0*. Besides, the differences of the modal EMCC of *A0-BT12* is smaller than those of *1L1MA0*, especially between the first and second mode. Then, as shown in Figure 6, the power densities (MSAPD) of *A0-BT12* around the first three modes are more evenly distributed and relatively larger than those of *1L1MA0*. For a specified acceleration input, it is straightforward and convenient to use the resonance frequencies and mass ratios to evaluate the structural performance of broadband VEHs initially. Once the system coupling in multiple modes is not too weak, the model with good structural performance can generate broadband power output. Then, the performance of the selected VEH model can be thoroughly analysed by predicting the corresponding MSAPD FRFs in multiple modes.

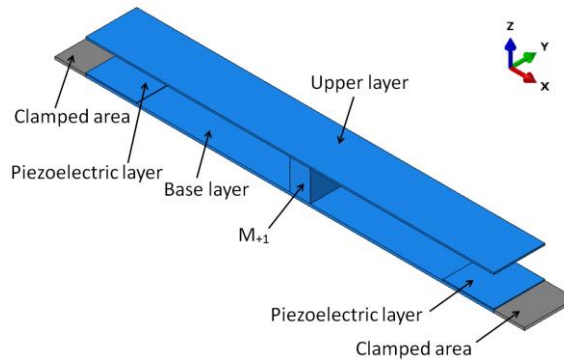


Figure 5: Doubly-clamped two-layer VEH model *A0-BT12*

Table 3: Modal parameters of the first four transverse vibration modes of model *A0-BT12*

Mode No.	f_r (Hz)	m_m ($\times 10^{-3}$ Kg)	γ	m_e ($\times 10^{-3}$ kg)	m_r ($\times 10^{-3}$ kg)	$N=m_e/M$	k	$k^2 Q_m$
1	58.70	4.537	2.139	20.75	112.8	18.40%	0.076	0.143
2	72.07	4.314	2.520	27.40		24.29%	0.089	0.200
3	116.1	22.50	1.383	43.06		38.18%	0.184	0.846
4	315.4	14.67	0.069	0.071		0.063%	0.004	0.000

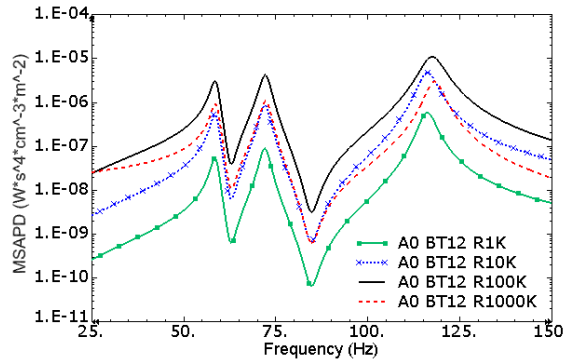


Figure 6: MSAPD FRFs of the model *A0-BT12* with different resistive loads.

The modal approach and the structural screening sub-process are used in sections 4.2 and 4.3 for the optimal multi-layer VEH designs. Once the configurations with preferred structural performance have been selected, the full analyses have also been carried out for the determination of the system coupling and MSAPD FRFs of VEHs with optimal loads.

4.2 Optimal design of two-layer VEH

The two-layer model contains two rectangular beams and one extra mass (see Figure 5). The two-layer model is *ILIMA0* (see Figure 1) with an attached upper layer beam, and the upper layer is fixed on the extra mass named M_{+1} . The width and length of the upper layer are the same as the substrate layer of *ILIMA0*. The thickness of the upper layer is fixed as 0.8mm.

In this paper, in order to determine the optimal or near optimal configurations of the multi-layer VEHs, the thickness of the base layer is varied from 0.8mm (denoted *BT08*) to 1.6mm (denoted *BT16*) while the locations of the extra masses are designed to be changeable. Since the width of an extra mass is 10mm, and the half length of the beam is 100mm, the positions of the masses on one half of the beam from the centre to the clamped end are divided into 10 portions and they are identified by numbers from 0 to 9. However, since the mass positions from 7 to 9 are occupied by the piezoelectric layer, the mass positions from 0 to 6 are eligible. In order to demonstrate the naming of mass positions of all multi-layer VEHs conveniently, a three-layer model is given in Figure 7 (the three-layer VEH will be discussed in greater details in section 4.3). The mass located on the right side is designated as *A* side and the left side is designated as *B* side. For instance, the mass position of Figure 5 is *A0* (mass M_{+1}) and the mass position of Figure 7 (three-layer VEH) is *A0-B1* (masses M_{+1} and M_{-1}). All models in section 4 are named after “mass position + base layer thickness”. For example, model *A0-BT12* is a model with mass position *A0* and the base layer thickness is 1.2mm. The extra mass M_{+1} firstly serves as a spacer between the two layers. It also separates the upper layer into two cantilevered parts and tunes the resonance frequency from the base layer. Therefore, the base layer and the two cantilevered parts of the upper layer can generate close resonance frequencies in the first three transverse vibration modes. By relocating M_{+1} and altering the thickness of the base layer, the first three modes can be tuned to be close enough to achieve broadband power output. Besides, since the two-layer VEHs with the mass positions from *B0* to *B6* are symmetric to the models with mass positions from *A0* to *A6*, the predicted performance of the two-layer VEHs with mass positions *B0* to *B6* are identical to those of *A0* to *A6*. Therefore, only the results for *A0* to *A6* are presented.

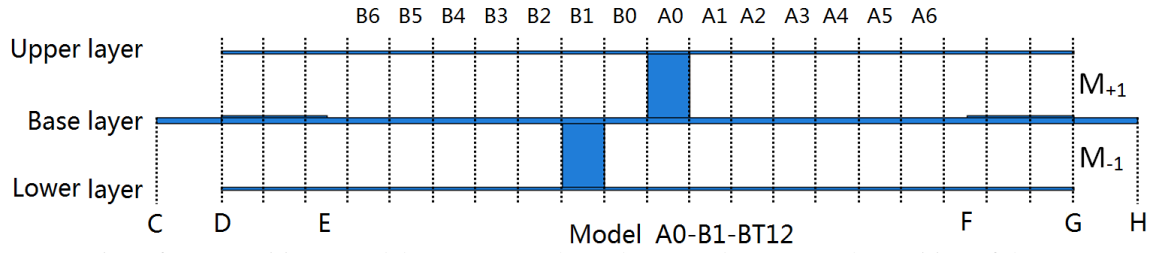


Figure 7: Naming of mass positions; model $A0-B1-BT12$ has 3 layers and 2 masses, the position of the upper mass M_{+1} is $A0$ and the position of the lower mass M_{-1} is $B1$. CD and GH = clamped length of base layer; DE and FG =covered by the piezoelectric layer.

Figure 8(a), (b) and (c) show contours of the natural frequencies of the first three modes. Obviously, when the thickness of the base layer is increased, the natural frequencies of the three modes are all increased. When the mass position is altered from $A0$ to $A6$, the first natural frequency is decreased but the second and third natural frequencies are increased. This is because one cantilevered part becomes longer and generates a lower natural frequency, while another part becomes shorter and generates a higher natural frequency, and the base layer also generates a higher natural frequency. Figure 8(d), (e) and (f) show contours of the mass ratio of the first three modes. The dark blue and red represent the configurations with too small and too large mass ratios, respectively. Figure 9(a) and (b) show the contours of the frequency ratios f_2/f_1 and f_3/f_2 , respectively. The blue colour represents the configurations with small frequency ratios. Obviously, when the mass positions are altered from $A2$ to $A6$, the frequency ratio f_2/f_1 becomes too large due to the large differences between the first two natural frequencies generated by the two cantilevered parts.

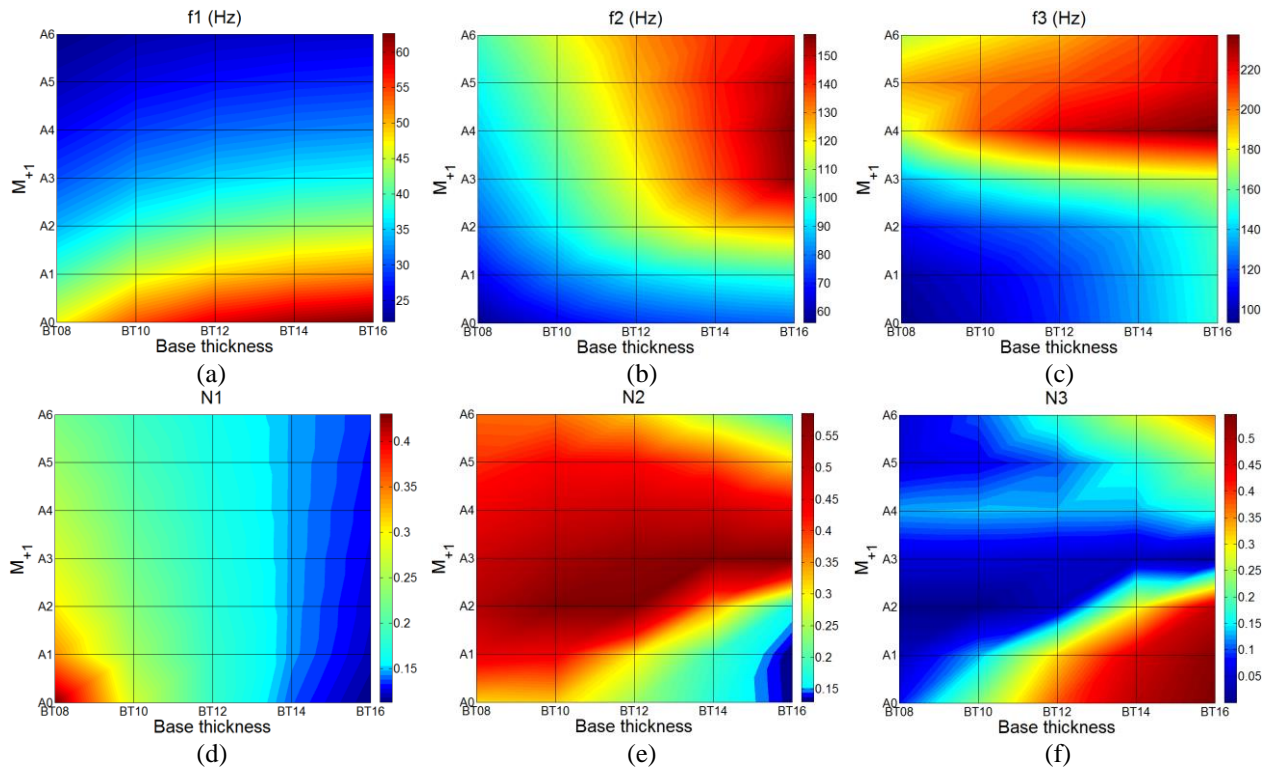


Figure 8: Contours of the resonance frequencies and mass ratio of the first two modes with different mass positions of M_{+1} and different base thicknesses for the two-layer VEH. (a)-(c): resonance frequencies of mode 1, 2 and 3; (d)-(f): mass ratios of mode 1, 2 and 3.

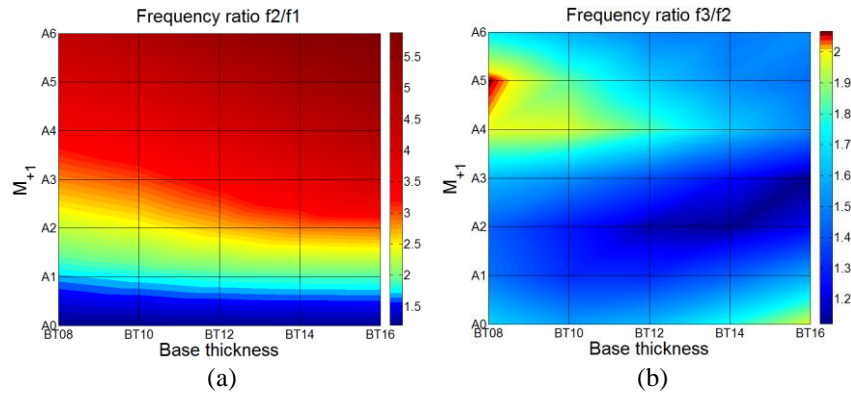


Figure 9: Contours of the frequency ratios: (a): f_2/f_1 ; (b): f_3/f_2 .

Since the combinations of the 7 different mass positions and 5 different base thicknesses are 35, deriving all configurations by running full analysis is ineffective. Thus, the structural screening process is used to select the mass positions with the preferred values of frequency ratio and mass ratio. The screening criteria are specified as frequency ratios < 2 and mass ratios > 0.1 or frequency ratios < 1.75 and mass ratios > 0.15 . The second screening criterion is stricter than the first one. Then, screening results which meet the second screening criterion should contain a reduced number of acceptable configurations. Figure 10 shows the screening results, and the selected configurations are located in the shaded area. Figure 10(b) shows a reduced number of preferred configurations which have better structural performance than most of the results given in Figure 10(a), and Figure 10(b) shows that the two-layer VEH configurations $A0-BT10$ and $A0-BT12$ have optimal structural performance.

Moreover, some configurations can partly fulfil the screening criteria and these configurations may still achieve acceptable performance. Figure 11(a) shows the screening results of the configurations that meet the screening criteria frequency ratios < 1.75 and mass ratios > 0.15 in modes 1 and 2 and Figure 11(b) shows the screening results that meet the same screening criteria in modes 2 and 3. In fact, the overlapped area of Figure 11(a) and (b) are the configurations $A0-BT10$ and $A0-BT12$ given in Figure 10(b). Apparently, the screening results have shown that a lot of configurations have poor structural performance. Instead of operating full analyses, using the modal approach to screen the VEHs initially is much more convenient, straightforward, quicker and cheaper to implement in terms of computing time.

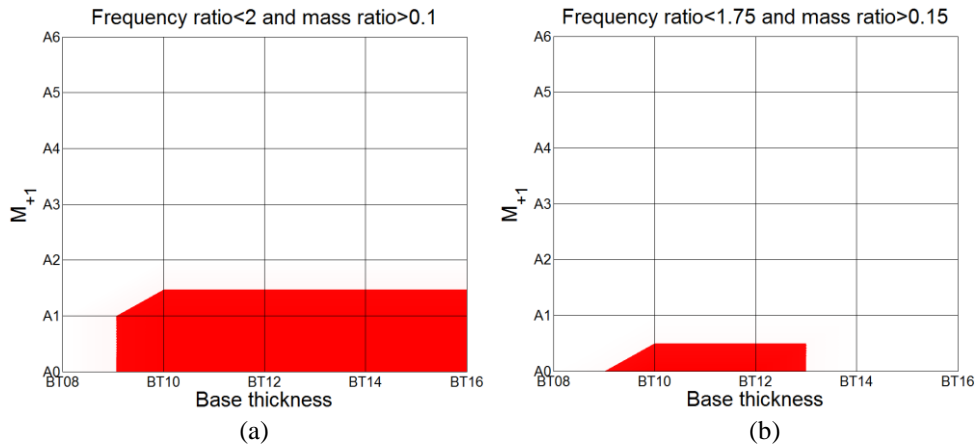


Figure 10: Configurations of two-layer model which meet the screening criteria in the first three modes. The shaded area is the selected configurations: (a) $f_2/f_1 < 2$ and $N > 0.1$; (b) $f_2/f_1 < 1.75$ and $N > 0.15$

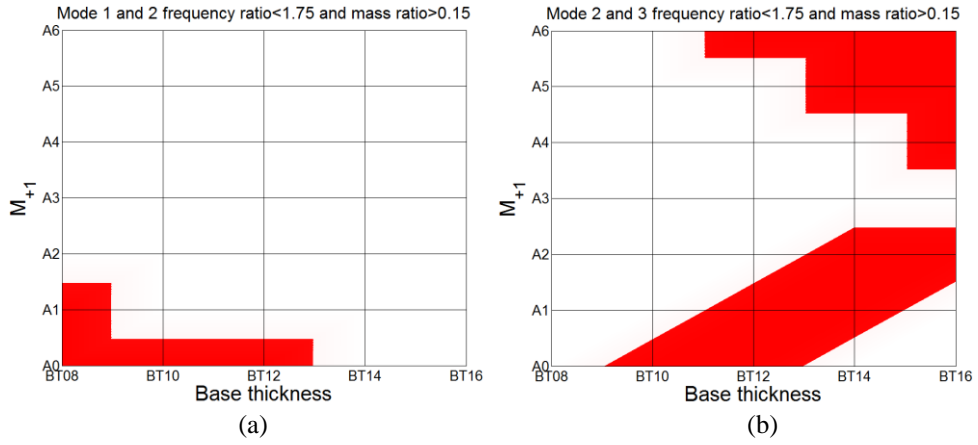


Figure 11: Configurations of two-layer model that partly meet the screening criteria: (a) $f_2/f_1 < 1.75$ and $N > 0.15$ in modes 1 and 2; (b) $f_3/f_2 < 1.75$ and $N > 0.15$ in modes 2 and 3

After operating the structural screening process to determine the configurations with better structural performance, full analyses are carried out to demonstrate thoroughly the performance of some typical models. Table 4 shows that when the mass position is varied from A_0 to A_3 , f_1 is decreased, but f_2 and f_3 are increased simultaneously, while the frequency ratio f_2/f_1 is increased. The mass ratios of models with mass positions in A_0 and A_1 are evenly distributed, but for models with mass positions in A_2 and A_3 , N_2 becomes too large, while N_3 becomes too small. Besides, when N is increased or decreased in each mode, k is also increased or decreased simultaneously. The MSAPD FRFs with optimal load given in Figure 12 show that, for the models with base thickness 1.2mm, the models with mass positions A_0 and A_1 can produce better broadband power output than the models with mass positions A_2 and A_3 . This confirms the structural screening results and the modal data shown in Figure 10 and Table 4, respectively.

Table 4: Modal performance of two-layer VEH with different mass positions

Models	f_1 (Hz)	N_1	k_1	f_2 (Hz)	N_2	k_2	f_3 (Hz)	N_3	k_3	f_2/f_1	f_3/f_2
A_0 -BT12	58.70	18.4%	0.076	72.07	24.3%	0.089	116.1	38.2%	0.184	1.23	1.61
A_1 -BT12	48.77	18.3%	0.071	90.08	30.5%	0.114	118.0	31.6%	0.173	1.85	1.31
A_2 -BT12	41.20	17.9%	0.068	110.4	58.5%	0.193	127.3	3.24%	0.083	2.68	1.15
A_3 -BT12	35.35	17.5%	0.067	118.3	56.2%	0.207	164.2	4.54%	0.025	3.35	1.39

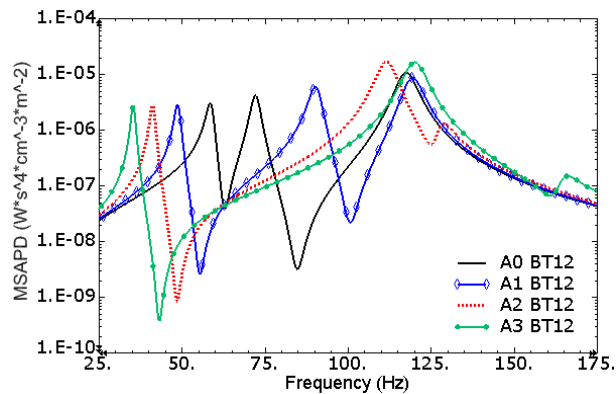


Figure 12: MSAPD FRFs of the two-layer model with different mass positions

Table 5 and Figure 13 show that, with mass position A_0 or A_1 , when the thickness of the base layer is increased from 0.8mm to 1.6mm, resonance frequencies of the first three modes are all increased. Mass ratios and EMCC in the first two modes are decreased significantly, but they are increased in the third mode. Figure 14 shows the vibration mode shapes of A_0 -BT12 in the first three modes. Modes 1 and 2 are

generated by the interaction between the two cantilevered parts of the upper layer and the corresponding halves of the base layer, and mode 3 is generated by the interaction between the whole base layer and the whole upper layer. In fact, when the mass is fixed near the centre of the base layer, modes 1 and 2 are largely affected by the cantilevered parts of the upper layer. This assertion can be seen from the results in Table 5 for the models with mass position $A0$. When the thickness of the upper layer is constant, the frequency ratio $f2/f1$ for these models remain approximately constant as the thickness of the base layer is varied. Thus, when the upper layer becomes thinner and lighter, the vibration in modes 1 and 2 will have weaker effects on the base layer. In particular, when the base thickness is 0.8mm, $N1$ is too large while $N3$ is too small. When the base layer is thicker than 1.2mm, $N3$ is too large, and the EMCC in the first two modes are too weak. Therefore, the preferred base thickness should be 1mm and 1.2mm. The MSAPD FRFs with optimal load given in Figure 13 confirm the structural screening results and the modal data. They show that the configurations with $BT10$ and $BT12$ can produce better broadband power output. In fact, the mass ratio and EMCC are associated and display a regular pattern of relationship such that the configurations with evenly distributed mass ratios normally have acceptable EMCC in all three modes.

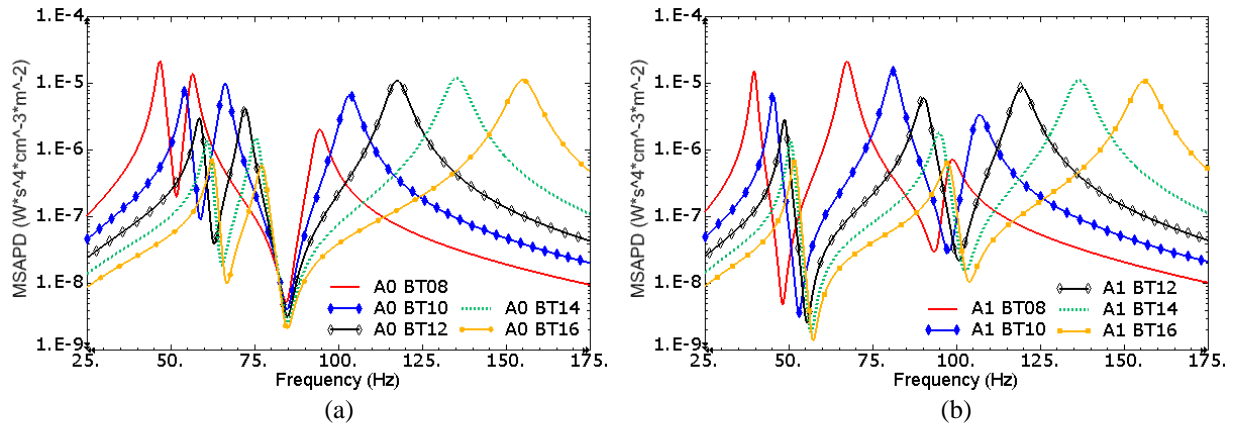


Figure 13: MSAPD FRFs of the two-layer VEH with different base thicknesses for: (a) mass position $A0$; (b) mass position $A1$

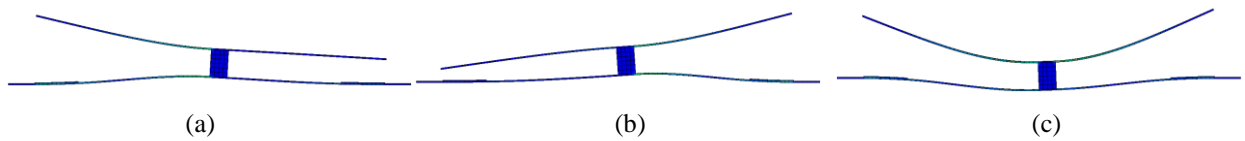


Figure 14: Mode shapes of $A0-BT12$ in the first three modes; (a)-(c): mode 1, 2 and 3.

Table 5: Modal performance of two-layer VEHs with different base thicknesses

Models	f1 (Hz)	N1	k1	f2 (Hz)	N2	k2	f3 (Hz)	N3	k3	f2/f1	f3/f2
$A0-BT08$	46.75	43.0%	0.149	56.12	31.6%	0.135	93.64	8.40%	0.118	1.20	1.67
$A0-BT10$	54.31	27.3%	0.107	65.97	32.3%	0.122	102.4	22.4%	0.160	1.21	1.55
$A0-BT12$	58.70	18.4%	0.076	72.07	24.3%	0.089	116.1	38.2%	0.184	1.23	1.61
$A0-BT14$	61.19	13.9%	0.056	75.45	17.4%	0.062	133.4	48.7%	0.190	1.23	1.77
$A0-BT16$	62.66	11.3%	0.044	77.36	13.2%	0.043	152.8	54.7%	0.188	1.23	1.98
$A1-BT08$	39.62	34.1%	0.126	66.89	45.3%	0.175	97.76	3.55%	0.090	1.69	1.46
$A1-BT10$	45.41	24.7%	0.096	80.59	44.1%	0.160	105.8	12.9%	0.133	1.77	1.31
$A1-BT12$	48.77	18.3%	0.071	90.08	30.5%	0.114	118.0	31.6%	0.173	1.85	1.31
$A1-BT14$	50.70	14.5%	0.054	95.14	18.8%	0.073	134.7	46.1%	0.187	1.88	1.42
$A1-BT16$	51.85	12.1%	0.042	97.81	13.0%	0.049	153.9	53.3%	0.187	1.89	1.57

4.3 Optimal design of three-layer VEH

A three-layer VEH consists of a base layer, an upper layer, a lower layer and two masses M_{+1} and M_{-1} , which serve as spacers between the upper layer, lower layer and base layer as shown in Figure 15 for a typical model *A0-B1-BT12*. In this case, the locations of the two masses are variable, and the upper and lower layers are separated as four cantilevered parts. Therefore, the three-layer VEH can generate a wider broadband power output in the first five modes in comparison with the two-layer VEH. The dimensions of the lower layer and M_{-1} are the same as those of the upper layer and M_{+1} , respectively.

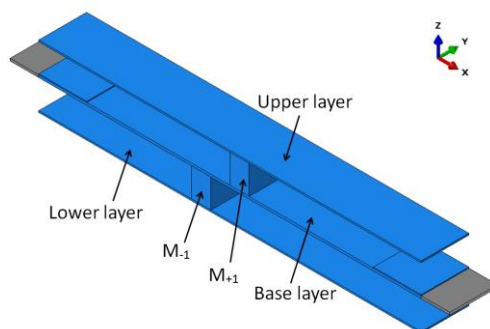


Figure 15: Doubly-clamped three-layer VEH model *A0-B1-BT12*

In this case, only the configurations with two masses located on different sides of the base layer are analysed. In particular, the location of M_{+1} is fixed on the A-side, and the location of M_{-1} is fixed on the B-side. Identical configurations can be formed by locating M_{+1} on the B-side and M_{-1} on the A-side. These identical configurations are not presented. The configuration with two masses located on the same side of the base layer will be discussed in section 5. Since the combinations of the different mass positions and base thicknesses are 245 (7*7 mass positions and 5 thicknesses), using the structural screening process based on the modal approach becomes far more effective than simply carrying out full analysis.

Figures 16 and 17 show contour slices of the natural frequencies and the mass ratios of the first five modes, respectively. Figure 18 shows the contour slices of the four frequency ratios f_2/f_1 , f_3/f_2 , f_4/f_3 and f_5/f_4 , while Figure 19 shows the structural screening results. Two sets of screening criteria are specified, namely (a) frequency ratios <2 and mass ratios >0.05 , (b) frequency ratios <1.75 and mass ratios >0.1 . The results of applying these two sets of screening criteria are shown by the shaded regions of Figure 19(a) and (b). In Figure 17(b), the selected configurations which meet the stricter screening criteria are annotated on the shaded area. Obviously, very few configurations can achieve satisfactory broadband structural performance. Generally, the configurations with mass positions far away from the centre of the base layer are not acceptable. This is because the long and short cantilevered parts generate too low and too high resonance frequencies. In addition, when the masses are symmetrically located, for instance, *A3-B3* and *A4-B4*, the two parts of the upper layer and lower layer have the same lengths, which cause two modes to become inactive and N_2 and N_4 become very small. Figure 20 shows the selected configurations that meet the screening criteria frequency ratios <1.75 and mass ratios >0.1 in the first four modes.

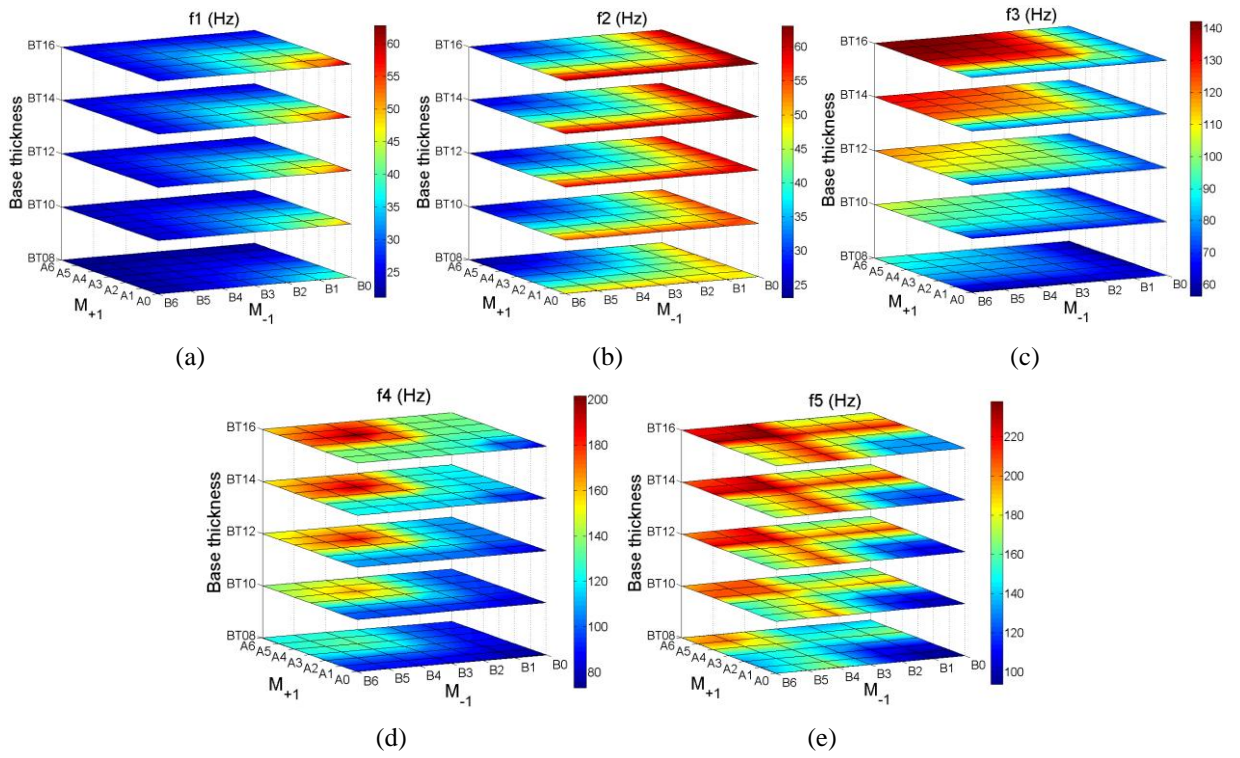


Figure 16: contour slices of the resonance frequencies of the first five modes with different mass positions of M_{+1} , M_{-1} and different base thicknesses of the three-layer VEH. (a)-(e): mode 1 to 5

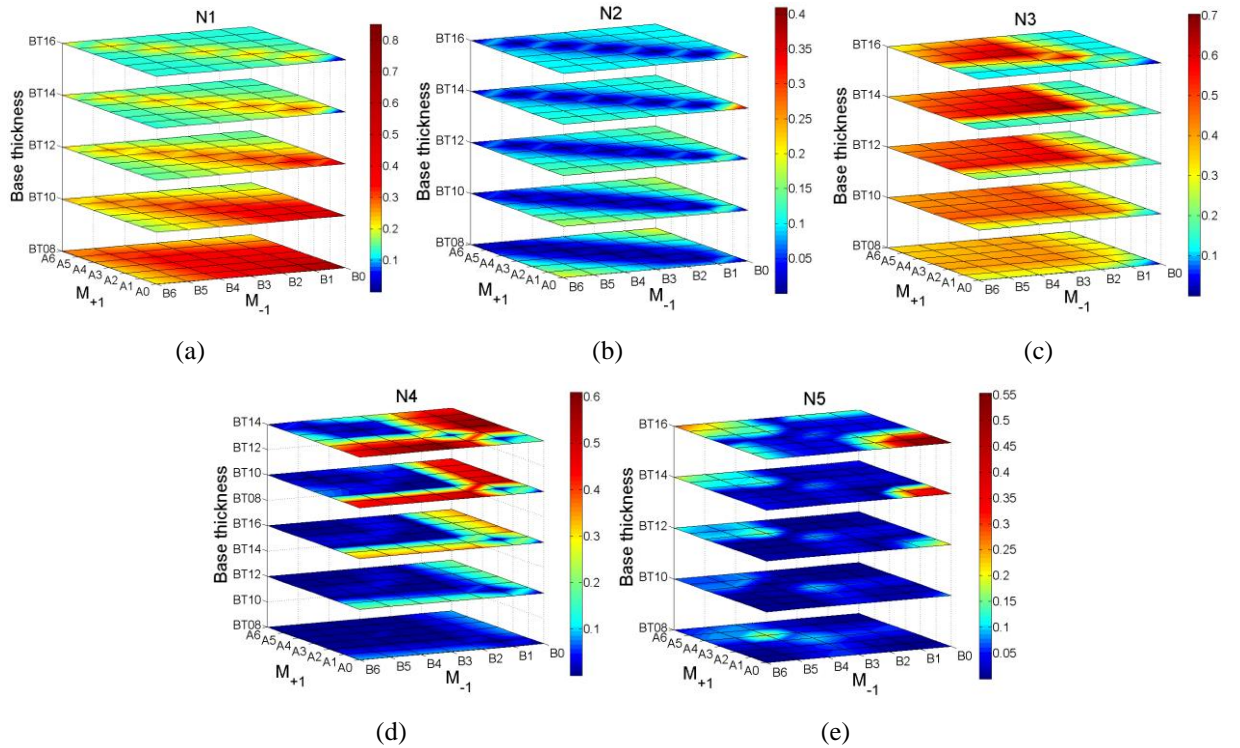


Figure 17: Contour slices of mass ratio of the first five modes. (a)-(e): mode 1 to 5

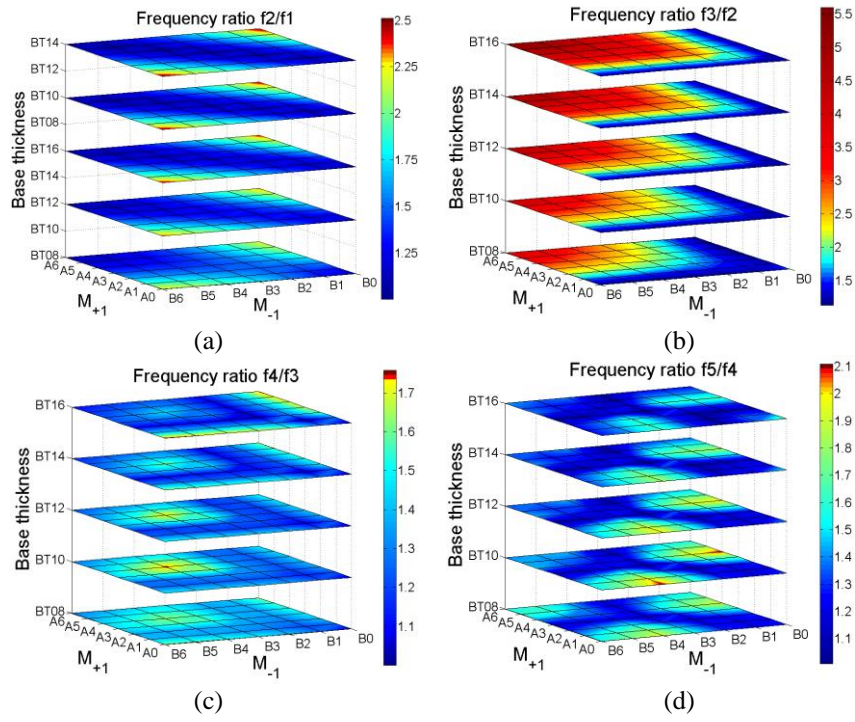


Figure 18: Contour slices of four frequency ratios. (a): f_2/f_1 ; (b): f_3/f_2 ; (c): f_4/f_3 ; (d): f_5/f_4

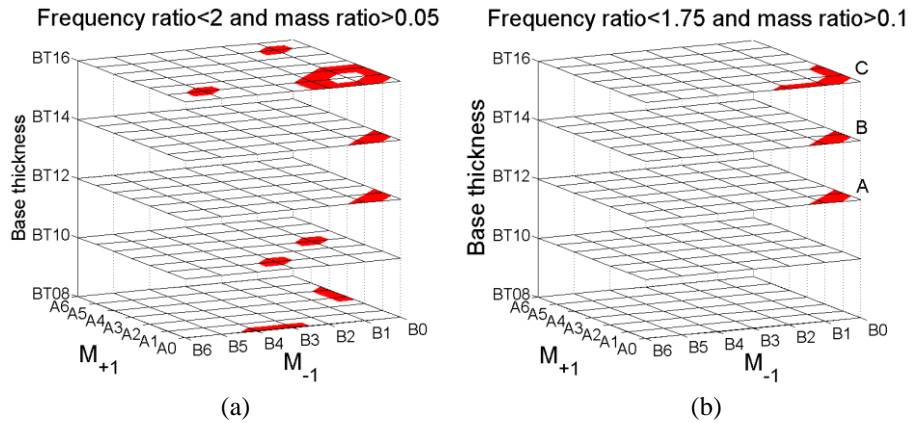


Figure 19: Configurations of three-layer VEH which meet the screening criteria in the first five modes. (a) $f_2/f_1 < 2$ and $N > 0.05$; (b) $f_2/f_1 < 1.75$ and $N > 0.1$; A: A_0-B_1, A_1-B_0 (BT12); B: A_0-B_1, A_1-B_0 (BT14); C: $A_0-B_1, A_0-B_2, A_1-B_0, A_2-B_0$ (BT16)

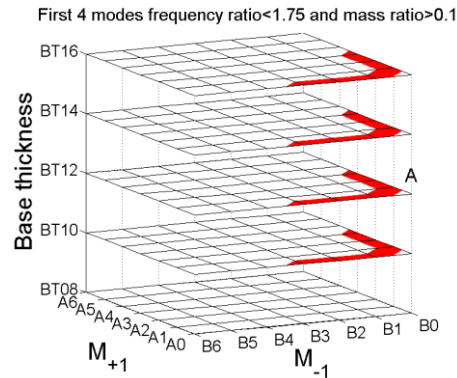


Figure 20: Configurations of three-layer VEH meet the screening criteria frequency ratio < 1.75 and $N > 0.1$ in the first four modes. A: $A_0-B_1, A_0-B_2, A_0-B_3, A_1-B_0, A_2-B_0, A_3-B_0$ (from BT10 to BT16)

In Table 6 and Figure 21, the position of M_{-1} is varied from B_0 to B_3 when the position of M_{+1} is fixed at A_0 and the base thickness is 1.2mm. For the configuration A_0-B_0 , since the masses are asymmetrically located,

N2 and N4 are nearly 0, and the MSAPD FRFs peaks of modes 2 and 4 disappear which indicates that these modes are inactive. For the configurations *A0-B2* and *A0-B3*, N5 is very small, and the MSAPD FRFs in mode 5 are either inactive (*A0-B2*) or has poor performance (*A0-B3*). Obviously, *A0-B1* can provide better broadband power output in the first five modes.

Table 6: modal performance of the three-layer stacked VEH with different mass positions

Models	f1 (Hz)	N1	k1	f2 (Hz)	N2	k2	f3 (Hz)	N3	k3	f4 (Hz)	N4	k4	f5 (Hz)	N5	k5
<i>A0-B0-BT12</i>	57.87	53.7%	0.161	58.40	0.00%	0.025	74.25	12.9%	0.108	75.49	0.00%	0.031	105.7	21.3%	0.151
<i>A0-B1-BT12</i>	48.64	26.6%	0.093	59.43	12.8%	0.066	72.74	16.3%	0.089	89.71	19.9%	0.114	107.4	11.9%	0.118
<i>A0-B2-BT12</i>	41.07	21.4%	0.081	59.49	12.5%	0.066	72.25	18.1%	0.092	100.2	34.6%	0.170	123.9	0.30%	0.021
<i>A0-B3-BT12</i>	35.22	18.4%	0.075	59.28	12.8%	0.067	72.11	18.4%	0.092	102.6	32.5%	0.170	163.8	4.00%	0.038

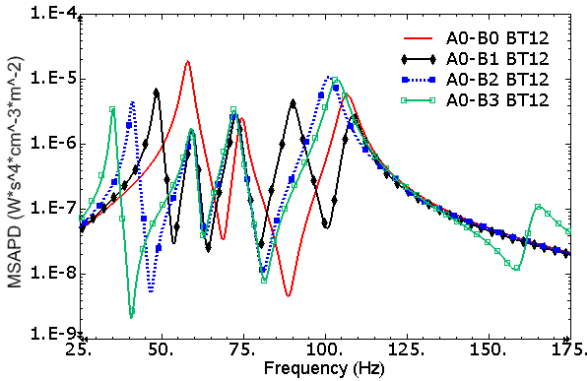


Figure 21: MSAPD FRFs of the three-layer VEH with different mass positions

In Figure 22 and 23 and Table 7, the configurations *A0-B1* and *A0-B2* with different base thicknesses are analysed. The results show that, for the configuration *A0-B1*, when the base thickness is increased, N1 is decreased while N5 is increased, and k is decreased in the first four modes while it is increased in mode 5. The configurations *A0-B1-BT12* and *A0-B1-BT14* have evenly distributed mass ratios and acceptable EMCC. For the configuration *A0-B2*, N5 is always too small unless the base thickness is increased to 1.6mm. However, the broadband performance of the configuration with 1.6mm base thickness is still poor due to its weak EMCC and small mass ratios in the first three modes. If only considering the broadband performance in the first four modes, the configurations *A0-B2-BT10* and *A0-B2-BT12* can still achieve acceptable broadband power output.

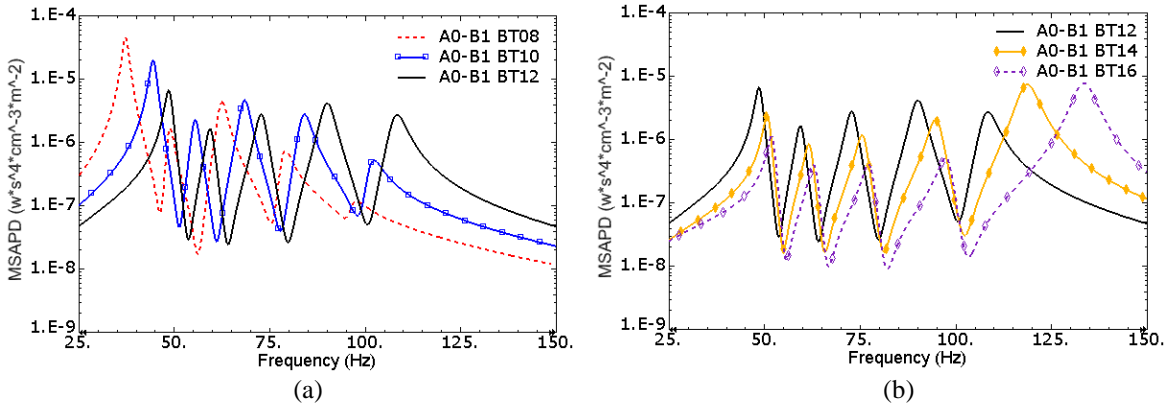


Figure 22: MSAPD FRFs of the three-layer VEH with different base thicknesses and mass position *A0-B1*. (a): from *BT08* to *BT12*; (b) from *BT12* to *BT16*

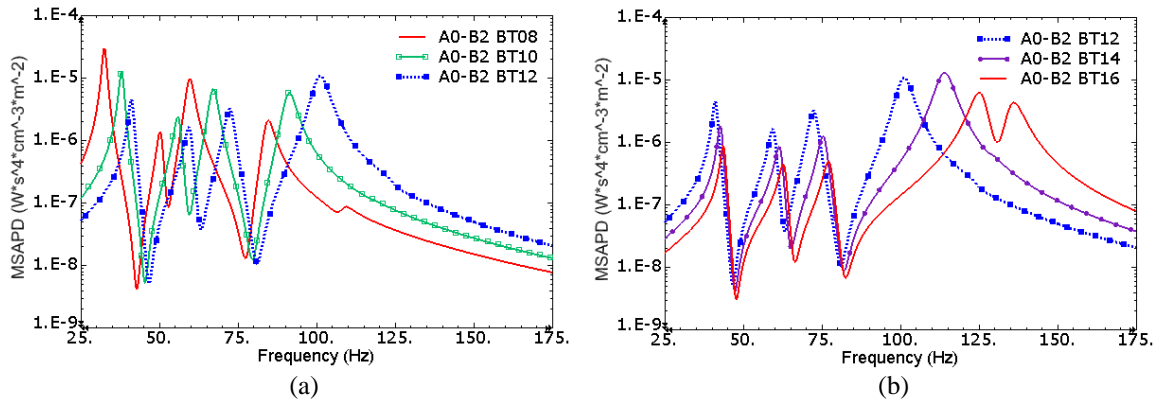


Figure 23: MSAPD FRFs of the three-layer VEH with different base thicknesses and mass position *A0-B2*. (a): from *BT08* to *BT12*; (b) from *BT12* to *BT16*

Table 7: modal performance of three-layer VEH with different base thicknesses

Models	f1 (Hz)	N1	k1	f2 (Hz)	N2	k2	f3 (Hz)	N3	k3	f4 (Hz)	N4	k4	f5 (Hz)	N5	k5
<i>A0-B1-BT08</i>	37.17	62.8%	0.176	48.60	8.46%	0.071	62.19	13.9%	0.114	78.38	4.01%	0.071	96.48	0.51%	0.037
<i>A0-B1-BT10</i>	44.41	43.5%	0.135	55.37	12.7%	0.077	68.19	17.6%	0.110	83.52	12.0%	0.105	101.2	2.78%	0.072
<i>A0-B1-BT12</i>	48.64	26.6%	0.093	59.43	12.8%	0.066	72.74	16.3%	0.089	89.71	19.9%	0.114	107.4	11.9%	0.118
<i>A0-B1-BT14</i>	50.85	17.2%	0.066	61.75	10.7%	0.050	75.68	12.3%	0.063	94.80	16.9%	0.085	117.5	29.4%	0.157
<i>A0-B1-BT16</i>	52.05	12.4%	0.050	63.08	8.77%	0.038	77.46	9.41%	0.044	97.71	11.6%	0.055	131.7	43.4%	0.172
<i>A0-B2-BT08</i>	32.41	48.0%	0.149	50.30	8.42%	0.068	59.35	23.8%	0.140	83.99	8.45%	0.109	108.1	1.04%	0.013
<i>A0-B2-BT10</i>	37.93	32.6%	0.113	55.93	13.3%	0.078	66.89	22.4%	0.121	90.55	19.0%	0.143	117.6	0.89%	0.002
<i>A0-B2-BT12</i>	41.07	21.4%	0.081	59.49	12.5%	0.066	72.25	18.1%	0.092	100.2	34.6%	0.170	123.9	0.30%	0.021
<i>A0-B2-BT14</i>	42.76	15.1%	0.059	61.66	10.3%	0.050	75.49	13.1%	0.064	112.7	46.9%	0.179	128.5	0.27%	0.024
<i>A0-B2-BT16</i>	43.72	11.6%	0.045	62.97	8.56%	0.039	77.38	9.84%	0.044	124.7	37.5%	0.141	134.6	17.1%	0.123

5. Factors affecting performance of multi-layer VEHs

5.1 Effect of structural damping

In the last section, the damping ratio was fixed to 0.02 for the convenience of analysis. In fact, altering the damping ratio can directly affect the coupling criterion $k^2 Q_M$ and the mechanical response simultaneously, which eventually affects the magnitude of the power density. In Figure 24, damping ratio is varied from 0.002 to 0.05 in configuration *A0-B1-BT12*. The results show that the magnitude of the power density around each mode is significantly affected. When the smaller damping ratio is used, it can generate sharper responses. However, the changes of damping ratio not only affect the magnitude of power density around resonance, but they can also affect the performance around anti-resonance. Therefore, when the damping ratio is small, more modes may be required in narrower frequency range in order to achieve smoother broadband power output.

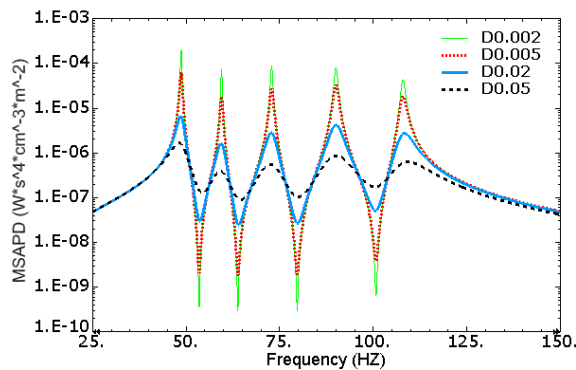


Figure 24: MSAPD FRFs of *A0-B1-BT12* with different damping ratios.

5.2 Effect of mass positions and dimensions

For the three-layer VEH, the masses located at different positions can separate the upper and lower layers into four cantilevered parts. For the optimal mass position *A0-B1* determined in the last section, the lengths of the four cantilevered parts are from 80mm to 110mm as illustrated in Figure 25(a). By denoting the cantilevered parts from the shortest to the longest as *L1* to *L4*, Table 8 shows that the length difference between each two adjacent parts with mass position *A0-B1* is 10mm. In fact, the length difference can be even smaller, and these configurations have not been discussed in section 4.

Some typical configurations with smaller length differences are shown in Table 8 with length differences from 10mm to 2.5mm. Figure 26 and Table 9 show the modal performance and the MSAPD FRFs of these configurations. The results show that, when the length difference is decreased, the first two modes become closer and dominant while modes 3 and 4 also become closer but inactive. In particular, the values of mass ratios and EMCC in modes 1 and 2 are increased but they are decreased significantly in modes 3 and 4. For the resonance frequencies, f_1 is increased while f_4 is decreased, and f_2 and f_3 are barely changed. In fact, decreasing the length difference to generate closer modes could generate strong structural coupling in adjacent modes and eventually affect the modal performance and the number of modes effectively participating in the vibration.

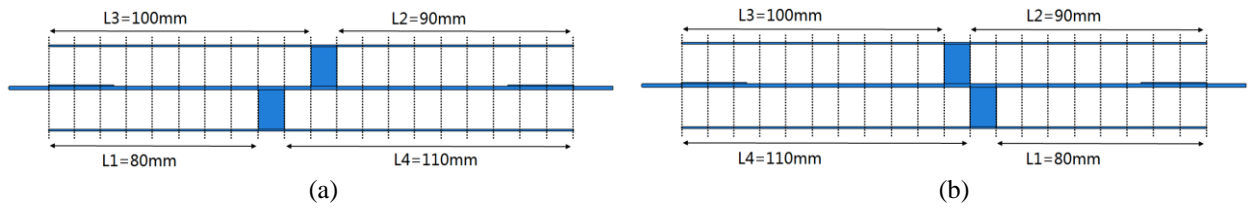


Figure 25: Illustration of the length of four cantilevered parts in the three-layer VEH. (a) mass position *A0-B1*; (b) mass position *A0-A1*

Table 8: Length difference between each adjacent two cantilevered parts with different mass positions

Models	L1 (mm)	L2 (mm)	L3 (mm)	L4 (mm)	Length difference (mm)
<i>LD100 (A0-B1)</i>	80	90	100	110	10
<i>LD075</i>	83.75	91.25	98.75	106.25	7.5
<i>LD050</i>	87.5	92.5	97.5	102.5	5
<i>LD025</i>	91.25	93.75	96.25	98.75	2.5

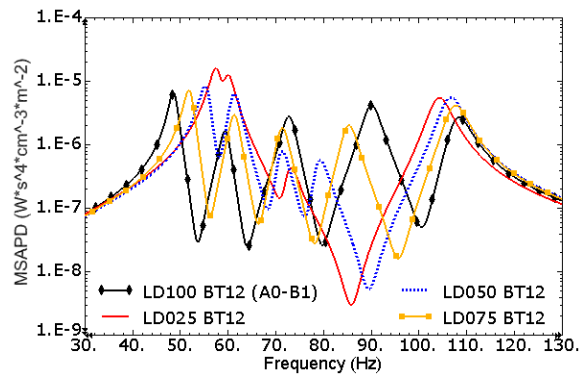


Figure 26: MSAPD FRFs of the three-layer VEH with typical length differences of four cantilevered parts

Table 9: Modal performance of three-layer VEHs with typical length differences of four cantilevered parts

Models	f1 (Hz)	N1	k1	f2 (Hz)	N2	k2	f3 (Hz)	N3	k3	f4 (Hz)	N4	k4	f5 (Hz)	N5	k5
<i>LD100</i>	48.64	26.6%	0.093	59.43	12.8%	0.066	72.74	16.3%	0.089	89.71	19.9%	0.114	107.4	11.9%	0.118
<i>LD075</i>	51.92	27.7%	0.097	61.30	17.3%	0.079	71.26	12.5%	0.077	85.09	13.3%	0.088	106.8	16.9%	0.136
<i>LD050</i>	55.37	28.6%	0.104	61.09	25.4%	0.096	71.06	6.58%	0.059	78.95	6.41%	0.053	105.8	20.9%	0.148
<i>LD025</i>	57.52	37.8%	0.129	59.76	26.1%	0.096	72.49	1.72%	0.059	75.07	1.51%	0.007	103.4	20.5%	0.147

The two masses can also be located on the same side of the base layer. Figure 22(b) illustrates a typical configuration A0-A1, which has the same length differences of the four cantilevered parts as the configuration A0-B1. Figure 27 shows the comparison of MSAPD FRFs between the configurations with the same length differences but different mass locations. The configuration with masses located on the same side has “S” after its name. The results show that, modes 2 and 3 become closer when masses are located on the same side, but this slightly affects the broadband performance. When the masses are located on different sides, smoother broadband output can be achieved.

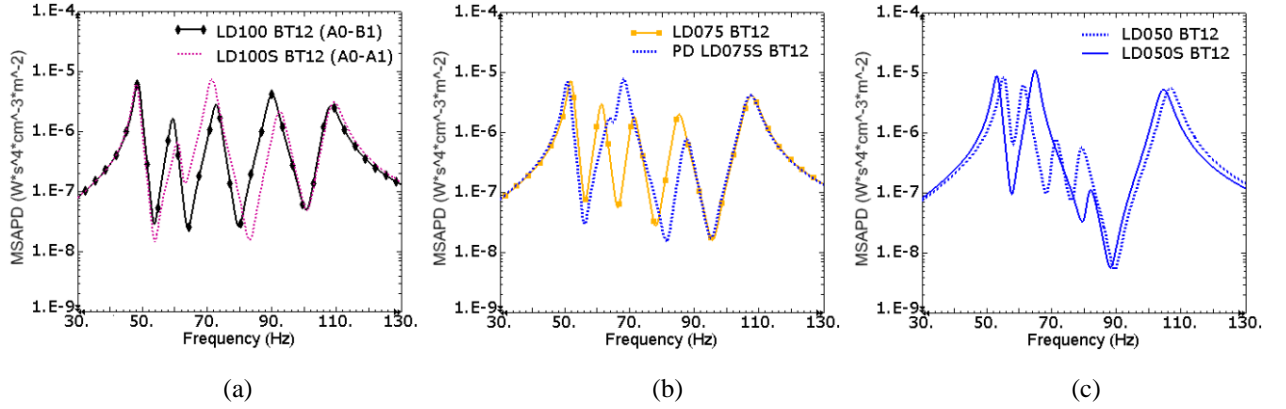


Figure 27: MSAPD FRFs of the three-layer VEH with different mass positions. (a): model *LD100* (length difference 10mm); (b) model *LD075*; (c) model *LD050*

Figure 28 shows the MSAPD FRFs of configurations *A0-B1-BT12* when the thicknesses and widths of masses are changed. The original thickness and width of the masses are 15mm and 10mm, respectively. In Figure 28 (a), the thickness is varied from 10mm (*MT10*) to 20mm (*MT20*) while the width is fixed at 10mm. The results show that, using thinner masses generate poorer performance around the first four modes in comparison with using thicker masses. Using thicker masses can improve the performance around the first four modes, but it also reduces the magnitude of power density of the fifth mode.

In Figure 28 (b), the width is varied from 5mm (*MW05*) to 15mm (*MW15*) while the thickness is fixed at 15mm. It should be noted that, for configuration *A0-B1*, the centre of the masses are not changed when the widths of masses are changed. Obviously, using narrower masses can significantly decrease the performance around the first four modes and using wider masses generates lower power density in the fifth mode. In general, the dimensions of masses should be chosen carefully for designs using different dimensions and scales.

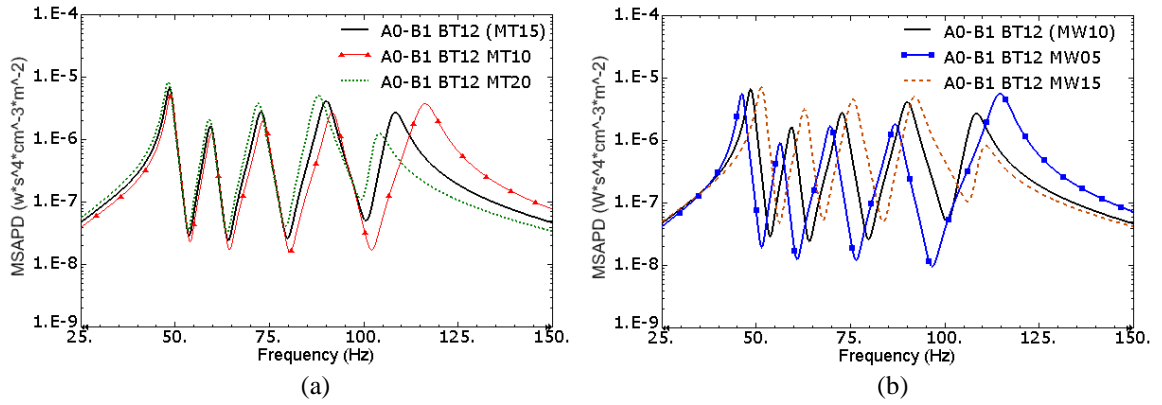


Figure 28: MSAPD FRFs of A0-B1-BT12 with different thicknesses and widths of masses. (a) mass thickness varied from 10mm to 20mm; (b) mass width varied from 5mm to 15mm

Since the extra masses serve as spacers, the mass needs to be adequately thick to provide adequate space for vibration. The maximum relative displacement between each two adjacent layers in any mode should be smaller than the thickness of the mass, which is 15mm. In Table 10, under a 9.81 m/s^2 (1 g acceleration) base excitation, the maximum relative displacements of two typical configurations are given. In particular, $U1(U2)$ is defined as the maximum relative displacement between the top surface of the base layer and the bottom surface of the upper layer on the A(B) side. $U3(U4)$ is defined as the maximum relative displacement between the bottom surface of the base layer and the top surface of the lower layer on the A(B) side. The results show that these configurations have enough space for vibration in any mode. Moreover, since the original damping ratio is 0.02, thicker masses or smaller base excitation are required for the system with smaller damping ratios. Normally, for a smaller base excitation like 5 m/s^2 , all models can operate without reaching the vibration amplitude limit.

Table 10: Maximum relative displacements of typical models with damping ratio 0.02 under 9.81 m/s^2 base excitation

Models	Mode No.	Maximum relative displacement (mm)			
		$U1$	$U2$	$U3$	$U4$
A1-BT12	1	0.27	5.39		
	2	2.15	0.24		
	3	0.73	0.48		
A0-B1-BT12	1	1.08	1.30	7.67	0.24
	2	0.44	3.77	1.16	0.55
	3	2.88	0.48	0.86	0.13
	4	0.63	0.80	0.25	1.89
	5	0.48	0.30	0.33	0.86

5.3 Effect of piezoelectric dimensions on EMCC

The dimensions of the piezoelectric layer are fixed in the last section. In this section, geometric studies are performed, which involve varying the length and thickness of the piezoelectric layer to determine the dimensional effects on EMCC. In Table 11, for the configuration with the name PL , the length of the piezoelectric layer is varied from the original length of 50 mm ($25 \text{ mm} * 2$) while the thickness is kept constant. The configuration $PLmax$ has a fully covered piezoelectric layer, which covers the base layer from the two clamped ends to the two masses. Then, since the mass position is A0-B1, the piezoelectric patch attached on A-side is 90 mm long, and on B-side it is 80 mm long. The EMCC of the first five modes and the MSAPD FRFs, given in Table 11 and Figure 29, show that when the length of the piezoelectric layer is increased from 20 mm to 50 mm, the values of EMCC and power density have significantly increased. When the length is increased to 80 mm, EMCC is slight increased. After that, the longer length of

piezoelectric layer starts to generate lower EMCC. In fact, once the piezoelectric layer is longer than a critical length, the strain distributions along the length of the doubly-clamped base layer cause the electric displacement along the thickness of the piezoelectric layer to be partly reversed, and the electrical current starts to be cancelled by itself. The electrical displacement mode shapes of model *A0-B1* with fully covered piezoelectric layer are shown in Figure 30. The lengths and directions of the vector arrows on the beam indicate the distributed values and directions of electrical displacement. As shown in Table 11, when the base layer is fully covered, k_3 is almost zero and MSAPD FRF peak for mode 3 disappears; instead, a very strong anti-resonant trough appears. This is due to the effect of complete self-cancellation. Therefore, the 50 mm long piezoelectric layer can produce high EMCC and save materials.

Table 11: EMCC of *A0-B1-BT12* with different lengths and thicknesses of piezoelectric layer

Model	Length/thickness (mm)	k1	k2	k3	k4	k5
PL10	20	0.069	0.049	0.065	0.079	0.068
PL25 (A0-B1)	50	0.093	0.066	0.089	0.114	0.118
PL40	80	0.100	0.070	0.093	0.118	0.137
PL55	110	0.097	0.063	0.084	0.102	0.127
PL70	140	0.082	0.044	0.059	0.065	0.099
PLmax	170	0.039	0.029	0.000	0.013	0.045
PT25	0.25	0.082	0.057	0.075	0.090	0.079
PT50 (A0-B1)	0.5	0.093	0.066	0.089	0.114	0.118
PT75	0.75	0.088	0.063	0.084	0.113	0.142
PT100	1	0.077	0.055	0.074	0.099	0.150

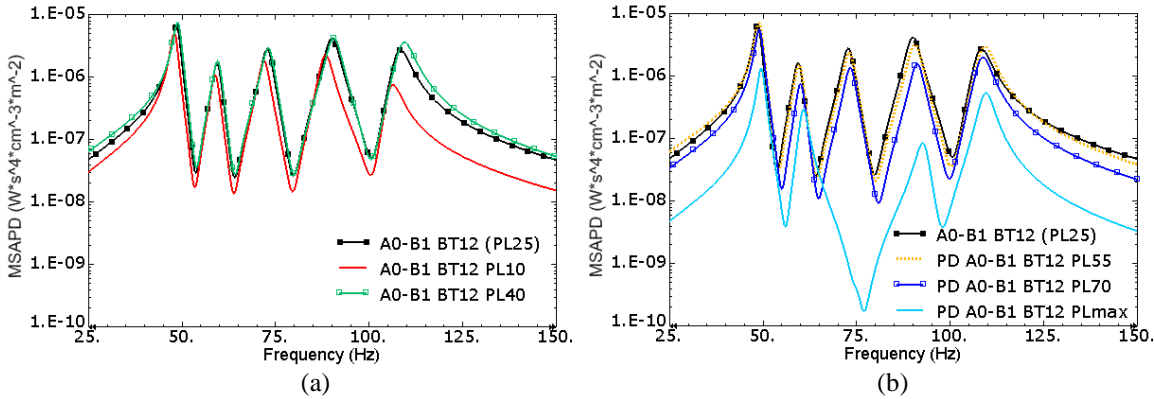


Figure 29: MSAPD FRFs of the three-layer VEH with different lengths of piezoelectric layer. (a) from 20mm to 80mm (b) from 110mm to 170mm (*PLmax*)

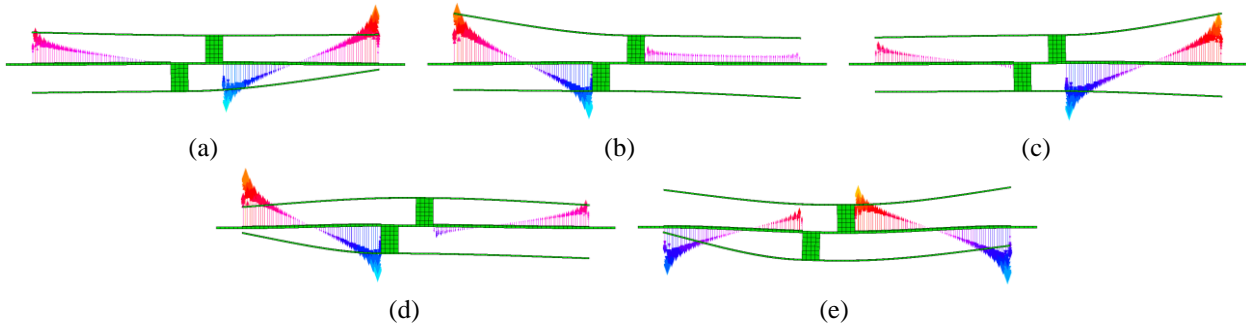


Figure 30: Electrical displacement mode shapes of model *A0-B1-BT12-PLmax* (full coverage of piezoelectric layer). (a)-(e): mode 1 to 5

For the configuration with the designation *PT*, the thickness of the piezoelectric layer is varied from the original thickness of 0.5 mm while the length is kept constant. The EMCC of the first five modes and MSAPD FRFs given in Table 11 and Figure 31 show that the thicker piezoelectric layer can produce higher EMCC in mode 5, in which the vibration is mainly generated by the base layer. However, the EMCC can be even weaker in the first four modes when the piezoelectric layer is thicker than 0.5mm. This is because the vibrations generated on the four cantilevered parts have less vibration effects on the base layer when the base layer becomes stiffer due to the combined effects of the initial thickness of the base layer and the thickness of the piezoelectric material bonded to it, which eventually decreases the EMCC in the first four modes. Therefore, the thickness of the piezoelectric layer should be carefully chosen in order to produce acceptable EMCC in all five modes.

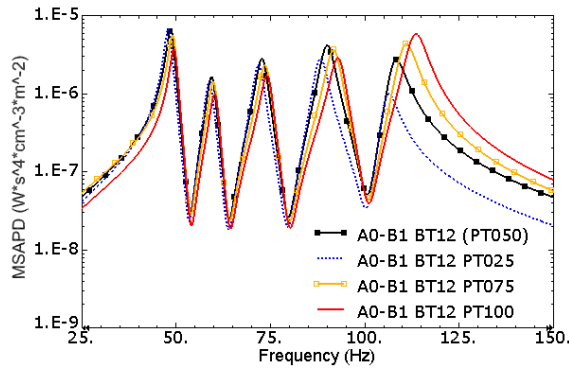


Figure 31: MSAPD FRFs of the three-layer VEH with different thicknesses of piezoelectric layer

5.4 Multi-layer VEHs for larger and smaller systems

In all the above cases, the designs of the multi-layer VEHs have specified dimensions. In fact, the designs and preferred configurations can be used at different scales. In this section, two typical configurations are developed, namely: a small-scale VEH and a larger-scale VEH. The dimensions of the components of the two systems are given in Table 12. The length of the masses is still 1/20 of the length of the base layers, and the thickness of the base layer is 1.5 times thicker than the upper and lower layers. However, the aspect ratios of these beam layers are different. The smaller model is narrower and longer than the original model while the larger one is wider and shorter.

Table 12: Dimensions of the components of the multi-layer VEHs in smaller and larger systems.

VEH sizes	Components	Dimensions (mm)		
		Length	Width	Thickness
Small	Base layer	25	2	0.12
	Upper/lower layer	25	2	0.08
	Piezoelectric layer	3	2	0.05
	Masses	1.25	2	1.5
Large	Base layer	800	120	6
	Upper/lower layer	800	120	4
	Piezoelectric layer	100	120	3
	Masses	40	120	60

In Table 13 and Figure 32, the modal performance and power output (due to 1m/s^2 base excitation) with two typical configurations “A0” and “A0-B1” are given. Obviously, the larger model can generate much lower resonance frequencies, and the smaller model has higher resonance frequencies. For the same configuration, there are only slight differences in the mass ratios and EMCC between the larger and smaller systems, and the corresponding FRFs are also quite similar. Therefore, the optimal designs in this paper can be used to design systems with different sizes, frequency ranges and power outputs from a low to high frequency and with the power range from microwatts to milliwatts.

Table 13: Modal performance of the VEH models in a smaller and a larger system with typical configurations

Models	f1 (Hz)	N1	k1	f2 (Hz)	N2	k2	f3 (Hz)	N3	k3	f4 (Hz)	N4	k4	f5 (Hz)	N5	k5
Small A0	374.3	18.7%	0.072	459.4	24.3%	0.085	738.4	38.0%	0.175						
Large A0	18.50	16.5%	0.074	22.79	22.8%	0.089	38.78	39.7%	0.202						
Small A0-B1	310.4	26.7%	0.088	379.2	13.0%	0.063	463.8	16.4%	0.084	571.7	19.8%	0.108	685.4	11.8%	0.113
Large A0-B1	15.35	23.9%	0.092	18.72	11.6%	0.064	23.01	14.6%	0.085	28.65	17.9%	0.109	35.15	17.9%	0.151

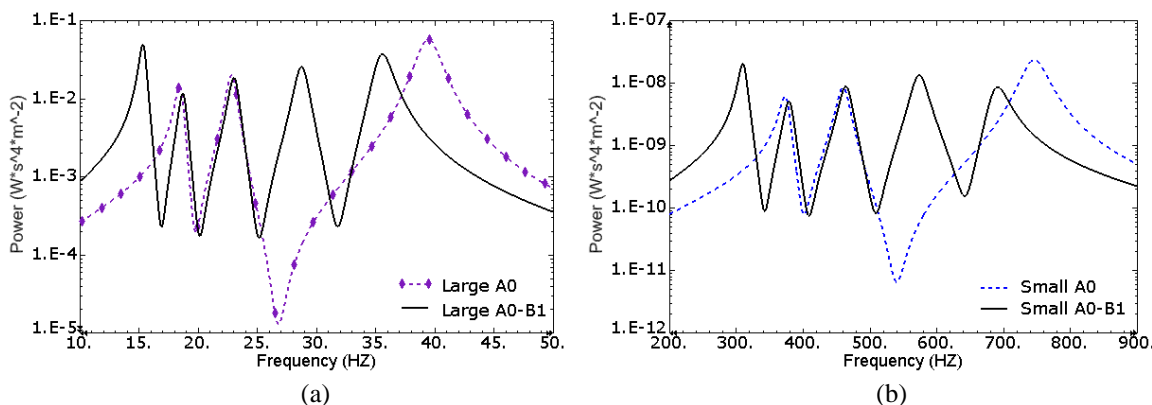


Figure 32: MSAPD FRFs of VEH models with typical configurations. (a) larger VEH; (b) smaller VEH

6. Potential effects of large vibration amplitudes

In this section, the potential effects of large vibration amplitudes, including the possibilities for nonlinear responses and considerations for linear versus nonlinear analysis in designing the doubly-clamped multi-layer VEHs, are briefly discussed. In existing multi-resonance VEH designs, due to the complexity of the configurations, harvesting energy from several modes efficiently is not easy. Without proper design, some modes can be far away from others, and some modes are barely active due to poor modal structural or electromechanical performance. Then, the capabilities for broadband power output are limited. This paper operated the structural screening process based on the modal approach to select the configurations with optimal structural broadband performance in multi-modes. The aim of using linear analysis (DPM) in the current work is to evaluate the power output FRFs of these selected configurations with optimal or near optimal broadband performance. It should be noted that the optimisation in this paper is configurational whereas linear-versus-nonlinear consideration is dynamics or phenomenological optimisation. Since the modal structural characteristics of a VEH is unique, once its best performance in linear system with harmonic vibration is enhanced due to the improvement of modal behaviour, its performance in other more complicated conditions should also be enhanced simultaneously.

It is also widely known that, VEHs can behave nonlinearly with high vibration amplitude and large deflection. The nonlinear behaviours are mainly caused by the nonlinear stiffness that has been introduced into the motion. For example, for monostable nonlinear VEHs with softening or hardening conditions, the resonance frequencies shift and the resonance curves are bent to the left or to the right. For such cases, the non-linear models would be required to predict more accurate power output FRFs. In fact, the main motivation for designing a nonlinear VEH in some existing works is that the nonlinear VEH can generate wider bandwidth than the linear VEH around a single vibration mode (Lihua Tang et al. 2010). However, to successfully achieve broadband performance, the VEH needs to always be operated in the upper branch region of the nonlinear behaviour (Lihua Tang et al. 2010, Cammarano et al. 2014). Cammarano et al. (2014) argue that, if assuming a VEH operates always in the lower branch solution of the nonlinear behaviours, the linear system will generate higher maximum power output. After the damping of the linear system is increased to maintain the same maximum power compared to the nonlinear system, the bandwidth of the linear system increases and it is wider than the bandwidth of the nonlinear system. Therefore, in order to successfully exhibit wider bandwidth, the operational conditions of nonlinear VEHs should be carefully investigated and the following conditions are required to be met: small damping, high nonlinearity and operating the VEH in the upper branch region of the nonlinear behaviour (Cammarano et al. 2014).

For the doubly-clamped multi-layer VEHs, in order to achieve large deflections and high nonlinearity, thicker masses should be used since there is a vibration limitation due to the mass thickness. However, for real applications, too large deflections can reduce the lifecycle or even damage the piezoelectric ceramic PZT patches, which are used in this design. Then, flexible piezoelectric composite devices, such as the 1-3 and 0-3 piezoelectric composite devices, should be used to avoid damage. However, these piezoelectric composite devices sacrifice the electromechanical coupling of system, which also significantly affect the performance.

7. Conclusions

In this paper, the doubly-clamped multilayer VEHs have been developed. Initially, an optimization strategy is introduced based on a modal structural approach, which can evaluate the mechanical resonance performance of the VEHs using mass ratio as the performance criteria. Mass ratio represents the influences of the modal mechanical response on the volumetric power output directly. Any mode with large mass ratio will cause the remaining modes to have small mass ratios and poor performance. Besides, the anti-resonance can significantly affect the capability for broadband power output if the modes are far away from each other. Then, the modal optimisation process selects the configurations with close resonances and evenly distributed mass ratios in multiple modes. These selected configurations are subsequently subjected to full electromechanical analysis to determine the EMCC and the MSAPD FRFs with optimal load.

By altering mass positions and the thickness of the base layer, the multilayer VEHs can be tuned to generate up to five close modes with large power output in those modes. The optimisation results show that, when the base layer is nearly 1.5 times thicker than the upper and lower layers, and the mass positions are close to the centre of the beam layer, the configurations can easily achieve broadband power output. However, if the

length difference between the four cantilevered parts is too small, two modes become inactive. The piezoelectric coverage can also significantly affect the electromechanical coupling. The thickness of masses should be chosen carefully to ensure enough space for vibration. The case study shows that the optimized configurations of the multilayer VEHs can be directly used in different scales of VEH designs from low to high frequency ranges with power output ranges from microwatts to milliwatts.

Declaration of conflicting interests

The authors declare that there is no conflict of interest.

Funding

This research received no specific grant from any funding agency in the public, commercial or not-for-profit sectors.

References

- Anton, S.R. and Sodano, H. A. 2007. A review of power harvesting using piezoelectric materials (2003-2006), *Smart Mater. Struct.*, 16 R1–R21.
- Berdy, D. F., Jung, B., Rhoads, J. F., and Peroulis, D. 2012. Wide-bandwidth, meandering vibration energy harvester with distributed circuit board inertial mass. *Sensors and Actuators A: Physical*, 188, 148-157.
- Cammarano, A., Neild, S. A., Burrow, S. G., and Inman, D. J. 2014. The bandwidth of optimized nonlinear vibration-based energy harvesters. *Smart Materials and Structures*, 23(5), 055019.
- Erturk, A. and Inman, D.J. 2008a. “A Distributed Parameter Electromechanical Model for Cantilevered Piezoelectric Energy Harvesters,” *Journal of Vibration and Acoustics*, 130:041002.
- Erturk, A. and Inman, D.J. 2008b. On Mechanical Modeling of Cantilevered Piezoelectric Vibration Energy Harvesters, *Intell. Mater. Syst. Struct.*, 19; 1311.
- Erturk, A., Renno, J. M., and Inman, D. J. 2009. Modeling of piezoelectric energy harvesting from an L-shaped beam-mass structure with an application to UAVs. *Intell. Mater. Syst. Struct.*, 20(5), 529-544.
- Erturk, A. and Inman, D.J. 2011. Piezoelectric Energy Harvesting, *John Wiley and Sons*, 978-1-1199-9135-9
- Ferrari, M., Ferrari, V., Guizzetti, M., Marioli, D., and Taroni, A. 2008. Piezoelectric multifrequency energy converter for power harvesting in autonomous microsystems. *Sensors and Actuators A: Physical*, 142(1), 329-335.
- Guyomar, D., Sebald, G., Pruvost, S., Lallart, M., Khodayari, A. and Richard, C. 2009. Energy harvesting from ambient vibrations and heat, *Intell. Mater. Syst. Struct.*, 20(5), 609–624.
- Hudak, N. S., and Amatucci, G. G. 2008. Small-scale energy harvesting through thermoelectric, vibration, and radiofrequency power conversion. *Journal of Applied Physics*, 103(10), 101301.
- Karami, M. A., and Inman, D. J. 2011. Analytical modeling and experimental verification of the vibrations of the zigzag microstructure for energy harvesting. *Journal of Vibration and Acoustics*, 133(1), 011002.
- Lee, S., Youn, B. D., and Jung, B. C. 2009. Robust segment-type energy harvester and its application to a wireless sensor. *Smart Materials and Structures*, 18(9), 095021.
- Lumentut, M. F., Francis, L. A., and Howard, I. M. 2012. Analytical techniques for broadband multielectromechanical piezoelectric bimorph beams with multifrequency power harvesting. *Ultrasonics, Ferroelectrics and Frequency Control, IEEE Transactions on*, 59(11), 2555-2568.
- Ou, Q., Chen, X., Gutschmidt, S., Wood, A., Leigh, N., and Arrieta, A. F. (2012). An experimentally validated double-mass piezoelectric cantilever model for broadband vibration-based energy harvesting. *Intell. Mater. Syst. Struct.*, 23(2), 117-126.
- Patel, R. 2013. Modelling analysis and optimisation of cantilever piezoelectric energy harvesters (Doctoral dissertation, *University of Nottingham*).

- Qi, S., Shuttleworth, R., Oyadiji, S. O., and Wright, J. 2010. Design of a multiresonant beam for broadband piezoelectric energy harvesting. *Smart Materials and Structures*, 19(9), 094009.
- SIMULIA Corp. 2010. "Abaqus Theory Manual in ABAQUS 6.10 Documentations"
- Song, H. J., Choi, Y. T., Purekar, A. S., and Wereley, N. M. 2009. Performance evaluation of multi-tier energy harvesters using macro-fiber composite patches. *Intell. Mater. Syst. Struct.*, 20(17), 2077-2088.
- Tang, L., Yang, Y., and Soh, C. K. 2010. Toward broadband vibration-based energy harvesting. *Intell. Mater. Syst. Struct.*, 21(18), 1867-1897.
- Wu, H., Tang, L., Yang, Y., and Soh, C. K. 2013. A novel two-degrees-of-freedom piezoelectric energy harvester. *Intell. Mater. Syst. Struct.*, 24(3), 357-368.
- Xiong, X., and Oyadiji, S. O. 2013. Modal electromechanical optimization of cantilevered piezoelectric vibration energy harvesters by geometric variation. *Intell. Mater. Syst. Struct.*, 25 (10), 1177-1195.
- Xue, H., Hu, Y., and Wang, Q. M. 2008. Broadband piezoelectric energy harvesting devices using multiple bimorphs with different operating frequencies. *Ultrasonics, Ferroelectrics and Frequency Control, IEEE Transactions on*, 55(9), 2104-2108.
- Zhou, W., Penamalli, G. R., and Zuo, L. 2012. An efficient vibration energy harvester with a multi-mode dynamic magnifier. *Smart Materials and Structures*, 21(1), 015014.

CHAPTER 10 AN EQUIVALENT CIRCUIT MODEL USING CORRECTED LUMPED MODAL PARAMETERS FOR MULTI-RESONANCE PIEZOELECTRIC VIBRATION ENERGY HARVESTING

Xingyu Xiong and S Olutunde Oyadiji

IEEE/ASME Transactions on Mechatronics (under review)

An Equivalent Circuit Model Using Corrected Lumped Modal Parameters for Multi-Resonance Piezoelectric Vibration Energy Harvesting

Xingyu Xiong and S Olutunde Oyadiji *

School of Mechanical, Aerospace and Civil Engineering,
The University of Manchester, M13 9PL, UK

ABSTRACT

This paper presents a coupled equivalent circuit model (ECM) using lumped modal parameters for multi-resonance piezoelectric vibration energy harvesters. The lumped modal parameters of each mode are derived by the finite element (FE) method using FE analysis software and transferred to the electrical circuit simulation software SPICE to generate the multi-mode ECM. Since the conventional circuit analysis normally uses lumped single degree of freedom model, which oversimplifies the structural modal behaviour, the modal participation factor is introduced in the lumped modal parameters to correctly represent the modal behaviour of each mode to the overall motion. A fully coupled distributed parameter electromechanical model (DPM) is used to compare with the ECM for the average power output with resistive loads in different multi-resonance harvester models. The results show that, by using the modal participation factors as the correction factors, the ECM using lumped modal parameters directly in SPICE can successfully predict the fully coupled frequency response functions of power output around multi-mode resonances. Since the implementation of the ECM is simplified, it is effective and convenient for the circuit analysis of the multi-resonance harvesters.

Keywords: piezoelectric, energy harvesting, vibration, equivalent circuit model, multi-resonance.

1. INTRODUCTION

In recent years, in order to develop self-powered, batteryless wireless sensor and sensor nodes for structural health monitoring, harvesting small-scale ambient energy has become a central issue [1]. As a popular technique with good potential to provide adequate power, vibration energy harvesting using piezoelectric materials has attracted a lot of attention in the last decade [2]. The vibration energy

* Corresponding author. Tel: 00 44 161 275 4348 Fax: 00 44 161 275 3844
E-mail address: s.o.oyadiji@manchester.ac.uk

harvesters can convert mechanical strain energy into electrical energy based on the piezoelectric effect. The performance analyses of harvesters in existing researches normally focus on varying the resistive loads. However, the analysis of nonlinear electrical components cannot be involved in these models. Therefore, to develop an effective method to combine the mechanical and electrical analyses together become necessary. Besides, the conventional beam-shaped harvesters have limited bandwidth, which is ineffective in real applications. Therefore, broadband techniques are being developed in order to achieve relatively large power output in a wider frequency bandwidth [3]. In particular, multi-resonance harvesters normally contain multiple beam parts, which can generate close resonance frequencies in multiple modes [4-9].

It is necessary to develop certain prediction models at the design stage to determine the performance of harvesters. Erturk and Inman [10] established an analytical model for rectangular cantilevered beam harvesters based on the Euler-Bernoulli beam assumptions and predicted the power output with resistive loads using a distributed parameter electromechanical model (DPM). The analytical model has been validated experimentally by Erturk and Inman as well as other researchers. They also introduced a correction factor for the lumped single degree-of-freedom (SDOF) model and found a good agreement between the predicted relative motion transmissibility using the Euler-Bernoulli beam model and the corrected SDOF model [11]. However, Erturk and Inman did not show how the correction factor affects the power output, and the corrected SDOF model is not available for the harvester with multi-mode. This is because the corrected SDOF model can only give valid frequency response function (FRF) around a single mode. Besides, for multi-resonance harvesters with non-uniform configurations, it is hard to derive the modal parameters using the analytical method. To overcome the limitations of the analytical model, the well-established approximate engineering solution, the finite element method (FEM) using the commercial finite element analysis (FEA) software packages, such as ABAQUS and ANSYS, has been widely used in existing works [6, 9, 12-18]. The FEM is able to deal with complicated models and derive modal data conveniently in multiple modes.

Also, since the circuit analysis with nonlinear electrical components cannot be used in conjunction with conventional structural models, the electrical equivalent circuit model (ECM) has been widely used as an alternative analysis technique in existing energy harvesting researches [16, 17, 19, 20]. Richter et al [20] demonstrated mechanical and electrical representations to explain the electro-mechanical analogies and presented the prediction of power output with resistive loads in a SDOF system. However, the ECM based on the uncorrected SDOF model is oversimplified. Elvin and Elvin [16] developed a FEA-ECM model by running an automatic post-processing program. However, the program needs to extract and transfer modal displacement and coupled voltage between the ABAQUS solver and the circuit simulation

software SPICE in each iteration, which is difficult to implement for multi-resonance harvester designs. Yang and Tang [17] derived the ECM parameters by decomposing FEA data using DPM and manually transferring them to the circuit simulation in SPICE. However, in their work, all ECM parameters are determined by drawing the Nyquist plots of the complex admittance FRFs, which requires running steady-state analysis in FEA solver in the wide range of frequencies around each mode. Therefore, using Yang and Tang's method to analyse the multi-resonance harvesters requires long computing time. This is due to the fact that the full steady-state analysis within a wide frequency band is needed in FEA solver, and the process of derivation of the ECM parameters also requires a long computing time.

In this paper, an easy implementation of a fully coupled ECM, which uses lumped modal parameter with correction factors, is introduced for multi-resonance harvester designs. The ECM parameters are represented by the lumped modal parameters of each mode directly and these modal parameters are transferred to the multi-mode circuit simulation in SPICE. The outlines of this paper are as follows: in section 2, the electro-mechanical analogies of the ECM using the corrected lumped modal parameters is presented; section 3 is on the derivation process of the ECM parameters from modal data produced by the FEA, and the procedure for the multi-mode ECM in the SPICE solver; section 4 presents the comparison of the analytical basis of the DPM and ECM; in section 5, the power output FRFs of some typical multi-resonance harvesters with different resistive loads generated between the ECM and the DPM are presented; section 6 outlines the findings in this paper.

2. EQUIVALENT CIRCUIT MODEL

For a harmonic base motion, the structural motion and electrical governing equations of the harvester (in transducer mode) with a resistive load in a lumped SDOF system are:

$$\begin{cases} m_m \ddot{z} + c_m \dot{z} + k_m z - \alpha U = F_m \\ C_p \dot{U} + \frac{U}{R_l} - \alpha \dot{z} = 0 \end{cases} \quad (1)$$

where m_m is the generalized modal mass, c_m is the modal damping coefficient and k_m is the modal stiffness. F_m is the modal mechanical force, z is the relative displacement related to the base motion y , U is the generated voltage, C_p is the static clamped piezoelectric capacitance, R_l is the resistive load and α is the modal electro-mechanical coupling factor. By assuming the harvester is working in short circuit condition ($U=0$), the steady-state solution of the motion equation given by Eq. 1 is equivalent to the steady-state solution of a series RLC circuit, which is illustrated by **Fig 1(a)**. The equivalence of the system parameters is shown in **Table 1**. The mechanical force, velocity, mass, stiffness and damping can be

represented by their electrical counterparts namely voltage source, current, inductor, reciprocal of the capacitor and resistor in a series RLC circuit.

Table 1: Electro-mechanical analogies of piezoelectric system

Steady-state solution analogy	Mechanical elements	Electrical counterparts
<i>Motion:</i> $Z_m(j\omega) = F_m/\dot{z}(j\omega) = c_m + j\omega m_m - jk_m/\omega$	Force	Voltage
	Velocity	Current
<i>Series RLC:</i> $Z_E(j\omega) = U/I(j\omega) = R + j\omega L - j/\omega C$	Mass	Inductance
	Stiffness	1/Capacitance
	Damping	Resistance

When the harvester is working in the actuator mode, by applying voltage on it without external mechanical force ($F_m=0$) and removing the resistive load, the electrical admittance Y is given by the total current I (replace U/R_l in Eq.1) over the applied voltage (the negative symbol of the voltage U is changed because the harvester is in actuator mode):

$$Y_{SDOF}(j\omega) = \frac{I}{U} = \frac{C_p \dot{U} + \alpha \dot{z}}{U} = j\omega C_p + \frac{\alpha^2}{c_m + j\omega m_m + k_m/j\omega} \quad (2)$$

Using Butterworth-Van Dyke topology [19], a lumped equivalent circuit in actuator mode is shown in **Fig 1(b)**. The admittance of the lumped circuit is:

$$Y_{SDOF}(j\omega) = \frac{I}{U} = j\omega C_p + \frac{1}{R_m + j\omega L_m - j/\omega C_m} \quad (3)$$

The topologies are:

$$L = \frac{m_m}{\alpha^2}; \quad R = \frac{c_m}{\alpha^2}; \quad \frac{1}{C} = \frac{k_m}{\alpha^2} \quad (4)$$

Fig 1(c) is the ECM of the SDOF model given by Eq. 2. The mechanical and electrical domains are connected by the ideal transformer, which is the modal electromechanical coupling factor α .

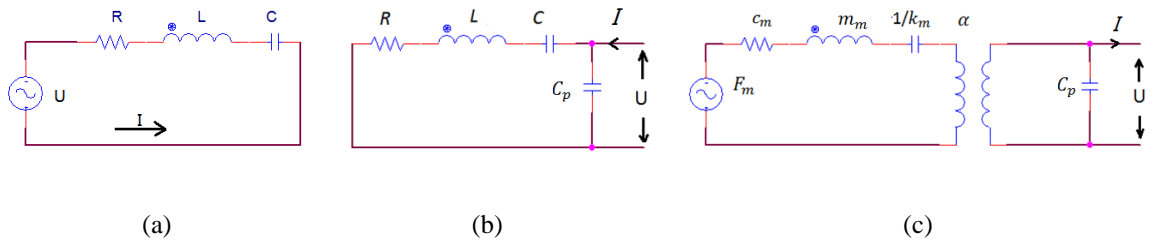


Fig 1: (a) a series RLC circuit; (b) lumped equivalent circuit in actuator mode; (c) SDOF ECM using lumped modal parameters.

The modal parameters are

$$c_m = 2\zeta\sqrt{k_m m_m}; \quad \omega_0 = \sqrt{k_m/m_m} \quad (5)$$

where ζ is the damping ratio and ω_0 is the resonance frequency. When $\omega=\omega_0$, the admittance can be simplified to:

$$Y_{SDOF}(j\omega)|_{\omega=\omega_0} = j\omega_r C_p + \frac{\alpha^2}{c_m} \quad (6)$$

It contains the real part $\Re Y$ and imaginary part $\Im Y$, and the modal electromechanical coupling factor α from which the electromechanical coupling coefficient k is desired as:

$$\alpha = \sqrt{\Re Y c_m}; \quad k^2 = \frac{\alpha^2}{k_m C_p + \alpha^2} \quad (7)$$

To allow the lumped SDOF model to be used in multi-mode ECM, the correction factor γ is added in the lumped forcing function [11]:

$$F_m = -\gamma m_m \ddot{y} \quad (8)$$

The correction factor γ is the modal participation factor, which indicates how strongly motion in the x-, y- or z-direction or rotation about one of these axes is represented in the eigenvector of that mode [22]. For the short circuit condition ($U=0$), the corrected relative motion transmissibility is:

$$T(j\omega) = \frac{z}{y} = \frac{\gamma_r \omega^2 m_m}{k_m - \omega^2 m_m + j\omega c_m} \quad \text{and} \quad |T|_{\omega=\omega_0} = \frac{\gamma}{2\zeta} = \gamma Q_M \quad (9)$$

where Q_M is the mechanical quality factor. It is well known that, the SDOF system is only applied in the neighborhood of the resonance. In a multi-mode ECM, the mechanical terminals of multiple modes are connected in parallel (see **Fig 2**), and the admittance is:

$$Y(j\omega) = j\omega C_p + \sum_{r=1}^{\infty} \frac{\alpha_r^2}{c_{mr} + j\omega m_r + k_{mr}/j\omega} \quad (10)$$

For the r-th mode, the admittance can be simplified as [17]:

$$Y_r(j\omega) = j\omega C_{dr} + \frac{\alpha_r^2}{c_{mr} + j\omega m_r + k_{mr}/j\omega} \quad (11)$$

where C_{dr} is called the damped capacitance [21], which includes the contributions of the equivalent mechanical capacitance C_m in other modes and it is larger than C_p .

3. ECM IMPLEMENTATION

According to the explanation of the above sections, the general procedure to derive the ECM parameters by FEA simulation is as follows:

Step 1: Run the natural frequency extraction analysis to obtain the short circuit angular resonance frequency ω_r , generalized modal mass m_m and the modal participation factor γ . Use Eq. (5) to derive c_m and k_m , and use Eq. (8) to derive F_m .

Step 2: Run the steady-state dynamics analysis at each natural frequency ($\omega=\omega_r$), apply a harmonic voltage excitation to derive the modal eletromechanical coupling factor α using Eq. (7).

Since the ECM parameters are derived for multiple modes from FEA results, a circuit simulation software SPICE can be used to build up a coupled multi-modes ECM. **Fig 2** demonstrates the ECM in the OrCAD PSpice software. The electrical components on the mechanical side represent the corresponding lumped modal parameters. By changing the resistance of the resistor connected on electrical side of the circuit, the power FRFs can be obtained conveniently from PSpice.

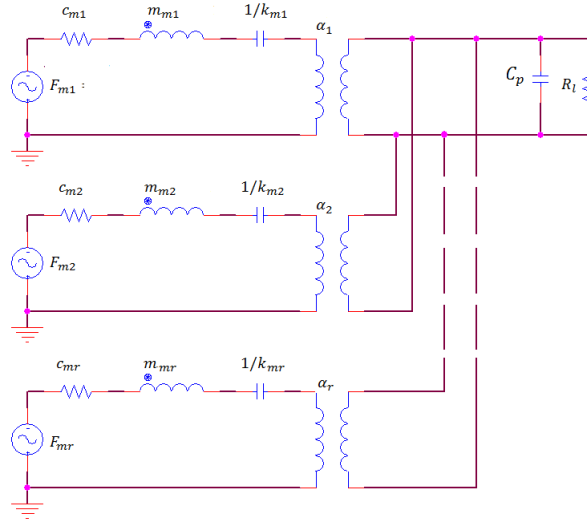


Fig 2: Multi-mode ECM circuit in SPICE.

4. ANALYSIS OF MULTI-RESONANCE HARVESTERS USING ECM AND DPM

4.1 A distributed parameter model

It is necessary to compare the ECM to another existing analysis method. Therefore, the DPM is introduced in this section. The governing equations of the modal vibration response and electrical behaviour of the harvester model with a resistive load are given as [21]:

$$\frac{d^2\eta_r(t)}{dt^2} + 2\zeta_r\omega_r \frac{d\eta_r(t)}{dt} + \omega_r^2\eta_r(t) + \chi_r v(t) = F_r(t) \quad (12)$$

$$\frac{v(t)}{R_l} + C_p \frac{dv(t)}{dt} - \sum_{r=1}^{\infty} \chi_r \frac{d\eta_r(t)}{dt} = 0 \quad (13)$$

where $\eta_r(t)$ is the corresponding modal coordinates of the r^{th} mode, v is the generated voltage, ζ_r is the modal damping ratio, ω_r is angular resonance frequency, χ_r is the equivalent modal electromechanical coupling term, F_r is the modal mechanical forcing function. The steady state solution of Eq. (12) is:

$$\eta_r(t) = \frac{F_r - \chi_r v}{\omega_r^2 - \omega^2 + j2\zeta_r \omega_r \omega} e^{j\omega t} \quad (14)$$

The voltage across R_l can be represented by:

$$v(t) = \frac{\sum_{r=1}^{\infty} \frac{j\omega F_r \chi_r}{\omega_r^2 - \omega^2 + j2\zeta_r \omega_r \omega}}{\sum_{r=1}^{\infty} \frac{j\omega \chi_r^2}{\omega_r^2 - \omega^2 + j2\zeta_r \omega_r \omega} + \frac{1}{R_l} + j\omega C_p} e^{j\omega t} \quad (15)$$

The complex power in the frequency domain is $v(j\omega)(\frac{v(j\omega)}{R_l})^*$ and the average power output is $|v|^2/2R_l$ (ignore electric losses). The vibration response of the beam relative to its base is:

$$u_{rel}(x, t) = \sum_{r=1}^{\infty} \phi_r(x) \frac{F_r - \chi_r v}{\omega_r^2 - \omega^2 + j2\zeta_r \omega_r \omega} e^{j\omega t} \quad (16)$$

With a vertical harmonic base excitation $\ddot{u}_b = Y_0 \omega^2 e^{j\omega t}$ and short-circuit condition ($v=0$), the forcing function F_r at each resonance frequency can be determined in the frequency domain from Eq. (14). For the r^{th} mode:

$$F_r = (\omega_r^2 - \omega^2 + j2\zeta_r \omega_r \omega) \eta_r(j\omega_r) = -j2\zeta_r \ddot{u}_{rel} \sqrt{m_{mr}} \Big|_{\omega=\omega_r} \quad (17)$$

By replacing $v(t)/R_l$ by $i(t)$, Eq. (13) gives:

$$i = \sum_{r=1}^{\infty} j\omega \chi_r \eta_r(j\omega_r) = \sum_{r=1}^{\infty} \frac{j\omega F_r \chi_r}{\omega_r^2 - \omega^2 + j2\zeta_r \omega_r \omega} \Big|_{\omega=\omega_r} \quad (18)$$

Then, once the relative displacement and electrical current data are derived from the FEA results ($v=0$), F_r and χ_r can be determined using Eq. (17) and Eq. (18), respectively.

4.2 Comparisons of ECM and DPM

In the flow charts given by **Fig 3**, ECM using corrected lumped parameters has been compared with DPM of harvester performance prediction. In particular, using ECM and DPM to derive the modal parameters from FEA data both require four steps. Instead of using Eq. 15 in DPM, SPICE is used to predict the power output with resistive loads in ECM. The ECM procedure used by Yang and Tang [17] is also presented as a flow chart in **Fig 3(c)**. However, Yang and Tang's approach not only requires six steps to derive the modal parameters, it also requires longer computing time for the FEA and longer time to process the FEA data to derive the ECM parameters. Thus, it is obvious that the ECM approach presented in this paper is easier to implement and quicker to run.

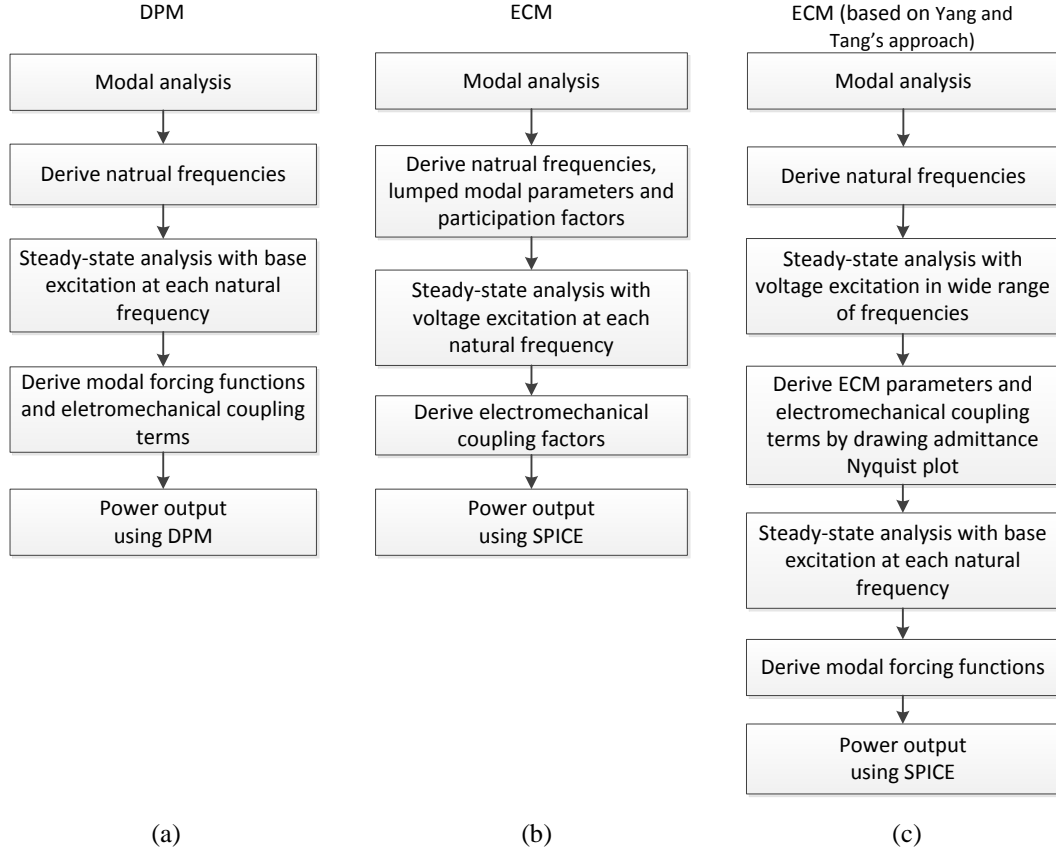


Fig 3: Flow charts comparing (a) DPM, (b) ECM using lumped parameters, and (c) ECM based on Yang and Tang's approach [17] to determine the power output of the harvester using FEA

5. RESULTS AND DISCUSSIONS FOR STACKED VEHS

5.1 Case study one: a two-layer two-mass harvester

In this and the next sections, two broadband harvester models with multi-resonance are developed in the FEA software ABAQUS. The average powers for different resistive loads and 1 m/s^2 base acceleration are computed. **Table 2** shows the material properties that have been used in the simulations. Structural damping is used and defined as 0.04 in this paper for the convenience of analysis ($\zeta_r = 0.02$).

Table 2: Materials properties

Density of piezoelectric layer	7750 kg/m^3
Clamped dielectric constant ϵ_{33}^S	$7.349 \times 10^{-9} \text{ F/m}$
Piezoelectric constant e_{31}	-5.4 C/m^2
Transverse coupling factor k_{31}	0.344
Density of structural layer/ mass	7850 kg/m^3
Young's modulus	
Structural layer/ mass	$200 \times 10^9 \text{ N/m}^2$
Piezoelectric layer	$60.9 \times 10^9 \text{ N/m}^2$

Fig 4 presents a two-layer two-mass stacked harvester, which can generate two close resonances with relatively large power outputs [9]. It consists of a base cantilevered beam which is attached to an upper beam by a spacer to develop a two-layer configuration. Two masses (M_{+1} and M_{+2}) are attached to each layer to tune the resonance frequencies and one of these masses (M_{+1}) also serves as the spacer. The piezoelectric layer is bonded on the base layer near the clamped area. The dimensions of the base/upper layers are (excluding the clamped area): 100*25*1 mm. The dimensions of the two masses are: 10*25*10 mm. The dimensions of the piezoelectric layer are 25*25*0.5 mm. In this configuration, the location of M_{+2} is 40mm away from the free tip of the upper layer.

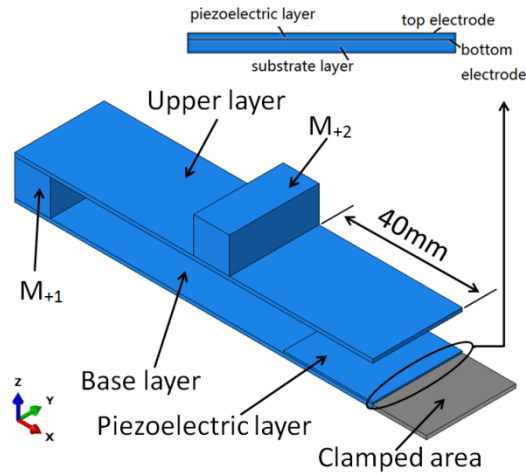


Fig 4: A two-layer two-mass multi-resonance harvester.

Table 3 gives the modal parameters for ECM and DPM in the first three modes. The derivation of the ECM parameters has followed the procedure given in section 3 and the implementation of DPM is also given in section 4. **Fig 5** is the three-mode ECM circuit of the two-layer two-mass harvester in SPICE, and the corresponding electrical components are assigned the values given in **Table 3**. It should be noted that the large resistor connected under the first transformer α_1 in **Fig 5** is used to ensure the electrical side is grounded and valid in the SPICE solver.

Table 3: Modal parameters in the first three modes of the two-layer two-mass harvester

Mode	f (Hz)	ECM						DPM	
		lumped modal parameters						parameters	
		m_m ($\times 10^{-3}$ kg)	c_m ($\times 10^{-3}$ Ns/m)	k_m ($\times 10^3$ N/m)	γ	F_M ($\times 10^{-3}$ N)	α ($\times 10^{-3}$)	F ($\times 10^{-3}$)	χ ($\times 10^{-3}$)
1	39.62	28.57	284.5	1.771	1.053	30.09	0.907	178.5	5.363
2	55.25	10.50	145.9	1.266	1.916	20.13	0.394	196.5	3.786
3	345.5	6.517	565.9	30.71	0.510	3.320	1.701	41.09	2.094

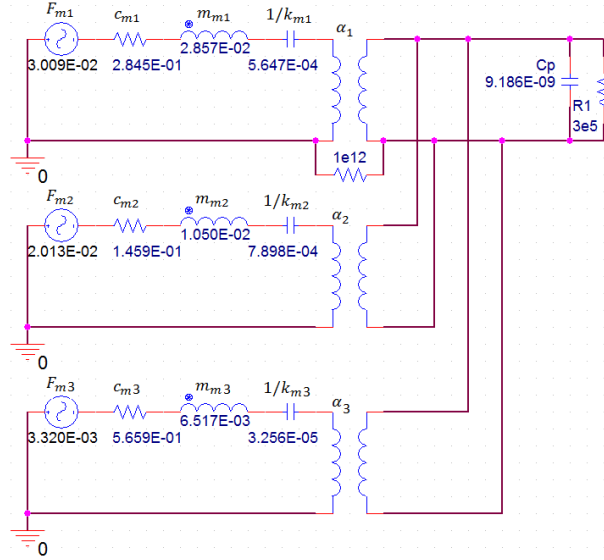


Fig 5: Three-mode ECM circuit simulation of the two-layer two-mass harvester in SPICE.

Since the first two modes are very close and the third mode is far away from the first two modes, only the average power FRFs around the first two modes is discussed. **Fig 6** shows the voltage and average power FRFs with different resistive loads from 10k ohm (R1E4) to 10M ohm (R1E7) using both ECM and DPM. The results show that the ECM using lumped modal parameters with corrected forcing function in SPICE can generate almost the same FRFs compared with the DPM. When the connected resistance is increased, the peaks of the FRFs shift from the short-circuit natural frequencies to the open-circuit natural frequencies due to the significantly increased voltages which generate back coupling effects. When the connected resistance is from 100k ohm to 1M ohm, the power outputs of the two modes maintain higher levels.

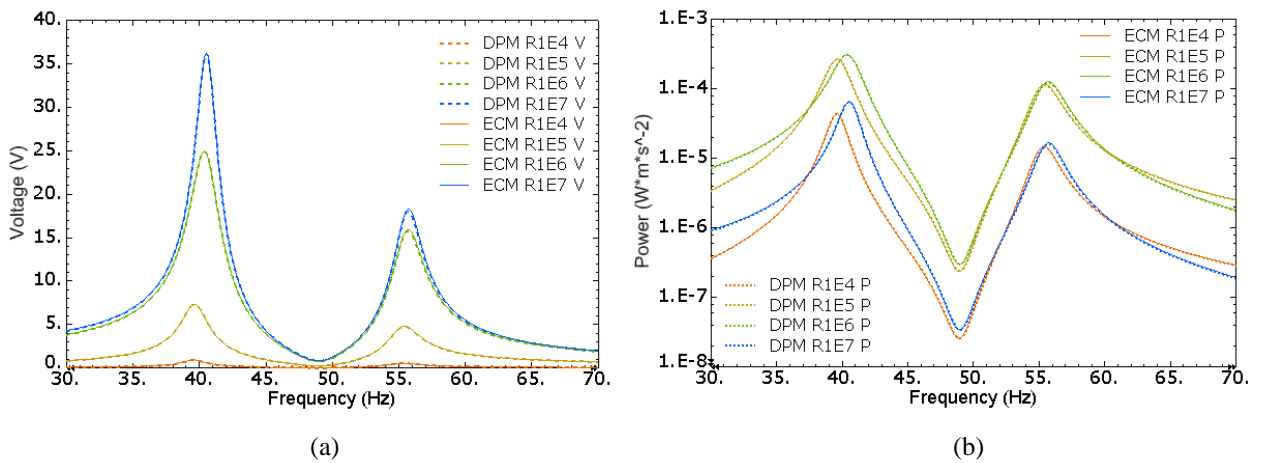


Fig 6: FRFs of the two-layer two-mass harvester around the first two modes using the ECM and DPM with different resistive loads; (a) voltage FRFs; (b) average power FRFs.

5.2 Case study two: a three-layer four-mass harvester

In this section, a three-layer four-mass stacked harvester is developed. Comparing the configuration of the three-layer four-mass harvester to the two-layer two-mass harvester configuration, it is seen that two additional masses and an additional layer are attached beneath the base layer. The dimensions of each layer, each mass and the piezoelectric layer of the three-layer four-mass harvester are the same as those components given in the two-layer two-mass harvester. **Fig 7(a)** illustrates a 3D view of the three-layer four-mass harvester. **Fig 7(b)** illustrates the locations of the attached four masses.

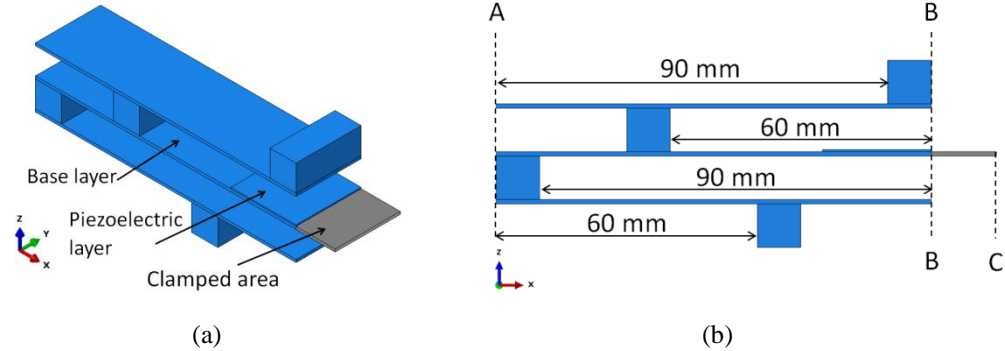


Fig 7: a three-layer four-mass harvester; (a) 3D view; (b) mass positions; A= tip of base layer; BC= clamped length of base layer.

Table 4 gives the modal parameters for ECM and DPM in the first four modes. **Fig 8** shows the voltage and average power FRFs with different resistive loads using the four-mode ECM and DPM. Only the FRFs around the first three modes are shown because the fourth mode is far away from the first three modes. The results prove that the ECM still generates almost the same FRFs compared with the DPM. When the connected resistive load is greater than 100k ohm but less than 1M ohm, the power outputs around the first three modes are much higher than when the lowest (10k ohm) and the highest (10M ohm) resistive loads are connected.

Table 4: Modal parameters in the first four modes of the three-layer four-mass harvester

Mode	f (Hz)	ECM						DPM	
		lumped modal parameters						parameters	
		m_m ($\times 10^{-3}$ kg)	c_m (Ns/m)	k_m ($\times 10^3$ N/m)	γ	F_M ($\times 10^{-3}$ N)	α ($\times 10^{-3}$)	F ($\times 10^{-3}$)	χ ($\times 10^{-3}$)
1	33.50	43.27	0.364	1.917	0.949	34.50	0.921	166.4	4.425
2	50.51	13.06	0.166	1.316	1.546	27.81	0.398	243.2	3.439
3	76.38	23.46	0.450	5.404	1.185	31.49	0.901	205.9	5.785
4	312.9	29.07	2.286	112.4	0.903	9.309	3.676	54.53	21.24

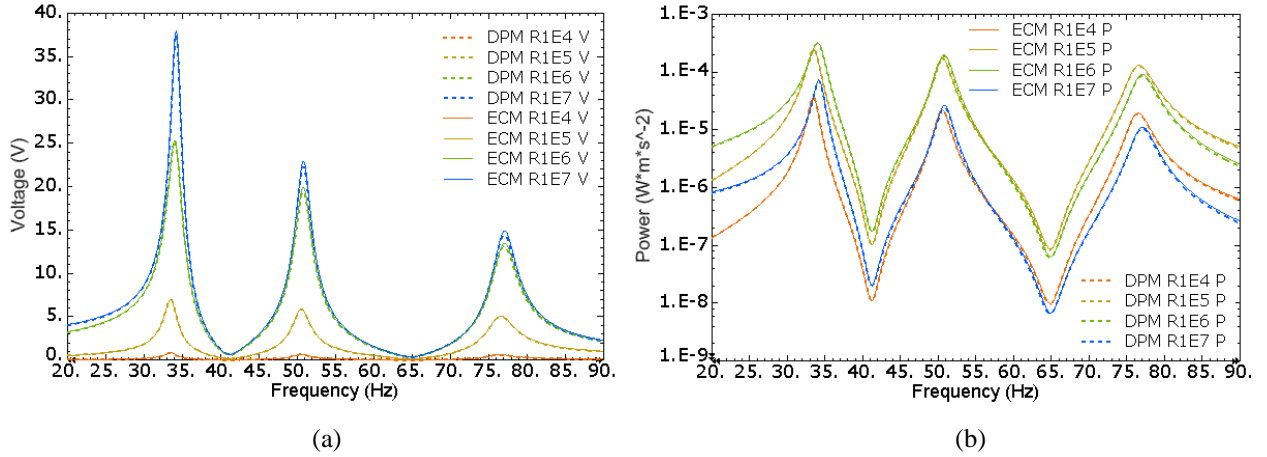


Fig 8: FRFs of the three-layer four-mass harvester around the first three modes using the ECM and DPM with different resistive loads; (a) voltage FRFs; (b) average power FRFs.

In section 5.1, the two-layer two-mass harvester, which generates relatively large power output in two close modes, has a better broadband performance than a conventional beam-shaped harvester. However, because of the two close modes, the harvester still has limited broadband performance. Therefore, the three-layer four-mass harvester, which has three close resonance frequencies with relatively large power output, is introduced in this section. **Fig 9** shows the broadband performance comparison of three harvesters with optimal resistive loads. The configuration of the one-layer one-mass harvester is the base layer with mass M_{+1} (see **Fig 4**). Therefore, it is actually a single cantilevered beam with a tip mass. Apparently, in comparison with a single beam harvester, the multi-layer stacked harvester with close multiple resonances can significantly improve the broadband performance.

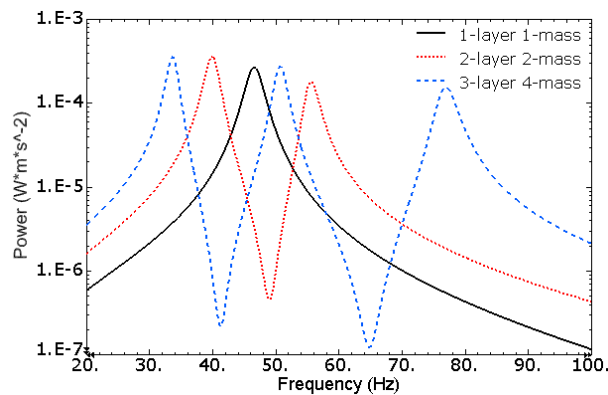


Fig 9: Broadband performance comparing between one-layer one-mass (cantilevered beam with tip mass), two-layer two-mass, and three-layer four-mass harvesters.

6. CONCLUSIONS

This article has presented an easily implemented and fully coupled ECM, which transfers the corrected lumped modal parameters to SPICE. The lumped modal parameters and the correction factors are derived using FEA. The ECM has been compared with DPM in the case studies on the two-layer and the three-layer multi-resonance harvesters. The results show that using the corrected lumped modal parameters in SPICE can successfully predict the performance of the harvester around multiple modes with resistive loads. Once the multi-resonance harvesters are well designed and optimized, the ECM can be used in SPICE, which overcomes the limitations of the conventional predictive models, to simulate the electrical behaviours connected with nonlinear electrical components such as the storage capacitors.

REFERENCES

- [1] N. S. Hudak and G. G. Amatucci, "Small-scale energy harvesting through thermoelectric, vibration, and radio frequency power conversion," *Journal of Applied Physics*, 103(10), 101301, 2008.
- [2] S.R. Anton, and H. A. Sodano, "A review of power harvesting using piezoelectric materials (2003-2006)," *Smart Materials and Structures*,16(3), R1, 2007.
- [3] L. Tang, Y. Yang, and C. K. Soh, "Toward broadband vibration-based energy harvesting," *Intell. Mater. Syst. Struct.*, 21(18), 1867-1897, 2010.
- [4] W. Wang, T. Yang, X. Chen and X.Yao, "Vibration energy harvesting using a piezoelectric circular diaphragm array," *IEEE Trans. Ultrason. Ferroelectr. Freq. Control*, 59(9), 2022-2026, 2012
- [5] M. F. Lumentut, L. A. Francis and I. M. Howard, "Analytical techniques for broadband multielectromechanical piezoelectric bimorph beams with multifrequency power harvesting," *IEEE Trans. Ultrason. Ferroelectr. Freq. Control*, 59(11), 2555-2568, 2012
- [6] W. Zhou, G. R. Penamalli and L. Zuo, "An efficient vibration energy harvester with a multi-mode dynamic magnifier," *Smart Materials and Structures*, 21(1), 015014, 2012.
- [7] Q. Ou, X. Chen, S. Gutschmidt, A. Wood, N. Leigh and A. F. Arrieta, "An experimentally validated double-mass piezoelectric cantilever model for broadband vibration-based energy harvesting," *Intell. Mater. Syst. Struct.*, 23(2), 117-126, 2012.
- [8] A. Erturk, J. Hoffmann and D.J. Inman, "Modeling of piezoelectric energy harvesting from an L-shaped beam mass structure with an application to UAVs," *Intell. Mater. Syst. Struct.*20: 529–544,2009.
- [9] X. Xiong and S. O. Oyadiji, "Optimal design of two-layer vibration energy harvesters using a modal approach," *Smart Materials and Structures*, 23(3), 035005, 2014.
- [10] A. Erturk, and D. J. Inman, "A Distributed Parameter Electromechanical Model for Cantilevered Piezoelectric Energy Harvesters," *Journal of Vibration and Acoustics*, 130(4), 041002, 2008.

- [11] A. Erturk, and D. J. Inman, "On Mechanical Modeling of Cantilevered Piezoelectric Vibration Energy Harvesters," *Intell. Mater. Syst. Struct.*, 19, 1311, 2008.
- [12] L. Zhang, "Analytical Modeling and Design Optimization of Piezoelectric Bimorph Energy Harvester," Doctoral Dissertation, the University of Alabama, 2010
- [13] R. Patel, "Modelling analysis and optimisation of cantilever piezoelectric energy harvesters," Doctoral dissertation, the University of Nottingham, 2013
- [14] H. Wu, L. Tang, Y. Yang and C. K. Soh, "A novel two-degrees-of-freedom piezoelectric energy harvester," *Intell. Mater. Syst. Struct.* 24(3), 357-368, 2013
- [15] X.Xiong and S.O.Oyadiji, "Modal electromechanical optimization of cantilevered piezoelectric vibration energy harvesters by geometric variation," *Intell. Mater. Syst. Struct.*, DOI: 10.1177/1045389X13502872, 2013
- [16] N. G. Elvin and A. A. Elvin, "A Coupled Finite Element-circuit Simulation Model for Analyzing Piezoelectric Energy Generator," *Intell. Mater. Syst. Struct.*, 20:587-595, 2009
- [17] Y. Yang and L. Tang, "Equivalent circuit modelling of piezoelectric energy harvesters," *Intell. Mater. Syst. Struct.*, 20(18), 2223-2235, 2009
- [18] Q. Tang and X. Li, "Two-Stage Wideband Energy Harvester Driven by Multimode Coupled Vibration," *IEEE/ASME Transactions on Mechatronics*, DOI: 10.1109/TMECH.2013.2296776, 2014
- [19] L. Tang, L. Zhao, Y. Yang and E. Lefevre, "Equivalent Circuit Representation and Analysis of Galloping-Based Wind Energy Harvesting," *IEEE/ASME Transactions on Mechatronics*, 10.1109/TMECH.2014.2308182, 2014
- [20] B. Richter, J. Twiefe and J. Wallaschek, "Chapter4: Piezoelectric Equivalent Circuit Models," In: *Energy Harvesting Technologies*, Springer Science+Business Media, DOI 10.1007/978-0-387-76464-1_4, 2009
- [21] T. Ikeda, "Fundamentals of Piezoelectricity," Oxford University Press, 1990
- [22] SIMULIA Corp, *Abaqus Theory Manual in ABAQUS 6.10 Documentations*, 2010
- [23] A.Erturk and D.J.Inman, "Piezoelectric Energy Harvesting," John Wiley & Sons 978-1-1199-9135-9, 2011.

CHAPTER 11 DESIGN, ANALYSIS AND EXPERIMENTAL VALIDATION OF THE PERFORMANCE OF MULTI-LAYER STACKED VIBRATION ENERGY HARVESTERS

Xingyu Xiong and S Olutunde Oyadiji

Design, Analysis and Experimental Validation of the performance of Multi-layer Vibration Energy Harvesters

Xingyu Xiong and S Olutunde Oyadiji *

School of Mechanical, Aerospace and Civil Engineering,
The University of Manchester, M13 9PL, UK

Abstract

Multi-layer vibration energy harvesters using piezoelectric materials are designed, analysed and experimentally tested in this article. They consist of a cantilevered base beam and some upper and lower layer beams with rigid masses bonded between the beams as spacers. A piezoelectric ceramic plate is bonded on the cantilevered base near the clamped end. The cantilevered base is mounted on an electromagnetic shaker and subjected to random base excitations. The rigid masses are designed to be movable on each layer in order to tune the resonance frequencies of the harvesters. For a four-layer harvester, relocating the mass positions leads to the generation of up to four close resonance frequencies over the frequency range from 10Hz to 100Hz with relative large power output. The harvesters are connected with a resistance decade box and the frequency response functions of the voltage and power on resistive loads are determined. The experimental results are compared with the simulation results to validate the optimization strategy, which is based on a modal approach using the finite element method to select configurations with optimal or near-optimal mechanical performance in multiple modes. On a certain level of power output, the experimental results show that the multi-layer harvesters can generate a frequency band that is more than two times greater than the frequency band produced by a single layer harvester.

Keywords: vibration energy harvesting, piezoelectric, multiple resonances, experimental study.

1. Introduction

For the development of structural healthy monitoring strategies, there is a current need to harvest small-scale ambient energy for the self-powered, batteryless wireless sensor nodes [1, 2]. Harvesting the vibration energy from resonance has drawn much attention since it has good potential to provide adequate power. Piezoelectric materials are used to convert mechanical strain energy into electrical energy. However, there is a limitation for the conventional beam-shaped harvesters in real applications due to their limited bandwidth. In order to achieve wider bandwidth and relative large power output, harvesters with different broadband techniques have been developed in recent years. For example, the multi-resonance harvesters, nonlinear

* Corresponding author. Tel: 00 44 161 275 4348 Fax: 00 44 161 275 3844

E-mail address: s.o.oyadiji@manchester.ac.uk

harvesters with magnet and the harvesters with frequency tuning mechanism are widely reported in existing literatures [3, 4].

In order to provide broadband power output, typical multi-resonance harvesters can generate close resonance frequencies in multiple modes. However, to generate relative large power output in every mode is a tough task. A vibration energy harvester comprising an array of beams is widely used since it can easily generate close resonance frequencies and smooth power output. It normally consists of several individual beam structures. In most existing works, several cantilevered beams are electrically connected while physically decoupled [5-8]. Without the interference of strong vibration coupling, the fundamental modes of different beams can be tuned easily to generate close resonance frequencies and nearly the same level of power outputs. However, around each vibration mode, most of the cantilevered beams are barely active while their bonded piezoelectric materials only undergo small strains. This has led to negative influence on both mechanical energy and electromechanical coupling, which substantially reduce the power density of the harvesters if too many beams are used. There is another widely reported multi-resonance design, which is designated as dual-mass harvesters [9-11]. It consists of two masses and one cantilevered beam. One mass is bonded at the free tip and another mass is bonded at the centre of the beam. The two masses separate the cantilevered beam into two parts, and the interaction of the two parts can generate the first two transverse vibration modes. However, the dual-mass harvester only generates two close modes, which still have limited broadband performance. Besides, the existing dual-mass harvesters are normally special designs without giving systematic analysis of how the changes of configurations affect the mechanical and electromechanical performance.

Apart from the multi-resonance harvesters described above, there are some other designs that have been reported in existing literature, such as L-shaped [12] and Zigzag-shaped harvesters [13]. However, except for the array of beams designs, developing an effective multi-resonance harvester, which can efficiently harvest energy from several modes, is not easy. In many investigations, although the resonance frequencies of the harvesters are enough close, one or more vibration modes can be dominant. This significantly affects the broadband performance since the performance of the remaining modes is reduced. This is clearly due to the lack of proper design. However, in the existing multi-resonance harvester designs, optimization study for either mechanical structure or electromechanical coupling are barely provided due to the complexity of the configurations.

Xiong and Oyadiji [14] developed a two-layer harvester consisting of a base cantilevered beam that is connected to an upper beam by a spacer. Two masses are attached to each layer to tune the resonance frequencies of the harvester and one of these masses serves as the spacer. By varying the dimensions of the harvester and the positions of the masses, the harvester can generate close resonance frequencies and considerable power output in the first two modes. Based on the study of the two-layer harvester, Xiong and Oyadiji [15] subsequently developed multi-layer harvesters with up to five layers, which can generate five close resonance frequencies. In Xiong and Oyadiji's researches, a modal approach is introduced to evaluate the modal structural and electromechanical performance using the finite element method. A configurational

optimization strategy based on the modal approach is developed to select the configurations with better modal mechanical performance and close resonance frequencies in multiple modes. Using this optimization strategy obviates the need to run the full analysis at the first stage and it is effective and convenient for general multi-resonance harvester designs.

In this paper, an experimental study is provided to validate the previous optimal design study of multi-layer harvesters. The harvesters with up to four layers are tested and the modal approach and optimization strategy are validated based on the test results. This paper is organised into six sections. Section 2 is a brief introduction on harvester modelling using a general distributed electromechanical parameter model (DPM) with the utilization of the finite element analysis (FEA) technique, and on the introduction of the modal approach for modal performance determination. Section 3 is on multi-layer harvester design development and configurational optimisation of multi-layer harvesters. Section 4 is on the introduction of Experimental test setup. Section 5 is on experimental validation of the performance of multi-layer harvesters. The last section presents the conclusions of this paper.

2. Vibration energy harvesting model

2.1 A distributed parameter electromechanical model

The modal analysis technique can be used to represent the steady-state linear vibration response of a harvester model that is subjected to continuous harmonic excitation. The displacement of the transverse vibration relative to the moving base of the harvester at time t is:

$$u_{rel}(t) = \sum_{r=1}^{\infty} \phi_r \eta_r(t) \quad (1)$$

where ϕ_r is the mass-normalised eigenfunction and $\eta_r(t)$ is the corresponding modal coordinates of the r^{th} mode. The equations governing the vibration modal response and electrical behaviour of the harvester model with a resistive load are given as [16, 17]:

$$\frac{d^2 \eta_r(t)}{dt^2} + 2\zeta_r \omega_r \frac{d\eta_r(t)}{dt} + \omega_r^2 \eta_r(t) + \chi_r v(t) = F_r(t) \quad (2)$$

$$\frac{v(t)}{R_l} + C_p \frac{dv(t)}{dt} - \sum_{r=1}^{\infty} \chi_r \frac{d\eta_r(t)}{dt} = 0 \quad (3)$$

where $\eta_r(t)$ is the corresponding modal coordinates of the r^{th} mode, v is the generated voltage, ζ_r is the damping ratio, ω_r is angular resonance frequency, χ_r is the modal electromechanical coupling term, F_r is the modal mechanical forcing term, C_p is the piezoelectric capacitance and R_l is the resistive load. The steady state solution of Eq.2 is:

$$\eta_r(t) = \frac{F_r - \chi_r v}{\omega_r^2 - \omega^2 + j2\zeta_r \omega_r \omega} e^{j\omega t} \quad (4)$$

In fact, the derivations of the eigenfunction ϕ_r , coupling term χ_r , and F_r can be tough and tedious when the configuration of the harvester is not uniform. Therefore, FEA software like ABAQUS and ANSYS are used at this stage to derive those parameters. For the short-circuit condition ($v = 0$) of the harvester with a harmonic base excitation $Y_0 \omega^2 e^{j\omega t}$ at each resonance frequency, the absolute displacement relative to the

moving base can be derived from the FEA results. Then, for the r^{th} mode, the forcing function F_r determined from Eq. 4 in the frequency domain is given as follows:

$$F_r = (\omega_r^2 - \omega^2 + j2\zeta_r\omega_r\omega)\eta_r(j\omega_r) = -2\zeta_r\ddot{u}_{rel}\sqrt{m_{mr}}\Big|_{\omega=\omega_r} \quad (5)$$

where m_m is the generalized modal mass. By replacing $v(t)/R_l$ with $i(t)$ in Eq.3, the complex current i_r under the short-circuit condition can be derived from the FEA results and it is given by:

$$i_r = \sum j\omega\chi_r\eta_r(j\omega_r) = \sum_{r=1}^{\infty} \frac{j\omega F_r\chi_r}{\omega_r^2 - \omega^2 + j2\zeta_r\omega_r\omega}\Big|_{\omega=\omega_r} \quad (6)$$

Then, with the known i_r , the modal coupling term χ_r can be determined. The voltage across R_l can be represented by [17, 18]:

$$v(t) = \frac{\sum_{r=1}^{\infty} \frac{j\omega F_r\chi_r}{\omega_r^2 - \omega^2 + j2\zeta_r\omega_r\omega}}{\sum_{r=1}^{\infty} \frac{j\omega\chi_r^2}{\omega_r^2 - \omega^2 + j2\zeta_r\omega_r\omega} + \frac{1}{R_l} + j\omega C_p} e^{j\omega t} \quad (7)$$

The complex power in the frequency domain is $v(j\omega)(\frac{v(j\omega)}{R_l})^*$ and the average power output is $|v|^2/2R_l$ (ignore electric losses). In this paper, the damping ratio ζ_r of each mode is experimentally derived.

2.2 A modal approach for modal performance determination

The maximum average power output of a vibration harvester can be evaluated using a modal electromechanical criterion k^2Q_m , and it is given as follows (for a standard rectifier interface with no electrical losses) [18]:

$$P_{max} = \begin{cases} \frac{F_m^2}{2c_m} \frac{\pi k^2 Q_m}{(\pi + k^2 Q_m)^2} & \text{when } k^2 Q_m \leq \pi \\ \frac{F_m^2}{8c_m} & \text{when } k^2 Q_m \geq \pi \end{cases} \quad (8)$$

Eqs. (8) and (9) are based on the lumped single degree-of-freedom (SDOF) model, where k is the modal electromechanical coupling coefficient (EMCC); $Q_m = 1/2\zeta$ is the quality factor; F_m and c_m are lumped mechanical force and damping coefficient, respectively. In order to use the lumped SDOF model for multiple degrees of freedom systems, the modal participation factor γ should be added as the correction factor [19].

The corrected lumped forcing function is:

$$F_{mr} = -\gamma_r m_m \ddot{y} \quad (10)$$

and the EMCC and other lumped parameters are:

$$k^2 = \frac{\alpha_r^2}{k_m C_p + \alpha_r^2} = \frac{\omega_{oc}^2 - \omega_{sc}^2}{\omega_{oc}^2}; \quad c_{mr} = 2\zeta_r \sqrt{k_{mr} m_{mr}}; \quad \omega_r = \sqrt{k_{mr}/m_{mr}} \quad (11)$$

where y is the base motion; $\alpha_r = \chi_r \sqrt{m_{mr}}$ is the lumped coupling factor; m_m is the generalized modal mass; k_m is the effective stiffness; ω_{oc} and ω_{sc} are the open-circuit and short-circuit angular resonance frequencies, respectively. The maximum power given by Eq. 9 can be rewritten as:

$$P_{max} = \frac{F_{mr}^2}{8c_{mr}} = \frac{\gamma_r^2 m_{mr}}{16\zeta_r \omega_r} \dot{y}^2 = \frac{m_{er}}{16\zeta_r \omega_r} \dot{y}^2 \quad (12)$$

where m_e is called the effective mass which represents the mass participating in the forcing function and motion. The sum of the effective masses for all modes is the total mass M of the whole model [19]:

$$m_{er} = \gamma_r^2 m_{mr}; \quad \sum_{r=1}^{\infty} m_{er} = M \quad (13)$$

Then, for the r^{th} mode, mass ratio is defined as:

$$N_r = \frac{\gamma_r^2 m_{mr}}{M} = \frac{m_{er}}{M} \quad (14)$$

The mass ratio N is the percentage ratio of the effective mass to the total mass. For multiple degrees of freedom system, the sum of all mass ratios equals to one. If one mode has a very large mass ratio, the remaining modes will have small mass ratios. Mass ratio represents how much mass of each mode effectively participates in the overall motion and it is used as a modal criterion to evaluate the modal mechanical performance of each mode on the power density directly [20]. The average power per 1m/s^2 base excitation per cubic centimetre (cm^3) using the mass ratio N is given as:

$$PD = \frac{N_r \rho}{16 \xi_r \omega_r} * 10^{-6} (\text{W s}^4 / \text{cm}^3 \text{ m}^2) \quad (15)$$

where ρ is the mass density (kg/m^3). A parametric study on the normalized power density of harvesters as a function of $k^2 Q_m$ for different mass ratios and for $f=46$ Hz, $Q_m=25$ and $\rho \approx 7840$ kg/m^3 , is given in Figure 1. The results are determined using DPM with the optimal resistive load. The results show that mass ratio linearly affects the maximum power density. When the electromechanical coupling is not sufficiently strong, the EMCC can also significantly affect the power density. Therefore, a modal approach is developed using the two criteria of mass ratio and EMCC to evaluate the modal mechanical and electromechanical performance of harvesters [14, 15]. Figure 2 gives a flow chart to describe the process for operating the modal approach.

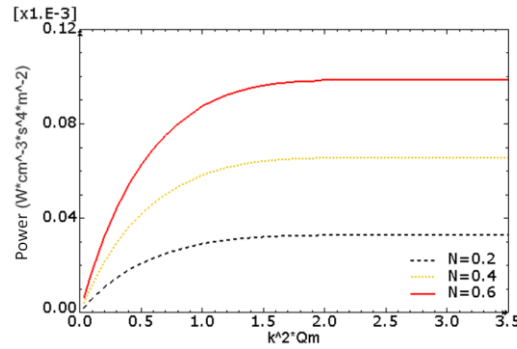


Figure 1: Power as function of $k^2 Q_m$ for different mass ratio N

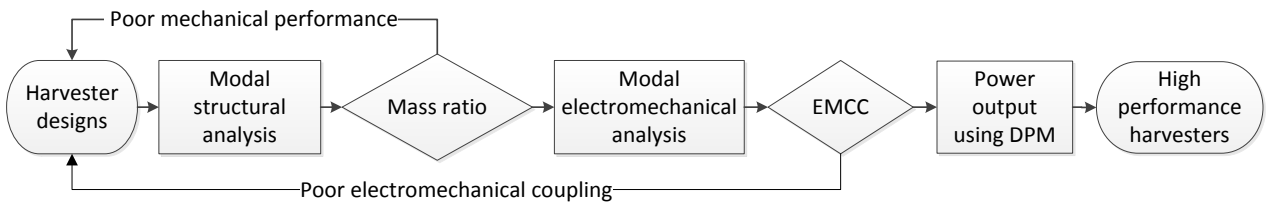


Figure 2: Flow chart of the modal approach for performance determination of harvester

3. Design, development and configurational optimisation of multi-layer harvesters

3.1 Design and development of multi-layer harvesters

In this section, the configurations of the multi-layer harvesters designed for the experimental test are illustrated initially. A multi-layer harvester consists of a longer cantilevered base (see Figure 3a), some shorter upper/lower layers (see Figure 3b) and masses bonded between each pair of adjacent beams. Figure 3 (c) shows the simulation model of the two-layer two-mass harvester *2L2M-P05* developed by the commercial FEA software ABAQUS. As Figure 3 shows, the effective length of the cantilevered base is 101 mm, and the remaining part is clamped. A plate of the piezoelectric ceramic PZT is bonded near the clamped end of the base layer. There is a 1 mm gap between the PZT and the clamped end. All upper/lower layers and the masses have the same dimensions. The thickness and width of the masses are 12 mm and 9 mm, respectively. The weight of each mass is 18.8 grams. Other properties of the harvester are given in Table 1.

Since the masses act as spacers and they are movable to tune the resonance frequencies, for the convenience of fixing and moving the masses, there are ten groups of through holes on the upper/lower layers and six groups of through holes on the base layer. Each group has two holes. In the experiment, each mass also has two through holes and screws and nuts are used to bond the mass. In the simulation, the masses, screws and nuts are simplified into uniform masses of the magnitudes, which are equivalent to the total mass of the spacers and screws and nuts. There are ten possible mass positions and the sketch for numbering of mass positions is illustrated in Figure 4. The positions of the masses from the free tip to the clamped end of the base layer are identified as *Pabc-de*, where *a*, *b* and *c* represent the positions of masses M_{+1} , M_{+2} and M_{+3} on the upper half and *d* and *e* represent the positions of masses M_{-1} and M_{-2} on the lower half by numbers from 0 to 9. For example, the two-layer two-mass harvester *2L2M* given in Figure 3 (c) has the mass position *P05* and the four-layer five-mass harvester *4L5M* given in Figure 4 has the mass position *P391-09*. Since the combinations of mass positions are too many, it is impossible to test and compare the performance of all possible positions in experiment. Therefore, a configurational optimization strategy, based on the modal approach, is also introduced here to select the mass positions with optimal performance.

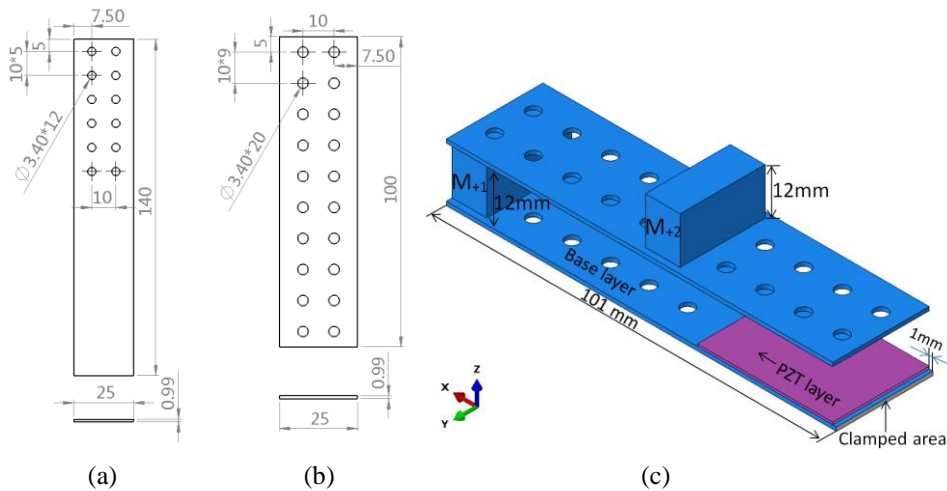


Figure 3: Sketches of (a) base layer (unit: mm) and (b) upper/lower layer (unit: mm) of the multi-layer harvesters, and (c) the simulation model of the two-layer two-mass harvester *2L2M-P05*.

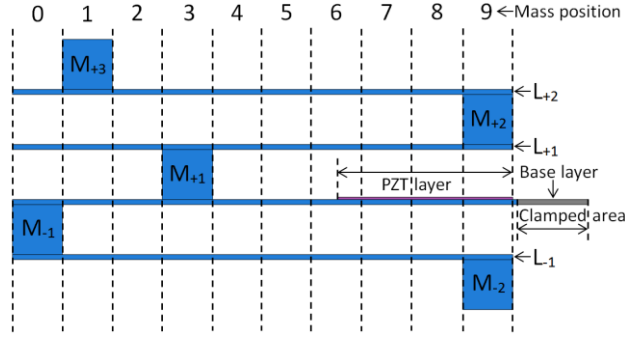


Figure 4: Sketch for numbering of mass positions (not the actual dimensions of the masses); four-layer five-mass model 4L5MP391-09; two upper layers and one lower layer are located on both sides of the base layer and the locations of masses on the upper half (M_{+1} , M_{+2} , M_{+3}) is 391 and the lower half (M_{-1} , M_{-2}) is 09.

Table 1: Properties of the multi-layer harvester

Parameters	Properties
Thickness of piezoelectric layer	0.65mm
Length of piezoelectric layer	34mm
Density of piezoelectric layer	7800kg/m ³
Clamped dielectric constant ϵ_{33}^S	1.1133x10 ⁻⁸ F/m
Piezoelectric layer Young's modulus	60.7x10 ⁹ N/m ²
Piezoelectric constant d_{31}	-210x10 ⁻¹² C/N
Transverse coupling factor k_{31}	0.38
Density of base/upper/lower layers	7930kg/m ³
Young's modulus of base layer	200x10 ⁹ N/m ²
Damping ratio	Measured

3.2 Configurational optimisation of multi-layer harvesters using modal approach

The previously introduced modal approach uses mass ratio to evaluate the modal mechanical performance. In fact, the natural frequencies and mass ratios can be determined directly by the FEA modal analysis. Since the multi-resonance harvester requires close natural frequencies and relative large power output in each mode, a structural screening process is developed using the mass ratio and frequency ratio as two filters to determine the configuration with optimal or near-optimal modal mechanical broadband performance (see Figure 5). The optimization strategy is used to select the configurations with close resonances and favourable values of mass ratio initially, which obviates the need for full steady-state analysis. A previous studied structural screening result of the two-layer model 2L2M is given in Figure 6 [15]. The shaded area is the selected mass positions of optimal or near-optimal configurations that meet the screening criteria frequency ratio $f_2/f_1 < 2$ and mass ratio $N > 0.2$ in each mode. It should be noted that the screening result is based on the analysis presented in previous work using the original configuration. The base and upper/lower layers of the original configurations have the same length 100 mm but they do not have through holes. The thickness and width of the masses are both 10 mm, and the thickness and length of PZT layer are 0.5 mm and 25 mm, respectively ($M_{+1}=6$ is unavailable in this article). It should be noted that these dimensions are slightly different from those used in the previous analyses. In fact, the experimental and simulated results provided in this article based on the modified configuration with through holes still follow the screening results based on the original configuration. More details about validating the structural screening results using experimental data

will be discussed in the sections 5.1 and 5.2.

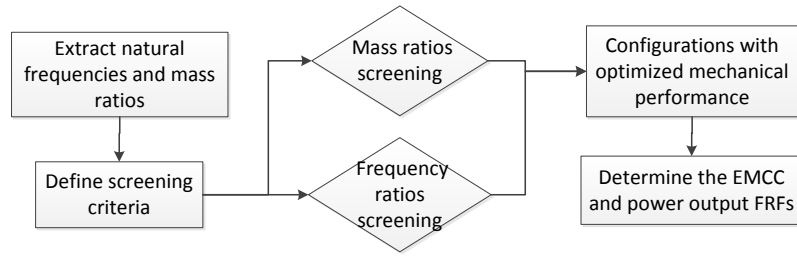


Figure 5: Flow chart of the structural screening process for configurational optimization of multi-resonance harvesters.

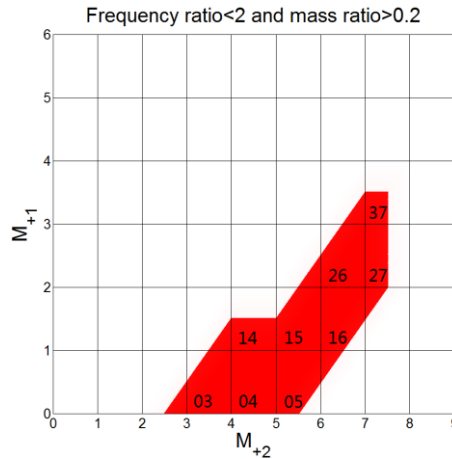


Figure 6: Result of structural screening for two-layer model (for the original configuration with no through hole in previous work [15]); the shaded area is the selected configurations meet the screening criteria $f_2/f_1 < 2$, and N_1 and $N_2 > 0.2$.

4. Experimental test setup and procedure

In this section, the experimental setup of the multi-layer harvesters is demonstrated. Figure 7 shows the components and devices used in the experiment. The LMS TEST LAB 7A software and LMS SCADAS III data acquisition system are used to collect and process the experimental data. A built-in source panel in the software generate a random signal (band-limited white noise) to the power amplifier, which is the power supply of the electromagnetic shaker. Figure 8 shows the measured random base excitation. The excitation level is controlled to preserve the linearity of the harvester dynamics. The clamped end of the base layer of the harvester is clamped between two stainless steel plates, which are mounted on the shaker. The mass of these plates helps to reduce the fundamental resonance frequency of the shaker. A piece of PZT plate (PIC151) is bonded on the base layer and connected to the resistance decade box. A PCB ICP accelerometer (sensitivity 99 mV/g) is mounted on the base right above the clamped part of the harvester to measure the base excitation. The accelerometer is connected to a signal conditioner. A M5L/4 laser sensor (sensitivity 5.17V/mm, resolution 1 μ m) is used to measure the displacement of the harvester. The measured voltage data from the decade box, signal conditioner and the laser sensor are collected by the LMS data acquisition system. Figure 9 shows the flow chart of the experimental setup. It should be noted that the LMS system has 1M Ω impedance and it is connected to the resistive load in parallel. Therefore, the actual resistive load on

the harvester is less than the selected resistance of the decade box. The actual resistive load is determined as $1/R_{Load}=1/R_{RBOX}+1/R_{LMS}$, and its magnitude cannot exceed $1M\Omega$. For example, when the decade box is set as $1M\Omega$, the actual resistive load equals $500K\Omega$.

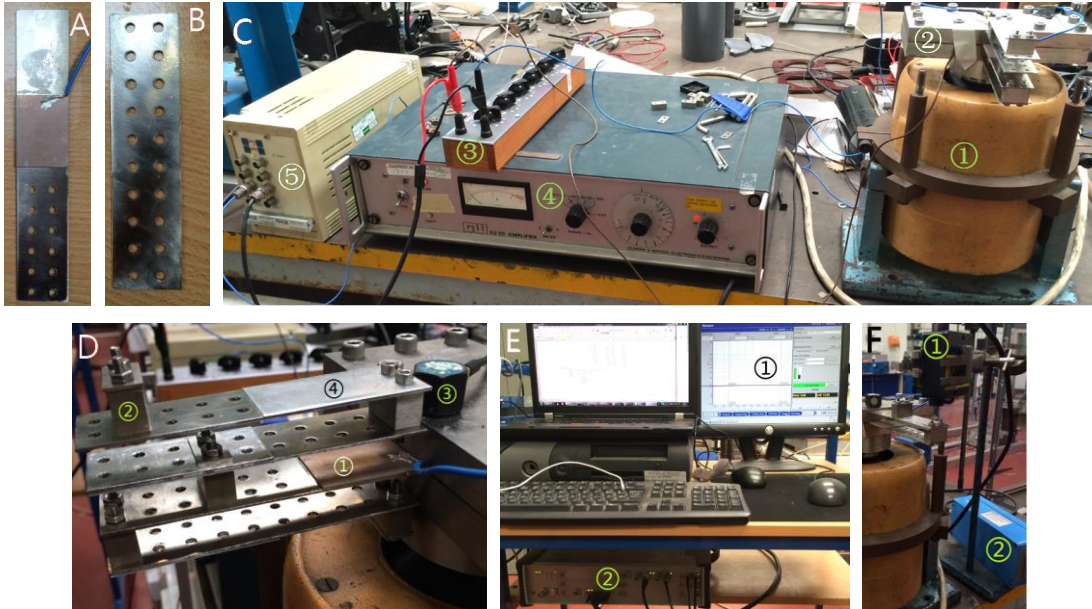


Figure 7: Experimental setup. **A:** the longer cantilevered base with bonded PZT layer. **B:** the upper/lower layer. **C:** (1) electromechanical shaker, (2) base to clamp the harvester, (3) resistance decade box, (4) power amplifier and (5) signal conditioner. **D:** (1) the four-layer five-mass harvester *4L5M-P391-09* and its PZT layer, (2) mass, screws and nuts, (3) ICP accelerometer mounted on the base and (4) damping foil. **E:** (1) LMS TEST LAB on PC and (2) LMS SCADAS III data acquisition system. **F:** (1) M5L/4 laser sensor head and (2) sensor monitor and power supply.

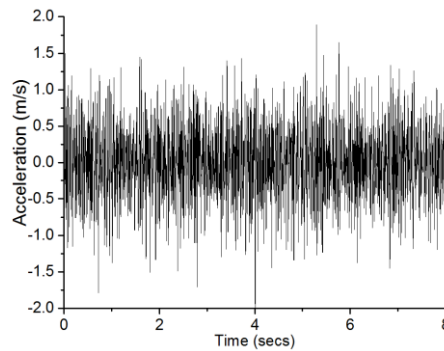


Figure 8: Measured base acceleration for random base excitation (white noise)

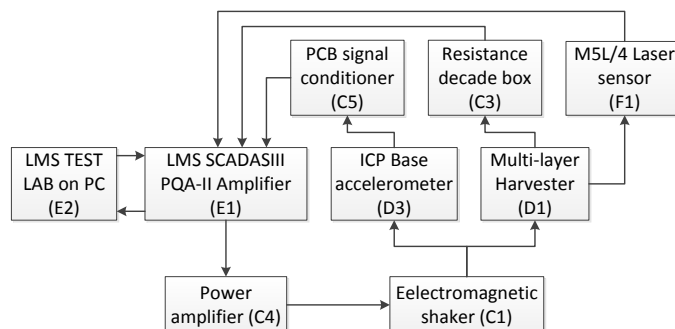


Figure 9: Flow chart of the experimental setup (C1, D1... F1 in brackets are shown in Figure 7).

5. Experimental validation of the performance of multi-layer harvesters

5.1 Two-layer harvester performance

In this section, the experimental study of the two-layer harvester is presented. Figure 10 shows the simulated and experimental power output FRFs with 100 k Ω resistive load for two-layer model $2L2M$ when the position of M_{+1} bonded on the base is 0. It should be noted that the presented power output FRFs are normalised power for acceleration per 1m/s^2 . There is a good agreement between the simulated and experimental results for the trend of the FRFs when the mass positions are changed. For the experimental results, there is some noise around the anti-resonance frequencies and the damping is slightly greater than the simulated results. A secondary reason could be because the random excitation causes some leakage in the signal processing and the amplitude is underestimated. Besides, the damping could be frequency-dependent between the two modes in the experiment. However, the errors around the anti-resonance frequencies could barely affect the configurational optimization using FEA since only performance around resonance frequencies are considered for energy harvesting. The power FRFs show that when the position of M_{+2} is varied from 6 to 9, the first two modes becomes in-phase, which the anti-resonance area is moved before the first mode, and the first mode only generate much lower power output than the second mode. When the position of M_{+2} is altered from 5 to 1, f_1 is slightly decreased and f_2 is considerably increased. Therefore, if it is assumed that the frequency ratio of the filter is smaller than 1.7 and that the power output of each mode is greater than 0.1 mW, the configurations with mass position P05, P04 and P03 have met the criteria.

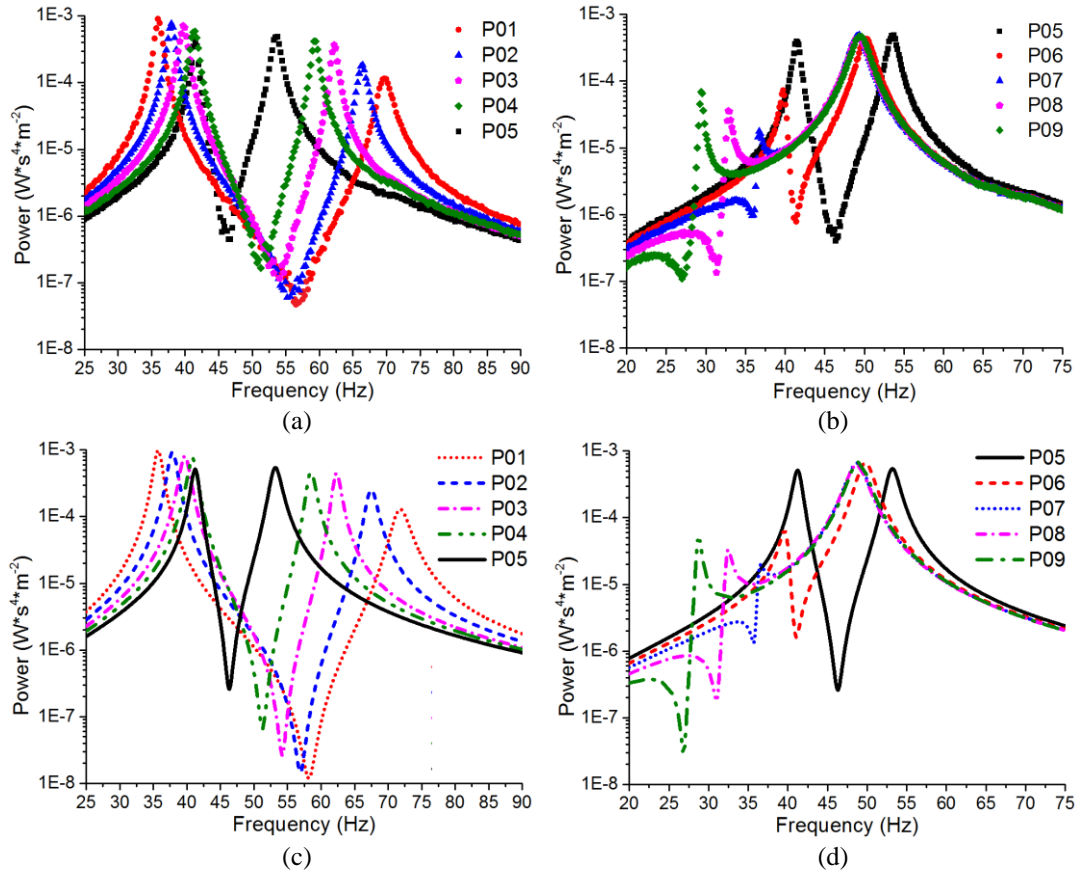


Figure 10: Comparison of the simulated and experimental power FRF with 100 k Ω resistive load for two-layer model $2L2M$ and $M_{+1}=0$. (a) and (b): experimental; (c) and (d) simulated.

Figure 11 shows the experimental power output FRF for some typical positions of M_{+2} when the positions of M_{+1} is fixed at 1 and 2. Since the effective length of the base layer is decreased, the resonance frequencies of the first two modes are both increased. The preferred mass positions using the same filter ($f_2/f_1 < 1.7$ and power output > 0.1 mW) are $P15$, $P16$, $P26$ and $P27$. The selected configurations from the experimental results actually have a good agreement with the previously mentioned screening results (see Figure 6).

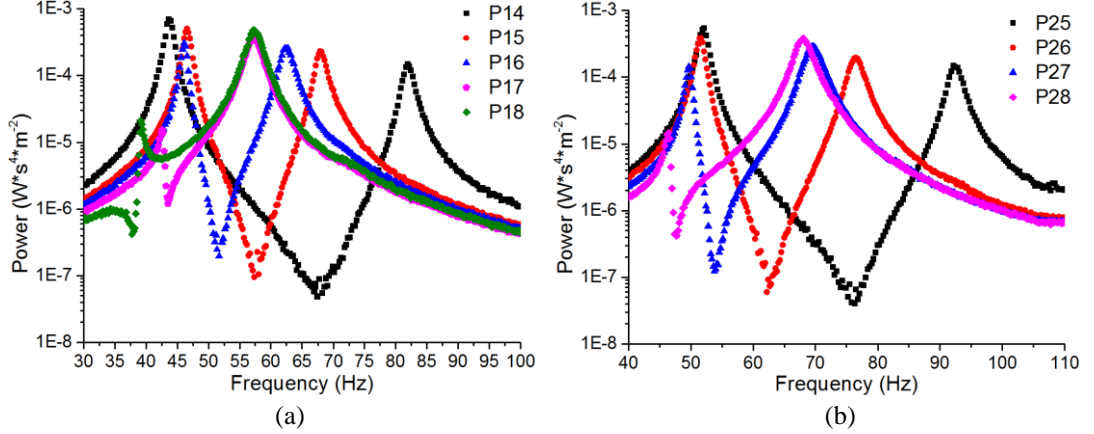


Figure 11: Experimental power FRF with 100 kΩ resistive load for two-layer model 2L2M. (a): $M_{+1}=1$; (b) $M_{+1}=2$.

Figure 12 (a) and (b) show the measured voltage FRFs near the two resonance frequencies of model 2L2M-P05 with different resistive loads from 10 kΩ to 909 kΩ. When the resistance is increased, the voltage is increased, and the resonance frequency is shifted due to the back coupling effect. The voltage only increases slightly when the resistance is larger than 500 kΩ. Figure 13 (a) and (b) show the average power output FRFs around the first two modes of model 2L2M-P05 determined using the measured voltage data. Figure 13 (c) and (d) show the average power output FRFs around the first two modes of model 2L2M-P01. In general, when the resistive load is increased from 100 kΩ to 150 kΩ, the harvester generates near-optimal power output in each mode. Since the optimal resistive load is mainly affected by the piezoelectric capacitance and the angular resonance frequency [18], for different configurations, the modes with close resonance frequencies should have similar ranges of the near-optimal resistance. Therefore, a 100 kΩ resistive load is used in all experimental tests in this article for the convenience of performance comparison.

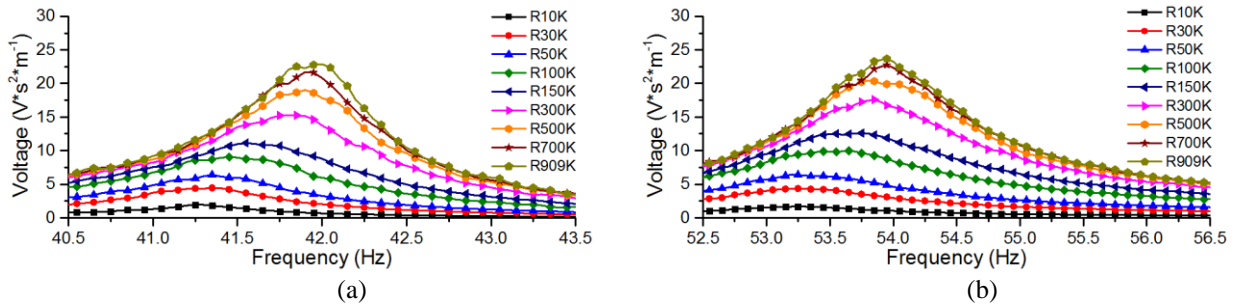


Figure 12: Experimental voltage FRFs around the first two modes for different resistive loads (e.g. R10K= 10kΩ resistance) for model 2L2M-P05. (a) mode 1; (b) mode 2.

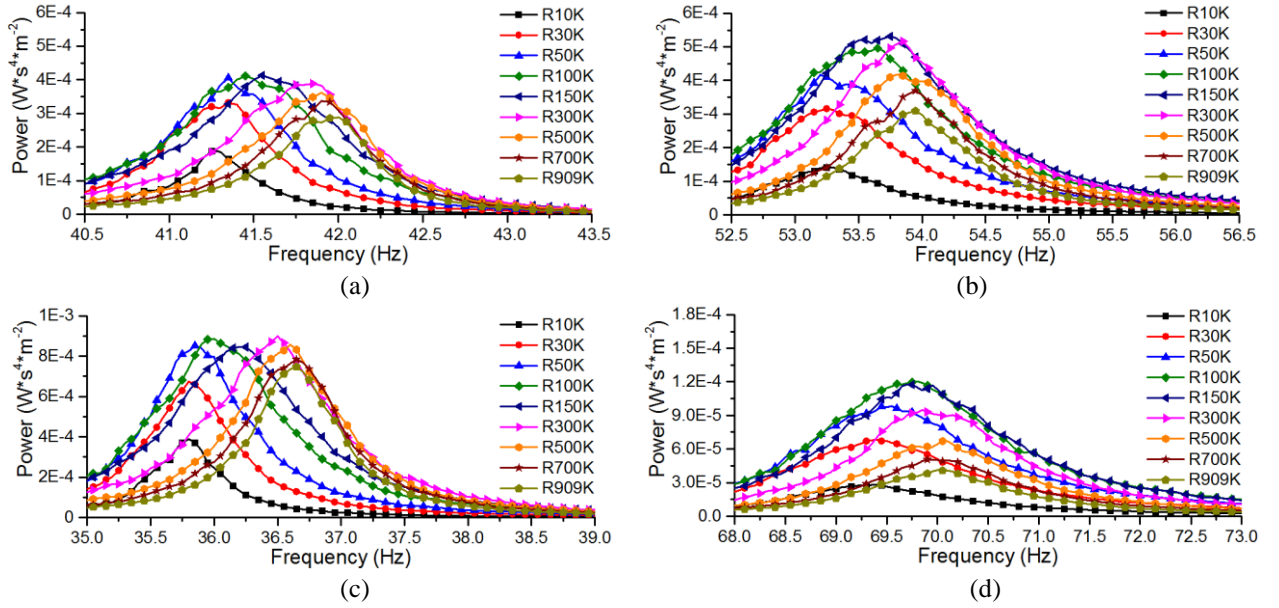


Figure 13: Experimental power FRFs around the first two modes for different resistive loads for two-layer harvester with mass position P05 and P01. (a) P05 mode 1; (b) P05 mode 2; (c) P01 mode 1; (d) P01 mode 2;

Figure 14 illustrates the two measurement points on model 2L2M using the laser sensor. Point 1 is to measure the free tip displacement of the base layer (at the clamped end of the upper layer). Point 2 is to measure the free tip displacement of the upper layer. Based on the FEA modal analysis, the maximum displacement of the first modes can be derived from either point 1 or point 2. Figure 15 shows the measured displacement FRFs around the first two modes of model 2L2M with typical mass positions. The displacement FRFs are measured under short-circuit condition, which means the two electrodes on the top and bottom of the PZT layer are directly connected. When the position of M_{+2} is less than 6, point 1 indicates the maximum displacement in mode 1. When the position of M_{+2} is greater than 6, point 1 indicates the maximum displacement in mode 2. For mass position P06, point 2 always indicates the maximum displacement. When the mass position is varied from P06 to P07, according to the base layer's displacement FRFs, the anti-resonance between the two modes is eliminated, and it is similar to the corresponding power FRF results.

Figure 16 shows some comparisons between the experimental and simulated data of model 2L2M for the validation of the modal approach and structural screening process. Figure 16 (a) is the modal participation factor γ ; and the experimental results are derived from the amplitudes of the displacement FRFs at each resonance frequency. Figure 16 (b) is the ratio of two short-circuit resonance frequencies f_2/f_1 . There are good agreements between the simulated and experimental results for both γ and f_2/f_1 . Table 2 shows the simulated modal mass and mass ratio N . Because γ is a quadratic function of N , when γ is too small in the first mode for the configuration with mass position from P06 to P09, N_1 is significantly small. For the mass positions P04 to P01, although the modal mass of mode 2 is small, N_2 is still large enough due to the larger γ_2 . Figure 16 (c) shows the electromechanical coupling coefficient EMCC; the experimental results are derived from the short-circuit and open-circuit displacement FRFs. There are larger errors between the

simulated and experimental EMCC than the structural data. The errors could be generated by several reasons such as the difference of piezoelectric properties due to the manufacturer, the conductive adhesive used to bond the PZT, the manner of measurement and assembly errors.

In conclusion, according to the experimental results, when the mass positions are varied from P01 to P05, the first mode is largely affected by the base layer. The varied position of M_{+2} on the upper layer largely affects f_2 (see Figure 10 b), and the base layer generates larger displacements in mode 1 (see Figure 15 a-c). Because the amplitude of displacement FRF directly affects the strain generated near the clamped end, which is covered by the PZT layer, mode 1 has larger EMCC than mode 2 (see Figure 16 c). Similarly, for the mass positions varied from P07 to P09, the second mode is largely affected by the base layer. The varied positions of M_{+2} on the upper layer largely affects f_1 , and the base layer generates larger displacements in mode 2, and mode 2 has large EMCC than mode 1. For mass position P06, the strong interaction between the base and upper layer in both modes generates the smallest frequency ratio (see Figure 16 b), close amplitude of base layer displacement and close EMCC.

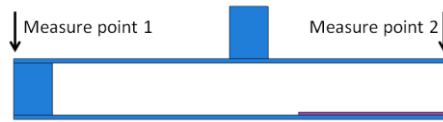


Figure 14: Sketch of the displacement measurement points 1 and 2 on the $2L2M$ model for the laser sensor.

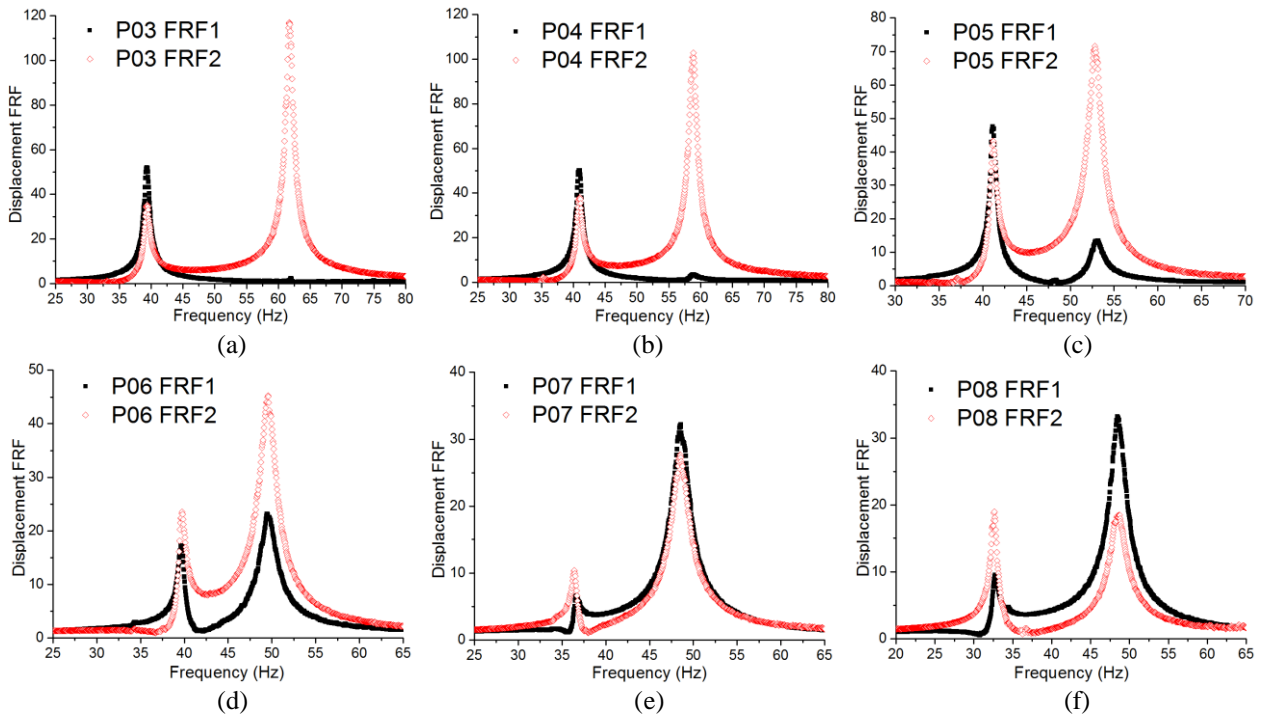


Figure 15: Experimental displacement FRF of two-layer model $2L2M$ under short-circuit condition. FRF1: point 1; FRF2: point 2; (a) to (f): P03 to P08.

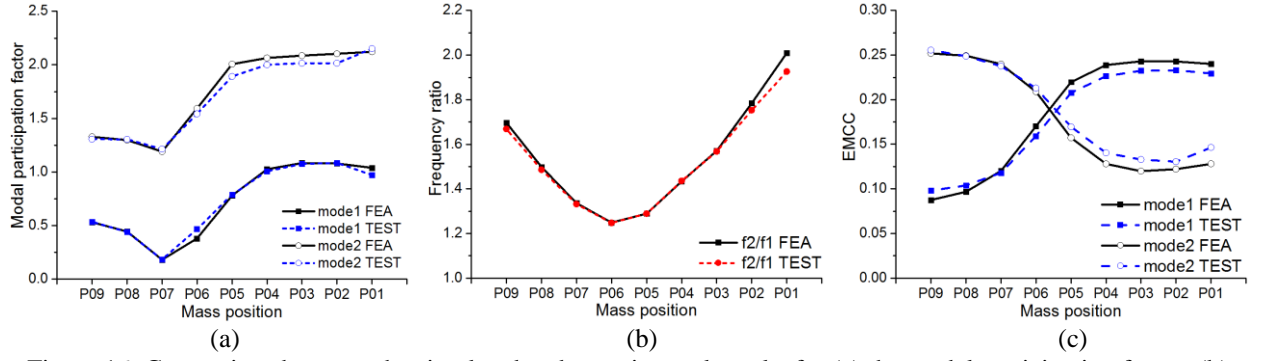


Figure 16: Comparison between the simulated and experimental results for (a) the modal participation factor; (b) frequency ratio, and (c) electromechanical coupling coefficient EMCC

Table 2: Simulated modal parameters of two-layer model 2L2M

Model	m_{m1} (g)	m_{m2} (g)	γ_1	γ_2	N_1	N_2
P09	23.9	33.8	0.529	1.327	8.5%	75.1%
P08	19.5	37.2	0.443	1.298	4.8%	79.0%
P07	16.9	46.7	0.179	1.190	0.7%	83.4%
P06	18.7	25.3	0.378	1.592	3.4%	80.9%
P05	29.8	12.1	0.779	2.006	22.8%	61.6%
P04	29.5	8.5	1.025	2.065	39.0%	45.6%
P03	31.1	6.9	1.083	2.086	46.1%	38.1%
P02	34.2	6.1	1.079	2.103	50.3%	33.9%
P01	38.4	5.6	1.037	2.122	52.2%	31.9%

There are also other factors that can affect the performance of the two-layer harvester. For example, Figure 17 shows the experimental power output FRFs of the two-layer model with mass position P09 but different magnitudes of mass M_{+2} . The original value of each mass is 18.8 g. When the value of M_{+2} equals 0 g, the model has only mass M_{+1} . By changing the value of M_{+2} , similar responses can be observed as altering mass positions. When the value of M_{+2} is from 0 to 4.6 g, the acceptable performance for both two modes can be found.

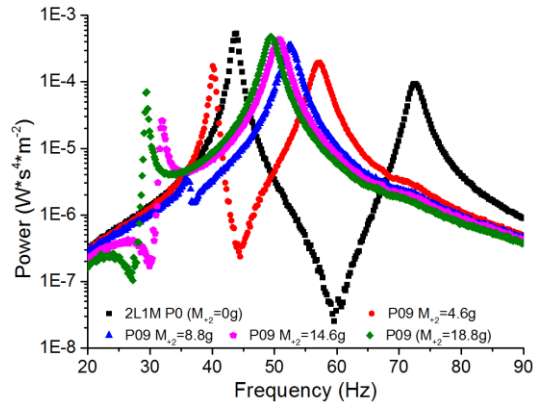


Figure 17: Experimental power FRF with 100 kΩ resistive load for model P09 with different values of M_{+2} .

5.2 Multi-layer harvester performance

In this section, the power outputs FRFs of some typical multi-layer harvesters are presented. Figure 18 shows the experimental and simulated power FRFs of some typical one-sided three-layer model *3L3M*, which consists of three masses (M_{+1} , M_{+2} and M_{+3}), two upper layers (L_{+1} and L_{+2}). Figure 19 shows the experimental and simulated power FRFs of some typical two-sided three-layer model *3L4M*, which consists of four masses (M_{+1} , M_{+2} , M_{-1} and M_{-2}) and one upper layer (L_{+1}) and one lower layer (L_{-1}). Figure 20 (a) and (b) show the structural screening results for the three-layer models *3L3M* and *3L4M* (when $M_{+1}=0$), respectively. These results are based on the original configurations which used beams without holes as reported in previous work [15].

According to the experimental power output FRFs of model *3L3M* given in Figure 18 (a), if it is assumed that the criteria is power output close to 0.1 mW and the ratio of adjacent resonance frequencies is smaller than 2, then the mass position P090 is the only acceptable position, which has been selected in the “ $M_{+1}=0$ ” layer of the screening results. In Figure 18(b), P192 and P292 are acceptable and they have been selected in the “ $M_{+1}=1$ and $M_{+1}=2$ ” layers of the screening results. A good agreement can be found between the simulated and experimental FRFs for resonance and off-resonance conditions. The amplitudes of power outputs in some modes are slightly overestimated in simulation.

For model *3L4M*, none of the mass positions given in Figure 19 (a) is acceptable and they have not been selected in the screening results. All of the mass positions given in Figure 19 (b) are acceptable, and they have all been selected in the “ $M_{-1}=3$ ” layer of the screening results. The simulated results also have similar response compared with the experimental results. For some mass positions with poor performance, some errors can be observed. However, this does not affect the screening results.

Obviously, the structural screening results can successfully present the preferred mass positions with better performance of the two kinds of three-layer models. However, the dimensions and parameters of the experimental harvesters presented in this article are slightly different from those of the previous analyses as stated earlier. It was found that these slight difference in dimensions and values of parameters only have little effect on the structural screening results. For the multi-resonance harvester designs, using the configurational optimization strategy can significantly save analysing and computing time. It can pre-select the configuration with better structural broadband performance and obviates the need to running full analysis at the first stage.

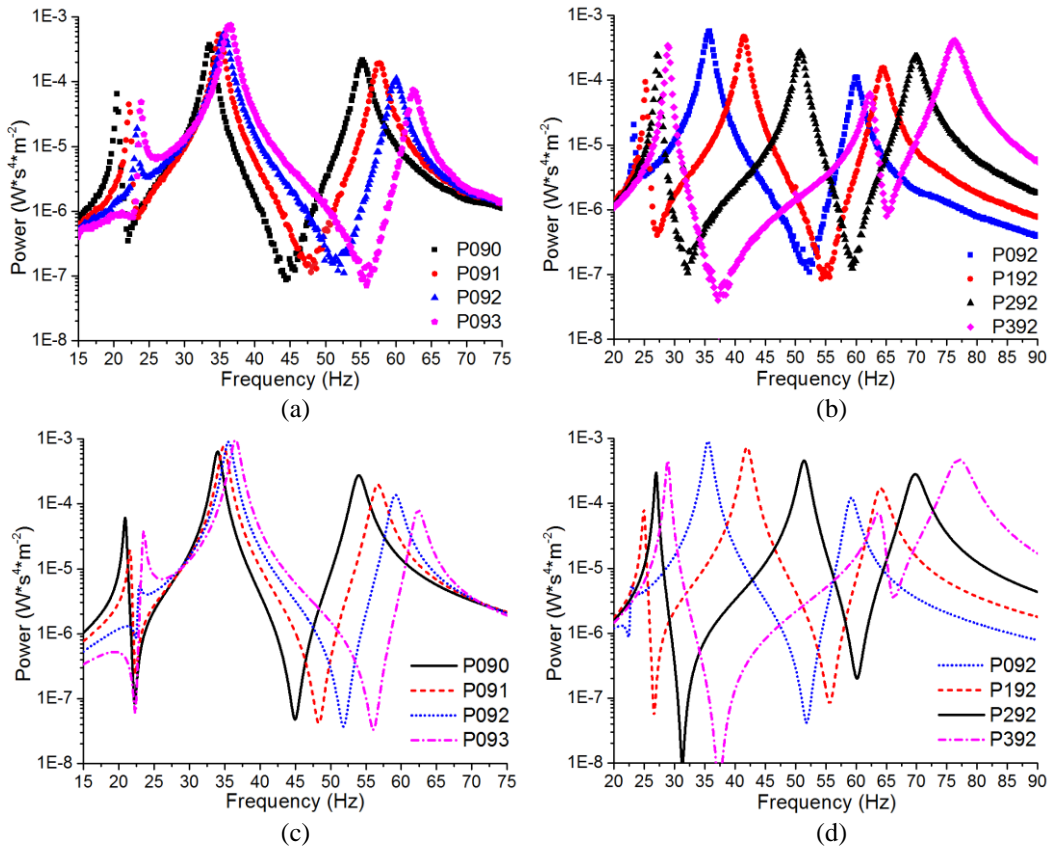


Figure 18: Experimental and simulated power FRF with 100 k Ω resistive load for one-sided three-layer model *3L3M* with typical mass positions. (a) and (b): experimental; (c) and (d) simulated

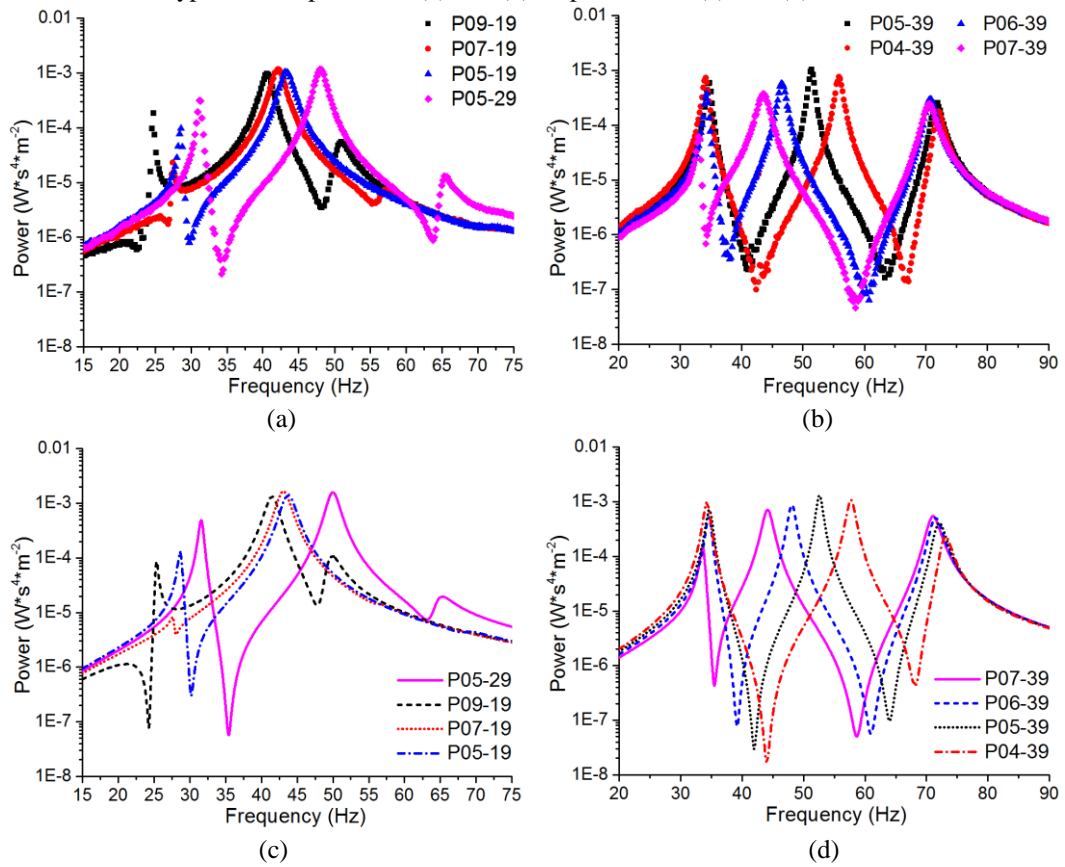


Figure 19: Experimental and simulated power FRF with 100 k Ω resistive load for two-sided three-layer model *3L4M* with typical mass positions. (a) and (b): experimental; (c) and (d) simulated

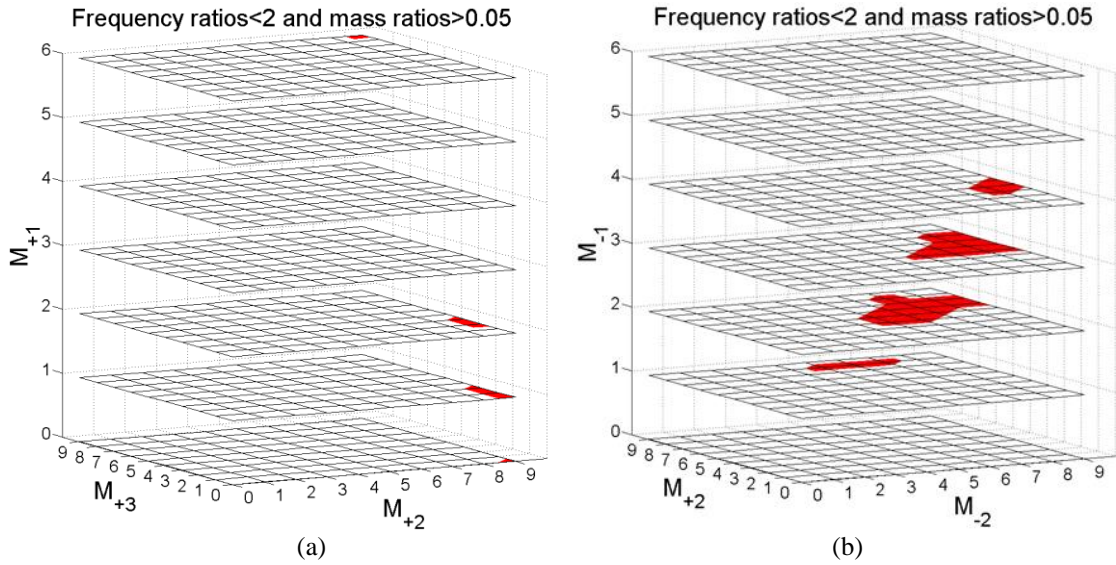


Figure 20: Result of structural screening for three-layer model (for the original configuration with no through hole in previous work [15]); the shaded area is the selected configurations meet the screening criteria f_2/f_1 and $f_3/f_2 < 2$ and $N > 0.05$ in three modes. (a) one-sided three masses model 3L3M; (b) two-sided four masses model 3L4M ($M_{+1}=0$).

Figure 21 shows the power output FRFs for three different positions of the four-layer harvesters. For mass positions $P191-09$ and $P291-09$, the fourth mode is inactive. The configuration with mass position $P391-09$ can generate four close resonance frequencies with acceptable performance in each mode. Besides, there are also very small peaks after the third and fourth modes of these power FRFs. They are probably due to the rotational effect produced by the shaker. Since the possible mass positions are too many, the structural screening results are not presented. Actually, if too many layers are used, the performance of a multi-layer harvester can be degraded, and this will be discussed with further details in the following section.

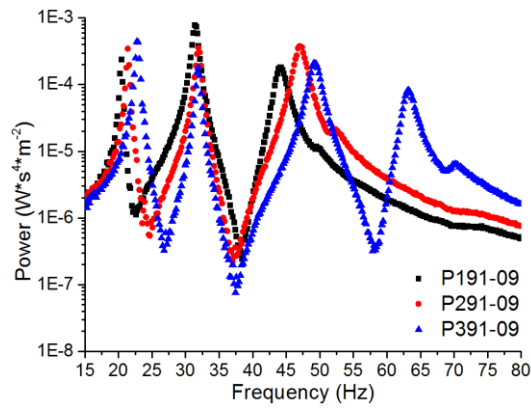


Figure 21: Experimental power FRF with 100 k Ω resistive load for one-sided three-layer model 4L5M

5.3 Bandwidth of multi-layer harvesters

Figure 22 shows the comparison of power output between some typical multi-layer harvesters and a single layer harvester $1L1M$ with mass position $M_{+1}=0$ (a cantilevered beam harvester with a tip mass). Since the multi-layer harvesters can generate close resonance frequencies and relatively large power output in each mode, the effective bandwidth of the power output FRF has been increased in comparison with a single layer

harvester. Figure 23 shows the bandwidth comparison between the single layer and multi-layer models. In Figure 23 (a), the effective bandwidth is for the minimal power output $10^{-5} \text{ W per m}^2$, which correspond to minimal voltage 1.41 V for 100 k Ω resistive load. In Figure 23 (b), the bandwidth is for the power output larger than $5 \cdot 10^{-6} \text{ W}$, which correspond to voltages larger than 1 V due to the 100 k Ω resistive load. The results show that the two-layer harvester can generate more than 1.5 times wider bandwidth and the three-layer harvesters can have more than 2 times the bandwidth of the *1L1M* harvester. However, the four-layer harvester *4L5M-P391-09* generates narrower bandwidth than the three-layer harvesters do. This is due to several reasons. First, the configuration of the four-layer harvester has not been optimized using the design strategy. Besides, the reduced electromechanical coupling significantly affects the power output. This is probably due to the fact that the PZT layer is only bonded near the clamped end of the base layer, which probably does not have the largest strain distribution for a four-layer harvester. Table 3 shows the experimental EMCC of these multi-layer harvesters. The single layer harvester has the largest EMCC in the fundamental mode. The EMCC of the two-layer harvester in the first two modes are slightly reduced compared to the single layer harvester. The EMCC of the three-layer harvesters are significantly reduced in some modes but are still acceptable. The four-layer harvester generates the lowest EMCC in modes 2 and 4.

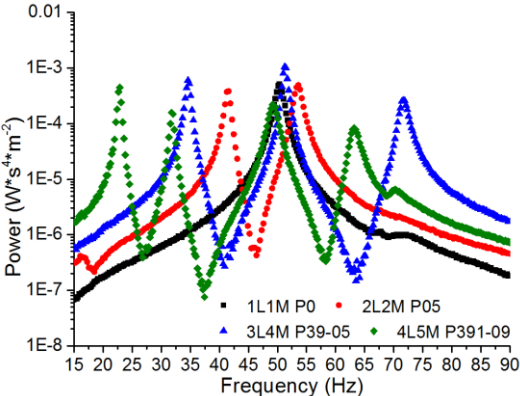


Figure 22: Comparison of experimental power FRF with 100 k Ω resistive load.

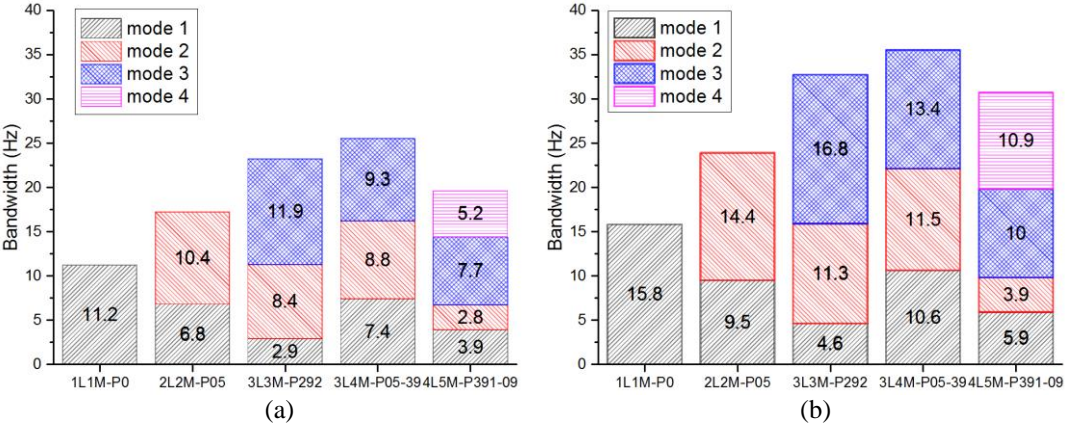


Figure 23: Experimental bandwidth comparison between the single layer and multi-layer models with 100K Ω resistive load; (a) bandwidth for $1 \cdot 10^{-5} \text{ W*s}^4/\text{m}^2$ (1.41 $\text{V*s}^2/\text{m}$); (b) bandwidth for $5 \cdot 10^{-6} \text{ W*s}^4/\text{m}^2$ (1 $\text{V*s}^2/\text{m}$).

Table 3: Experimental EMCC of multi-layer harvesters in different modes

Model	k1	k2	k3	k4
1L1M P0	0.210			
2L2M P05	0.204	0.173		
3L3M P292	0.143	0.154	0.178	
3L4M P39-05	0.199	0.156	0.123	
4L5M P391-09	0.162	0.114	0.158	0.094

6. Conclusions

In this article, experimental studies for the multi-layer harvesters are presented. By altering the mass positions, the four-layer harvesters are able to generate up to four close resonance frequencies with relatively large power output. The experimental results are compared with the FEA results to validate the modal approach and the configurational optimization strategy. The comparison shows that the configurational optimization strategy using FEA software can successfully pre-select the configuration with optimal or near-optimal structural performance and the screening results can be directly used to manufacture harvesters, which are guaranteed to have optimal or near-optimal experimental performance. Although the geometrical dimensions and parameters of the harvesters manufactured and tested are slightly different from those of the theoretical models, their structural performances are similar to those of the theoretical models analysed previously. The experimental results also show that the three-layer harvesters can generate more than two times wider bandwidth in comparison with the single layer cantilevered beam harvester. However, the four-layer harvester generates narrower bandwidth than the three-layer harvesters do.

Reference

- [1] Beeby, S. P., Tudor, M. J. and White, N. M. (2006). Energy harvesting vibration sources for microsystems applications. *Measurement science and technology*, 17(12), R175.
- [2] Anton, S. R. and Sodano, H. A. (2007). A review of power harvesting using piezoelectric materials (2003–2006). *Smart materials and Structures*, 16(3), R1.
- [3] Tang, L., Yang, Y. and Soh, C. K. (2010). Toward broadband vibration-based energy harvesting. *Journal of Intelligent Material Systems and Structures*, 21(18), 1867-1897.
- [4] Pellegrini, S. P., Tolou, N., Schenk, M. and Herder, J. L. (2013). Bistable vibration energy harvesters: A review. *Journal of Intelligent Material Systems and Structures*, 24(11), 1303-1312.
- [5] Wang, W., Yang, T., Chen, X. and Yao, X. (2012). Vibration energy harvesting using a piezoelectric circular diaphragm array. *IEEE Transactions on Ultrasonics, Ferroelectrics and Frequency Control*, 59(9), 2022-2026.
- [6] Lumentut, M. F., Francis, L. A. and Howard, I. M. (2012). Analytical techniques for broadband multielectromechanical piezoelectric bimorph beams with multifrequency power harvesting. *IEEE Transactions on Ultrasonics, Ferroelectrics and Frequency Control*, 59(11), 2555-2568.
- [7] Ferrari, M., Ferrari, V., Guizzetti, M., Marioli, D. and Taroni, A. (2008). Piezoelectric multifrequency energy converter for power harvesting in autonomous microsystems. *Sensors and Actuators A*:

Physical, 142(1), 329-335.

- [8] Qi, S., Shuttleworth, R., Oyadiji, S. O. and Wright, J. (2010). Design of a multiresonant beam for broadband piezoelectric energy harvesting. *Smart Materials and Structures*, 19(9), 094009.
- [9] Ou, Q., Chen, X., Gutschmidt, S., Wood, A., Leigh, N. and Arrieta, A. F. (2012). An experimentally validated double-mass piezoelectric cantilever model for broadband vibration-based energy harvesting. *Journal of Intelligent Material Systems and Structures*, 23(2), 117-126.
- [10] Zhou, W., Penamalli, G. R. and Zuo, L. (2012). An efficient vibration energy harvester with a multi-mode dynamic magnifier. *Smart Materials and Structures*, 21(1), 015014.
- [11] WU, H., TANG, L., YANG, Y. and SOH, C. K. (2013). A novel two-degrees-of-freedom piezoelectric energy harvester. *Journal of intelligent material systems and structures*, 24(3), 357-368.
- [12] Erturk, A., Renno, J. M. and Inman, D. J. (2008). Modeling of piezoelectric energy harvesting from an L-shaped beam-mass structure with an application to UAVs. *Journal of intelligent material systems and structures*, 20(5), 529-544.
- [13] Karami, M. A. and Inman, D. J. (2011). Analytical modeling and experimental verification of the vibrations of the zigzag microstructure for energy harvesting. *Journal of Vibration and Acoustics*, 133(1), 011002.
- [14] Xiong, X. and Oyadiji, S. O. (2014). Optimal design of two-layer vibration energy harvesters using a modal approach. *Smart Materials and Structures*, 23(3), 035005.
- [15] Xiong, X. and Oyadiji, S. O. (2014). A general modal approach for the development of optimal multi-layer stacked vibration energy harvesters. *Journal of Sound and Vibration*. (21), 5386-5411
- [16] Erturk, A. and Inman, D. J. (2008). A distributed parameter electromechanical model for cantilevered piezoelectric energy harvesters. *Journal of Vibration and Acoustics*, 130(4), 041002.
- [17] Erturk, A. and Inman, D. J. (2011). Piezoelectric energy harvesting. *John Wiley and Sons*, 978-1-1199-9135-9
- [18] Guyomar, D., Sebald, G., Pruvost, S., Lallart, M., Khodayari, A. and Richard, C. (2009). Energy Harvesting from Ambient Vibrations and Heat. *Journal of Intelligent Material Systems and Structures*, 20(5), 609-624.
- [19] SIMULIA Corp, (2010) Abaqus Theory Manual in ABAQUS 6.10 Documentations.
- [20] Xiong, X. and Oyadiji, S. O. (2014). Modal electromechanical optimization of cantilevered piezoelectric vibration energy harvesters by geometric variation. *Journal of Intelligent Material Systems and Structures*, 25(10), 1177-1195.

CHAPTER 12 EXPERIMENTAL STUDY OF THE BROADBAND PERFORMANCE OF MULTI-LAYER VIBRATION ENERGY HARVESTERS USING PZT AND PIMNT

Xingyu Xiong and S Olutunde Oyadiji

Experimental Study of the Broadband Performance of Multi-Layer Vibration

Energy Harvesters using PZT and PIMNT

Xingyu Xiong and S Olutunde Oyadiji *

School of Mechanical, Aerospace and Civil Engineering,

The University of Manchester, M13 9PL, UK

Abstract

The broadband performance of multi-layer vibration energy harvesters are experimentally tested in this article. The multi-layer energy harvester consists of a cantilevered base beam and up to two upper beams. Rigid masses are used as spacers between two adjacent beam layers. By relocating the rigid masses, up to three close resonance frequencies can be generated over the frequency ranges from 10 Hz to 100 Hz. For the same configuration of the multi-layer harvester, the relaxor ferroelectric single-crystal PIMNT and the common piezoelectric ceramic PZT are used for comparison. The piezoelectric layer is bonded on the top surface of the base layer with two types of locations for comparison. The first location is near the clamped end and the second location is between the middle and the free tip. The multi-layer harvesters are connected to a decade resistance box and the voltage and power output on resistive loads are measured. The experimental results show that a PIMNT-harvester can generate significant power output over a frequency band that is around 3.5 times greater than the bandwidth of a PZT-harvester for the same configuration. Using the two-layer and three-layer configurations can generate 1.5 and 2 times wider bandwidth than a single layer harvester.

Keywords: vibration energy harvesting, piezoelectric, multiple resonances, broadband; PIMNT; PZT

1. Introduction

For the development of healthy monitoring strategies, there is a current need to harvest small-scale ambient energy for self-powered, batteryless wireless sensor nodes [1-3]. Harvesting vibration energy from resonance has drawn much attention since it has good potential to provide adequate power. Piezoelectric materials are used to convert mechanical strain energy into electrical energy. PZT (lead zirconium titanate, $\text{Pb}[\text{Zr}_x\text{Ti}_{1-x}]\text{O}_3$) is one of the most common piezoelectric materials and it is normally bonded on cantilevered beams to produce beam-shaped vibration energy harvesters. However, there is a limitation for the beam-shaped harvesters because they normally generate only one resonance over a wide frequency range, and they do not have broadband performance. In order to achieve relatively large power output over a wider bandwidth, different broadband techniques have been developed. For example, the multi-resonance harvesters, nonlinear harvesters with magnet and harvesters with frequency tuning mechanism are widely reported in the existing literatures [4]. Besides, the harvester using PZT can have limited performance due to the moderate piezoelectricity of the material. Therefore, some researches use high performance piezoelectric materials for

* Corresponding author. Tel: 00 44 161 275 4348 Fax: 00 44 161 275 3844

E-mail address: s.o.oyadiji@manchester.ac.uk

vibration energy harvesting. For example, the relaxor-based ferroelectric single crystals PMNT/PMN-PT ($\text{Pb}(\text{Mg}_{1/3}\text{Nb}_{2/3})\text{O}_3\text{-xPbTiO}_3$) are beginning to be used [5-9].

The broadband harvester using the multi-resonance technique can generate close resonance frequencies in multiple modes. However, it is not easy to generate relative large power output in every mode. As a common multi-resonance design, the array of beams harvester normally consists of several individual beam structures, which are electrically connected without the inference of vibration coupling [10, 11]. For such configuration, several beams can be tuned easily to generate close resonance frequencies with smooth power output. However, for each vibration mode, only one beam is active while the bonded piezoelectric materials of the other beams undergo small strains since they are barely active. This actually affects the mechanical performance and electromechanical coupling of the harvester simultaneously. If too many beams are used, the power output can be substantially reduced. Furthermore, the dual-mass harvesters, which are also widely reported, normally consist of two masses and one cantilevered beam [12-14]. The two masses, which are bonded at the free tip and the centre of the beam, separate the cantilevered beam into two parts. The interaction between the two parts can generate the first two transverse vibration modes. However, the dual-mass harvester only generates two close modes, which still have limited broadband performance. In this article, a novel multi-layer harvester is developed, which combines the benefits of array of beams and dual-mass designs simultaneously. It can generate up to three close modes with significant power output around each mode.

Existing works have shown that harvesters using relaxor-based ferroelectric single crystals can generate good performance [5, 6, 9]. However, the high performance materials are normally bonded on the conventional beam-shaped harvester, which has structural limitation that prevents the harvester from generating better broadband performance. Besides, in the existing literature, the performance comparisons using high performance materials and common piezo-ceramics PZT with the same configuration are barely provided. In this article, the power outputs of the harvesters under different resistive loads and the broadband performance of the multi-layer harvesters using relaxor-based ferroelectric single crystals PIMNT ($\text{Pb}[\text{In}_{1/2}\text{Nb}_{1/2}]\text{O}_3\text{-Pb}[\text{Mg}_{1/3}\text{Nb}_{2/3}]\text{O}_3\text{-PbTiO}_3$) and PZT are compared.

This article is organized into five sections. Section 2 is on the introduction of the design and experimental setup of the multi-layer harvesters. Section 3 is on the experimental performance determination of the multi-layer harvesters, while section 4 is on the broadband performance comparison between conventional beam-shaped harvesters and multi-layer harvesters using PIMNT and PZT. The last section presents the conclusions of this paper.

2. Design and experimental setup of multi-layer harvesters

In this section, the configurations of the multi-layer harvesters and the experimental setup are illustrated. Figure 1 shows components of the multi-layer harvesters and experimental devices. A multi-layer harvester consists of a longer cantilevered base and up to two shorter upper layers (see Figure 1b) and masses bonded between each two adjacent beams. In fact, the effective length of the longer base layer is approximately 1 mm longer than the shorter upper beam, and the remaining part of the base layer is clamped. The shorter

upper beam is 100 mm long. All upper layers have the same dimensions. Other properties of the harvester are given in Table 1. The piezoelectric layer is bonded on the top surface of the base layer and it consists of two pieces of piezoelectric materials. There are two types of bonded locations for the piezoelectric layer. The first type (Type 1) is shown in Figures 1(a) and 1(b) using PIMNT (manufactured by Shanghai Institute of Ceramics, Chinese Academy of Sciences) and PZT (PIC 151, manufactured by PI Ceramics), respectively. The second type (Type 2) is shown in Figures 1(c) and 1(d). The masses also serve as spacers and they are movable to tune the resonance frequencies. Groups of through holes are drilled on the base and upper layers to enable fixation of the masses at different locations. The distance between two adjacent groups of holes is 10mm. The masses also have two through holes and screws and nuts are used to mount the masses (see Figure 1 e2). The thickness and width of the masses are 12 mm and 9 mm, respectively. The total weight of each mass including screws and nuts is 18.8 grams. There are ten possible mass positions and the sketch for numbering of mass positions is illustrated in Figure 2. The positions of the masses from the free tip to the clamped end of the base layer are designated as $Pabc$, where a , b and c represent the positions of masses M_{+1} , M_{+2} and M_{+3} on the upper half of the base layer and have numerical values of 0 to 9. For example, the three-layer three-mass harvester $3L3M$ shown in Figures 1(e) and 2 have the mass position $P090$ and $P291$, respectively. Since the combinations of mass positions are too many, only some typical mass positions, which can generate close resonance frequencies, are presented in the experimental study.

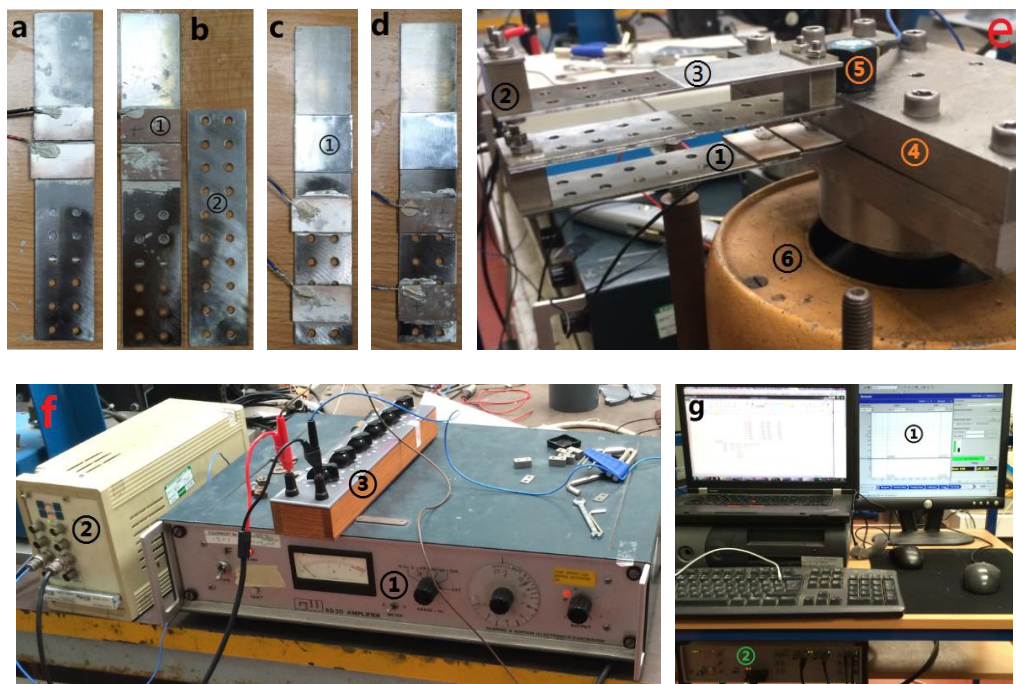


Figure 1: Experimental setup. (a): the longer cantilevered base using PIMNT patches bonded near the clamped end (type 1). (b): (b1) base layer with bonded PZT patches (Type 1) and (b2) shorter upper layer. (c): PIMNT bonded on the middle and tip of base (type 2) and (c1) damping foil. (d): PZT (Type 2). (e): (e1) three-layer harvester $P090$, (e2) mass, screws and nuts, (e3) damping foil, (e4) base to clamp the harvester, (e5) ICP accelerometer mounted on the base and (e6) electromagnetic shaker. (f): (f1) power amplifier, (f2) signal conditioner and (f3) resistance decade box. (g): (g1) LMS TEST LAB on PC; (g2) LMS SCADAS III data acquisition system.

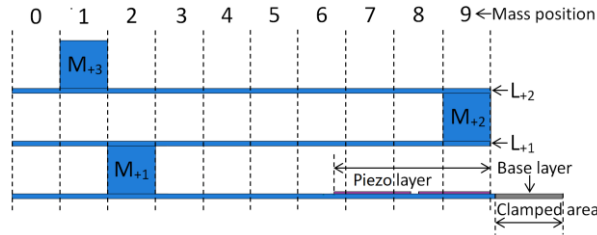


Figure 2: Sketch for numbering of mass positions (not the actual dimensions); three-layer harvester *P29I*: two upper layers (L_{+1} and L_{+2}) are bonded above the base layer and the locations of masses M_{+1} , M_{+} , and M_{+3} is 29I.

Table 1: Properties of the multi-layer harvester

Parameters	Properties
Thickness of piezoelectric layer	1mm
Total length of piezoelectric layer	30mm (approx.)
Thickness of base/upper layers	0.99mm
Thickness of masses	12mm
Width of base/upper layer	25mm
Density of base/upper layers and masses	7930kg/m ³
Young's modulus of base/upper layers and masses	200×10 ⁹ N/m ²

The experimental setup of the multi-layer harvesters is demonstrated in Figure 3. The LMS TEST LAB 7A software and LMS SCADAS III data acquisition system are used to acquire and process the experimental data. A built-in source panel in the software generates a random signal (band-limited white noise) which is sent in the power amplifier to excite the electromagnetic shaker. In this article, all the experimental tests are carried out under random base excitation. Figure 4 shows a sample of the measured base acceleration for random base excitation. The excitation level is controlled to preserve the linearity of the harvester dynamics. The base, which is mounted on the shaker, consists of two stainless steel plates. The multi-layer harvester is clamped to the centre of the base and the bonded piezoelectric device is connected to the resistance decade box. A PCB ICP accelerometer (sensitivity 99 mV/g) is mounted on the base right above the clamped part of the harvester to measure the base excitation. The accelerometer is connected to a signal conditioner. The measured voltage data from the decade box and signal conditioner are sampled by the LMS data acquisition system. It should be noted that the LMS system has a 1 M Ω impedance and it is connected to the resistive load in parallel. Therefore, the actual resistive load needs to be calculated as $1/R_{Load}=1/R_{RBOX}+1/R_{LMS}$, and its magnitude cannot exceed 1M Ω .

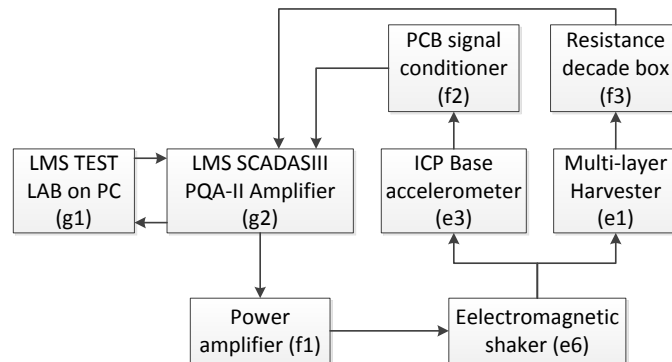


Figure 3: Flow chart of the experimental setup (e1, e3...g2 in brackets are shown in Figure 7).

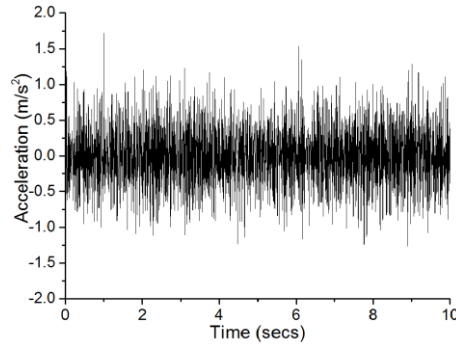


Figure 4: Measured base acceleration for random base excitation (white noise)

3. Comparisons of PIMNT and PZT Multi-layer harvester performance

3.1 Two-layer harvesters (type 1)

In this section, the performances of the two-layer harvesters with type 1 piezoelectric layer are analysed. The two-layer harvester only consists of the base layer and one upper layer L_{+1} and two masses M_{+1} and M_{+2} . The average power output frequency response functions (FRFs) of the two-layer harvester with 200 k Ω resistive loads for typical mass positions P01 to P09 are presented in Figure 5. The average power output is determined from the measured voltage on a resistive load as $P=|v|^2/2R_{Load}$, where v is the measured voltage on resistive loads. When the mass position is varied from P01 to P06, the resonance frequency of mode 2 is decreased significantly while the resonance frequency of mode 1 is increased slightly. When the mass position is altered from P06 to P09, the resonance frequency of mode 2 is decreased slightly while the resonance frequency of mode 1 is decreased significantly. However, for mass position P07, P08 and P09, the first mode only generates very lower power output in comparison with the second mode. Besides, for mass position P08 and P09, the anti-resonance area between mode 1 and mode 2 is eliminated and it appears before mode 1.

From these results, it can be determined that the two-layer harvester with mass positions P05 and P06 generates the closest resonance frequencies with significant power output. Furthermore, the harvester using PIMNT always generates approximately 10 times larger power output than the harvester using PZT for the whole frequency band for both resonance and off-resonance regions. When varying the positions of the masses, the trend of the changes of the corresponding power output FRFs using PIMNT and PZT are similar with only slight differences. Figure 6 presents the corresponding voltage FRFs of the two-layer harvesters with 200 k Ω resistive loads. Obviously, with the same resistive load, the harvester using PIMNT can generate much higher voltage than using PZT. It should be noted that the voltage and power output FRFs presented in this paper are normalised by the acceleration per m/s^2 .

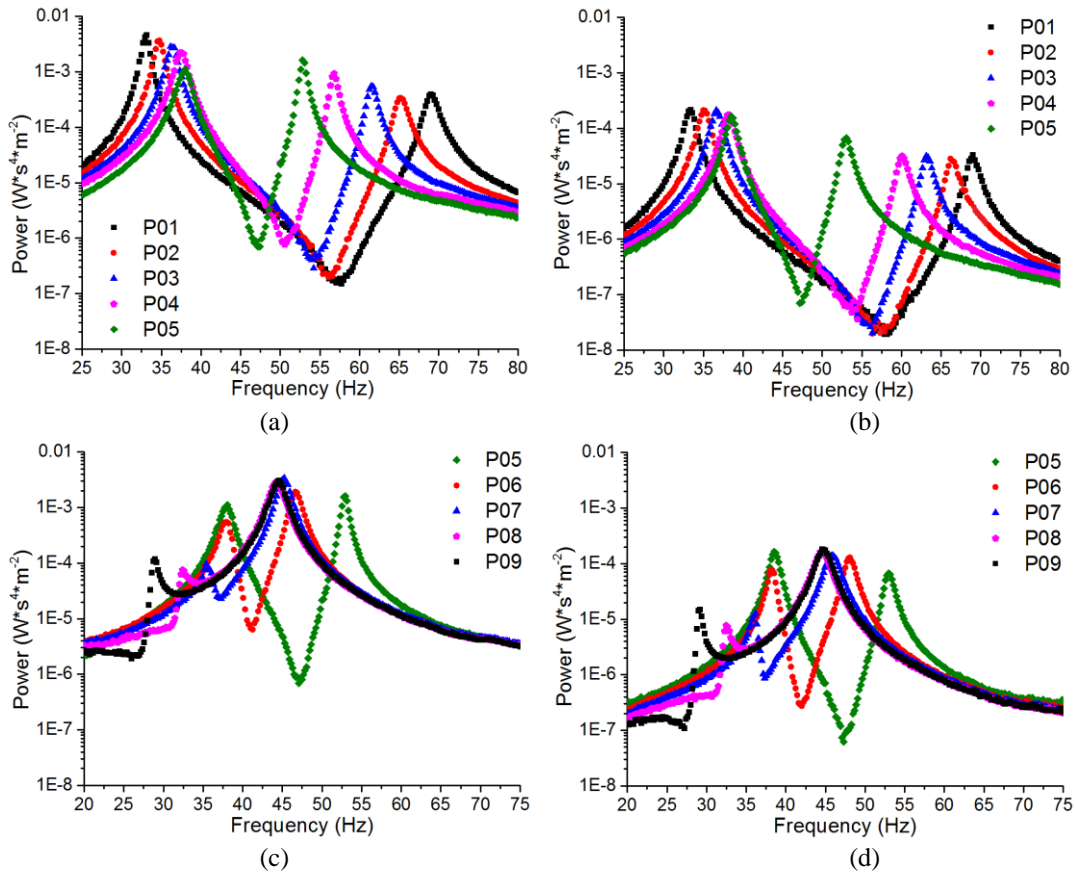


Figure 5: Power FRFs of the two-layer harvester using PIMNT and PZT with 200 kΩ resistive load. (a) and (c): PIMNT; (b) and (d) PZT.

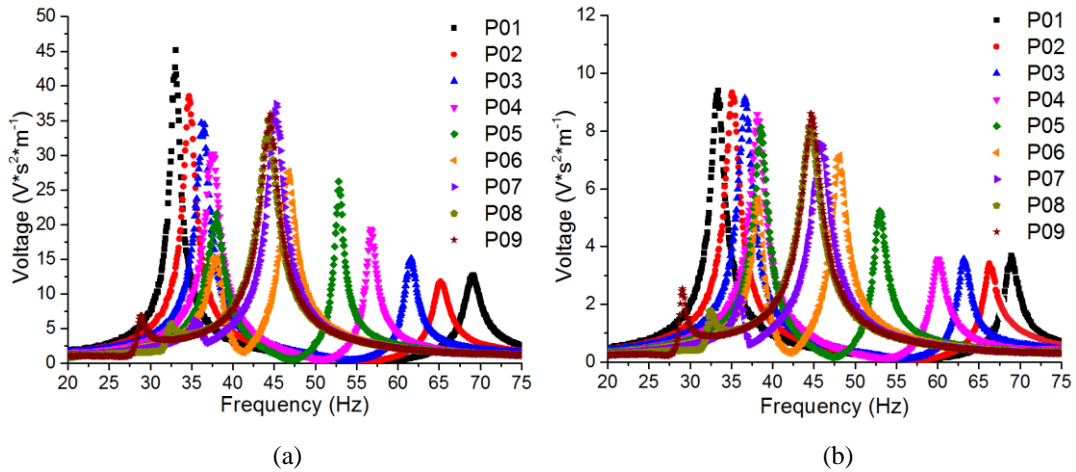


Figure 6: Voltage FRFs of the two-layer harvester using PIMNT and PZT with 200 kΩ resistive load. (a): PIMNT; (b): PZT.

The above case only presents the FRF data measured with a fixed resistive load. Figure 7 presents the power output FRFs with different resistive loads from 30 kΩ to 909 kΩ around the first two modes of the two-layer harvester with mass position P05. When the connected resistance is increased, the resonance frequency is shifted from the short-circuit resonance frequency to the open-circuit resonance frequency due to the back-coupling effect. The results show that for both PIMNT (Figure 7a and 7c) and PZT (Figure 7b and 7d), the near-optimal power output can be achieved when the connected resistance is around 200 kΩ. Therefore, a 200 kΩ resistive load is used in all the experimental tests in this article for the convenience of performance comparison. Figure 8 presents the corresponding voltage FRFs with different resistive loads. When the connected resistance is increased, the voltage is significantly increased. When the resistance is larger than

500 k Ω , the voltage is increased slowly and it is close to the open-circuit voltage. The voltage with the largest resistance is about 1.5 to 2 times higher than the voltage for near-optimal power output with 200 k Ω resistance. Besides, with different resistive loads, the harvester using PIMNT can generate about 3 to 4 times higher voltages than using PZT for both resonance and off-resonance conditions.

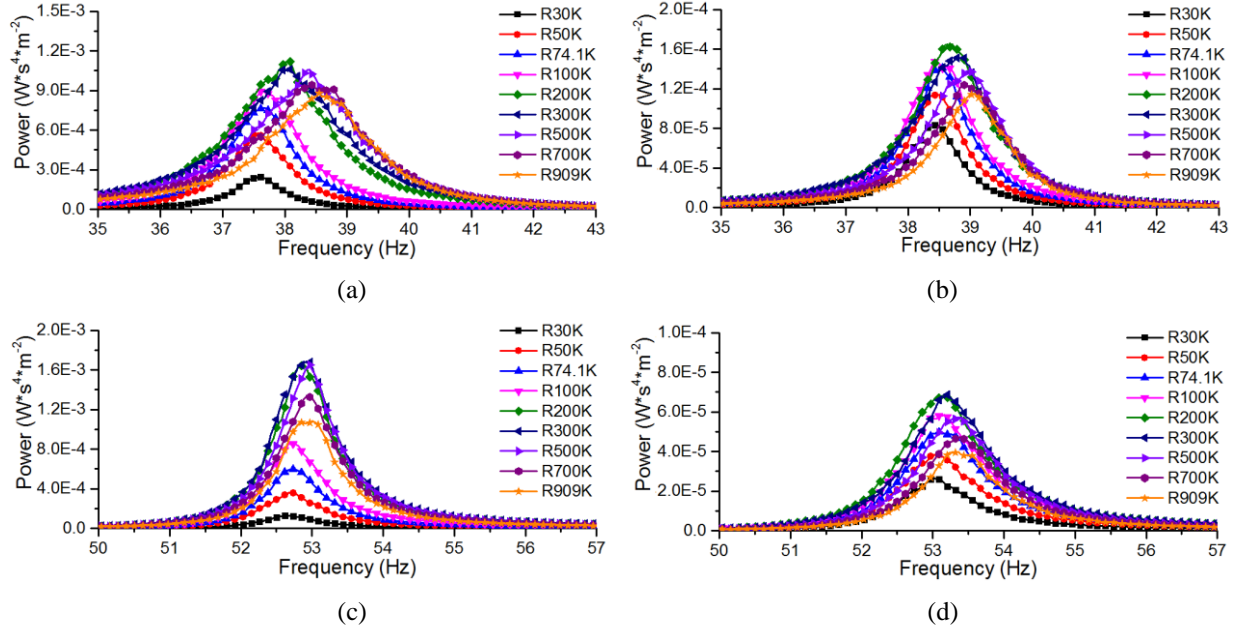


Figure 7: Power FRFs around the first two modes with different resistive loads (e.g. R30K= 30k Ω resistance) for the two-layer harvesters with mass position P05 using PIMNT (figures a and c) and PZT (b and d). (a) and (b): modes 1; (c) and (d): mode 2.

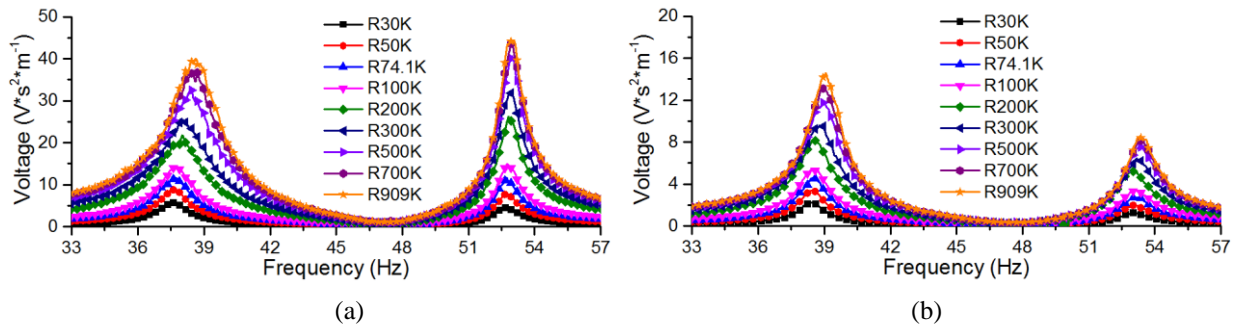


Figure 8: Voltage FRFs with different resistive loads for the two-layer harvesters with mass position P05. (a): PIMNT; (b): PZT.

Apart from varying the mass positions, there are other factors that can affect the performance of the two-layer harvester. Figure 9 presents the power output FRFs of the two-layer harvester with mass position P09 but different magnitude of M_{+2} . The original magnitude of each mass is 18.8 g. When the magnitude of M_{+2} equals 0 g, the harvester has only one mass M_{+1} and it is designated as *2LIM-P0*. By increasing the magnitude of M_{+2} from 0 g to 18.8 g, it can be observed that the power FRFs have similar trends to the FRFs obtained when the mass positions are varied. For the original mass position P09, the first mode only generates much lower power than the second mode. When the magnitude of M_{+2} is around 4.6 g, the close resonance frequencies and acceptable performance can be observed for both modes.

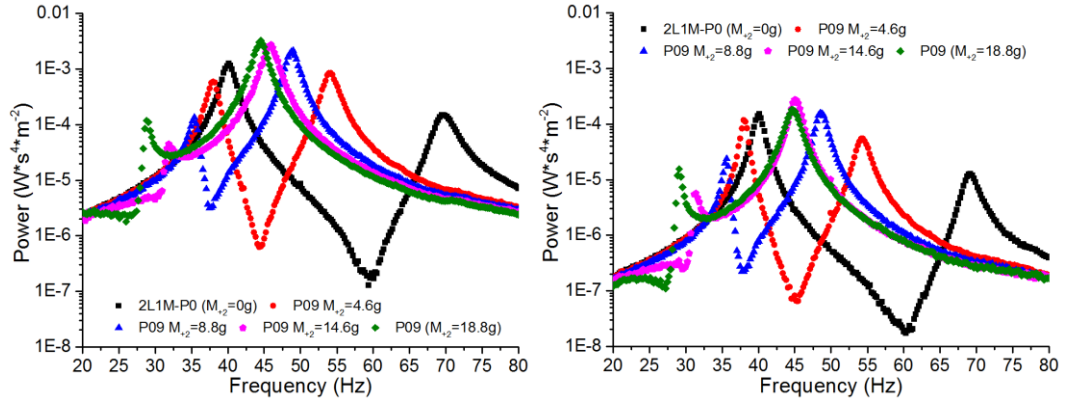


Figure 9: Power FRFs of the two-layer harvester with mass position P09 and different magnitude of M_{+2} . (a): PIMNT; (b): PZT.

3.2 Three-layer harvesters with Type 1 piezoelectric layer

In this section, the performances of the three-layer harvesters with Type 1 piezoelectric layer are analysed. The three-layer harvester consists of the base layer and two upper layers L_{+1} and L_{+2} and three masses M_{+1} , M_{+2} and M_{+3} . Figures 10 and 11 present the power output FRFs of the three-layer harvester with some typical mass positions. In Figures 10 (a) and 10 (b), only the position of M_{+3} is altered from 0 to 3 and the other two masses are fixed. The results show that modes 1 and 3 generate smaller power than mode 2, which actually affect the broadband performance of the harvester. It should be noted that, the damping in modes 1 and 2 of the harvester using PIMNT is significantly small, which results in the generation of much higher peaks at the two resonance frequencies. The reason could be due to the effect of the conductive adhesive, damping foil and assembly generated by homemade process. However, the magnitude of damping can barely affect the off-resonance performance and the harvester using PIMNT still generate much higher performance than using PZT for off-resonance condition. In Figures 11 (a) and 10 (b), only the position of M_{+1} is varied from 0 to 2 while the other two masses are fixed. With mass position P292, the harvester can generate three close resonance frequencies and relatively large power in each mode.

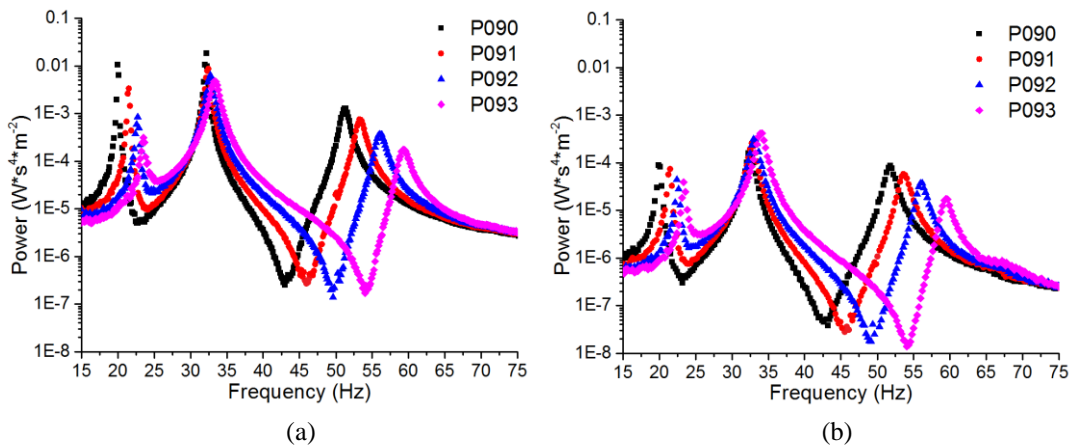


Figure 10: Power FRFs of the three-layer harvester with typical mass positions. (a) PIMNT; (b) PZT.

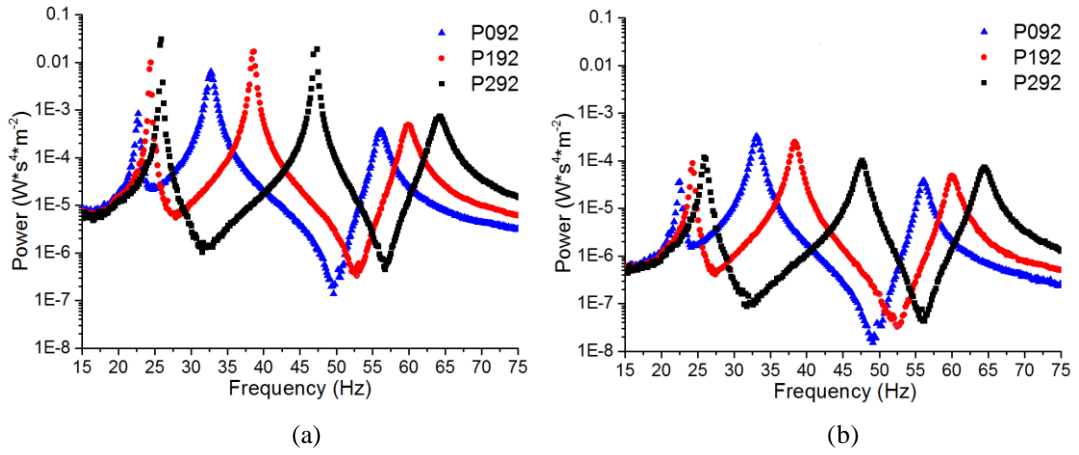


Figure 11: Power FRFs of the three-layer harvester with typical mass positions. (a) PIMNT; (b) PZT.

3.3 Multi-layer harvesters with Type 2 piezoelectric layer

In this section, the performances of the multi-layer harvesters with Type 2 piezoelectric layer location are analysed. Figure 12 presents the power output FRFs of the two-layer harvester with some typical mass positions. Apparently, the performances of the harvesters with Type 2 piezoelectric layer location are very different since the anti-resonance areas between modes 1 and 2 are always eliminated. When the two modes get closer, the lowest power output around the anti-resonance area is significantly increased. This may help to improve the broadband performance of the harvester. For instance, the lowest power output between modes 1 and 2 of the harvester using PIMNT with mass position P08 is larger than $40 \mu\text{W}\cdot\text{s}^4/\text{m}^2$ and the corresponding voltage on the $200 \text{ k}\Omega$ resistive load is larger than $4 \text{ V}\cdot\text{s}^2/\text{m}$. The maximum power outputs of mode 2 of the harvesters using PZT are significantly high due to the very small damping. However, the small damping barely increases the bandwidth of low-level power output since the peak is quite narrow, and the off-resonance performance using PZT is still much worse than using PIMNT. Figure 13 shows the power output FRFs of the two-layer harvester with mass position P09 but different magnitudes of M_{+2} . A similar trend of the power FRFs can be observed when the mass positions are varied. When the magnitude of M_{+2} is around 8.8 g , the harvester can generate good off-resonance performance over a relatively wide frequency band.

Figure 14 shows the power output FRFs of the three-layer harvester with the Type 2 piezoelectric layer location. In this case, because the tip of the base is occupied by the piezoelectric layer, the positions of M_{+1} is fixed to 0. Apparently, the anti-resonance areas between modes 1 and 2 and modes 2 and 3 are both eliminated. However, although the off-resonance performance is good between modes 1 and 2, the performance around mode 3 is much worse than modes 1 and 2. If all the three modes have close resonance frequencies with the same level of power output, the off-resonance performance can be significantly improved.

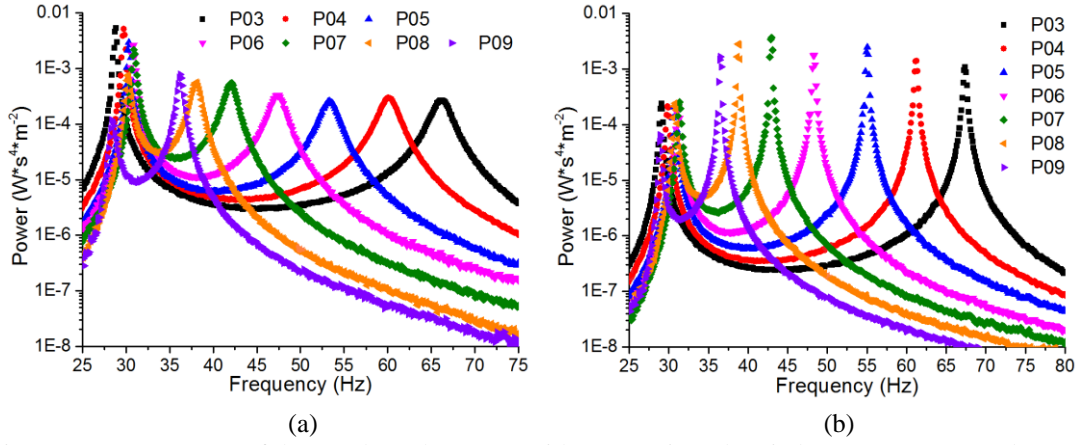


Figure 12: Power FRFs of the two-layer harvester with type 2 piezoelectric layer. (a): PIMNT; (b): PZT.

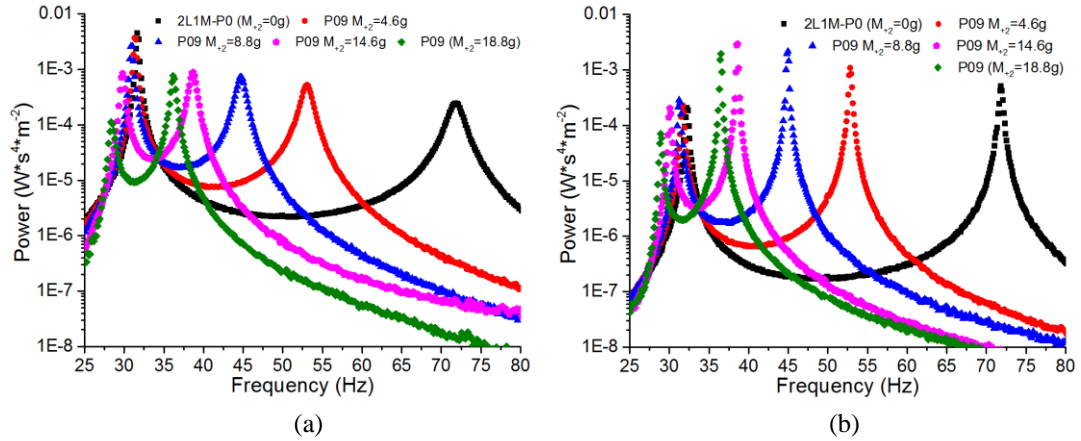


Figure 13: Power FRFs of the two-layer harvester with mass position P09 and different magnitude of M_{+2} (type 2). (a): PIMNT; (b): PZT.

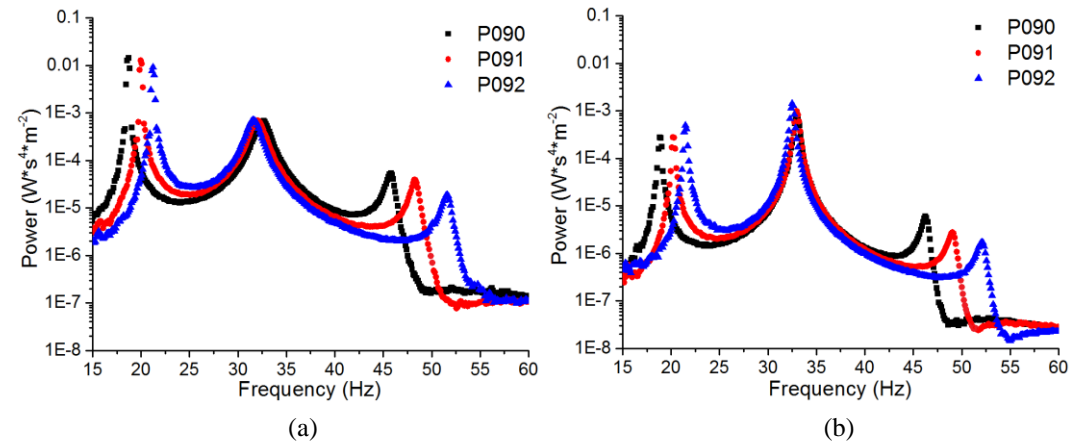


Figure 14: Power FRFs of the three-layer harvester (type 2). (a): PIMNT; (b): PZT.

4. Broadband performance comparison

Figure 15 shows the comparison of power output FRFs between some typical multi-layer harvesters and a single layer harvester *ILIM* with mass position $M_{+1}=0$ (a cantilevered beam harvester with a tip mass) using both PIMNT and PZT. The three-layer harvester with mass position P292 has very good performance in comparison with the single layer and the two-layer harvesters. However, the two-layer harvester with Type 2 piezoelectric layer location has not provided evident improvement.

Since the multi-layer harvesters can generate close resonance frequencies and relatively large power output in each mode, the effective bandwidth over a specified power level should be increased in comparison with a single layer harvester. The chosen power level should be low to avoid the effects of damping at each resonance. Figure 16 shows the bandwidth comparison between the single layer and multi-layer harvesters. In Figure 16 (a), the effective bandwidth is for the minimal power output $10^{-5} \text{ W*s}^4/\text{m}^2$, and the corresponding minimal voltage with $200 \text{ k}\Omega$ resistive load is $2 \text{ V*s}^2/\text{m}$. In Figure 16 (b), the bandwidth is for the power output larger than $4*10^{-5} \text{ W*s}^4/\text{m}^2$ and the corresponding voltage is larger than $4 \text{ V*s}^2/\text{m}$. The results show, firstly, that the two-layer harvester can generate nearly 1.5 times wider bandwidth and the three-layer harvesters can generate nearly 2 times wider bandwidth compared with the single layer cantilevered harvester *ILIM*. However, the two-layer harvester with the Type 2 piezoelectric layer location does not improve the bandwidth. This is due to several reasons. The Type 2 piezoelectric layer location may not cover the area with maximum strain and self-cancellations may occur due to the strain distribution of the beam in the higher modes. Furthermore, for the same configuration, the harvester using PIMNT can generate more than 3.5 times wider bandwidth than using PZT. Therefore, in comparison with the three-layer harvester using PIMNT and the single cantilevered beam harvester using PZT, 7 times wider bandwidth can be generated. This allows the harvester to provide a 43.3 Hz bandwidth over the frequency range from 10 Hz to 100 Hz.

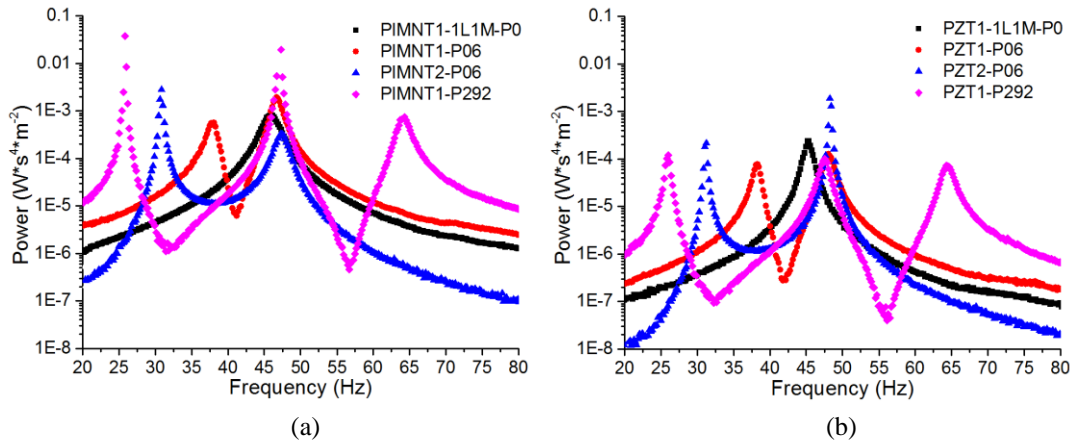


Figure 15: Comparison of power FRFs between single layer harvester *ILIM-PO* and typical multi-layer harvesters. (a): PIMNT; (b): PZT.

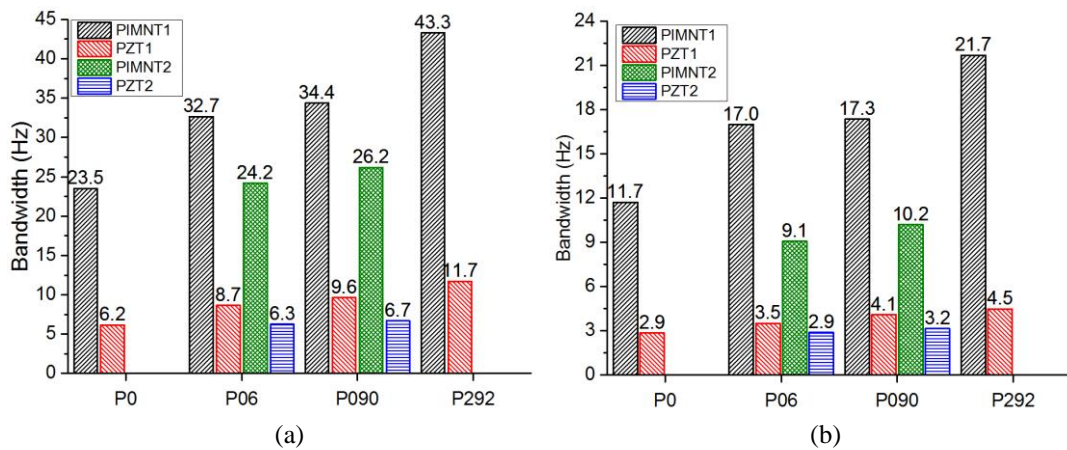


Figure 16: Bandwidth comparison between the multi-layer harvesters using PIMNT and PZT with Type 1 and Type 2 piezoelectric layer; (a) bandwidth for $1*10^{-5} \text{ W*s}^4/\text{m}^2$ ($2 \text{ V*s}^2/\text{m}$); (b) bandwidth for $4*10^{-5} \text{ W*s}^4/\text{m}^2$ ($4 \text{ V*s}^2/\text{m}$).

5. Conclusions

In this article, the broadband performances of multi-layer vibration energy harvesters are measured experimentally and compared. The multi-layer energy harvester consists of a cantilevered base beam and up to two upper beams. Rigid masses are used as spacers between two adjacent beam layers. The two-layer and three-layer harvesters can generate two and three close resonance frequencies, respectively. By varying the mass positions, relatively large power output in each mode can be achieved. The mass positions P05 and P06 for the two-layer harvester and the mass position P292 for the three-layer harvester are preferred to generate better performance. In comparison with a single cantilevered beam harvester with a tip mass, the two-layer and three-layer harvesters can generate nearly 1.5 and 2 times wider bandwidth of power output.

Two different piezoelectric materials, PIMNT and PZT, are used with the same configuration for comparison. The piezoelectric layer is bonded on the top surface of the base layer with two types of locations, which are designated as Type 1 and Type 2. In Type 1 location, the piezoelectric layer is near the clamped end. In Type 2 location, it is between the middle and the free tip of the base layer. For the same configuration, using PIMNT can generate nearly 10 times larger power output than using PZT for both resonance and off-resonance conditions. For the broadband performance comparison with Type 1 piezoelectric layer location, using PIMNT can generate more than 3.5 times wider bandwidth than using PZT. In particular, if the minimal power output is set as $10^{-5} \text{ W}\cdot\text{s}^4/\text{m}^2$, the three-layer harvester using PIMNT can generate 43.3 Hz bandwidth over the frequency range from 10 Hz to 100 Hz, whereas the single cantilevered beam harvester with a tip mass only generates 6.2 Hz bandwidth. The results show that using the Type 2 piezoelectric layer location can eliminate the anti-resonance area between two adjacent modes. However, it does not improve the broadband performance effectively.

Reference

- [1] Cook-Chennault, K. A., Thambi, N. and Sastry, A. M. (2008). Powering MEMS portable devices—a review of non-regenerative and regenerative power supply systems with special emphasis on piezoelectric energy harvesting systems. *Smart Materials and Structures*, 17(4), 043001.
- [2] Anton, S. R. and Sodano, H. A. (2007). A review of power harvesting using piezoelectric materials (2003–2006). *Smart materials and Structures*, 16(3), R1.
- [3] Roundy, S., Wright, P. K. and Rabaey, J. (2003). A study of low level vibrations as a power source for wireless sensor nodes. *Computer communications*, 26(11), 1131-1144.
- [4] Tang, L., Yang, Y. and Soh, C. K. (2010). Toward broadband vibration-based energy harvesting. *Journal of Intelligent Material Systems and Structures*, 21(18), 1867-1897.
- [5] Song, H. J., Choi, Y. T., Wang, G. and Wereley, N. M. (2009). Energy harvesting utilizing single crystal PMN-PT material and application to a self-powered accelerometer. *Journal of Mechanical Design*, 131(9), 091008.
- [6] Moon, S. E., Lee, S. Q., Lee, S. K., Lee, Y. G., Yang, Y. S., Park, K. H. and Kim, J. (2009). Sustainable vibration energy harvesting based on Zr-doped PMN-PT piezoelectric single crystal cantilevers. *ETRI journal*, 31(6), 688-694.
- [7] Rakbamrung, P., Lallart, M., Guyomar, D., Muensit, N., Thanachayanont, C., Lucat, C. and Sukwisut, P. (2010). Performance comparison of PZT and PMN–PT piezoceramics for vibration energy harvesting using standard or nonlinear approach. *Sensors and Actuators A: Physical*, 163(2), 493-500.

- [8] Ren, K., Liu, Y., Geng, X., Hofmann, H. F. and Zhang, Q. M. (2006). Single crystal PMN-PT/epoxy 1-3 composite for energy-harvesting application. *IEEE Transactions on Ultrasonics, Ferroelectrics and Frequency Control*, 53(3), 631-638.
- [9] Wang, Q. M., Sun, C. and Qin, L. (2008). Piezoelectric energy harvesting using single crystal Pb (Mg_{1/3}Nb_{2/3}) O₃-xPbTiO₃ (PMN-PT) device. *Journal of Intelligent Material Systems and Structures*. 20(5), 559-568.
- [10] Ferrari, M., Ferrari, V., Guizzetti, M., Marioli, D. and Taroni, A. (2008). Piezoelectric multifrequency energy converter for power harvesting in autonomous microsystems. *Sensors and Actuators A: Physical*, 142(1), 329-335.
- [11] Lumentut, M. F., Francis, L. A. and Howard, I. M. (2012). Analytical techniques for broadband multielectromechanical piezoelectric bimorph beams with multifrequency power harvesting. *IEEE Transactions on Ultrasonics, Ferroelectrics and Frequency Control*, 59(11), 2555-2568.
- [12] Ou, Q., Chen, X., Gutschmidt, S., Wood, A., Leigh, N. and Arrieta, A. F. (2012). An experimentally validated double-mass piezoelectric cantilever model for broadband vibration-based energy harvesting. *Journal of Intelligent Material Systems and Structures*, 23(2), 117-126.
- [13] Zhou, W., Penamalli, G. R. and Zuo, L. (2012). An efficient vibration energy harvester with a multi-mode dynamic magnifier. *Smart Materials and Structures*, 21(1), 015014.
- [14] WU, H., TANG, L., YANG, Y. and SOH, C. K. (2013). A novel two-degrees-of-freedom piezoelectric energy harvester. *Journal of intelligent material systems and structures*, 24(3), 357-368.

CHAPTER 13 CONCLUSIONS AND FUTURE WORKS

13.1 Conclusions and summary of findings

The investigation presented in this thesis has been focused on the multi-resonance vibration energy harvester designs. A modal approach is introduced to identify the modal structural and eletromechanical performance of harvesters using mass ratio and EMCC, respectively. A configurational optimization strategy for multi-resonance harvesters is developed using the modal approach before operating full DPM analysis. Several novel multi-resonance harvesters are developed with in-depth analysis. The multi-resonance harvesters with optimal or near-optimal performances selected by the configurational optimization strategy significantly improve the broadband performance. The experimental results are compared to the theoretical results and the modal approach and the optimization strategy have been successfully validated.

The detailed findings and conclusions from Chapters 5 to 12 are summarised in this section.

Summary of findings of cantilevered beam harvesters (chapter 5)

This chapter presents a detailed and in-depth optimization of mass ratio and EMCC of cantilevered beam harvesters with geometric parameter study. The system modal electromechanical coupling combines the effects from EMCC and damping ratio simultaneously. The EMCC does not affect the maximum power density when the eletromechanical coupling is adequately strong. The influences of modal mechanical behaviour on the volumetric power can be represented by the mass ratio, which represents how much mass effectively participates in the motion and affects power density linearly.

For harvesters with full piezoelectric coverage, due to self-cancellations in the higher modes, the EMCC of the RC harvester in mode 1 is nearly 2 and 3 times larger than in modes 2 and 3, respectively. A wide and short RC harvester can generate 10% more EMCC in mode 1 than a long and narrow RC harvester. For harvesters with limited

piezoelectric coverage, using DTC structure is able to generate good EMCC with much smaller coverage than using RC and CTC structures. Moving masses from the tip to the centre of the beam is able to decrease the effective length of the beam and increase EMCC in mode 1 by more than 25%.

Using tip masses can increase mass ratio and power density by more than 40% in mode 1. Besides, when the extra mass is located between the free tip and the centre of the beam, the mass ratio is only slightly changed. Using DTC structure can increase the mass ratio by 20% in mode 1. However, using CTC structure decreases the mass ratio in mode 1 by more than 20%. If the system coupling is not too weak, using CTC structure will actually generate lower power density than using RC and DTC structures.

Summary of findings of multi-layer harvesters (chapters 6 to 9)

Novel multi-layer harvesters, which consist of a base beam that is connected to upper/lower beams by rigid masses, are developed and systematically analysed in these chapters. It has been found that a mode with too large a mass ratio will make the rest of the modes to have small mass ratios and poor performance. Meanwhile, if the interval between two modes becomes too large, the anti-resonance can also significantly affect the performance. Therefore, the primary design objective of the multi-layer harvesters is to determine preferred configurations that can have modes that are close enough and evenly distributed mass ratio. The modal frequencies and mass ratio can be more easily varied by simply relocating the mass positions in harvester models.

For two-layer harvesters with one mass, CTC models are able to provide better broadband power output than RC models, and DTC models cannot generate good broadband performance. DTC models with two masses can generate a good structural broadband performance in comparison with DTC models with one mass. For DTC, RC and CTC two-layer harvesters, the model with evenly distributed mass ratios in multi-modes normally also generates acceptable EMCC in multi-modes. This may emphasise the importance and convenience for using the configurational optimization strategy in general multi-resonance harvester designs.

For multi-layer harvesters, using the optimization strategy enables the analysis and

comparison of all possible configurations conveniently, and ultimately enables significant reduction of the number of configurations that require full analysis. The screening results using the optimization strategy show that the two-sided three-layer configuration is better for the three-layer harvester designs.

The anti-resonance between two adjacent modes can be eliminated when the base layer is fully covered with PZT. However, for the three-layer and four-layer harvesters, the resonance performances at some modes are significantly reduced due to the strong self-cancellation. Moreover, variation of the structural damping level barely affects the off-resonance but it significantly affects the resonance and anti-resonance performance. Therefore, a model without anti-resonance between two modes may help to enhance the ability for broadband power output.

For multi-layer harvesters with doubly clamped base layer, the preferred base thickness is around 1.25 to 1.5 times thicker than the upper/lower layers. If the masses are located very close to the centre of the base layer, the length difference between the four cantilevered beam parts is too small. Then, some vibration modes become too close and generate strong structural coupling, and some modes become inactive.

Summary of findings of equivalent circuit method (chapter 10)

In this chapter, an easy implementation of a fully coupled ECM, which uses lumped modal parameter with correction factors, is introduced for multi-resonance harvester designs. Using FEA-ECM-SPICE model can generate almost the same power output FRFs with resistive loads in comparison with using FEA-DPM.

The findings also indicate that four steps are required to derive the modal parameters from FEA data using ECM and DPM while the ECM given by Yang and Tang [28] not only requires six steps, it also requires longer computing time for the FEA and a longer time to process the FEA data. Thus, the FEA-ECM-SPICE approach presented in this chapter is easier to implement and quicker to run.

Summary of findings of experimental study of multi-layer harvesters (chapters 11 and 12)

These chapters present experimental studies to validate the optimal design study of multi-layer harvesters. The harvesters with up to four layers are tested and the modal approach and the optimization strategy are validated based on the test results.

The bandwidth comparison shows that the two-layer and three-layer harvesters can generate more than 1.5 and 2 times wider bandwidth, respectively, than a single layer harvester with a tip mass. For minimal power output of over $10^{-5} \text{ W*s}^4/\text{m}^2$ ($1.41 \text{ V*s}^2/\text{m}$), the three-layer harvester can generate 25.5 Hz bandwidth over the frequency range from 10 Hz to 100 Hz. However, the four-layer harvester generates narrower bandwidth than the three-layer harvesters due to the smaller values of its EMCC. The EMCC of the two-layer harvester in the first two modes are slightly reduced compared with a cantilevered beam harvester. The EMCC of the three-layer harvesters in some modes are reduced significantly but they are still acceptable. The four-layer harvester generates the lowest EMCC in modes 2 and 4.

Under the same configuration, using PIMNT can generate approximately 10 times larger power output than using PZT for both resonance and off-resonance conditions. Besides, using PIMNT can generate more than 3.5 times wider bandwidth than using PZT. For minimal power output of over $10^{-5} \text{ W*s}^4/\text{m}^2$ ($2 \text{ V*s}^2/\text{m}$), the three-layer PIMNT-harvester can generate 43.3 Hz bandwidth over the frequency range from 10 Hz to 100 Hz, and this bandwidth is 7 times wider than the bandwidth of a single layer harvester with a tip mass (with the same piezo-layer location).

When the piezo-layer is bonded between the middle and the free tip of the base layer, the anti-resonance area between two adjacent modes can be eliminated. It does not effectively improve the total bandwidth. However, in real applications, if the vibration energy is distributed over a wide frequency band between multiple modes, the deep notch of the anti-resonance area may affect the broadband performance. Then, successful elimination of the anti-resonance will generate a smoother bandwidth and enhance the broadband performance of a harvester.

13.2 Proposals for future work

In this section, critical thinking of the thesis and recommendation of areas in which further work can be undertaken is outlined.

- The theoretical analysis provided in this thesis is FEA-based numerical analysis. Although several multi-resonance harvesters with good broadband performance are successfully developed, optimized and experimentally validated, the corresponding analytical models have not been provided due to the complexity of the configurations. Hence, it may significantly contribute to the research field if the analytical solutions for the multi-layer harvesters can be successfully developed in future work.
- The nonlinear harvester with magnets can also significantly improve the broadband performance. The advantage is that the bent response curve of a nonlinear harvester can widen the bandwidth and improve the off-resonance performance in comparison with the linear harvester. For multi-layer harvester designs, the extra masses can be replaced by magnets to introduce external magnetic forces. If the nonlinear behaviour can be successfully achieved with close resonance frequencies and large power output in each mode, the anti-resonance areas between two adjacent modes may be effectively eliminated. Then, a much smoother power output in an even wider frequency band may be achieved.
- Damping is also an important factor that affects the performance of harvesters significantly. Because this thesis mainly focuses on the configurational study of the multi-resonance harvesters, structural damping has been used in simulation for the convenience of performance comparison. Experimental devices are normally controlled to have light to medium damping using damping foils. The performance with different level of damping has not been adequately explored. Besides, the real damping can be frequency dependent and nonlinear. For example, the strong nonlinear behaviour of harvester can be achieved in conjunction with a very small damping. Therefore, an in-depth study of the effect of damping is recommended in future work especially for the development of nonlinear harvesters.
- PIMNT is used and tested in this thesis. However, due to the limitation of experimental condition in the laboratory, the accurate piezoelectric performance of the PIMNT patches cannot be tested. The manufacturer, Shanghai Institute of Ceramics, Chinese Academy of Sciences, also cannot provide the accurate material properties. Therefore, material performance determination is recommended for future work.

Besides, since the nonlinear harvester normally requires large deflection, 1-3 and 2-2 piezoelectric composites using PIMNT is highly recommended for nonlinear harvester study.

- This thesis has not provided any circuit investigation for energy storage. Although it is beyond the scope of the study, in real application, the storage circuit is a very important component of the vibration energy harvesting system. Hence, the ECM provided in this thesis may be used to develop the nonlinear circuit simulation for multi-resonance harvesters in future works. Since SPICE is widely used for nonlinear circuit simulation, the FEA-ECM-SPICE model presented in this chapter can be developed further to include linear and nonlinear power storage circuit.

REFERENCE

- [1] Chopra, I. and Sirohi, J. (2013). *Smart structures theory*. Cambridge University Press.
- [2] Arms, S. W., Townsend, C. P., Churchill, D. L., Galbreath, J. H. and Mundell, S. W. (2005). Power management for energy harvesting wireless sensors. *SPIE Smart Structures/NDE proceedings*, 267-275.
- [3] Beeby, S. P., Tudor, M. J. and White, N. M. (2006). Energy harvesting vibration sources for microsystems applications. *Measurement science and technology*, 17(12), R175.
- [4] Cook-Chennault, K. A., Thambi, N. and Sastry, A. M. (2008). Powering MEMS portable devices—a review of non-regenerative and regenerative power supply systems with special emphasis on piezoelectric energy harvesting systems. *Smart Materials and Structures*, 17(4), 043001.
- [5] Hudak, N. S. and Amatucci, G. G. (2008). Small-scale energy harvesting through thermoelectric, vibration, and radiofrequency power conversion. *Journal of Applied Physics*, 103(10), 101301.
- [6] Paradiso, J. A. and Starner, T. (2005). Energy scavenging for mobile and wireless electronics. *Pervasive Computing, IEEE*, 4(1), 18-27.
- [7] Harrop, P. (2009). Energy harvesting and storage for electronic devices 2009-2019. *IDTechEx report*.
- [8] Anton, S. R. and Sodano, H. A. (2007). A review of power harvesting using piezoelectric materials (2003–2006). *Smart materials and Structures*, 16(3), R1.
- [9] Sodano, H. A., Inman, D. J. and Park, G. (2004). A review of power harvesting from vibration using piezoelectric materials. *Shock and Vibration Digest*, 36(3), 197-206.
- [10] Khaligh, A., Zeng, P. and Zheng, C. (2010). Kinetic energy harvesting using piezoelectric and electromagnetic technologies—state of the art. *IEEE Transactions on Industrial Electronics*, 57(3), 850-860.
- [11] Beeby, S. P., Torah, R. N., Tudor, M. J., Glynne-Jones, P., O'Donnell, T., Saha, C. R. and Roy, S. (2007). A micro electromagnetic generator for vibration energy harvesting. *Journal of Micromechanics and microengineering*, 17(7), 1257.
- [12] Roundy, S., Leland, E. S., Baker, J., Carleton, E., Reilly, E., Lai, E., ... and Sundararajan, V. (2005). Improving power output for vibration-based energy scavengers. *Pervasive Computing, IEEE*, 4(1), 28-36.
- [13] Roundy, S., Wright, P. K. and Rabaey, J. (2003). A study of low level vibrations as a power source for wireless sensor nodes. *Computer communications*, 26(11), 1131-1144.
- [14] Ikeda, T. 1990. *Fundamentals of Piezoelectricity*, Oxford University Press, Oxford.
- [15] Siu Wing Or, “Overview of Smart Materials Technology”. http://resources.emb.gov.hk/physics/articleIE/smartmaterials/SmartMaterials_e.htm
- [16] Crawley, E. F. and De Luis, J. (1987). Use of piezoelectric actuators as elements of intelligent structures. *AIAA journal*, 25(10), 1373-1385.
- [17] Dineva, P., Gross, D., Müller, R. and Rangelov, T.(2014). “Chapter 2: Piezoelectric Materials” in *Dynamic Fracture of Piezoelectric Materials*, Springer, 2014
- [18] Gordon, C. G. (1999). Generic vibration criteria for vibration-sensitive equipment. *SPIE's International Symposium on Optical Science, Engineering, and Instrumentation, proceedings* ,22-33.
- [19] Berdy, D. F., Srisungsitthisunti, P., Jung, B., Xu, X., Rhoads, J. F. and Peroulis, D. (2012). Low-frequency meandering piezoelectric vibration energy harvester. *IEEE Transactions on Ultrasonics, Ferroelectrics and Frequency Control*, 59(5), 846-858.
- [20] Erturk, A. and Inman, D. J. (2008). A distributed parameter electromechanical model for cantilevered piezoelectric energy harvesters. *Journal of Vibration and Acoustics*, 130(4), 041002.
- [21] Erturk, A. and Inman, D. J. (2011). Piezoelectric energy harvesting. *John Wiley and Sons*, 978-1-1199-9135-9
- [22] Bourisli, R. I. and Al-Ajmi, M. A. (2010). Optimization of Smart Beams for Maximum

- Modal Electromechanical Coupling Using Genetic Algorithms. *Journal of Intelligent Material Systems and Structures*, 21(9), 907-914.
- [23] Tang, L. and Yang, Y. (2012). A multiple-degree-of-freedom piezoelectric energy harvesting model. *Journal of Intelligent Material Systems and Structures*, 23(14), 1631-1647.
- [24] Renno, J. M., Daqaq, M. F. and Inman, D. J. (2009). On the optimal energy harvesting from a vibration source. *Journal of Sound and Vibration*, 320(1), 386-405.
- [25] Guyomar, D., Sebald, G., Pruvost, S., Lallart, M., Khodayari, A. and Richard, C. (2009). Energy Harvesting from Ambient Vibrations and Heat. *Journal of Intelligent Material Systems and Structures*, 20(5), 609-624.
- [26] Lee, S., Youn, B. D. and Jung, B. C. (2009). Robust segment-type energy harvester and its application to a wireless sensor. *Smart Materials and Structures*, 18(9), 095021.
- [27] WU, H., TANG, L., YANG, Y. and SOH, C. K. (2013). A novel two-degrees-of-freedom piezoelectric energy harvester. *Journal of intelligent material systems and structures*, 24(3), 357-368.
- [28] Yang, Y. and Tang, L. (2009). Equivalent circuit modeling of piezoelectric energy harvesters. *Journal of Intelligent Material Systems and Structures*. 20(18), 2223-2235.
- [29] Lesieutre, G. A. and Davis, C. L. (1997, June). Can a coupling coefficient of a piezoelectric device be higher than those of its active material?. *SPIE Smart Structures/NDE proceedings*, 281-292.
- [30] Xiong, X. and Oyadiji, S. O. (2014). Modal electromechanical optimization of cantilevered piezoelectric vibration energy harvesters by geometric variation. *Journal of Intelligent Material Systems and Structures*, 25(10), 1177-1195.
- [31] Baker, J., Roundy, S. and Wright, P. (2005). Alternative geometries for increasing power density in vibration energy scavenging for wireless sensor networks. *3rd Int. Energy Conversion Engineering Conf. Proc. (San Francisco, CA, Aug.)*, 959-970.
- [32] Song, H. J., Choi, Y. T., Wereley, N. M. and Purekar, A. (2014). Comparison of monolithic and composite piezoelectric material-based energy harvesting devices. *Journal of Intelligent Material Systems and Structures*, 1045389X14530592.
- [33] Sodano, H. A. (2003). Macro-fiber composites for sensing, actuation and power generation, *Doctoral dissertation, Virginia Polytechnic Institute and State University*.
- [34] Tobin, A. G. and Pak, E. (1993, July). Effect of electric fields on fracture behavior of PZT ceramics. *SPIE Smart Structures/NDE proceedings*, 78-86.
- [35] Taylor, G. W., Burns, J. R., Kammann, S. A., Powers, W. B. and Welsh, T. R. (2001). The energy harvesting eel: a small subsurface ocean/river power generator. *Oceanic Engineering, IEEE Journal of*, 26(4), 539-547.
- [36] Sodano, H. A., Inman, D. J. and Park, G. (2005). Comparison of piezoelectric energy harvesting devices for recharging batteries. *Journal of Intelligent Material Systems and Structures*, 16(10), 799-807.
- [37] Fang, H. B., Liu, J. Q., Xu, Z. Y., Dong, L., Wang, L., Chen, D., ... and Liu, Y. (2006). Fabrication and performance of MEMS-based piezoelectric power generator for vibration energy harvesting. *Microelectronics Journal*, 37(11), 1280-1284
- [38] Dai, X., Wen, Y., Li, P., Yang, J. and Zhang, G. (2009). Modeling, characterization and fabrication of vibration energy harvester using Terfenol-D/PZT/Terfenol-D composite transducer. *Sensors and Actuators A: Physical*, 156(2), 350-358.
- [39] Yang, Y., Tang, L. and Li, H. (2009). Vibration energy harvesting using macro-fiber composites. *Smart materials and structures*, 18(11), 115025.
- [40] Newnham, R. E., Bowen, L. J., Klicker, K. A. and Cross, L. E. (1980). Composite piezoelectric transducers. *Materials and Design*, 2(2), 93-106.
- [41] Xu, D., Qin, L., Huang, S. and Cheng, X. (2012). Fabrication and properties of piezoelectric composites designed for process monitoring of cement hydration reaction. *Materials Chemistry and Physics*, 132(1), 44-50.
- [42] Huang, S., Chang, J., Lu, L., Liu, F., Ye, Z. and Cheng, X. (2006). Preparation and polarization of 0-3 cement based piezoelectric composites. *Materials research bulletin*, 41(2), 291-297

- [43] Jeon, Y. B., Sood, R., Jeong, J. H. and Kim, S. G. (2005). MEMS power generator with transverse mode thin film PZT. *Sensors and Actuators A: Physical*, 122(1), 16-22.
- [44] Dorey, R. A. and Whatmore, R. W. (2004). Electrical properties of high density PZT and PMN-PT/PZT thick films produced using ComFi technology. *Journal of the European Ceramic Society*, 24(6), 1091-1094.
- [45] Kok, S. L., White, N. M. and Harris, N. R. (2009). Fabrication and characterization of free-standing thick-film piezoelectric cantilevers for energy harvesting. *Measurement Science and Technology*, 20(12), 124010.
- [46] Banerjee, S. and Cook-Chennault, K. A. (2011). Influence of Al Particle Size and Lead Zirconate Titanate (PZT) Volume Fraction on the Dielectric Properties of PZT-Epoxy-Aluminum Composites. *Journal of Engineering Materials and Technology*, 133(4), 041016.
- [47] Le, D. T., Do, N. B., Kim, D. U., Hong, I., Kim, I. W. and Lee, J. S. (2012). Preparation and characterization of lead-free (K_{0.47}Na_{0.51}Li_{0.02})(Nb_{0.8}Ta_{0.2})O₃ piezoceramic/epoxy composites with 0–3 connectivity. *Ceramics International*, 38(Supplement 1), S259-S262.
- [48] Ferrari, M., Ferrari, V., Marioli, D. and Taroni, A. (2006). Modeling, fabrication and performance measurements of a piezoelectric energy converter for power harvesting in autonomous microsystems. *IEEE transactions on instrumentation and measurement*, 55(6), 2096-2101.
- [49] Kim, Y.K., Lee, J.H. and Kim, D. (2007). Performance of PZT-epoxy Composite Power Generator for Vibration Energy Harvesting. *10th International Conference and Exhibition of the European Ceramic Society*
- [50] Wang, L. (2011). Design, Fabrication and Experimental Analysis of Piezoelectric Energy Harvesters with Non-traditional Geometries. *Master of Science Thesis, The State University of New Jersey*.
- [51] Wegener, M. and Arlt, K. (2008). PZT/P (VDF-HFP) 0–3 composites as solvent-cast thin films: preparation, structure and piezoelectric properties. *Journal of Physics D: Applied Physics*, 41(16), 165409.
- [52] Oyadiji, S. O., Qi, S. and Shuttleworth, R. (2010). Development of Multiple Cantilevered Piezo Fibre Composite Beams Vibration Energy Harvester for Wireless Sensors. In *Engineering Asset Lifecycle Management* (pp. 697-704). Springer London.
- [53] Qi, S., Shuttleworth, R., Oyadiji, S. O. and Wright, J. (2010). Design of a multiresonant beam for broadband piezoelectric energy harvesting. *Smart Materials and Structures*, 19(9), 094009.
- [54] Swallow, L. M., Luo, J. K., Siores, E., Patel, I. and Dodds, D. (2008). A piezoelectric fibre composite based energy harvesting device for potential wearable applications. *Smart Materials and Structures*, 17(2), 025017.
- [55] Song, H. J., Choi, Y. T., Wang, G. and Wereley, N. M. (2009). Energy harvesting utilizing single crystal PMN-PT material and application to a self-powered accelerometer. *Journal of Mechanical Design*, 131(9), 091008.
- [56] Moon, S. E., Lee, S. Q., Lee, S. K., Lee, Y. G., Yang, Y. S., Park, K. H. and Kim, J. (2009). Sustainable vibration energy harvesting based on Zr-doped PMN-PT piezoelectric single crystal cantilevers. *ETRI journal*, 31(6), 688-694.
- [57] Roundy, S. and Wright, P. K. (2004). A piezoelectric vibration based generator for wireless electronics. *Smart Materials and structures*, 13(5), 1131.
- [58] Ferrari, M., Ferrari, V., Guizzetti, M., Marioli, D. and Taroni, A. (2008). Piezoelectric multifrequency energy converter for power harvesting in autonomous microsystems. *Sensors and Actuators A: Physical*, 142(1), 329-335.
- [59] Ren, K., Liu, Y., Geng, X., Hofmann, H. F. and Zhang, Q. M. (2006). Single crystal PMN-PT/epoxy 1-3 composite for energy-harvesting application. *IEEE Transactions on Ultrasonics, Ferroelectrics and Frequency Control*, 53(3), 631-638.
- [60] Zhang, Y., Wang, S., Liu, D. A., Zhang, Q., Wang, W., Ren, B. and Luo, H. (2011). Fabrication of angle beam two-element ultrasonic transducers with PMN-PT single crystal and PMN-PT/epoxy 1–3 composite for NDE applications. *Sensors and Actuators*

- A: Physical*, 168(1), 223-228.
- [61] Richter, B., Twiefel, J., Sattel, T. and Wallaschek, J. (2007, April). Design method for piezoelectric bending generators in energy harvesting systems. *SPIE Smart Structures/NDE proceedings*, 652504.
- [62] Erturk, A. and Inman, D. J. (2008). On Mechanical Modeling of Cantilevered Piezoelectric Vibration Energy Harvesters. *Journal of Intelligent Material Systems and Structures*, 19(11), 1311-1325.
- [63] Erturk, A. and Inman, D.J.(2007). On Mechanical Modeling of Cantilevered Piezoelectric Vibration Energy Harvesters. *IDETC/CIE*, September 4-7.
- [64] Zhu, M.Z., Worthington, E. and Tiwari, A. (2010). Design Study of Piezoelectric Energy-Harvesting Devices for Generation of Higher Electrical Power Using a Coupled Piezoelectric-Circuit Finite Element Method. *IEEE Transactions on Ultrasonics, Ferroelectrics, and Frequency Control*, vol. 57, no. 2
- [65] Patel, R., McWilliam, S. and Popov, A. A. (2011). A geometric parameter study of piezoelectric coverage on a rectangular cantilever energy harvester. *Smart Materials and Structures*, 20(8), 085004.
- [66] Erturk, A., Tarazaga, P. A., Farmer, J. R. and Inman, D. J. (2009). Effect of strain nodes and electrode configuration on piezoelectric energy harvesting from cantilevered beams. *Journal of Vibration and Acoustics*, 131(1), 011010.
- [67] Friswell, M. I. and Adhikari, S. (2010). Sensor shape design for piezoelectric cantilever beams to harvest vibration energy. *Journal of Applied Physics*, 108(1), 014901.
- [68] Glynne-Jones, P., Beeby, S. P. and White, N. M. (2001). Towards a piezoelectric vibration-powered microgenerator. *IEEE Proceedings-Science, measurement and technology*, 148(2), 68-72.
- [69] Wang, W., Yang, T., Chen, X. and Yao, X. (2012). Vibration energy harvesting using a piezoelectric circular diaphragm array. *IEEE Transactions on Ultrasonics, Ferroelectrics and Frequency Control*, 59(9), 2022-2026.
- [70] Lumentut, M. F., Francis, L. A. and Howard, I. M. (2012). Analytical techniques for broadband multielectromechanical piezoelectric bimorph beams with multifrequency power harvesting. *IEEE Transactions on Ultrasonics, Ferroelectrics and Frequency Control*, 59(11), 2555-2568.
- [71] Ou, Q., Chen, X., Gutschmidt, S., Wood, A., Leigh, N. and Arrieta, A. F. (2012). An experimentally validated double-mass piezoelectric cantilever model for broadband vibration-based energy harvesting. *Journal of Intelligent Material Systems and Structures*, 23(2), 117-126.
- [72] Zhou, W., Penamalli, G. R. and Zuo, L. (2012). An efficient vibration energy harvester with a multi-mode dynamic magnifier. *Smart Materials and Structures*, 21(1), 015014.
- [73] Chen, Z., Yang, Y., Lu, Z. and Luo, Y. (2013). Broadband characteristics of vibration energy harvesting using one-dimensional phononic piezoelectric cantilever beams. *Physica B: Condensed Matter*, 410, 5-12.
- [74] Erturk, A., Renno, J. M. and Inman, D. J. (2008). Modeling of piezoelectric energy harvesting from an L-shaped beam-mass structure with an application to UAVs. *Journal of intelligent material systems and structures*, 20(5), 529-544.
- [75] Karami, M. A. and Inman, D. J. (2011). Analytical modeling and experimental verification of the vibrations of the zigzag microstructure for energy harvesting. *Journal of Vibration and Acoustics*, 133(1), 011002.
- [76] Karami, M. A. and Inman, D. J. (2011). Electromechanical modeling of the low-frequency zigzag micro-energy harvester. *Journal of Intelligent Material Systems and Structures*, 22(3), 271-282.
- [77] Tang, L., Yang, Y. and Soh, C. K. (2010). Toward broadband vibration-based energy harvesting. *Journal of Intelligent Material Systems and Structures*, 21(18), 1867-1897.
- [78] Pellegrini, S. P., Tolou, N., Schenk, M. and Herder, J. L. (2013). Bistable vibration energy harvesters: A review. *Journal of Intelligent Material Systems and Structures*, 24(11), 1303-1312.
- [79] Cammarano, A., Neild, S. A., Burrow, S. G. and Inman, D. J. (2014). The bandwidth of

- optimized nonlinear vibration-based energy harvesters. *Smart Materials and Structures*, 23(5), 055019.
- [80] Tang, L., Yang, Y. and Soh, C. K. (2012). Improving functionality of vibration energy harvesters using magnets. *Journal of Intelligent Material Systems and Structures*, 23(13), 1433-1449.
- [81] Erturk, A., Hoffmann, J. and Inman, D. J. (2009). A piezomagnetoelastic structure for broadband vibration energy harvesting. *Applied Physics Letters*, 94(25), 254102.
- [82] Eichhorn, C., Goldschmidtboeing, F. and Woias, P. (2008). A frequency tunable piezoelectric energy converter based on a cantilever beam. *Proceedings of PowerMEMS*, 9(12), 309-312.
- [83] Reissman, T., Wolff, E. M. and Garcia, E. (2009). Piezoelectric resonance shifting using tunable nonlinear stiffness. *SPIE Smart Structures/NDE proceedings*, 72880G.
- [84] Roundy, S. and Zhang, Y. (2005). Toward self-tuning adaptive vibration-based microgenerators. *SPIE Smart Structures/NDE proceedings*, pp. 373-384
- [85] Ottman, G. K., Hofmann, H. F., Bhatt, A. C. and Lesieutre, G. A. (2002). Adaptive piezoelectric energy harvesting circuit for wireless remote power supply. *IEEE Transactions on Power Electronics*, 17(5), 669-676.
- [86] Lefeuvre, E., Badel, A., Richard, C. and Guyomar, D. (2005). Piezoelectric energy harvesting device optimization by synchronous electric charge extraction. *Journal of Intelligent Material Systems and Structures*, 16(10), 865-876.
- [87] Rakbamrung, P., Lallart, M., Guyomar, D., Muensit, N., Thanachayanont, C., Lucat, C., ... and Sukwisut, P. (2010). Performance comparison of PZT and PMN-PT piezoceramics for vibration energy harvesting using standard or nonlinear approach. *Sensors and Actuators A: Physical*, 163(2), 493-500.
- [88] Qi, S. (2011). Investigation of a novel multiresonant beam energy harvester and a complex conjugate matching circuit. *Doctoral dissertation, University of Manchester*.
- [89] Shu, Y. C., Lien, I. C. and Wu, W. J. (2007). An improved analysis of the SSHI interface in piezoelectric energy harvesting. *Smart Materials and Structures*, 16(6), 2253
- [90] Lefeuvre, E., Badel, A., Richard, C. and Guyomar, D. (2005). Piezoelectric energy harvesting device optimization by synchronous electric charge extraction. *Journal of Intelligent Material Systems and Structures*, 16(10), 865-876.
- [91] Inman, D. J. and Singh, R. C. (2001). Engineering vibration. *Upper Saddle River: Prentice Hall*.
- [92] SIMULIA Corp, (2010) Abaqus Theory Manual in ABAQUS 6.10 Documentations.

APPENDIX A PIEZOELECTRIC CONSTITUTIVE EQUATIONS AND COUPLING COEFFICIENTS

Under the definition of IEEE standard for piezoelectricity (ANSI/IEEE Std 176, 1987), the d -form constitutive equation of piezoelectric material is given by

$$\begin{pmatrix} \mathbf{S} \\ \mathbf{D} \end{pmatrix} = \begin{pmatrix} \mathbf{s}^E & \mathbf{d}' \\ \mathbf{d} & \boldsymbol{\varepsilon}^T \end{pmatrix} \begin{pmatrix} \mathbf{T} \\ \mathbf{E} \end{pmatrix} \quad (\text{A. 1})$$

All above quantities are order 1 and 2 tensors. In particular, \mathbf{S} is the strain and \mathbf{T} is the stress. \mathbf{D} is the electric displacement, which is also known as the dielectric charge density displacement, and \mathbf{E} is the electric field. \mathbf{s}^E is the mechanical elastic compliance matrix defined as strain generated per unit stress under constant electric field (such as when $E_3 = 0$, $s_{11}^E = S_1/T_1$). $\boldsymbol{\varepsilon}^T$ is the electric permittivity defined as electric displacement per unit electric field under constant stress (such as when $T_1 = 0$, $\varepsilon_{33}^T = D_3/E_3$). \mathbf{d} is the piezoelectric coupling matrix in strain form, which represents the relationship between charge and stress and \mathbf{d}' are the transposed matrix of \mathbf{d} . For the transverse effect as well as operating in 31-mode for a harvester, the reduced scalar d -form is written as,

$$S_1 = s_{11}^E T_1 + d_{31} E_3 \quad (\text{A. 2})$$

$$D_3 = d_{31} T_1 + \varepsilon_{33}^T E_3 \quad (\text{A. 3})$$

Obviously, the relationship between strain and stress in piezoelectric materials is not only determined by the compliance but it is also related with the electric field. In addition, the strength of its electric displacement is correlated with both mechanical stress and electric field. The system interacts between mechanical and electrical domains, and a coupling coefficient gives the connection between them. The square of piezoelectric electro-mechanical coupling coefficient k^2 is defined as,

$$k_{31}^2 = \frac{d_{31}^2}{\varepsilon_{33}^T s_{11}^E} \quad (\text{A. 4})$$

In d -form, the independent variables are mechanical stress \mathbf{T} and electric field \mathbf{E} . In fact, the constitutive equations can be transformed into h -form, which has \mathbf{S} and \mathbf{D} as independent variables. The h -form is written as,

$$\begin{pmatrix} \mathbf{T} \\ \mathbf{E} \end{pmatrix} = \begin{pmatrix} \mathbf{c}^D & -\mathbf{h}' \\ -\mathbf{h} & \boldsymbol{\beta}^S \end{pmatrix} \begin{pmatrix} \mathbf{S} \\ \mathbf{D} \end{pmatrix} \quad (\text{A. 5})$$

Since the independent variables are changed, above factors are given in different terms, where \mathbf{c}^D is the elastic stiffness matrix under constant charge density and $\boldsymbol{\beta}^S$ is the

dielectric impermeability under constant strain condition. The reduced h -form's scalar equation of 31-mode is

$$T_1 = c_{11}^D S_1 - h_{31} D_3 \quad (\text{A. 6})$$

$$E_3 = -h_{31} S_1 + \beta_{33}^S D_3 \quad (\text{A. 7})$$

The corresponding scalar equations can also be presented using d -form's coefficients as,

$$T_1 = \frac{1}{S_{11}^E (1 - k_{31}^2)} S_1 - \frac{1}{d_{31}} \left(\frac{k_{31}^2}{1 - k_{31}^2} \right) D_3 \quad (\text{A. 8})$$

$$E_3 = -\frac{1}{d_{31}} \left(\frac{k_{31}^2}{1 - \vartheta_{31}^2} \right) S_1 + \frac{1}{\varepsilon_{33}^T (1 - k_{31}^2)} D_3 \quad (\text{A. 9})$$

The coupling coefficient in h -form is

$$k_{31}^2 = \frac{h_{31}^2}{\beta_{33}^T c_{11}^D} \quad (\text{A. 10})$$

Concerning the above two types of the constitutive equations, d -form is the intensive type which gives the expression of strain and charge density displacement, and h -form is the extensive type which presents the equation of stress and electric field. There are two other forms, which have the mixed relationship of the independent variables. The more common one is called e -form, and its constitutive equation is

$$\begin{pmatrix} \mathbf{T} \\ \mathbf{D} \end{pmatrix} = \begin{pmatrix} \mathbf{c}^E & -\mathbf{e}' \\ \mathbf{e} & \boldsymbol{\varepsilon}^S \end{pmatrix} \begin{pmatrix} \mathbf{S} \\ \mathbf{E} \end{pmatrix} \quad (\text{A. 11})$$

Its scalar equations for 31-mode for e -form is written as (given in Chapter 3),

$$T_1 = c_{11}^E S_1 - e_{31} E_3 \quad (\text{A. 12})$$

$$D_3 = e_{31} S_1 + \varepsilon_{33}^S E_3 \quad (\text{A. 13})$$

It should be noticed that, a different coupling coefficient has been introduced for the mixed situation as,

$$k_{e31}^2 = \frac{e_{31}^2}{c_{11}^E \varepsilon_{33}^S} \quad (\text{A. 14})$$

The relationship of k^2 and k_e^2 is given by

$$k_e^2 = \frac{k^2}{1 - k^2} \quad (\text{A. 15})$$